Space VLBI studies of internal structure and physical processes in extragalactic relativistic jets

INAUGURAL-DISSERTATION

zur
Erlangung des Doktorgrades
der Mathematisch-Naturwissenschaftlichen Fakultät
der Universität zu Köln

vorgelegt von

Laura Vega García

aus Benavides de Órbigo, Spanien

Köln 2019

Berichterstatter: Prof. Dr. Andreas Eckart
Prof. Dr. J. Anton Zensus

Tag der letzten mündlichen Prüfung: 18.10.2018

Abstract

Very Long Baseline Inteferometry (VLBI) provides imaging capability at a resolution smaller than one milliarcsecond, enabling detailed studies of the innermost regions of jets in Active Galactic Nuclei (AGN). The resolution of VLBI observations can be further improved by employing antennas on board of a satellite orbiting the Earth. In this thesis, we present multifrequency images of four prominent radio sources, 0836+710, 1642+690, 3C273, and 3C345, obtained with the space VLBI mission *RadioAstron*, and use these images to reconstruct the physical conditions in their parsec-scale jets. The observations were performed as part of the *RadioAstron* Key Science Program on strong AGN. The main scientific goals of this study are to obtain the distribution of spectral index, turnover frequency and flux density, to estimate the magnetic field in the nuclear regions, and to investigate the development of Kelvin-Helmholtz instability in the jet flow. The *RadioAstron* observations made at 1.6 GHz, 5 GHz, and 22 GHz were amended by ground VLBI data taken at 15 GHz, and 43 GHz when available. The resulting multifrequency data were used to investigate the spectral and opacity properties of the jets. To enable this study, we have developed a software which combines multifrequency image alignment, opacity measurements via the "core shift" effect, spectral index calculation, and mapping the distribution of the turnover frequency/flux density and magnetic field in the jet. The development of Kelvin-Helmholtz instability is studied based on the analysis of internal structure (ridgelines and internal filaments) of the flow obtained from transverse profiles of the jet brightness.

0836+710 was observed with *RadioAstron* at 1.6 GHz, 5 GHz, and 22 GHz between October 2013 and January 2014. A spectral analysis, together with a kinematic analysis, reveals the presence of a recollimation shock in the jet, at a distance of 0.15 mas from the jet origin. We use the core shift analysis and synchrotron spectrum fitting to estimate the magnetic field strength in the jet core, with both methods providing a consistent estimate of $B_{\rm core} \sim 0.03$ G at 5 GHz. We complement the analysis with an study of long-term kinematic evolution in the jet of 0836+710, relating it to the observed γ-ray flaring activity of the source. We find that intermittent flaring states of the source and the intensity of the flares could be explained by interactions between travelling shocks and the recollimation shock identified from the analysis of the *RadioAstron* observations. We use

the 1.6 GHz data to determine the ridgeline of the jet in 0836+710 and use it for investigating the development of Kelvin-Helmholtz instability in the flow. We identify several distinct modes of the instability and determine their wavelengths and growth lengths. This study allows us to derive relevant physical parameters such as the jet classical Mach number and density ratio with respect to the ambient medium. At last, the space VLBI image of 0836+710 at 22 GHz reveals a rich, asymmetric jet structure, which we interpret as resulting either from the differential Doppler boosting in a mildly rotating jet, or from a helical magnetic field.

The well-known quasar 3C 273 was observed with *RadioAstron* in April 2014 at 5 GHz and 22 GHz. Due to the challenging nature of the resulting data set, it was not possible to perform an extensive spectral analysis for this jet. A direct comparison of the jet transversal structure between our observations and previous VSOP observations at 5 GHz obtained in 1997, reveals a change in the angle of injection of the jet ridgeline. This allows us to obtain the pattern speed and rotational speed of the radio jet. This result is corroborated using publicly available multi-epoch VLBI data at 15 GHz from the MOJAVE monitoring program.

The quasar 1642+690 was observed with *RadioAstron* between December 2014 and January 2015 at 1.6 GHz, 5 GHz, and 22 GHz. A spectral analysis of this source also suggested the presence of a recollimation shock, located at $\sim$0.75 mas from the compact core. A study of the synchrotron spectrum reveals the potential presence of a strong magnetic field in the core region, as well as in the region of the putative recollimation shock.

At last, the quasar 3C 345 was observed with *RadioAstron* in April 2014 at 5 GHz and 22 GHz. However, no fringes with the space antenna were found at either of the two frequencies for most of the duration of the experiment, and therefore it is not possible to obtain additional information from the *RadioAstron* baselines with respect to the ground array observations. We use the resulting images to perform a spectral and turnover analysis of the source, estimating a magnetic field of $\sim$0.07 G in the core region at 5 GHz which is in a good agreement with previous estimates.

Zusammenfassung

Die bildgebende Technik Very Long Baseline Inteferometry (VLBI) bietet eine Bildauflösung von weniger als einer Millibogensekunde und ermöglicht detaillierte Untersuchungen der innersten Regionen von Jets in aktiven galaktischen Kernen (AGN). Die Auflösung der VLBI-Beobachtungen kann durch den Einsatz von Antennen an Bord eines die Erde umkreisenden Satelliten weiter verbessert werden. In dieser Arbeit präsentieren wir Multifrequenz-Aufnahmen von vier prominenten Radioquellen, 0836+710, 1642+690, 3C273 und 3C345, die mit der VLBI-Mission *RadioAstron* aufgezeichnet wurden, und verwenden diese Bilder zur Rekonstruktion der physikalischen Bedingungen in ihren Jets auf Parsec Skalen. Die Beobachtungen wurden im Rahmen des *RadioAstron* Key Science Programms, starke AGNs, durchgeführt. Die wichtigsten wissenschaftlichen Ziele dieser Studie sind die Ermittlung der Verteilung von Spektralindizes, der Turnoverfrequenz und der Flussdichte, die Abschätzung des Magnetfeldes in den Kernregionen und die Untersuchung der Entwicklung der Kelvin-Helmholtz-Instabilität im Jet. Die bei 1,6 GHz, 5 GHz und 22 GHz durchgeführten *RadioAstron* -Beobachtungen wurden durch VLBI-Bodendaten ergänzt, die bei 15 GHz und 43 GHz aufgenommen wurden, wenn verfügbar. Die resultierenden Multifrequenzdaten wurden zur Untersuchung von Spektral- und Opazitätseigenschaften der Jets herangezogen. Um diese Studie zu ermöglichen, haben wir eine Software entwickelt, die Multifrequenz-Bildausrichtung, Opazitäts-Messungen mit Hilfe des "Core-Shift"-Effekts, Spektralindexberechnung und ortsaufgelöste Darstellung der Verteilung der Turnoverfrequenz/Flussdichte und des Magnetfeldes im Jet generieren kann. Die Entwicklung der Kelvin-Helmholtz-Instabilität wird anhand der Analyse der inneren Struktur (Randlinien und innere Filamente) der Jet-Strömung aus Querprofilen der Strahlhelligkeit analysiert.

0836+710 wurde mit *RadioAstron* bei 1.6 GHz, 5 GHz und 22 GHz, zwischen Oktober 2013 und Januar 2014 beobachtet. Eine Spektralanalyse zusammen mit einer kinematischen Analyse, zeigt das Vorhandensein eines Rekollimationsschocks im Jet, bei einem Abstand von 0.15 mas vom Jetursprung. Wir verwenden die core-shift Analyse und das Synchrotron-Spektrum zur Abschätzung der magnetischen Feldstärke in den Jet-Zentren, wobei beide Methoden eine konsistente Abschätzung von Bcore liefern ~ 0.03 G bei 5 GHz. Wir ergänzen die Analyse mit

einer Studie über langfristige kinematische Entwicklung im Jet von 0836+710, bezogen auf die beobachtete γ-ray Flare-Aktivität der Quelle. Wir stellen fest, dass intermittierende Flare-Zustände der Quelle und die Intensität der Flares durch Wechselwirkungen zwischen propagierenden Schocks und dem aus der Analyse der *RadioAstron* -Beobachtungen ermittelten Rekollimationsschocks erklärt werden können. Wir verwenden die 1.6 GHz Daten, um die Randlinien des Jets in 0836+710 zu bestimmen und die Entwicklung der Kelvin-Helmholtz-Instabilität im Jet zu untersuchen. Wir identifizieren verschiedene Modi der Instabilität und bestimmen deren Wellenlängen und Wachstumslängen. Aus dieser Studie können wir ableiten, dass die physikalischen Parameter, wie z.B. die klassische Machzahl und das Dichteverhältnis zum umgebenden Medium, sehr hoch sind. Das Space-VLBI-Bild von 0836+710 bei 22 GHz zeigt eine prominente, asymmetrische Jet-Struktur, die wir entweder mittels differentiellen Doppler-Boostings in einem leicht rotierenden Jet oder durch ein schraubenförmiges Magnetfeld interpretieren können.

Der bekannte Quasar 3C 273 wurde mit *RadioAstron* im April 2014 bei 5 GHz und 22 GHz beobachtet. Aufgrund der anspruchsvollen Natur des resultierenden Datensatzes war es nicht möglich, eine umfangreiche Spektralanalyse für diesen Jet durchzuführen. Ein direkter Vergleich der Jetquerstruktur zwischen unseren Beobachtungen und früheren VSOP-Beobachtungen bei 5 GHz aus dem Jahr 1997 zeigen eine Änderung des Injektionswinkels der Randlinien des Jets. Dies ermöglicht uns, die Geschwindigkeit der Anordnung und die Rotationsgeschwindigkeit des Jets zu ermitteln. Dieses Ergebnis wird durch öffentlich zugängliche Multi-Epochen-VLBI-Daten bei 15 GHz aus dem MOJAVE-Monitoring-Programm bestätigt.

Der Quasar 1642+690 wurde mit *RadioAstron* zwischen Dezember 2014 und Januar 2015 bei 1.6 GHz, 5 GHz und 22 GHz beobachtet. Eine Spektralanalyse dieser Quelle deutet auch auf einen Rekollimationsschock hin, der sich bei ~ 0.75 mas vom kompakten Kern befindet. Eine Untersuchung des Synchrotron-Spektrums zeigt die potentielle Präsenz eines starken Magnetfeldes in der Kernregion sowie im Bereich des vermeintlichen Rekollimationsschocks.

Zuletzt wurde der Quasar 3C 345 mit *RadioAstron* im April 2014 bei 5 GHz und 22 GHz beobachtet. Allerdings wurden bei beiden Frequenzen über den Großteil der Laufzeit des Experiments keine Fringes gefunden, und daher ist es nicht möglich, zusätzliche Informationen aus den *RadioAstron* -Basislinien in Bezug auf das Ground-Array zu erzielen. Wir verwenden die resultierenden Bilder, um eine Spektral- und Turnover-Analyse der Quelle durchzuführen. Dies ermöglicht die Abschätzung eines Magnetfeldes von ~ 0.07 G in der Kernregion bei 5 GHz, was in guter Übereinstimmung mit früheren Schätzungen ist.

Contents

List of Figures

List of Tables

Chapter 1

Active Galactic Nuclei and Relativistic Jets

Active Galactic Nuclei (AGN) are among the most studied astronomical objects in the sky. The first identification of these objects dates back to the 1940's, when Seyfert (1943) reported a detection of strong nuclear emission in spiral nebulae that also showed broad and strong emission lines. He related the width of the lines to the nuclear emission and showed that width of these lines increased with the ratio of the nuclear luminosity to the total luminosity of the nebula.

It was not until the 1950's, however, that Seyfert's work was considered in more detail. At the time, radio astronomy was developing, and the first systematic surveys of the radio sky were being carried out (e.g., Edge et al. 1959; Bennett 1962, for the 3C catalog). Some sources in these first catalogs were labelled as radio "stars" with unusual properties such as a double-lobe morphology. Optical counterparts were soon found for many of these sources. While studying one of these radio loud sources, Cygnus A, Baade & Minkowski (1954) and Minkowski & Greenstein (1954) identified its optical counterpart and found similar properties to those reported by Seyfert. Radio sources, however, were at that time only related to stars and the galaxies were understood as quiescent aggregates of stars, dust and gas, and no new source class was established. In the following decade, Schmidt (1963) reported a spectroscopic analysis of the "radio star" 3C 273, and found that the wavelength of the emission lines could only be explained if they were redshifted by a large amount, and 3C 273 was therefore identified as a distant source outside our galaxy.

Through the study of similar sources, it became clear in the following years that all of them had similar characteristics: compact, star-like morphology, broad emission lines, large redshifts, and variable emission. This class of objects was branded "quasi stellar radio sources" or "quasars". However, the cause of such a large energy output was unclear. In the case of 3C 273, its large distance implies that its nucleus has a luminosity of around 100 times more than that of a normal

galaxy. The observed fast variability of quasars also implies that they must have a very compact emission region. Soon after the first discovery of quasars, the idea that their huge energy production could be due to the existence of an accreting supermassive black hole was suggested (Salpeter 1964; Zel'dovich & Novikov 1964). This idea was initially considered not plausible, until Lynden-Bell (1969) showed that supermassive black holes should be expected to be common in AGN.

With more detailed studies of galactic activity, a number of distinct observational properties have been identified in active galaxies, first leading to identifications of different classes of AGN (Antonucci 1993) and later culminating in establishment of the unified model of galactic activity (Urry & Padovani 1995) which attempts to unite the entire populations of active galaxies within a single phenomenological framework.

1.1 Main constituents of an AGN

In this section we describe the different constituents of an AGN. We describe first the central engine, i.e., the SuperMassive Black Hole (SMBH) and its accretion disk. Then, we describe the properties of the surrounding clouds of gas and finally we describe the jets, which are commonly assumed to be launched in a direction roughly perpendicular to the rotation plane of the central SMBH. This thesis focuses on understanding the underlying physics of relativistic jets which are only present in a small fraction of all AGN.

Supermassive Black Hole

There is substantial observational evidence that SMBHs are present in the centers of most AGN and their mass ranges from 10^7 (Mezcua 2017) to $10^{10} M_\odot$ (Ichikawa & Inayoshi 2017), where $M_\odot$ is defined as one solar mass. SMBHs are the only known objects capable of producing the large amount of energy emitted by AGN. This is accomplished through the conversion of kinetic energy of infalling matter into thermal and non-thermal radiation. The thermal radiation is produced through friction of the infalling matter as it rotates in the surrouding accretion disk. SMBHs are the only known massive objects compact enough to be consistent with the observed properties of AGN. Their size is defined by the Schwarzschild radius, r_S, which depends only on the mass of the black hole and is defined as the radius at which the escape velocity is equal to the speed of light. This radius also corresponds to the SMBHs event horizon. The Schwarzschild radius is given by: $r_s = \frac{2GM_\bullet}{c^2}$, where $M_\bullet$ is the black hole mass, c the speed of light and $G = 6.67 \times 10^{-11} \mathrm{Nm}^2/\mathrm{kg}^2$. We point out that in the case of a spinning black hole the distances at which we find the event horizon are different. The spin of a black hole, α^*, is defined by $\alpha^* = Jc/(GM_\bullet)$, where J is the momentum. If a black hole is rotating with maximum spin, $\alpha^* = 1$, the scale at which we find

the event horizon is reduced to $0.5r_S$. There is also a further difference between a non-rotating and a rotating black hole. This is the existence of the ergosphere, which is the location where the space-time is dragged by the black hole rotation (Thirring 1918).

Accretion Disk

An accretion disk is formed by matter falling onto a black hole. This matter forms a disk surrounding the black hole which then emits strong optical-UV radiation. This emission is the main characteristic of an AGN. X-ray observations have revealed the existence of an additional component, referred to as the corona which is thought to consist of hot electrons which upscatter accretion disk photons up to hard X-rays, which may then also reflect on the disk producing soft X-rays (Haardt & Maraschi 1991).

There is an upper limit to the luminosity that can be reached through the accretion process. The accretion will be quenched if the radiative pressure on the infalling material is larger than the gravitational force. This leads to a limit given by the so called Eddington luminosity, $L_{\rm edd}$, defined as:

$$L_{\rm edd} = \frac{4\pi c G M_\bullet \mu m_p}{\sigma_T} \approx 1.3 \times 10^{38} \left(\frac{M_\bullet}{M_\odot}\right) \text{ erg/s}, \tag{1.1}$$

where $\sigma_T = \frac{8\pi r_0^2}{3} = 6.65\,10^{-25}\,\text{cm}^{-2}$ is the Thomson scattering cross-section, $r_e = \frac{e^2}{m_e c^2}$ the classical electron radius, e the electron charge, m_e the electron mass, c the speed of light, m_p the proton mass, μ the mean molecular weight, and $M_\odot$ the solar mass.

This luminosity defines the characteristic accretion rate onto a black hole: the Eddington accretion rate:

$$\dot{M}_{\rm edd} = \frac{L_{\rm edd}}{\epsilon c^2}, \tag{1.2}$$

where ϵ is the radiation efficiency, usually considered to be of the order of 0.1 (Soltan 1982). The value of this parameter depends on the properties of the disk. Its value will be maximized if the disk is optically thick and geometrically thin (Shakura & Sunyaev 1973). However, the infalling material can also take the form of an advection dominated accretion flow (Begelman 1979), which radiates much less efficiently than a thin disk.

Broad Line Region

The BLR is close to the central nucleus and extends up to 1 pc in distance. This region is formed by gas clouds with a column density of 10^{23} cm^{-2}, and a typical particle density of $10^{10}\,\text{cm}^{-3}$ (Netzer 2006). The clouds are gravitationally

bound to the SMBH, and they show typical velocities of the order of 10^4 km s^{-1} causing broad emission lines with widths ranging between 10^3 and 10^4 km s^{-1}. This widening is due to Doppler effect.

The lines observed in this region include some forbidden and semi-forbidden lines. On Earth, where the particle density is high, the mean time between two collisions is much shorter than the average lifetime required for forbidden or semi-forbidden transition to lose their energy radiatively, but this is possible in low-density environments such as the BLR (Netzer 2006).

Narrow Line Region

The NLR extends up to 3 kpc from the SMBH. This region has gas clouds with velocities ranging from 300 to 500 km s^{-1} and shows a column density of order $10^{20} - 10^{21}$ cm^{-2} and particle density smaller than the BLR, of order 10^4 cm^{-3} (Netzer 2006). This low density implies than the main lines observed in this region are forbidden and semi-forbidden lines. The lower velocity leads to smaller line widths of up to several 100 km s^{-1}.

Torus

The torus is a region with an extent that ranges from 1 to 100 pc (Pier & Krolik 1993). It is composed primarily of dust and clouds with a particle density of $\sim 10^4 - 10^6$ cm^{-3} and a high column density, of the order of $\sim 10^{25}$ cm^{-2} (Netzer 2006). It emits in the mid-IR due to the absorption and reprocessing of continuum emission from the accretion disk. This gas is optically thick up until the hard X-rays band. Furthermore, it can obscure the inner regions of the AGN, such as the disk itself and the BLR. It typically shows a low temperature, but this temperature may vary within the torus as a function of distance from the central engine (Elitzur 2006).

1.2 AGN taxonomy

The observed AGN properties are quite diverse, in terms of their emission lines and their radio emission. This can lead to different observed properties due to the viewing angle between the AGN and the line of sight, because an AGN is not spherically symmetric. This section shortly describes the main different classes of AGN.

One of the basic foundations of AGN classification are the emission lines, dividing active galaxies into **type 1** and **type 2** AGN. A **Type 1** AGN shows broad and narrow emission lines. If, however, the spectrum only has narrow lines it is classified as **type 2**. The second generic AGN classification criterion is based on the radio properties of active galaxies. If they show strong radio emission (in

comparison to the optical emission), they are called **radio loud** AGN. If, however, strong radio emission is not present, they are called **radio quiet**. An AGN falls inside the radio loud category if the ratio between its radio flux density at 5 GHz and its opical flux at 6.8×10^{14} Hz is larger than 10 (Kellermann et al. 1989). Based on other specific observational properties of galactic activity, it is possible to define various AGN classes:

- **Quasar**. It stands for QUAsi StellAr Radio sources. They show strong and compact radio emission with broad emission lines and they are typically found in elliptical galaxies. We can find quasars at high redshifts since they are bright throughout the whole spectrum. The appear point-like at large distances because the nucleus is brighter than the host galaxy. They can be radio loud or radio quiet.

- **Seyfert galaxy**. They are less bright than quasars, and are usually radio quiet. The host galaxy is typically a spiral. They are classified further as *Seyfert type I* and *Seyfert type II* depending of the presence or absence of broad emission lines.

- **Radio Galaxy**. Radio galaxies, as the name suggests, show strong and extended radio emission. For most of radio galaxies, their optical host galaxy is elliptical. Type I radio galaxies are called *Broad Line Radio-Galaxies* (BLRG) and type 2 *Narrow Line Radio-Galaxies* (NRLG). Based on the morphological properties of their radio emission, radio galaxies have been historically classified within the Fanaroff and Riley classification (Fanaroff & Riley 1974). **Fanaroff and Riley type I** (FRI) galaxies show bright jets, usually double sided, and a diffuse structure with edge-darkened lobes. **Fanaroff and Riley type II** (FRII) show bright lobes and jets with decreasing brightness when approaching the core, i.e., fainter jets. This type shows predominantly one-sided jet structures, edge brightened.

- **Blazar**. Blazars are radio-loud and bright sources with jets oriented at a small angles with respect to the line of sight. They show strong flux variability. These are further divided into Flat Spectrum Radio Quasars (FSRQs), and BL Lacertae (BL Lacs). The former show broad emission lines whereas the latter show only weak or no emission and absorption lines.

1.3 Unification Model

The different kinds of AGN described above show different observational properties. However, an underlying idea that projection effects can explain the different types of AGN led to the development of a unification model. Rowan-Robinson (1977) created a model which could describe the different observed properties of

the AGN based on orientation. Eight years later, Antonucci & Miller (1985) concluded that the missing broad emission lines could be caused by the obscuration of the central source due the presence of an optically thick torus. This gave rise to the unification model that describes the observed differences between different AGN based on varying orientation of the torus and jet(s) towards the observer (see Fig. 1.1).

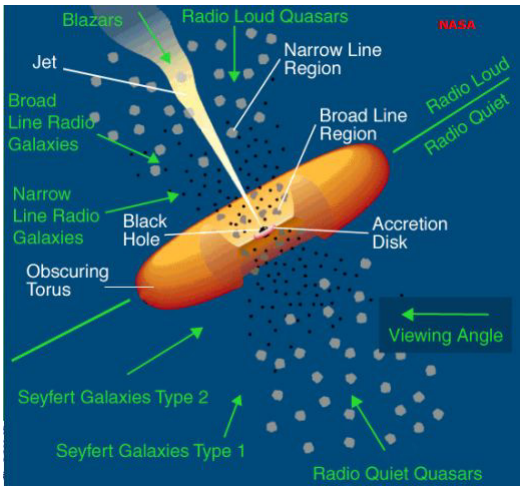

Figure 1.1: The figure describes the basic model of an AGN with their different components written in white. In green, we can find the different types of AGN based on the observer location (Urry & Padovani 1995).

The unified model describes the different physical components that make up an AGN and explains how the observed properties change depending on the viewing angle. If we consider an AGN observed face-on, the torus does not hide the BLR resulting in the presence of broad emission lines. We can explain the lack of broad emission lines if the AGN is observed edge-on, since the torus will hide the BLR. We can also explain the inferred radio properties of these sources. Almost all AGN radio emission comes from relativistic jets. If the jet is absent, we find a radio-quiet source, otherwise the AGN will be radio-loud. The jet emission dominates the observed properties if the viewing angle is very small due to Doppler boosting (discussed further in section 1.4.1).

1.4 Relativistic jets

Relativistic jets are collimated plasma outflows. Usually they are considered to be conical, supersonic and freely moving. Their main constituents are electron-positron or electron-proton plasma and magnetic fields (e.g., Blandford & Königl 1979). The main radiation mechanisms occurring in jets are synchrotron and inverse Compton processes. Owing to the relativistic speeds of the plasma and

the small viewing angle of the jet, we observe apparent superluminal motions and Doppler beaming. The latter is the main reason why the jet appears brighter when it is approaching us and fainter if it is receding, and why we predominantly observe one-sided jet sources in blazars. Another surprising fact is that jets remain relativistic at distances far from the central engine where the particles should decelerate due to radiative losses. One possible reason can be the presence of shocks that might re-accelerate the plasma. The jet will also be subject to hydrodynamical instabilities, due to the different speeds of the fluid and the ambient medium. Instabilities can describe the evolution of the plasma and studying them could allow us to investigate why jets do not usually get disrupted up to large distances.

1.4.1 Relativistic Effects

The electrons that are part of the relativistic plasma in AGN have high Lorentz factors, reaching up to 10^5. The bulk motion of the jet plasma is also relativistic, with Lorentz factors of the order of 10 (Lister et al. 2013). Due to this high Lorentz factor, relativistic effects strongly affect the observed radiation, and the way we estimate some of the characteristic parameters of the plasma (see, for example, Lister et al. 2013). In this section, we consider these effects and how they impact the observable quantities of the jet.

Before going in depth into these details, it is important to consider the two basic effects of special relativity: length contraction and time dilation, because a firm understanding of these physical effects simplifies the more complicated concepts we are dealing with in this section. The observed time and length in the lab frame (stationary) are not the same as those measured in the jet's co-moving frame. When we consider the time in the lab frame, the time interval is longer compared to the one measured in the co-moving frame. The observed length is shorter, which is known as length contraction. These effects are parametrized by Eq. 1.3.

$$\begin{aligned} \Delta t &= \gamma \Delta t', \\ \Delta x &= \frac{\Delta x'}{\gamma}, \end{aligned} \tag{1.3}$$

where the prime quantities are in the co-moving (fluid) frame and the quantities with un-primed notation are in the observer's frame and $\gamma = 1/\sqrt{(1 - \beta^2)}$ is the jet Lorentz factor, with $\beta = v/c$.

Doppler effect

We consider a jet moving with a velocity $v = \beta c$ with an angle θ with respect to our line of sight. We also consider a jet component which is emitting radiation and moves during a certain time interval, (t_1, t_2), from position A to B (see Fig. 1.2).

The time interval in the lab frame is calculated using the time dilation equation. However, when we measure the emitted radiation, we have to take in account that the first and last emitted photons are in different locations, hence the distance they have to travel is different. The time difference between the arrival of the two photons to the observer is then:

$$\Delta t^{\mathrm{a}} = t_2^{\mathrm{a}} - t_1^{\mathrm{a}} = \Delta t^{\mathrm{e}} - \frac{v\Delta t^{\mathrm{e}}\cos\theta}{c} = \Delta t^{\mathrm{e}}\left(1-\beta\cos\theta\right) = \Delta t'^{\mathrm{e}}\gamma\left(1-\beta\cos\theta\right) = \frac{\Delta t'^{\mathrm{e}}}{\delta}, \tag{1.4}$$

where the superscript "a" refers to the received photon, the superscript "e" to the emitted photon, and $\delta = \dfrac{1}{\gamma\left(1-\beta\cos\theta\right)}$ is the Doppler factor.

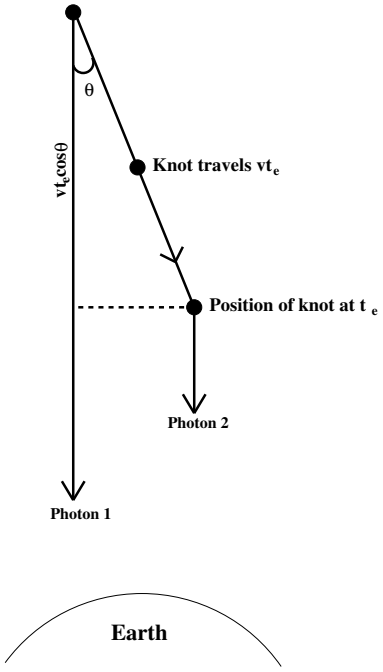

Figure 1.2: Illustration of the trajectory of moving photons in a jet. The diagonal arrow indicates the direction of motion and the straight arrows indicate the direction of the emitted photons.

If we now consider that $\Delta t'^{\mathrm{e}} = 1/\nu'$, we have then that for the frequency:

$$\nu = \delta\nu'. \tag{1.5}$$

Upon inspection of Eq. 1.5, it can be easily concluded that if the source is moving towards the observer ($\theta \sim 0°$), the radiation is blue-shifted ($\nu > \nu'$), and if the source is moving away from the observed ($\theta \sim 180°$) the radiation is red-shifted ($\nu < \nu'$).

Superluminal motion

The intrinsic jet speed is quite challenging to measure. As only the brightest spots of the jets are observed, the speed is only calculated for these regions (Rees 1966; Whitney et al. 1971).

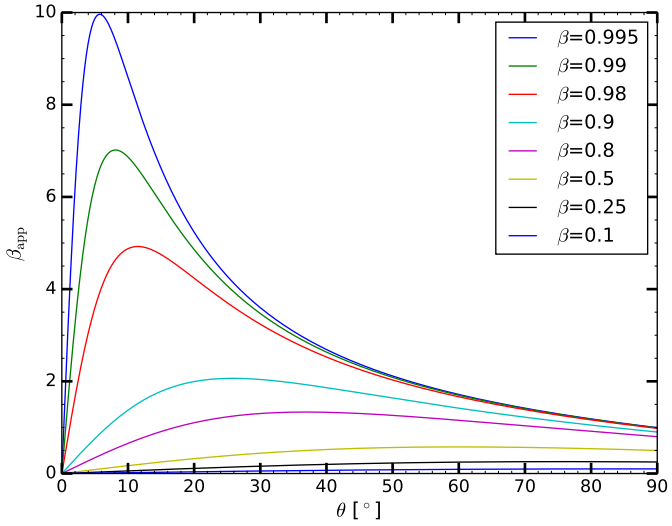

Figure 1.3: Apparent speed for different β. The higher the velocity of the jet the faster the observer sees it.The legend shows the different speeds. Furthermore, the higher the speed, the larger the effect of the critical angle.

The method to obtain the apparent speed of a moving jet component is quite similar to the one used during the Doppler effect section. The apparent time interval between two photons emitted by a moving component is given in Eq. 1.4. The apparent distance, l, over which the component has travelled during that time interval is:

$$l = \beta \Delta t'^{e} \sin\theta. \tag{1.6}$$

Hence, the apparent speed is:

$$\beta_{\rm app} = \frac{\beta \sin\theta}{1 - \beta\cos\theta}. \tag{1.7}$$

The apparent speed will be maximized for a given viewing angle. This can be seen if we calculate the derivative of the apparent speed with respect to the viewing angle, which yields $\cos\theta_{\rm crit} = \beta$ and $\sin\theta_{\rm crit} = \frac{1}{\gamma}$. In this case, $\beta_{\rm app} = \beta\gamma$, which leads to the maximum possible apparent speed. Figure 1.3 shows that for a given viewing angle and intrinsic speed, the observed velocity of the plasma can be much higher than the speed of light. The higher the speed, the larger the effect of the

critical viewing angle. For the case of $\beta = 0.995$, the maximum apparent speed is obtained for a critical angle of around 6°. In general, considering the high speed at which relativistic jets travel, this critical angle is rather small.

Aberration and beaming

a) **Aberration**. We consider a reference frame that is moving at a certain speed with respect to the observer, who is considered to be at rest. The effect of aberration describes the difference in the propagation direction of a photon as seen in two different frames, and therefore a change on the angle due to the laws of transformation of velocities. The observed viewing angle is (Hughes 1991):

$$\begin{aligned} \cos\theta &= \frac{\beta + \cos\theta'}{1 + \beta\cos\theta'}, \\ \sin\theta &= \frac{\sin\theta'}{\gamma\,(1 + \beta\cos\theta')}, \end{aligned} \tag{1.8}$$

where θ and θ' are the viewing angles, i.e., the angles between the velocity vector and the line of sight in the two different frames.

b) **Doppler beaming and boosting**. We consider now the case where a source is emitting radiation at right angles with respect to its direction of motion. Relativistic effects will cause the emitted radiation to be beamed in the direction of motion and collimated into a cone with half opening angle $\sin\varphi \approx \varphi \sim \frac{1}{\gamma}$.

This effect contributes to Doppler boosting, which makes radio-loud AGN appear often as one-sided sources, since the approaching jet is more luminous than the counter-jet. Doppler boosting modifies the observed spectral distribution of the emission as well. To understand this effect, we start from the definition of specific intensity:

$$I(\nu) = h\nu \frac{dN}{dt d\nu d\Omega dA}. \tag{1.9}$$

The transformation of the parameters in the above equations are:

- $dN = dN^{'}$, since the number of particles does not change,
- $dA = dA^{'}$, since the surface area is Lorentz invariant,
- the solid angle transforms as: $d\Omega = \dfrac{d\Omega^{'}}{\delta^3}$,
- the time and frequency changes as given in Eq. 1.3 and Eq. 1.5 respectively.

This leads to the specific intensity transformation:

$$I(\nu) = \delta^3 I^{'}(\nu^{'}). \tag{1.10}$$

Integrating over frequencies, we obtain that the bolometric intensity or flux that transforms as:

$$F = \delta^4 F^{'}. \tag{1.11}$$

The dependence on frequency of the bolometric intensity will cancel out in the case of monocromatic radiation and the monochromatic flux density transforms as $S_\nu = \delta^3 S_\nu^{'}$. Since the observed spectrum has a power law dependence on frequency, $S_\nu \propto \nu^\alpha$, where α is the spectral index, the relationship between the observed and emitted flux density is:

$$S_\nu = S_\nu^{'} \delta^{(3-\alpha)}. \tag{1.12}$$

However, in the case of a steady-state flow, we have one Doppler factor less since we are not studying a moving structure subject to time dilation. This leads to:

$$S_\nu = S_\nu^{'} \delta^{(2-\alpha)}. \tag{1.13}$$

This effect allows us to calculate the flux density ratio between the jet and counter-jet, R, as a function of the jet speed and viewing angle, considering that the observable flux density of the receding jet decreases and the flux density of the approaching jet is enhanced. Since the angle between the velocity and the line of sight is $\theta + \pi$ for the counter-jet, its Doppler factor is given by, $\delta_{\mathrm{counter-jet}} = \frac{1}{\gamma(1+\beta\cos\theta)}$. This leads to the following flux density ratio:

$$R = \frac{S_{\nu\mathrm{jet}}}{S_{\nu\mathrm{counter-jet}}} = \left(\frac{1+\beta\cos\theta}{1-\beta\cos\theta}\right)^{2-\alpha}. \tag{1.14}$$

1.4.2 Radiation Processes

Synchrotron radiation

Synchrotron radiation is produced by charged particles moving at relativistic speeds in the presence of a magnetic field. The particles are accelerated due to a curvilinear motion along the magnetic field line. This acceleration produces electromagnetic radiation. The absorption process related to synchrotron radiation is called synchrotron self-absorption (see Chap. 2 for more details).

Inverse Compton radiation

Low-energy photons are scattered by charged particles with high Lorentz factors, which produces inverse Compton radiation. In the process, the photon gains energy by a factor of γ^2, leading to $E_{\text{after}} = \gamma^2 E_{\text{before}}$, where E_{after} and E_{before} refer to the energy of the photon before/after collision with the relativistic electron. The total power emitted is given by (Rybicki & Lightman 1979):

$$P_{IC} = \frac{4}{3}\sigma_T c \gamma^2 \beta^2 U_{ph}, \tag{1.15}$$

where U_{ph} is the photon energy density. The photons that scatter off the electrons can be produced by synchrotron radiation in the source, **Synchrotron Self-Compton (SSC)**, or from a external source, such as the Cosmic Microwave Background (CMB), the accretion disk or the jet sheath, **External Compton (EC)**.

The spectrum of Inverse Comptom radiation is a power law with a spectral index of $\alpha = -\frac{s-1}{2}$.
This conversion of low-energy photons to high-energy photons is the main source of high energy radiation and is commonly thought to be the main driver of X-ray and γ-ray production in AGN jets.

1.4.3 Shocks

Shocks are caused by plasma condensations moving inside the jet with velocities higher than the sound speed of the bulk jet flow. Rees (1978), suggested that disturbances in the jet, even though they may be small at the beginning, may form shocks further down in the jet. These shocks can be seen as distinct regions (components) of enhanced emission in the jet, observed with Lorentz factors larger than the average jet flow (Blandford & Königl 1979). Marscher & Gear (1985) presented a model describing how a shock propagates within the jet. This model features three different evolutionary stages: the Compton, the synchrotron, and the adiabatic stage. At each of these stages, the shock emission is dominated by the energy losses via distinct physical processes.

Chapter 2

Synchrotron radiation

In this chapter we introduce the concept of synchrotron radiation and outline several physical parameters of the jet that can be obtained after performing a synchrotron analysis of the source radiation. This chapter is based on Chapter 14 of Jackson (1962), Chapter 8 of Longair (2011), Chapters 3 and 6 of Rybicki & Lightman (1979), Blumenthal & Gould (1970), and Ghisellini (2013). As the mathematical syntax is already described in detail in the above accounts, we will just highlight the salient points, with two main objectives: first is to have a common nomenclature, and second to make clearer the assumptions that have been made to obtain the final equations which will be important for the discussion of the results of this thesis. This chapter starts by describing the basics of synchrotron radiation. We then move to a discussion of the shape of the synchrotron spectrum. We then introduce physical quantities of AGN jets that can be inferred from their synchrotron emission such as: the brightness temperature, magnetic field, and particle density.

2.1 Synchrotron emission

Relativistic jets are thought to be composed of relativistic charged particles (mostly electrons) and strong magnetic fields. These two components interact by means of the Lorentz force, which causes the electrons to spiral around magnetic field lines (see Fig. 2.1), giving rise to synchrotron and cyclotron emission.

The Lorentz force is defined as:

$$\mathbf{F_L} = \frac{d}{dt}(\gamma m_e \mathbf{v}) = e(\mathbf{E} + \frac{\mathbf{v}}{c} \times \mathbf{B}),$$

where:

$\mathbf{E}$ is the electric field vector, and $\mathbf{B}$ the magnetic field vector.

If one assumes that: (i) the jet plasma has a small conductivity, and (ii) that synchrotron losses are negligible over the electron gyration time scale, one

can treat the jet velocity as being constant. However, there is acceleration in the direction perpendicular to the magnetic field. To show this, we solve the Lorentz force formula for the parallel and perpendicular acceleration components:

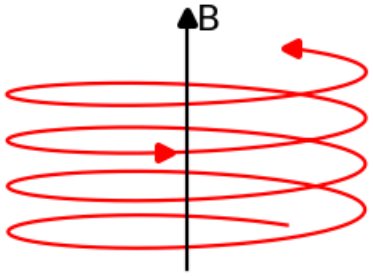

Figure 2.1: Illustration of the effect of the Lorentz force in a charged particle

$$\gamma m_e a_{\parallel/\perp} = \frac{e}{c} v_{\parallel/\perp} B \sin\Theta,$$

where Θ is the pitch angle, i.e. the angle between the magnetic field line and the electron velocity vector.

For the parallel component of the velocity, $\Theta \sim 0°$, which leads to $a_\parallel \sim 0$, and therefore negligible emission. However, for the case of the perpendicular component, $\Theta \sim 90°$, we have,

$$a_\perp = \frac{e v_\perp B \sin\Theta}{\gamma m_e c}.$$

2.1.1 Synchrotron radiation from one electron

A proper description of synchrotron radiation starts from the Liénard-Wiechert potentials, which describe the electromagnetic effects on a moving charge. They are a solution of the Maxwell equations of electrodynamics and are used to obtain a description of the electric and magnetic field of the charged particle as:

$$\mathbf{E} = -\frac{1}{c}\frac{\partial \mathbf{A}}{\partial t} - \nabla\phi,$$

$$\mathbf{B} = \nabla \times \mathbf{A},$$

where,

$\mathbf{A}$ is the Liénard-Wiechert potential vector, and
ϕ is the Liénard-Wiechert potential scalar.

In the Lorentz gauge, the potentials satisfy the wave equations, which gives us the Liénard-Wiechert potentials as a function of the retarded time, $t' = t - R(t')/c$, i.e., the time at which the radiation is emitted (not the time when it is observed), where $R(t') \equiv \mathbf{x} - \mathbf{r}(t')$. Therefore, the potentials take the following form:

$$\mathbf{A}(\mathbf{R},t) = \frac{1}{c}\int\int R^{-1}\mathbf{J}(\mathbf{r}^{'},t^{'})\delta\left(t^{'}-t+\frac{\mathbf{R}(t^{'})}{c}\right)d^3r^{'}dt^{'},$$
$$\phi(\mathbf{R},t) = \int\int R^{-1}\mathbf{Q}(\mathbf{r}^{'},t^{'})\delta\left(t^{'}-t+\frac{\mathbf{R}(t^{'})}{c}\right)d^3r^{'}dt^{'}, \tag{2.1}$$

where,

$\mathbf{J}$ is the current density of the emission element, $\mathbf{J}(\mathbf{r}^{'},t^{'}) = q\mathbf{v}(t^{'})\delta(r-r_0(t^{'}))$, $\mathbf{Q}$ is the charge density of the moving charge, $\mathbf{Q}(\mathbf{r}^{'},t^{'}) = q\delta(r-r_0(t^{'}))$, and, $R = \left|\mathbf{R}(t^{'})\right|$.

The solution of the integral is then:

$$\mathbf{A}(\mathbf{R},t) = \left[\frac{q\beta}{(1-\beta\mathbf{n})R}\right]_{t'},$$
$$\phi(\mathbf{R},t) = \left[\frac{q}{(1-\beta\mathbf{n})R}\right]_{t'}, \tag{2.2}$$

where $\mathbf{n}$ is the unit vector from the electron to the observer, $\mathbf{n} \equiv \mathbf{R}/R$.
Once we have the potentials, we can recalculate the electromagnetic fields due to a moving charge using Maxwell equations:

$$\mathbf{E}(\mathbf{R},t) = q\left[\frac{\mathbf{n}-\beta}{\gamma^2(1-\beta\mathbf{n})^3R^2}\right]_{t'} + \frac{q}{c}\left[\frac{\mathbf{n}\times(\mathbf{n}-\beta)\times\beta}{(1-\beta\mathbf{n})^3R}\right]_{t'},$$
$$\mathbf{B}(\mathbf{R},t) = \frac{1}{c}\left[\mathbf{n}\times\mathbf{E}(\mathbf{R},t)\right]_{t'}. \tag{2.3}$$

In Equation 2.3 the first term of the electric field is the velocity (near) field and the second term the acceleration (radiation) field. When the particle is at rest, the electric field reduces to Coulomb law.

With this, we can calculate the power radiated by a particle per unit area, as the flux is given by the Poynting vector, $\mathbf{S} = c/(4\pi)\mathbf{E}\times\mathbf{B}$, which leads to the expression for the power radiated per solid angle:

$$\frac{dP^{'}}{d\Omega} = \frac{cR^2}{4\pi}\left|\mathbf{E}\right|^2 = \frac{e^2}{4\pi c}\left|\mathbf{n}\times(\mathbf{n}\times\dot{\beta})\right|^2, \tag{2.4}$$

where the dot indicates the derivative of β.

For the non relativistic case, Eq. 2.4 reduces to the well-known Larmor equation:

$$\frac{dP^{'}}{d\Omega} = \frac{e^2}{4\pi c^3}a^{'2}\sin\Theta^2.$$

Integrating over all the pitch angles, which we assume to have an isotropic distribution, the total power emitted takes the following form:

$$P'_{\rm em} = \frac{2e^2}{3c^3} a'^2. \tag{2.5}$$

The radiated power is Lorentz invariant, $P'_{\rm em} = P_{\rm em}$. Therefore, we only need to transform the acceleration: as $a'^2 = a'^2_{\parallel} + a'^2_{\perp} = (\gamma^3 a_{\parallel})^2 + (\gamma^2 a_{\perp})^2$. As the acceleration in the parallel direction is negligible, we replace the acceleration in the perpendicular direction in Eq. 2.5, and obtain that the total synchrotron power emitted by a sigle particle is:

$$P_{\rm sync} = \frac{2e^4}{3m_e^2c^3}\gamma^2\beta^2B^2 = 2\sigma_T c u_B \gamma^2\beta^2. \tag{2.6}$$

The right hand side of Equation 2.6 was rewritten using the magnetic energy density, $u_B = B^2/(8\pi)$, the electron radius, $r_e = \dfrac{e^2}{m_e c^2}$ and the Thomson scattering cross section, $\sigma_T = 8\pi r_e^2/3$.

We now define the synchrotron cooling time which is a characteristic time scale for synchrotron energy losses as:

$$t_{\rm sync} = \frac{E}{< P_{\rm sync} >} = \frac{8\pi m_e c^2}{4/3\sigma_T c B^2 \gamma\beta^2} \approx 24.5\,\gamma^{-1}B^{-2} \quad \text{yr}. \tag{2.7}$$

This quantity can be used as a sanity check for the results related to the magnetic field. For example, in the case that the cooling time leads to an unrealistically small magnetic field, it would imply that we should not be able to see the jet at those scales unless re-acceleration exists.

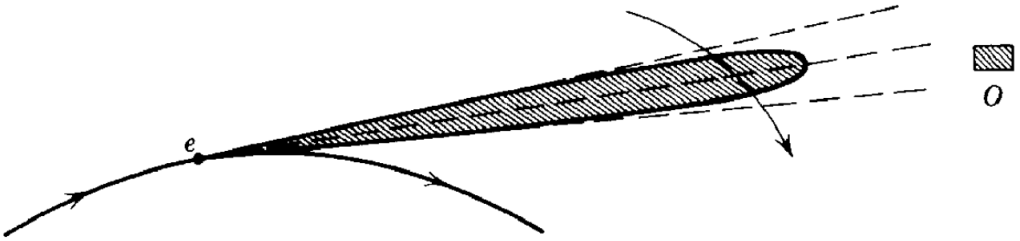

Figure 2.2: The figure shows the movement of the relativistic particle along the arc. You can see how the radiation is beamed in the direction of the observer (Jackson 1962).

We now discuss the shape of a synchrotron spectrum. The radiation emitted by a charged particle moving randomly at extreme relativistic speeds can be approximated by the radiation that the same particle would have moving along an

arc. The emission is distributed in a a cone directed along the velocity vector of the particle, as illustrated in Fig. 2.2. This radiation will only be seen when the particle velocity vector is pointing towards the observer, due to beaming effects. As the particle has an periodic motion, the observer will see a succession of pulses of very short duration. The synchrotron spectrum for one particle can be obtained by Fourier transforming the electric field:

$$\mathfrak{F}(\mathbf{E}(\omega)) = \frac{1}{2\pi}\int_{-\infty}^{\infty} dt e^{i\omega t}\mathbf{E}(t) \quad ; \quad \frac{dW}{d\omega d\Omega} = cR^2\left[(\mathbf{E}(\omega))\right]^2, \tag{2.8}$$

where $dW/d\Omega$ is the energy radiated per solid angle.

To solve Eq. 2.8, we relate the energy radiated by the particle to its probability of emitting a photon with energy $\hbar \mathrm{d}\omega$. This is written as $\mathrm{d}W = I(\omega)\mathrm{d}\omega R^2 \mathrm{d}\Omega$, where $I(\omega)$ is the spectral energy per revolution and is defined as $I(\omega) = c\left|E\right|^2$. This variable is related to the emitted power by $\Omega I(\omega) = 2\pi P(\omega)$. Replacing this quantity in Eq. 2.8, we obtain the spectrum of the emitted synchrotron radiation for one charged particle (in which the pitch angle is 90°):

$$P(\nu) = 2\pi P(\omega) = \frac{\sqrt{3}e^3 B}{m_e c^2}\frac{\nu}{\nu_c}\int_{\nu/\nu_c}^{\infty} K_{5/3}(x)dx, \tag{2.9}$$

where,

$K_{5/3}(x)$ is the modified Bessel function of order 5/3, and,

$\nu_c = \dfrac{3\gamma^2 eB}{4\pi m_e c}$ is the critical frequency.

At frequencies much higher than the critical frequency, the spectrum can be asymptotically approximated by:

$$P(\nu) \cong \left(\frac{3}{2}\pi\right)^{1/2}\frac{e^3 B}{m_e c^2}\left(\frac{\nu}{\nu_c}\right)^{1/2} e^{-\nu/\nu_c}. \tag{2.10}$$

For the case of frequencies much lower that the critical frequency, the result of the integration is:

$$P(\nu) \cong \frac{4\pi e^3 B}{\Gamma(1/3) m_e c^2}\left(\frac{\nu}{\nu_c}\right)^{1/3}. \tag{2.11}$$

It is important to remark that this analysis does not consider that the electron has a periodic motion. Therefore, the analysis is more accurate using Fourier series. However, as most of the power is emitted at frequencies much larger than the angular frequency along which the electron is spiraling along the magnetic field line, $\omega = (eB)/(\gamma m_e c)$, and the particles are highly relativistic, most of the

synchrotron radiation may be seen as continuous, with the exception of the very low frequency part.

Generalizing the above expressions and taking into account the particle pitch angle, Θ, will have the consequence that the power received is not the same as the power emitted. We already mentioned that the power is Lorentz invariant, $P_{\rm em} = P^{'}$, which leads to:

$$P_{\rm em} = (d\nu^{'}/d\nu)P^{'}(\nu^{'}) = \sin\Theta P^{'}(\nu^{'}).$$

We now define the standard formula for the spectral distribution of synchrotron emission from a single particle.:

$$P(\nu) = 2\pi P(\omega) = \frac{\sqrt{3}e^3 B\sin\Theta}{m_e c^2}\frac{\nu}{\nu_c}\int_{\nu/\nu_c}^{\infty} K_{5/3}(x)dx, \tag{2.12}$$

where the critical frequency is re-written to include the pitch angle, so that: $\nu_c = \dfrac{3\gamma^2 eB}{4\pi m_e c}\sin\Theta$.

In the same manner, we can calculate the received power, which is proportional to the received flux:

$$P_{\rm rec}(\nu){\rm d}\nu \propto \nu^2 {\rm d}n(\nu)/\nu.$$

This leads to the following relation between the emitted and received power spectrum:

$$P_{\rm rec}(\nu) = P_{\rm em}(\nu)/\sin\Theta, \tag{2.13}$$

which results in the received power independent of the pitch angle.

2.1.2 Synchrotron radiation from an ensemble of electrons

We will now extend the previous approximations to the case of an ensemble of charged emitting particles. We assume that the energy distribution of the electrons follows a power law distribution, as this kind of distribution is usually observed in most radio sources:

$$N(E){\rm d}E = \kappa E^{-s}{\rm d}E \quad ; \quad N(\gamma){\rm d}\gamma = \kappa\gamma^{-s}{\rm d}\gamma, \tag{2.14}$$

where $N(E)dE$ is the density of electrons with energies $E + {\rm d}E$, and, κ is a constant which depends on the pitch angle of the electron disribution.

The total power in this case is the integral over all energies of the total power radiated in the case of one particle times the energy distribution of electrons:

$$P_{\rm tot}(\nu) = \kappa \int_{\gamma_{\rm min}}^{\gamma_{\rm max}} P(\nu) N(\gamma) {\rm d}\gamma. \tag{2.15}$$

For wide energy ranges, we have that the result of the integration is then the well-known expression for the synchrotron spectrum:

$$P_{\rm tot}(\nu) \propto \nu^{-(s-1)/2} = \nu^{\alpha}, \tag{2.16}$$

where s is the particle spectral index, and $\alpha = -(s-1)/2$ the radiation spectral index.

In this case, as we are considering a fixed region in the sky where the electrons are emitting, the emitted and received power are the same.

2.1.3 Synchrotron self-absorption

The equations described previously only characterize emission of synchrotron radiation. However, to every emission process there is a corresponding absorption process. The synchrotron self-absorption is the main absorption mechanism for synchrotron radiation. As we are dealing with non-thermal particles, we cannot treat this absorption with Kirchhoff laws, and we need to use instead Einstein coefficients. We consider a photon transitioning from level 2, of energy E and momentum $\mathbf{p}$, to the level 1, of energy $E - {\rm d}E$ and momentum $\mathbf{p} - {\rm d}\mathbf{p}$. The spontaneous emission coefficient, A_{21}, is then:

$$A_{21} = \frac{j(\nu, E)}{h\nu},$$

where $j(\nu, E)$ is the emissivity per unit of frequency.

This is related to the stimulated emission coefficient, B_{21}, and to the absorption coefficient, B_{12}:

$$B_{21} = B_{12} = \frac{c^2}{2h\nu^3} A_{21}.$$

The absorption and emission coefficients, χ_ν and j_ν, are:

$$\chi_\nu = \hbar\omega(N_1 B_{12} - N_2 B_{21}),$$

$$j_\nu = \frac{h\nu}{4\pi} N_1 A_{21}.$$

After integrating both expressions over all possible pairs of electron momenta and converting the momentum spectrum into energy spectrum, we obtain:

$$\begin{aligned}\chi_\nu &= \kappa c_\chi(s)(\sin\Theta)^{(s+2)/2} B^{(s+2)/2}\nu^{-(s+4)/2},\\ j_\nu &= \kappa c_j(s)(\sin\Theta)^{(s+1)/2} B^{(s+1)/2}\nu^{-(s-1)/2},\end{aligned} \tag{2.17}$$

where the constants $c_\chi(s)$, and $c_j(s)$ are given by:

$$\begin{aligned}c_\chi(s) &= \frac{\sqrt{3}\pi}{72} e m_e^5 c^{10}\left(\frac{3e}{2\pi m_e^3 c^5}\right)^{(s+4)/2}\left(\frac{s+10}{3}\right)\Gamma\left(\frac{3s+2}{12}\right)\Gamma\left(\frac{3s+10}{12}\right),\\ c_j(s) &= \frac{\sqrt{3}e^3}{16\pi m_e c^2}\left(\frac{3e}{2\pi m_e^3 c^5}\right)^{(s-1)/2}\left(\frac{s+\frac{7}{3}}{s+1}\right)\Gamma\left(\frac{3s-1}{12}\right)\Gamma\left(\frac{3s+7}{12}\right),\end{aligned} \tag{2.18}$$

where Γ is in this case the complete Euler-Gamma function. For the case of random magnetic fields, these constants need to be averaged over the pitch angle. This is done by multiplying them by $c_{\chi,b}(s)$, and $c_{j,b}(s)$ respectively:

$$\begin{aligned}c_{\chi,b}(s) &= \frac{\sqrt{\pi}}{2}\Gamma\left(\frac{s+6}{4}\right)\left(\Gamma\left(\frac{s+8}{4}\right)\right)^{-1},\\ c_{j,b}(s) &= \frac{\sqrt{\pi}}{2}\Gamma\left(\frac{s+5}{4}\right)\left(\Gamma\left(\frac{s+7}{4}\right)\right)^{-1}.\end{aligned} \tag{2.19}$$

Assuming the absorption and emission coefficients are constant and there is no external radiation field, we can calculate the specific intensity, I_ν, using the radiative transfer equation:

$$I_\nu(\tau_\nu) = \frac{j_\nu}{\chi_\nu}\left(1-e^{-\tau_\nu}\right) = S_\nu\left(1-e^{-\tau_\nu}\right), \tag{2.20}$$

where τ_ν is the optical depth, and S_ν is the source function.
Equation 2.20 gives the dependence of the intensity on frequency. For the optically thin case, where $\tau_\nu \ll 1$ (high frequencies), defined in the previous section, the absorption coefficient will be negligible as the emission is optically thin. In that case, using Eq. 2.17 and Eq. 2.20, we derive that the intensity has the form already defined above:

$$I_\nu \propto \nu^{-(s-1)/2}.$$

For the optically thick case, where $\tau_\nu \gg 1$ (low frequencies), the absorption plays an important role, so the relationship of the intensity with the frequency will be affected by the absorption coefficient. In this case, again with Eq. 2.17 and Eq. 2.20, the dependence for a synchrotron self-absorbed source is:

$$I_\nu \propto \nu^{5/2}.$$

Now defining the frequency, ν_1 as the frequency where $\tau_\nu = 1$, the spectral intensity can be written as (Hughes 1991):

$$I_\nu = I_{\nu_1} \left(\frac{\nu}{\nu_1}\right)^{\alpha_{\rm thick}} \left(1 - \exp\left(\left(\frac{\nu}{\nu_1}\right)^{\alpha_{\rm thin}-\alpha_{\rm thick}}\right)\right), \tag{2.21}$$

where,

ν_1 the frequency where the optical depth is unity,

$\alpha_{\rm thin}$ the optically thin spectral index, and,

$\alpha_{\rm thick}$ the optically thick spectral index, which takes a value of 5/2.

In order to be able to use Eq. 2.21 for our radio data, it is necessary to recalculate it with respect to the turnover frequency, ν_m, instead of the characteristic frequency, ν_1. The result is (Türler et al. 1999):

$$S_\nu = S_m \left(\frac{\nu}{\nu_m}\right)^{\alpha_{\rm thick}} \frac{1 - \exp(-\tau_m(\nu/\nu_m)^{\alpha_{\rm thin}-\alpha_{\rm thick}})}{1 - e^{-\tau_m}}, \tag{2.22}$$

where,

τ_m the optical depth at the turnover, $\tau_m = \frac{3}{2}\sqrt{1 - \frac{8\alpha_{\rm thin}}{3\alpha_{\rm thick}}} - 1$, and,

S_m and ν_m are the turnover flux density and turnver frequency, i.e, the flux density and the frequency at which the spectrum peaks.

The spectrum takes into in account the optically thin and optically thick part as shown in Fig. 2.3. The figure shows different slopes for the optically thick part, resulting from different absorption processes that occur within the jet. As an example, Boccardi (2015) showed, by comparing a fit with synchrotron self-absorption only and a fit adding free free absorption, that the latter resulted in a better fit to the overall spectrum.

2.2 Brightness temperature

For non-thermal plasma one cannot easily find a quantity describing the kinetic energy of plasma particles, and brightness temperature is derived as such a quantity, analogous to normal temperature describing the blackbody radiation. In order to be able to define the brightness temperature, we need first to consider the Planck spectrum of black body radiation. Given the radiated intensity and the size of the emission region, we can obtain the brightness temperature using a formula that describes the intensity for a black body, given by the Planck law:

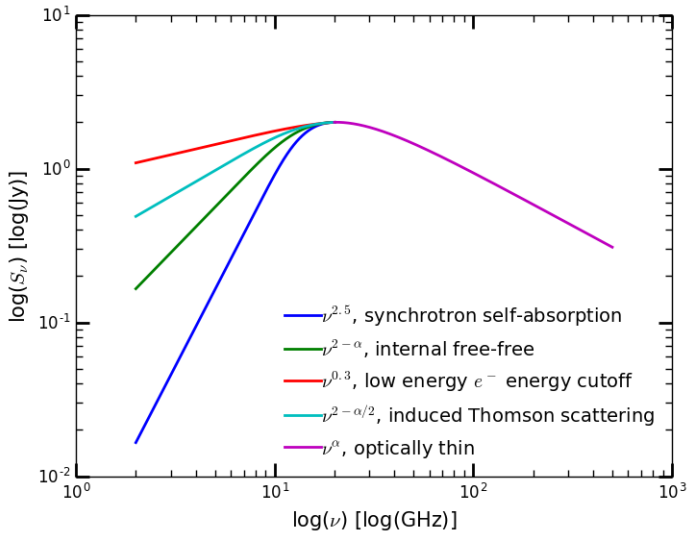

Figure 2.3: The figure shows the synchrotron spectrum of an ensemble of electrons with a power-law distribution of particle energy, $N(E)dE \propto E^{-s}dE$. The optically thin part of the spectrum is solely dependent upon the spectral index. The optically thick part of the spectrum, has a dependence on frequency of $v^{5/2}$ in the case of a pure synchrotron spectrum. Several different spectral slopes that account for varying absorption mechanisms are illustrated in the optically thick portion of the spectrum to the left. For instance, in the case the source has free-free radiation together with synchrotron radiation, the exponent of the frequency will be 4.5.

$$I_\nu = \frac{2h\nu^3}{c^2}\frac{1}{\exp\left(h\nu/kT_b\right)-1}, \tag{2.23}$$

where:

I_ν is the intensity of the radiation,
h is the Planck constant,
ν is the frequency,
c is the speed of light,
k is the Boltzmann constant, and,
T_b the brightness temperature used as an equivalent temperature of the emitting material.

The brightness temperature obtained from Eq 2.23 is only a lower limit, as no incoherent radiation process can emit more than a black body.

If we now use the Rayleigh -Jeans limit, $h\nu \ll kT$, as we are working with radio waves that correspond to the low frequency tail of the Planck spectrum, the intensity of the radiation can be rewritten as:

$$I_\nu = \frac{S_\nu}{\Omega_s} = \frac{2kT_b}{\lambda^2} = \frac{2k\nu^2T_b}{c^2}, \tag{2.24}$$

where

S_ν is the flux density of the radiation, and

Ω_s is the solid angle subtended by the emission, $\Omega_s \approx \theta_s^2$, where θ_s is the angular size of the emitting region.

Solving for the brightness temperature:

$$T_b = \frac{c^2}{2k}\frac{S_\nu}{\nu^2\theta_S^2}. \tag{2.25}$$

The application of Eq. 2.25, however, is not straight-forward, as we are dealing with non-thermal radiation which does not follow a Maxwellian velocity distribution. Equation 2.23 deals with thermal radiation, while we are concerned with non-thermal electrons. There are two reasons, however, that allow us to use Eq. 2.23 in order to obtain brightness temperatures of non-thermal distributions of electrons. The first is that the synchrotron spectrum peaks near its critical frequency. Therefore, the emission and absorption processes that we observe at a certain frequency should be caused by electrons of similar energy. The second is that, as the number density of electrons is typically low and its interaction times are long, the characteristic timescale for the electrons to reach an equilibrium state is very long. This also allows us to relate the associated temperature of electrons with their energy,

$$\gamma m_e c^2 = 3kT_e.$$

Since $\nu_c \approx \gamma^2\nu_g$, where $\nu_g = \dfrac{eB}{2\pi m_e c}$ is the gyrofrequency, B is the magnetic field and e the electron charge, we can easily rewrite the effective temperature of the electrons as:

$$T_e = \frac{m_e c^2}{3k}\gamma^{1/2} \approx \frac{m_e c^2}{3k}\left(\frac{\nu}{\nu_g}\right)^{1/2} = \frac{(2\pi)^{1/2}}{3}\frac{m_e^{3/2}c^{5/2}}{ke^{1/2}}\frac{\nu^{1/2}}{B^{1/2}}. \tag{2.26}$$

Equation 2.26 corresponds to the brightness temperature obtained with the Planck spectrum in the case of a self-absorbed source, where the brightness temperature of the radiation is equal to the effective kinetic temperature of the electrons. Therefore, it is possible to obtain an estimate of the magnetic field of a region using the brightness temperature for optically thick regions, such as the core component of an AGN jet.

2.2.1 Brightness temperature from visibility

In absence of a direct measurement of the angular size of an emiting region, we can also estimate the brightness temperature of the emitting region using the measured interferometric visibilities. This method will give us a lower limit of

the brightness temperature as well as a limitting brightness temperature, i.e., the maximum brightness temperature we are able to measure for a given data set due to its limitations. We will describe the method following Lobanov (2015).

As we do not have any information pertaining to the specific shape of the brightness distribution, we will apply a symmetry assumption which allows us to determine the size of the emitting region from the visibility amplitude, V_q, alone. Assuming that the distribution of the emitting region is gaussian, the visibility amplitude can be calculated with:

$$V_q = V_0 \exp -\frac{\pi^2 \theta_r^2 q^2}{4 \ln 2}, \tag{2.27}$$

where,

V_0 is the zero-spacing visibility amplitude,

θ_r the size of the emitting region, and,

$q = \frac{\lambda}{D}$ the spatial frequency.

For the size of the emitting region, we have:

$$\theta_r = \frac{2\sqrt{\ln 2}}{\pi} \frac{\lambda}{D} \sqrt{\ln \frac{V_0}{V_q}}, \tag{2.28}$$

where D is the baseline.

However to be able to estimate a size for the emitting region we need to know a value for zero-spacing visibility. Using Eq. 2.28, we obtain for the brightness temperature:

$$T_\mathrm{b} = \frac{\pi}{2k} \frac{D^2 V_0}{\ln V_0/V_q}. \tag{2.29}$$

Considering the brightness temperature as a function of the visibility/zero spacing visibility ratio, it can be shown that the lower limit of the brightness temperature is obtained when $V_0 = eV_q$. This removes the dependence on the zero-spacing visibility amplitude and gives us a lower limit on the brightness temperature:

$$T_\mathrm{b,min} = \frac{\pi e}{2k} D^2 V_q. \tag{2.30}$$

This approach also allows us to obtain a limiting brightness temperature, i.e., the maximum brightness temperature we can obtain given certain interferometric data. This does not mean it is the maximum brightness temperature the source can have, just that our data do not allow us to measure a higher brightness temperature. To obtain the minimum brightness temperature, we do not need to know the zero-spacing visibility. However, to obtain the limiting brightness temperature we need to have an estimate of the zero spacing visibility amplitude. As a

first approach, we could take the total given flux. This flux, however, contains information about all the scales in the map so it would be a poor approach. A better approach would be the total flux of the gaussian component obtained by approximating the source as an ensemble of gaussian components. However, in some cases, the incompleteness of available data sets does not allow us to use this approach. A better approach, therefore, is to use a lower limit of the zero-spacing visibility: $V_0 = V_q + \sigma_q$. This approach is valid with very long baselines and therefore applicable with space-VLBI data. With this marginal resolution, the size of the component should be larger than:

$$\theta_{\rm lim} = \frac{2\sqrt{\ln 2}}{\pi} \frac{\lambda}{D} \sqrt{\ln \frac{V_q + \sigma_q}{V_q}}. \tag{2.31}$$

As the size of the component should be larger than the limiting size, the brightness temperature cannot exceed:

$$T_{\rm b,lim} = \frac{\pi D^2 (V_q + \sigma_q)}{2k} \left[\ln \frac{V_q + \sigma_q}{V_q} \right]^{-1}. \tag{2.32}$$

2.3 Radio core and core shift

The concept of a "radio core" within the VLBI image of a jet comes from the model described in Blandford & Königl (1979). In this model, the feature known as the radio core is defined as the surface where the optical depth of synchrotron radiation equals unity. Therefore, the region inside the radio core is optically thick, while the region outside of the $\tau = 1$ surface is optically thin. Observations show that the position of the radio core changes with the observing frequency (see, for example, Gabuzda et al. 2001; Hovatta et al. 2014). The higher the frequency, the closer we observe the radio core to the central engine. Blandford & Königl (1979) defines the radio core as partially optically thick and the result of the combination of optically thin components with different turnover frequencies. As the position of the $\tau = 1$ surface changes with frequency, however, images made at different frequencies need to be properly aligned. Hybrid mapping removes information about the absolute position of the source, as it puts the brightness point of the image in the center, and unless we use phase referencing, this cannot be corrected in the imaging stage. We do this by referencing images at different frequencies on the positions of selected optically thin components in the jet (Fig. 2.4). As these components have the same position at different frequencies, we can use them as reference points to align the images and to measure the positional shift of the core.

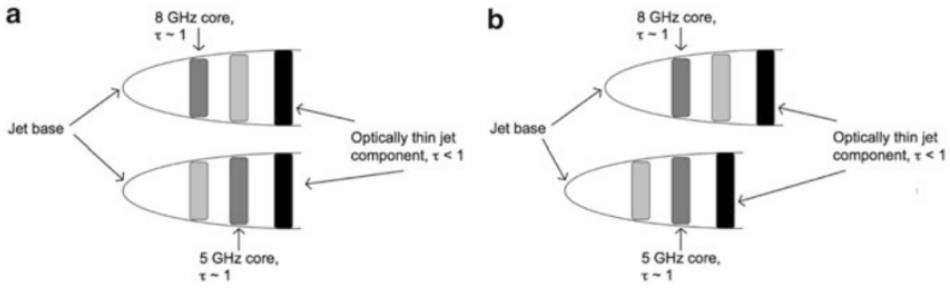

Figure 2.4: The above panels illustrate a jet with different features. The gray feature demarcates the radio-core, whereas the black feature shows an optically thin component. The upper part of the figure on both sides highlights an 8 GHz image of the jet and the bottom parts are of a corresponding 5 GHz image. a) Illustration of a well aligned jet in which the optically thin components are in the same position at different frequencies. b) Illustration of an incorrectly aligned jet. This misalignment occurs if by aligning images to the brightest feature after hybrid mapping.In both images, the jet base is close to the origin. However, optically thin components are not cospatial at both frequencies (Gabuzda 2015).

2.4 Magnetic fields and particle density in the jet

In this section we will make use of several of the concepts derived in the previous sections. This will allow us to have different estimates for the magnetic field of a source using different approaches.

2.4.1 Magnetic field from synchrotron self-absorption

This approach relies on the knowledge of the turnover frequency and turnover flux density. We follow the method described in Fromm et al. (2013b). For this case it is important that we correct for relativistic effects in order to obtain the intrinsic magnetic field of the source. In order to do this, we have to correct the emission and absorption coefficients. Taking into account relativistic and cosmological effects, their corrected values are:

$$\begin{aligned} \chi_\nu &= \frac{\chi'_{\nu((1+z)/\delta)}}{\delta}, \\ j_\nu &= \delta^2 j'_{\nu((1+z)/\delta)}. \end{aligned} \tag{2.33}$$

In order to derive an estimate of the magnetic field and particle density from the observed spectrum, we need to define the optically thin flux density and optical depth as follows:

$$\begin{aligned} S'_{\nu,\mathrm{thin}} &= \frac{\pi}{D_L^2} c_j(s) c_{j,b}(s) (1+z)^{-(s-3)/2} R'^3 \delta^{(s+5)/2} \kappa B'^{(s+1)/2} \nu^{-(s-1)/2}, \\ \tau_\nu &= c_\chi(s) c_{\chi,b}(s) (1+z)^{-(s-4)/2} R' \delta^{(s+4)/2} \kappa B'^{(s+2)/2} \nu^{-(s+4)/2}. \end{aligned} \tag{2.34}$$

Now we replace the flux density, optical depth, and frequency in Equation 2.34 with the corresponding turnover values. Solving for the normalization constant, κ, and the magnetic field, $B^{'}$, yields:

$$B^{'} = \frac{\pi^2}{D_L^4}\left[\frac{c_j(s)c_{j,b}(s)}{c_\chi(s)c_{\chi,b}(s)}\right]^2 (1+z)^7 R^{'4}\delta\nu_m^5 S_m^{-2}\tau_m^2, \tag{2.35}$$

$$\kappa = \frac{D_L^{2s+4}}{\pi^{s+2}}\frac{[c_j(s)c_{j,b}(s)]^{-s-2}}{[c_\chi(s)c_{\chi,b}(s)]^{s+1}}(1+z)^{-3s-5}R^{'(-2s-5)}\delta^{-s-3}\nu_m^{-(2s+3)}S_m^{(s+2)}\tau_m^{-(s+1)}. \tag{2.36}$$

Knowing the normalization constant, we can obtain the number density of particles by integrating Eq. 2.14 between $E_{\rm min} = \gamma_{\rm min} m_e c^2$ and $E_{\rm max} = \gamma_{\rm max} m_e c^2$ where $\gamma_{\rm min}$ and $\gamma_{\rm max}$ are the minimum and maximum electron Lorentz factor respectively. The final result of the integration is then:

$$N = \frac{\kappa}{s-1}(m_e c^2)^{1-s}\gamma_{\rm min}^{1-s}\left[1-\left(\frac{\gamma_{\rm max}}{\gamma_{\rm min}}\right)^{1-s}\right]. \tag{2.37}$$

2.4.2 Magnetic field from core shift

Starting from the definition of the core as the surface where the optical depth is unity, we can derive different jet parameters, under several assumptions. The first one is that the particle density and the magnetic field decrease with the distance, r, along the jet due to expansion. They can be approximated with a power law as $N = N_1 r^{-n}$ and $B = B_1 r^{-m}$ where N_1 and B_1 are the values of the particle density and the magnetic field at a distance of 1 parsec from the central engine (Lobanov 1998b; Hirotani 2005). We also assume magnetic flux conservation. Furthermore, the parameters m and n can also yield some information about the jet. In the case of a conical jet profile, in which particles are neither created nor destroyed, then, $n = 2$. Furthermore, applying magnetic flux conservation to a stationary superfast-magnetosonic jet, and assuming that the field is only toroidal, we get $m = 1$. The parameters m and n, together with the spectral index, α, also allows us to define another two parameters k_r and k_b, given by:

$$\begin{aligned} k_r &= \frac{2n + (3-2\alpha)m - 2}{5-2\alpha}, \\ k_b &= \frac{3-2\alpha}{5-2\alpha}. \end{aligned} \tag{2.38}$$

In equipartition, i.e., when the energy stored in the magnetic field equals the energy in the radiating particles, $k_r = 1$, and $m = 1$ and $n = 2$.

Since we are basing this approach on the apparent measured core position, we need to first define the core offset measure, $\Omega_{r\nu}$, (Lobanov 1998b) . When the core position has been measured for two frequencies, this parameter is given by:

$$\Omega_{r\nu} = 4.85 \times 10^{-9} \frac{\Delta r_{\rm mas} D_L \nu_1^{1/k_r} \nu_2^{1/k_r}}{(1+z)^2 \left(v_2^{1/k_r} - \nu_1^{1/k_r}\right)}, \tag{2.39}$$

where $\Delta r_{\rm mas}$ is the coreshift value measured between the frequencies ν_2 and ν_1 with $\nu_2 > \nu_1$. With the frequency in GHz and the coreshift in mas, the units of the coreshift measurement are pc GHz.

Applying the above assumptions, the starting point for this approach is the definition of the optical depth. From this point, we will describe separately two different approaches for determining the magnetic field from coreshift given in Hirotani (2005) and Lobanov (1998b) separately. The main reason for this is that the assumptions and the main final equations in these approaches differ.

In Lobanov (1998b), the starting equation for the optical depth is:

$$\tau(r) = C_2(\alpha) N_1 \left(\frac{eB_1}{2\pi m_e}\right)^{3/2-\alpha} \frac{\delta^{3/2-\alpha}\varphi}{r^{(3/2-\alpha)m+n-1}\nu^{5/2-\alpha}}, \tag{2.40}$$

where $C_2(-0.5) = 8.4 \times 10^{10}$ is given in Konigl (1981). Equating the optical depth to one, we have that the distance to the core from the central engine is:

$$r\,[\rm pc] = \left(\frac{B_1^{k_b} F}{\nu}\right)^{1/k_r}, \tag{2.41}$$

where $F = (1+z)^{-1} \left[6.2 \times 10^{18} C_2(\alpha) \delta^{3/2-\alpha} N_1 \varphi\right]^{1/(5/2-\alpha)}$.

To obtain the value of the magnetic field at 1 pc we set $r = 1$ in Eq. 2.41. Using Eq. 2.39, the value of B_1:

$$B_1 = \left(\frac{\Omega_{r\nu}}{\sin\theta}\right)^{k_r/k_b} F^{-1/k_b}. \tag{2.42}$$

We can also obtain the absolute distance between the core and the sonic point. This distance is much larger than the distance between the sonic point and the central engine, and as such can be approximated as the distance to the central engine, r_c, and is given by:

$$r_c(\nu) = \Omega_{r\nu} \sin\theta^{-1} \nu^{-1/k_r}. \tag{2.43}$$

This allows us to obtain an expression for the magnetic field in the core:

$$B_c = \nu^{m/k_r} \left(\frac{\Omega_{r\nu}}{(1+z)\sin\theta} \right)^{k_r/k_b - m} F^{-1/k_b}. \tag{2.44}$$

This approach suffers from the drawback, since we have not assumed equipartition, that it requires the knowledge of the particle density. This is only possible with optical observations or with some previous estimate obtained independently from this method. The magnetic field estimated depends strongly on the assumed particle density, so this method is only reliable when the estimated particle density is known with enough accuracy, since fixing the particle density will force the order of magnitude of the magnetic field.

Now we describe the procedure described in Hirotani (2005).

We start again with the equation describing the optical depth that we will set up to unity:

$$\tau(r) = C_1(\alpha) \frac{2\varphi}{\sin\theta} \frac{-2\alpha}{\gamma_{\min}^{2\alpha}} \left(\frac{\delta}{1+z} \right)^{3/2-\alpha} \left(\frac{\nu_0}{\nu} \right)^{5/2-\alpha} r^{1-n-m(3/2-\alpha)} \frac{r_1 N_1 e^4}{m_e^2 c^4} \left(\frac{eB_1}{2\pi m_e c \nu_0} \right)^{3/2-\alpha}, \tag{2.45}$$

where $C_1(\alpha)$ is a constant that is equal to (Gould 1979):

$$C_1(\alpha) = \frac{3^{1-\alpha}}{8} \sqrt{\pi} \Gamma \left(\frac{7-2\alpha}{4} \right) \Gamma \left(\frac{5-6\alpha}{12} \right) \Gamma \left(\frac{25-6\alpha}{12} \right) \left(\Gamma \left(\frac{9-2\alpha}{4} \right) \right)^{-1}.$$

We can obtain the distance to the central engine from Eq. 2.45. We set this value equal to unity and assume equipartition. This leads to Eq.2.43. We can also obtain the magnetic field strength at 1 pc, by setting $r = 1$ in Eq. 2.45. This results in:

$$B_1 \approx \frac{2\pi m_e^2 c^4}{e^3} \left[\frac{e^2}{m_e c^3} \left(\frac{\Omega_{r\nu}}{r_1 \sin\theta} \right)^{k_r} \right]^{\frac{5-2\alpha}{7-2\alpha}} \left[\pi C_1(\alpha) \frac{r_1 m_e c^2}{e^2} \frac{-2\alpha}{\gamma_{\min}^{2\alpha+1}} \frac{\varphi}{\sin\theta} K(\gamma,\alpha) \left(\frac{\delta}{1+z} \right)^{\frac{3}{2}-\alpha} \right]^{\frac{-2}{7-2\alpha}}, \tag{2.46}$$

where $K(\gamma,\alpha)$ is assumed to be constant and, in the case where equipartition in the core holds, its value is:

$$K(\gamma,\alpha) = \frac{\gamma_{\min}}{\langle \gamma_- \rangle} \sim \frac{2\alpha+1}{2\alpha} \frac{(\gamma_{\max}/\gamma_{\min})^{2\alpha} - 1}{(\gamma_{\max}/\gamma_{\min})^{2\alpha+1} - 1}.$$

The magnetic field in the core, B_c, is:

$$B_c \approx B_1 r_c^{-1}. \tag{2.47}$$

Now for both approaches (Lobanov 1998b; Hirotani 2005), if we assume that $\alpha = -0.5$, and $k_r = 1$, i.e. we assume equipartition between particle energy and magnetic field energy, the magnetic field at one parsec can be simplified to the following expression:

$$B_1 \approx 0.025 \left[\frac{\Omega_{r\nu}^3 (1+z)^2}{\varphi \delta^2 \sin\theta} \right]^{\frac{1}{4}}. \tag{2.48}$$

Knowing the magnetic field, we can also obtain the particle density, which is given by:

$$N_1 = \frac{K(\gamma, \alpha)}{8\pi m_e c^2} \gamma_{\min}^{-1} B_1^2. \tag{2.49}$$

Notice than in Hirotani's approach, we need the values the minimum and maximum Lorentz factor of the electrons to obtain the magnetic field when $k_r \neq 1$, which are also used in the synchrotron approach to calculate the number of particles. For the calculation of the magnetic field the real value of these parameters is not important because we are only interested in their ratio. However, the value of the minimum particle Lorentz factor is important to obtain the particle density.

We should notice that knowing the intrinsic magnetic field strength could also give us an approximation on $\gamma_{\max}$. The maximum Lorentz factor of the electron is given by equating the gyration and cooling timescale (Mimica et al. 2010; Mimica & Aloy 2012). This results in:

$$\gamma_{\max} = \left(\frac{3 m_e^2 c^4}{4\pi e^3 B'} \right)^{1/2}. \tag{2.50}$$

Furthermore, a lower limit to the minimum electron Lorentz factor can also be given without any further analysis in the case of blazars. By studying synthetic maps of AGN jet simulations, Mimica et al. (2009) found that in the case of blazars, this lower limit should be greater than or equal to 10.

Chapter 3

Magnetohydrodynamics

An AGN jet can be treated as a relativistic magnetized fluid. Since the plasma couples with the magnetic field, the trajectory of the charged particles bends with the Larmor radius. If we consider a proton which has a Lorentz factor γ, the Larmor radius would be $10^{-12}\gamma B^{-1}$ pc (Blandford & Rees 1974). If this curvature is much smaller than the typical scales of our system, the magnetic field causes the particles to be confined and bounds them together as in a fluid. Therefore, a jet can be described using the conservation laws and the equation of state (EOS). The conservation laws are the conservation of mass and the conservation of the total energy-momentum. They can be obtained with:

$$\nabla_\mu(\rho u^\mu) = 0, \tag{3.1}$$

$$\nabla_\nu T^{\mu\nu} = 0, \tag{3.2}$$

where ∇_μ is the covariant derivative with respect to the metric tensor $g_{\mu\nu} = \text{diag}(-1, 1, 1, 1)$. $T^{\mu\nu}$ is the energy-momentum tensor of the plasma and it is described by (Weinberg 1972):

$$T^{\mu\nu} = \rho h^* u^\mu u^\nu + p^* g^{\mu\nu} - b^\mu b^\nu, \tag{3.3}$$

where,

ρ is the rest mass density,

$u^\mu = \gamma\,(1, v)$, is the four velocity, with $\gamma = 1/\sqrt{(1 - v^2)}$ the Lorentz factor,

b^μ is the magnetic field in the comoving frame

$$b^\mu = (b^0, b^i) = \left(\gamma(vB), \frac{B^i}{\gamma} + v^i b^0\right), \tag{3.4}$$

h^* and p^* the hydromagnetic specific entalphy and total pressure

$$h^* = h + \frac{b^\mu b_\mu}{\rho} = 1 + \epsilon + \frac{p}{\rho} + \frac{b^\mu b_\mu}{\rho}, \qquad p^* = p + p_{\rm mag}. \tag{3.5}$$

where

$h = 1 + \epsilon + \dfrac{p}{\rho}$ is the specific entalphy,

ϵ the specific internal energy,

p the pressure and ,

$p_{\rm mag} = \frac{|b|^2}{2}$ the magnetic pressure, with $|b|^2 = b^\mu b_\mu = B^2\gamma^{-2} + ({\rm vB})^2$ the magnetic energy density.

The magnetic field has further constraints. It is described by the Maxwell equations, $\nabla_\mu \left(u^\mu b^\nu - u^\nu b^\mu\right) = 0$, which gives us two constraints in the spatial and temporal coordinates.

$$\frac{\partial \mathbf{B}}{\partial t} - \nabla \times (\mathbf{v} \times \mathbf{B} = 0), \qquad \nabla \mathbf{B} = 0, \tag{3.6}$$

which are the induction equation and the divergence constraint, respectively. These equations are also known as the Faraday equations.

Finally, we need to also consider the equation of state. In our case, we adopt the ideal equation of state with adiabatic index, Γ, so that one can write for the pressure:

$$p = (\Gamma - 1)\rho\epsilon. \tag{3.7}$$

This completes our set of RMHD equations, together with Eqs. 3.1, 3.2 and 3.6.

The magnetic field is parameterized by the magnetization β_m, which is defined as the ratio of magnetic to gas pressure:

$$\beta_m \equiv \frac{p_{\rm mag}}{p}. \tag{3.8}$$

In this thesis, we will consider a purely hydrodynamical case, i.e., neglecting the magnetic field terms, when studying plasma instability, and the magneto hydrodynamical case for high resolution images where regions close to the central engine are studied. To solve this, we use a 1D approach.

3.1 Purely hydrodynamical case

We begin describing the case without magnetic field. The use of hydrodynamical models can be justified since tens of parsecs away from the jet formation region, the jet probably starts to be dominated by the particles, since gas coming from the external medium enters in the system producing a conversion of part of the magnetic energy and magnetic acceleration in kinetic energy leading to a particle dominated jet (Vlahakis & Königl 2004; Komissarov et al. 2009; Komissarov 2012). We solve the equations 3.1 and 3.2. To obtain the equations corresponding to this case, we will derive the unperturbed and perturbed equations. We start with the unperturbed case, the derivation of the full system of equations can be found in appendix A. Here we only present the final result corresponding to the conservation equations. The final solution of the equations for the unperturbed case is (see, e.g., Ferrari et al. 1978):

$$\rho h\gamma\left[\left(\frac{\partial\gamma}{\partial t}\right)+(\mathbf{v}\nabla)\,\mathbf{v}\right]+\nabla P+\mathbf{v}\left(\frac{\partial P}{\partial t}\right)=0, \tag{3.9}$$

$$\gamma\left[\frac{\partial p}{\partial t}+(\mathbf{v}\nabla)\,\rho\right]+\rho h\left[\frac{\partial\gamma}{\partial t}+(\mathbf{v}\nabla)\,\gamma+\gamma\,(\nabla\mathbf{v})\right]=0. \tag{3.10}$$

Equation 3.9 corresponds to the conservation of momentum and equation 3.10 to the conservation of energy.

3.1.1 Perturbed state

Since the jet is affected by perturbations that alter to the stationary state, it is just natural to also consider a perturbed state of the jet and obtain the equations related to such a system. In order to do that, we will rewrite Eqs. 3.9 and 3.10 using the perturbed variables, which are described by the introduction of a linear perturbation in the variables ρ, P and v:

$$\begin{aligned} P &= P_0 + P_1 \\ (\rho h) &= (\rho h)_0 + (\rho h)_1 \\ \mathbf{v} &= \mathbf{v_0} + \mathbf{v_1}, \end{aligned} \tag{3.11}$$

where the index 0 indicates the stationary state values and the index 1 the perturbed ones. With this, the Lorentz factor is $\gamma = \gamma_0 + \gamma_0^3 \mathbf{v_0}\mathbf{v_1}$. Taking all this in account the conservation equations of a perturbed state are:

$$\gamma_0 \left[\frac{\partial \rho_1}{\partial t} + (\mathbf{v_1}\nabla)\,\rho_0 + (\mathbf{v_0}\nabla)\,\rho_1\right] + \gamma_1\,(\mathbf{v_0}\nabla)\,\rho_0 + (\rho h)_1\,[(\mathbf{v_0}\nabla)\,\gamma_0 + \gamma_0\,(+)\,\nabla \mathbf{v_0}] +$$

$$+ (\rho h)_0 \left[\frac{\partial \gamma_1}{\partial t} + (\mathbf{v_1}\nabla)\,\gamma_0 + (\mathbf{v_0}\nabla)\,\gamma_1 + \gamma_0\,(\nabla \mathbf{v_1}) + \gamma_1\,(\nabla \mathbf{v_0})\right] = 0 \tag{3.12}$$

$$\gamma_0^2\,(\rho h)_0 \left[\frac{\partial \mathbf{v_1}}{\partial t} + (\mathbf{v_1}\nabla)\,\mathbf{v_0} + (\mathbf{v_0}\nabla)\,\mathbf{v_1}\right] + [2\gamma_0^4 \mathbf{v_0}\mathbf{v_1}\,(\rho h)_0 + \gamma_0^2\,(\rho h)_1]\,[(\mathbf{v_0}\nabla)\,\mathbf{v_0}] +$$

$$+\nabla P_1 + \mathbf{v_0}\frac{\partial P_1}{\partial t} = 0 \tag{3.13}$$

This system of equations has wave-like solutions and can describe physical phenomena in the jet affected by the presence of a perturbation.

3.1.2 Flow instability

Kinematics and energy release in the jet can be dominated by magnetic field or particle energy at different stages and locations. Jets are formed by magneto-hydrodynamical processes involving large magnetic fields, therefore they will be magnetically dominated close to the launching region. When propagating, the energy of the magnetic field is gradually dissipated and converted into particle kinetic energy via, e.g., jet acceleration. In the magnetically-dominated regime, Current-Driven instability (CDI) may arise. In the particle-dominated regime, Kelvin-Helmholtz instability (KHI) can develop.

3.1.2.a Current-Driven Instability

When a toroidal component of the magnetic field is present in the jet, CDI can arise due to current transitions and the jet may become magnetically unstable. They can be stabilized by a strong poloidal, organized magnetic field acting against the flow distortion (Perucho 2012). There are two different instability modes that can develop in the jet: a pinch mode and a kink mode. A pinch creates a sausage-like jet. However, if the kink mode is excited, the jet develops helicoidal structures (Perucho 2012). These instabilities can develop up to distances of around a few hundred gravitational radii (McKinney & Blandford 2009) because the magnetic field is weaker the farther we are from the central engine and due to the contact of the jet with the medium.

3.1.2.b Kelvin-Helmholtz Instability

KHI is produced at the boundary between two fluids due to the presence of a velocity gradient between them. As a result different instability modes can grow, destabilizing the original jet structure. Transverse displacements generate a transfer of longitudinal momentum to the external medium which results from converting kinetic energy into internal energy. The regions where this effect take place become overpressured, which generates transversal waves, as the flow tries to correct the overpressure moving to an underpressured area. Instabilities appear when the reflection coefficient of the waves is larger than one at the jet boundary with the ambient medium, i.e, the amplitude of both waves is much larger than that of the incident wave (Payne & Cohn 1985). If the boundary consist of a shear-layer, the instability is suppressed if the wavelengths are shorter than the width of the shear layer (Ferrari et al. 1978). The growth of the instability depends on the velocity, energy content and density inside and outside the jet. The faster, colder, and denser the jet is, the more stable it is (Birkinshaw 1991; Perucho et al. 2005, 2010).

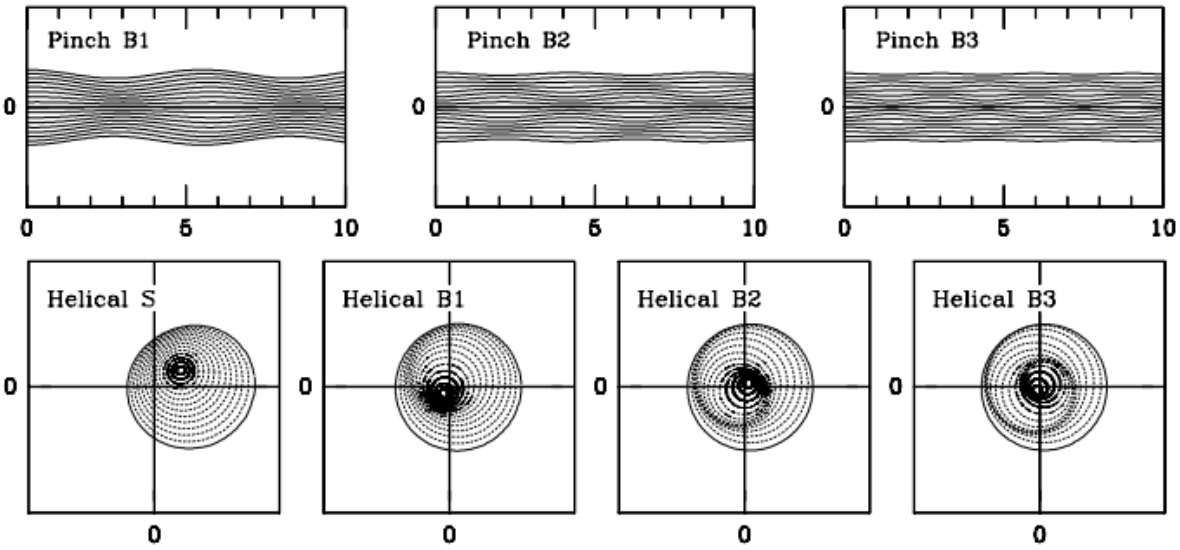

Figure 3.1: Fluid displacement due to lower modes of Kelvin-Helmholtz instability. On the top, axial cross-sections of a jet showing the first three pinch body modes are seen. At the bottom, transverse cross-sections of a jet showing the surface and first three helical body modes are seen. (Hardee 2006)

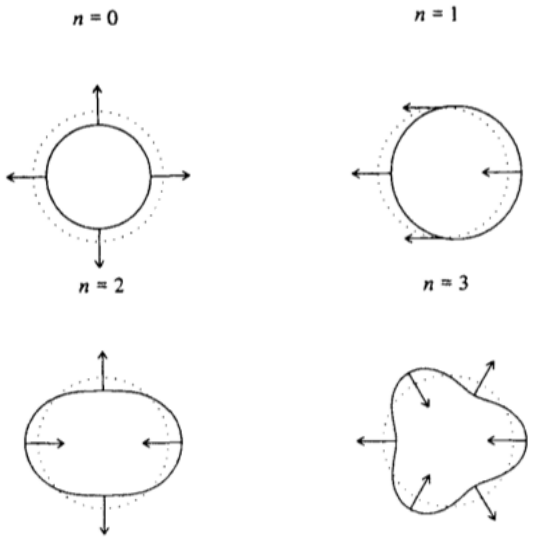

Figure 3.2: Deformations in the jets due to the effect of Kelvin-Helmholtz instability for n=0,1,2 and 3. (Birkinshaw 1991)

Linear analysis

We describe the flow using cylindrical coordinates, (r, z, ϕ), linearize the set of hydrodynamics equations considering a perturbation (Eq. 3.12, Eq. 3.13), and assuming wave like perturbations for relativistic, sheared jets to obtain a differential equation of the linearized stability problem relating the frequency and the wavenumber (see, e.g., Birkinshaw 1984, 1991):

$$\frac{d^2p_1(r)}{dr^2} + \frac{dp_1(r)}{dr}\left\{\frac{1}{r} + \frac{2\gamma_{0,\mathrm{j}}(r)^2\dfrac{dv_{0,z}(r)}{dr}(k - \dfrac{\omega v_{0,z}(r)}{c^2}}{w - kv_{0,z}(r)} - \frac{\dfrac{d\rho_0(r)}{dr}}{\rho_0 + \dfrac{p_0}{c^2}}\right\} + p_1(r)\left\{\gamma_{0,\mathrm{j}}(r)^2\left[\frac{\rho_0(r)(\omega - kv_{0,z}(r))^2}{\Gamma p_0} - \left(k - \frac{\omega v_{0,z}(r)}{c^2}\right)^2\right] - \frac{n^2}{r^2}\right\} = 0\,, \tag{3.14}$$

where the subscripts 0 and 1 refer to unperturbed and perturbed variables, respectively, r and z are the radial and axial coordinates, ω is the frequency, and k and n are the axial and azimuthal components of the wave number. The value $n = 0$ corresponds to a pinching mode. This mode alters the cross-sectional area of the jet, causing succesive jet expansions and contractions. The value $n = \pm 1$ corresponds to the helical mode. This mode displaces the jet axis and makes it oscillate around its mean direction. Due to pressure asymmetry within the jet, the particles move to zones of minimum pressure, leading to the displacement of

the jet axis. Modes with $n > 1$ do not displace the jet axis but modify its cross-section. Figure 3.1 shows the displacement in the jet due to the presence of pinch and helical modes and Figure 3.2 shows the deformations in the jet due to higher order modes. Furthermore, these unstable modes are also separated into surface and body modes (Hardee 2000; Perucho 2012).

In order to solve this differential equation (Eq. 3.14), the perturbations are assumed to be proportional to $g(r)\exp\left(i(k_z z - \omega t)\right)$, where $g(r)$ describes their radial structure (Hardee 2000). We also consider a shear layer that is described by the variable $a(r)$, corresponding to the velocity or rest-mass density:

$$a(r) = a_\infty + (a_0 - a_\infty)/\cosh r^m\,, \tag{3.15}$$

where a_0 is the value of the parameter at $r = 0$, a_∞ its value when $r \to \infty$, and m defines the steepness of the layer. This has been shown to converge to the vortex-sheet solution for large enough values of m (Perucho et al. 2005).

We adopt an ideal gas equation of state with adiabatic index $\Gamma = 4/3$ to describe both the jet and ambient medium. The role of the magnetic field is neglected in this approach. This can be justified since at the scales on which Kelvin-Helmholtz instability develops, the magnetic field is not expected to be dynamically important. (Vlahakis & Königl 2004; Komissarov et al. 2009; Komissarov 2012).

Finally, we impose the following boundary conditions:

i. no incoming waves at infinity (Sommerfeld condition), and

ii. symmetry or antisymmetry of the perturbation at its first derivative on the jet axis.

The solutions to the differential equation, Eq. 3.14, can be obtained by means of the shooting-method (see Perucho et al. 2005, 2007, for details). We can then solve the equation using two approaches:

i. Temporal. It is used to study the growth of the perturbations in time. The result is a complex frequency and a real wavenumber. The real part of the frequency corresponds to the frequency of the perturbation and the imaginary part to the growth rate. This approach considers a jet with periodic boundary conditions which is far from the inlet, letting the perturbations grow with time.

ii. Spatial. It is used to study the growth of the perturbations along the jet. The solutions are a real frequency and a complex wavenumber. The real part of the wavenumber describes the wavelength of the perturbation and the imaginary part represents the growth length.

As a final remark it should be noted that there are specific conditions that allow the jet to remain undisrupted by the growth of Kelvin-Helmholtz instability, such as (Hardee 2006; Perucho 2012):

- high Mach numbers and/or Lorentz factor,
- sheath/shear velocity around the jet,
- a high density ratio of the jet with respect to the cocoon or sheath.

Non-linear regime

Once the amplitude of the perturbation grows to similar values to the background, the jet enters the non-linear regime. In this regime, if the dominating mode has a long wavelength, the jet can be deformed, disrupted, and decelerated, forming a wide mixing region. If the dominating wavelength is short, the jet shows stronger collimation and forms a hot shear-layer (Perucho et al. 2004, 2005; Perucho 2012).

3.2 Magnetohydrodynamical case

In this section we will solve Eq. 3.1, Eq. 3.2, Eq. 3.6, and Eq. 3.7 considering the presence of a magnetic field. This is necessary when studying regions in relativistic jets close to the central engine where large magnetic fields are present.

3.2.1 Quasi one dimensional equations

Since the solution of the system of magnetohydrodinamical equations (Eq. 3.1, Eq. 3.2, Eq. 3.6, and Eq. 3.7) is computationally expensive, we will simplify these equations to one dimension, which allows the study of narrow jets. We follow Komissarov et al. (2015). This implies the following approximations:

- We consider narrow jets, i.e., $r \ll z$.
- Magnetic field configurations with the divergence constraint leading to: $B^r/B^z \simeq r/z \ll 1$.
- Since we consider axisymmetry, $E^\phi = 0$ and therefore $v^r/v^z = B^r/B^z \ll 1$.
- $v^\phi \ll 1$ together with $v^z \gg v^r, v^\phi$ leads to $v^z \simeq 1$.
- Far from the central engine, $B^\phi \gg B^z$.

Applying these conditions to the equation sets (Eq. 3.1, Eq. 3.2, Eq. 3.6 and Eq. 3.7), we simplify our system of equations. The continuity equation is reduced to:

$$\partial_t (\rho\gamma) + \nabla_r (\rho\gamma v^r) = 0.$$

The divergence free equation is written as:

$$\partial_r (rB^r) = 0 \rightarrow rB^r = \text{const.}$$

We divide the Faraday equation in its two components, since we do not have the radial part of the magnetic field. The ϕ component is simplified as:

$$\partial_t B^\phi + \partial_r \left(v^r B^\phi\right) = 0,$$

and the z component as:

$$\partial_t B^z + \frac{1}{r}\partial_r (r v^z B^z) = 0.$$

Finally, the energy-momentum equations are reduced to:

$$\partial_t (\rho h\gamma^2 v^r - b^0 b^r) + \nabla_r (\rho h\gamma^2 (v^r)^2 + p_t - (b^r)^2) = \frac{p_t - b^{\phi 2}}{r},$$

$$\partial_t (\rho h\gamma^2 - b^0 b^z) + \nabla_r (\rho h\gamma^2 v^r - b^r b^z) = 0,$$

$$\partial_t \left(-b^0 b^\phi\right) + \nabla_r \left(-b^\phi b^r\right) = \frac{b^\phi b^r}{r},$$

$$\partial_t (\rho h\gamma^2 - p_t - (b^0)^2 - \rho\gamma) + \nabla_r (\rho h\gamma^2 v^r - b^r b^0 - \rho\gamma) = 0,$$

where

$b^0 = \gamma v^z B^z$,
$b^r = \gamma v^r B^z$,
$b^\phi = B^\phi/\gamma$, and,
$b^z = \dfrac{\gamma^2 + 1}{\gamma} B^z$.

If magnetic field is taken into consideration, the definition of jet parameters may differ from that from the purely hydrodynamical approach. In this case, we can calculate the magnetosonic Mach number as:

$$M_{\rm ms} = \frac{\gamma}{\gamma_{\rm ms}} \frac{v}{c_{\rm ms}}, \tag{3.16}$$

where $\gamma_{\rm ms}$ is the magnetosonic Lorentz factor, and $c_{\rm ms}$ the magnetosonic speed, given by:

$$c_{\rm ms} = \sqrt{c_A^2 + c_s^2 (1 - c_A^2)}, \tag{3.17}$$

where the Alfen speed, c_A, is defined as:

$$c_a = \sqrt{\frac{b^2}{\rho h + b^2}},$$

and the sound speed with:

$$c_s = \sqrt{\frac{\Gamma p}{\rho h}}.$$

The approach and concepts presented above will be applied to the study of jet structures at extremely high resolution with Very Long Baseline Interferometry, using the code developed by Martí (2015).

Chapter 4

Radio Interferometry and Very Long Baseline Interferometry (VLBI)

This chapter describes the basics of radio interferometry and discusses the importance of VLBI and the background for the typical VLBI calibration and imaging steps. These descriptions are based on (Taylor et al. 1999)[1].

The most important objective of VLBI is to reach quite high angular resolutions. The angular resolution of a telescope, ϑ, is given by:

$$\sin\vartheta \sim \vartheta = 1.22\frac{\lambda}{D}, \tag{4.1}$$

where D is the diameter of the instrument and λ the wavelength of the electromagnetic radiation. The factor 1.22 comes from the diffraction formula of an Airy disc. We can improve the resolution either by increasing the diameter of the instrument or by decreasing the wavelength. Since building telescopes with a quite big diameter is not practical, VLBI was born. It consists on combining the signals recorded at several radio telescopes spread throughout the Earth to create a "virtual" interferometer. Its effective diameter is equal to the largest separation between the individual antennas. For a total number of N radio telescopes, $N(N-1)/2$ baselines will contribute to such an interferometer. The resolution at a given frequency can increase even further if the observations include a space antenna ($D >$ Earth Diameter) as well. This is known as space-VLBI.

[1]For some parts, the lecture notes of the radio astronomy course given by M.A. Garrett (https://www.astron.nl/~mag/dokuwiki/doku.php?id=radio_astronomy_course_description) and the lecture notes of the course "Radio Astronomy: Tools, Applications, and impacts" given in Bonn University by U. Klein were used.

4.1 Two-element interferometer

A two-element interferometer illustrates the concept of VLBI. We consider two telescopes pointing towards the same source (see Fig. 4.1). and assume that the source is located at large distances. This leads to an effectively plane wavefront measured on Earth. However, since the antennas are at different locations, the wavefront reaches one telescope earlier than the other. The geometrical delay, τ_g, is given by:

$$\tau_g = \frac{\mathbf{bs}}{c}, \tag{4.2}$$

where $\mathbf{b}$ is the baseline vector between the two antennas and $\mathbf{s}$ is an unit vector which indicates the direction of the source in the sky.

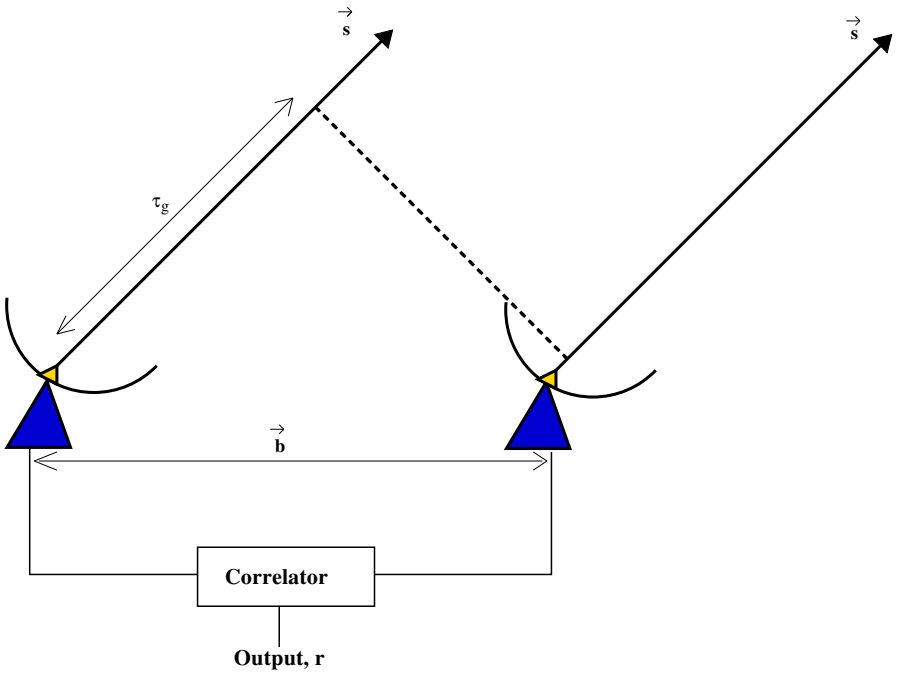

Figure 4.1: Two-element interferometer. The plane wavefront is arriving to both antennas from the direction s. In the sketch, the geometrical delay, τ_g, between both antennas is illustrated.

We detect an interference pattern once we compensate for the geometrical delay. This pattern consists of different maxima and minima, the so-called fringes. Furthermore, it depends on the orientation and the length of the baseline: fringes are perpendicular to the direction of the baseline. If a baseline is oriented North-South, the fringes are oriented East-West. Reciprocally, if the baseline is East-West oriented, the fringes are seen in the North-South direction. The distance between

maxima will be affected by the length of the baseline as well. The longest the baseline is, the tighter the fringes will be, indicating a higher angular resolution of the baseline. This is illustrated in Fig. 4.2.

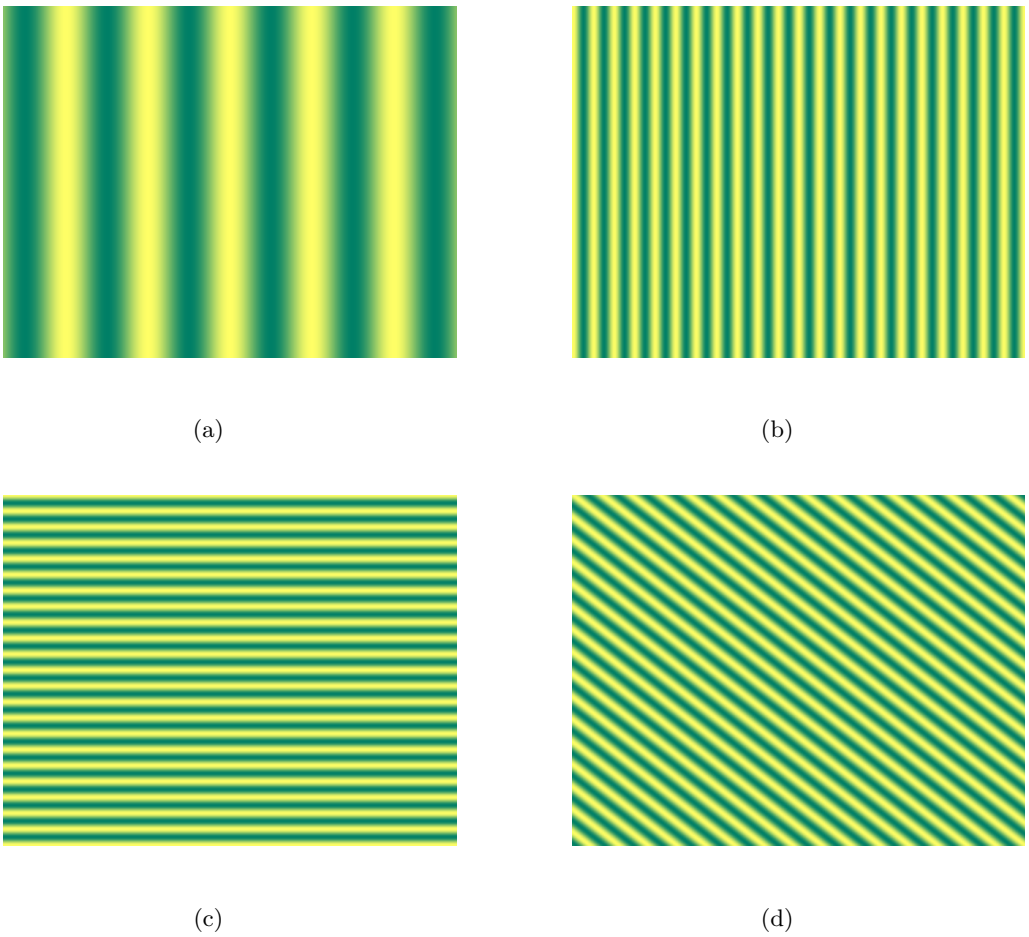

Figure 4.2: Fringe patterns for different baselines. The color scale is the following: yellow is bright, indicating an intensity equal to 1, and green is dark, indicating an intensity equal to 0. a) East-West baseline. The fringes can be observed in the North-South direction. The baseline chosen for this example is a short one. b) Long East-West baseline. Comparing it with a) it can be seen that the fringe spacing is tighter. c) Long North-South baseline. The fringes are observed in the East-West direction. d) This case illustrates a baseline Russia-South America. The fringes observed are perpendicular to this direction.

Fringes also provide information about the source. If we observe a point-like source, i.e., a source whose angular size is smaller than the distance between interference maxima, it falls into alternating maxima and minima patterns, as seen in Fig. 4.3 a). The source is not resolved. However, if the source is extended, it falls into several maxima and minima patterns, as seen in Fig. 4.3 b), and the fringes start to cancel out. This leads to a decrease of the detected amplitude. In

this case, the source is resolved.

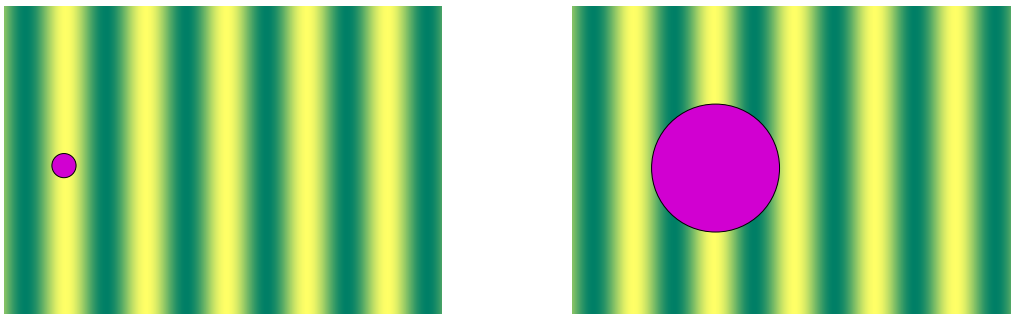

(a) (b)

Figure 4.3: Fringe pattern for a short East-West baseline. The color scale is the same as in Fig. 4.2. a) A compact source is plotted over the fringe pattern. It only falls into a single maxima pattern. This will have an effect in the answer of the interferometer to the extended signal. b) An extended source is plotted over the fringe pattern. Notice that it extends over several maxima and minima patterns.

The process of delay compensation and search for interferometric fringes is performed by combining the antenna signals in the correlator. To calculate the geometrical delay, the correlator should have an accurate model of the antenna array which includes: antenna positions, Earth Orientation Parameters (EOPs), atmospheric, and ionospheric parameters, clock offsets, etc. However, the model is not completely accurate and some errors need to be corrected later, during post-processing of the data. The calculation of τ_g is based on the correlation of the signals of both telescopes and in seeing at which time difference the correlated signal is maxima. That time difference is the geometrical delay. Before describing the different analysis taking place the correlator, it would be useful to describe how the signals are processed before reaching this point.

The signals measured at the individual telescopes are complex voltages. The incoming frequency (RF or sky frequency) of the signal needs to be down-converted to a lower frequency which is easier to store and post-process. To achieve this, a Local Oscillator, LO, and a mixer are introduced in the receiver backend. The LO produces a carrier signal at a certain frequency which is mixed with the RF signal in the mixer. The resulting output is the difference between the RF and LO signal, the so-called Intermediate Frequency (IF). The IF is selected using a filter which selects the desired frequency products of the down-conversion. After this procedure, further amplification of the weak signal can be made. Afterwards, the signals are sampled and quantized and finally, they are multiplied and time-averaged at the correlator: $\langle V_1(t)V_2(t)\rangle$ where the antenna voltages are $V_1(t)$ and $V_2(t)$. The form of both signals, after the geometrical delay has already been taken in account, is given by:

$$\begin{aligned} V_1(t) &= V\cos(2\pi\nu t) \\ V_2(t) &= V\cos[2\pi\nu(t-\tau_g)], \end{aligned} \tag{4.3}$$

where V is the maximum amplitude, ν is the frequency and t the time. In equation 4.3 two identical antennas are assumed. After multiplication and averaging, the correlator output takes the following form:

$$V_1(t)V_2(t) \equiv V^2\cos(2\pi\nu\tau_g) = r^2_{\cos}(\tau_g). \tag{4.4}$$

From inspection of Eq. 4.4, it is clear that V^2 reflects the flux density of the source. However, a cosine term is present in Eq. 4.4, which modulates the correlated flux density of the source. This cosine fringe term makes the correlated signal only sensitive to the even part. To recover the full flux density, a sine response is also needed. This response is obtained by shifting one of the two measured voltage signals by 90 degrees, which results in a signal with the following form $r^2_{\sin}(\tau_g) = V^2\sin(2\pi\nu\tau_g)$. These two fringe terms, cosine and sine, constitute, respectively, the real and imaginary parts of the interferometric visibility. In the present day, digital correlators produce directly a complex signal by using a complex multiplier, which calculates both terms simultaneously, instead of using two real multipliers and shifting one of the two voltage signals.

4.1.1 Visibility

The visibility function is a relationship between the interferometer response and the brightness distribution. It was first introduced by Michelson as a measure of the relative amplitude of the fringes: $V = \frac{S_{\max}-S_{\min}}{S_{\max}+S_{\min}}$. Going back to Fig. 4.3, we can see that if the source is unresolved, the visibility will take its maximum value, $V = 1$, and if the source is resolved (i.e., bigger than a certain fraction of the beam), then $V < 1$. Using the correlator outputs, the visibility can be described as:

$$V = r_{\cos}(\tau_g) + ir_{\sin}(\tau_g) = |V|\, e^{-i\phi_V}, \tag{4.5}$$

where $|V| = (r^2_{\cos}(\tau_g) + r^2_{\sin}(\tau_g))^{1/2}$ is the visibility amplitude, describing the information related with the correlated noise, and $\phi_V = \arctan\left(\frac{r_{\sin}(\tau_g)}{r_{\cos}(\tau_g)}\right)$ is the visibility phase providing the position information.

The visibility distribution can be converted to the brightness distribution in the sky using the van-Cittert-Zernike theorem (van Cittert 1934; Zernike 1938), which states that the spatial coherence function, visibility, is related with the brightness distribution via the Fourier transform, i.e.:

$$V \underset{\mathfrak{F}^{-1}}{\overset{\mathfrak{F}}{\rightleftarrows}} I_\nu.$$

Applying this theorem, the visibility takes the following form:

$$V = |V|\, e^{i\phi_V} = \int\int_{\text{source}} A_N(\sigma) I_\nu(\sigma) e^{-i2\pi \mathbf{b}\sigma} d\Omega, \tag{4.6}$$

where,

$A_N(\sigma)$ is the normalized antenna diagram,
$\sigma = \mathbf{s} - \mathbf{s_0}$,
$\mathbf{s}$ the position the antenna is pointing at,
$\mathbf{s_0}$ is the direction to the phase center,
$I_\nu(\sigma)$ the brightness distribution, and
$\mathbf{b}$ is the baseline.

We consider that the angular size of the source is small, leading to $A_N(\sigma) = 1$. Defining the orthogonal coordinates u and v, since the third coordinate, $w = 0$ because we assume a small source size, and introducing the directional cosines ξ and η as well, the visibility can be written as:

$$V(u,v) = \int\int I_\nu(\xi,\eta) e^{-i2\pi(u\xi+v\eta)} d\xi d\eta, \tag{4.7}$$

and therefore the brightness distribution:

$$I_\nu(\xi,\eta) = \int\int V(u,v) e^{i2\pi(u\xi+v\eta)} d\xi d\eta. \tag{4.8}$$

These relations gave rise to the concept of aperture synthesis which employs measuring the visibility distribution over finite (u,v) range to obtain the brightness distribution. Visibility measurements made on a number of independent baselines over a large time interval can be used for recovering the brightness distribution, assuming that it is constant in time. The projection of each baseline in the plane of the sky defines the location of every visibility data point, and all these points fill the Fourier plane as the Earth rotates. The sampling of the Fourier plane is the (u,v)-coverage, and the quality of the image of a source is directly related to a good sampling of this plane. An example of a good (u,v)-coverage in VLBI is shown in Fig. 4.4.

The effect of discrete sampling of the (u,v)-plane is accounted by the sampling function, $S(u,v) = \sum_k \delta(u-u_k, v-v_k)$. Adding the sampling function in Eq. 4.8:

$$I_\nu^D(\xi,\eta) = \int\int S(u,v) V(u,v) e^{i2\pi(u\xi+v\eta)} d\xi d\eta, \tag{4.9}$$

where I_ν^D is the so-called dirty map. The Fourier deconvolution theorem states that:

$$I_\nu^D(\xi,\eta) = \mathfrak{F}V_S = \mathfrak{F}S * \mathfrak{F}V = B(\xi,\eta) * I_\nu^C(\xi,\eta), \tag{4.10}$$

where $\mathfrak{F}S$ is the dirty beam or Point Spread Function (PSF) given by:

$$\mathfrak{F}S = B(\xi,\eta) = \int\int S(u,v)e^{i2\pi(u\xi+v\eta)}d\xi d\eta, \tag{4.11}$$

where $\mathfrak{F}V = I_\nu^C(\xi,\eta)$ is the visibility distribution and $*$ indicates convolution. Equation 4.10 shows the relation between the dirty image and the visibility distribution.

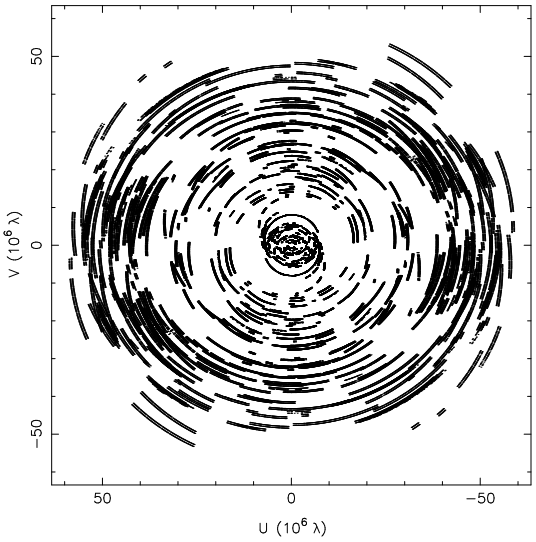

Figure 4.4: The (u,v)-coverage from a global VLBI observation of 1642+690 made in January 2015 at 1.6 GHz. Each individual track corresponds to visibility measurements made at a given frequency (notice that two sub-bands are used) for one of the baselines contributing to the observation.

4.2 Effects of finite sampling of visibilities

Fourier relations imply infinite number of harmonics and infinitely fine sampling. However, we are limited by sampling ranges and finite sampling of the data over time, frequency and (u,v)-space. The most important effect of the finite sampling of interferometric data is discussed below.

4.2.1 Effects of finite bandwidth and finite channel width

VLBI observations are performed recording at a finite frequency range, $\Delta\nu$ (bandpass). If we consider that the bandpass has a rectangular shape, its response is proportional to the sinc-funcion, $r \propto \frac{\sin(\pi\Delta\nu\tau_g)}{\pi\Delta\nu\tau_g}\cos(2\pi\nu_0\tau_g - \phi_V)$, as shown in Fig.

4.5. The result of this is that the observed fringes are modulated by this sinc function which will attenuate the visibilities. This function is called delay pattern or fringe washing function. This fringe washing effect can be minimized by tracking the source and introducing a computer controlled delay, τ_i, which shifts the fringe washing function to the center of the source of interest. The idea of introducing this delay is to keep the interferometer around the maximum of the fringe pattern which will give a full fringe amplitude.

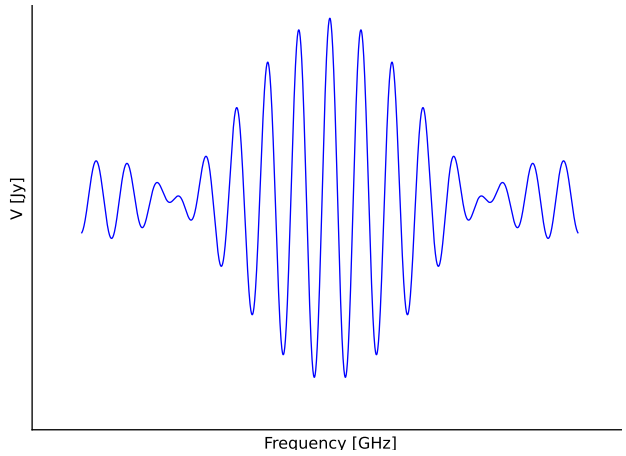

Figure 4.5: Bandpass response. The visibility is represented versus the frequency. It is an approximation to the form that the visibility takes once it goes through a bandpass.

Another undesired effect of the finite bandwidth is the bandwidth smearing or chromatic aberration. It is caused by finite channel bandwidth over which the data are averaged in frequency. It is considered that the signal of two antennas interferes at the frequency ν_0. However, if we deviate from ν_0 by some amount inside the bandwidth, it can happen that the signal of both antennas interferes, even at not exactly the same frequency, if the delay difference matches. This effect will result in smearing the object structure in a certain direction. It can be alleviated by reducing the width of individual spectral channels into which the observing bandwidth is divided.

4.2.2 Effects of frequency sampling and time averaging

1. **Sampling**. The signal needs to be sampled before arriving at the correlator. The rate of sampling has to be equal o exceed the rate specified by the Nyquist's sampling theorem for the signal to be successfully recovered. This theorem states that for a signal with maximum frequency, $\nu_{\max}$, the sampling frequency, ν_S must be greater that twice the maximum frequency value:

$$\nu_S > 2\nu_{\max}.$$

If the sampling frequency is smaller than this value, aliasing will appear in the final image, i.e. the image will display artifacts or reflections of structures of the map edge. The spurious nature of these structures can be demonstrated by changing the sampling interval to a higher one. The result will be that the structures move in the image (or disappear if the sampling frequency is larger than v_S). This would not happen with real source structure.

2. **Averaging**. The signals received are time-averaged in the correlator. If the target source was not located at the phase-tracking center, the sampling function varies slowly with time. In this situation, excessive time-averaging of the data will result in a loss of amplitude response from this object.

4.3 Calibration and imaging of VLBI data

This section describes the post-correlation analysis and imaging of VLBI data. The correlated data have to be first calibrated. Once the data are calibrated, they can be imaged using the hybrid mapping with the CLEAN algorithm (Högbom 1974). To improve the quality of a hybrid image, the technique of self-calibration can be applied to correct for phase and amplitude errors. Cleaning and self-calibration are performed in several iterative cycles until the noise properties approach the theoretical expectations.

4.3.1 Calibration

4.3.1.a Amplitude calibration

The amplitude calibration is based on the conversion of the correlation unitless coefficients, C_{ij}, to flux density in Jansky, Jy. The interferometric visibility measured, $V'_{i,j}(t)$, can be written as:

$$V'_{i,j}(\nu,t) = g_i(\nu,t)g_j(\nu,t)^* V_{ij}(\nu,t) + \epsilon_{ij}, \tag{4.12}$$

where $V_{i,j}(t)$ is the true visibility between the antennas i and j, g describes the complex gains of the two antennas, and ϵ_{ij} is the additive noise (which can be ignored). Calibrating the amplitude of the complex gain terms, we can obtain the corrected visibility. This calibration is usually done by using the system temperature measurements made during the observations.

The power received by a radio telescope is described by the radiometer equation which tells us that the power is related to an equivalent antenna temperature, T_i:

$$P_i = G^2 k T_i \Delta\nu, \tag{4.13}$$

where $\Delta\nu$ is the bandwidth, k is the Boltzmann constant and G is the voltage gain of the antenna (not the same as antenna gain), which appear in the formula due to the amplification of the signal.

If the source is small compared with the primary beam of the antenna, the antenna temperature due to the power received from the source is given by (Moran & Dhawan 1995):

$$T_A = \frac{SA}{2k}. \tag{4.14}$$

However, the antenna temperature measures noise from the receivers as wel. Therefore, we need to determine the system temperature, T_S, which describes the electronic contribution to the total antenna temperature.

It is possible to write the temperature of the system in Jy using the System Equivalent Flux Density, SEFD, defined as the source flux density that would double the total antenna power:

$$\mathrm{SEFD} = \frac{2kT_S}{A_e}, \tag{4.15}$$

where A_e is the effective collecting area. Equation 4.15 enables conversion of the visibility amplitudes to Jansky units:

$$V_{ij} = C_{ij} b \left(\frac{T_{Si} T_{Sj}}{A_i A_j} \right)^{1/2} = C_{ij} b \left(\mathrm{SEFD}_i \ \mathrm{SEFD}_j \right)^{1/2}, \tag{4.16}$$

where V_{ij} is the calibrated visibility amplitude, C_{ij} is the correlation coefficient (measured visibility amplitude) and b is a coefficient that counts for digitization losses at the correlator.

Another factor that may influence the amplitude is the opacity, τ, which represents the amount of radiation absorbed by the atmosphere. It is primarily important at high frequencies at which the atmosphere plays an important role. At frequencies larger than 20 GHz, we observe emission and absorption of water vapor and oxygen. Furthermore, if the weather is bad, the opacity of the atmosphere will be larger and it may also vary between stations. Due to these effects, the opacity needs to be corrected. It affects the system temperature as:

$$T_\mathrm{S} = T_A + T_\mathrm{atm}(1 - e^{-\frac{\tau}{\sin\delta}}), \tag{4.17}$$

where δ is the elevation. Equation 4.17 allows us to correct opacity effects.

The final factor to take into account when calibrating the amplitude is the antenna gain. The gain varies due to the changes in elevation in alt-azimuth telescopes and due to deformations of the antenna surface, which is characterized by the gain curve (Fig. 4.6). This dependence of the gain on the elevation of the

telescope pointing has to be corrected. Once all of this factors are corrected, the amplitude calibration is completed.

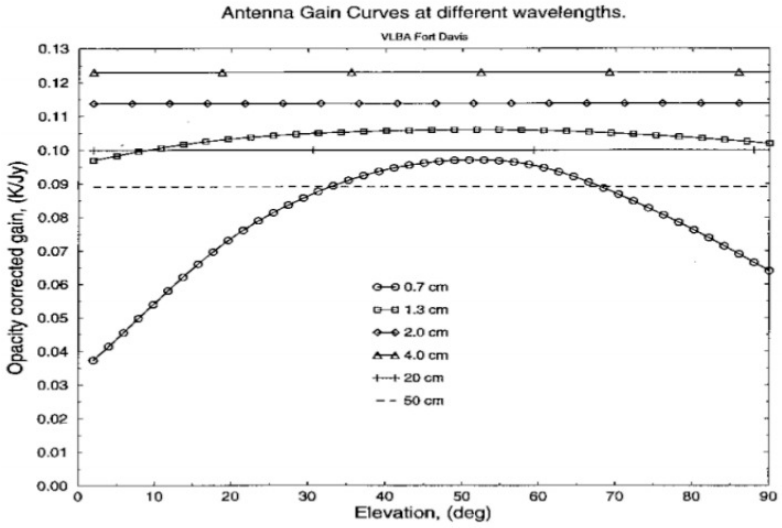

Figure 4.6: Gain Curve for the Very Long Baseline Array Fort Davis antenna. x-axis is the elevation in degrees and y-axis opacity corrected gain in K/Jy. The different symbols indicate the gain curve for different wavelengths (Moran & Dhawan 1995).

4.3.1.b Correction of antenna parallactic angles

The relative angle of the antenna feed with respect to the source is defined as the parallactic angle and changes during the observations for alt-azimuth antennas. Its phase effect has to be corrected.

4.3.1.c Phase calibration. Fringe fitting

For a successful imaging, the visibility phase also needs to be corrected. During the correlation, the array model is used to calculate the geometrical delay (Cotton 1995). The estimated delay between antennas, $\tau(t)$, is related to the phase, $\phi(\nu, t)$ as follows:

$$\phi(\nu, t) = 2\pi\nu\tau(t), \tag{4.18}$$

Errors in the array model introduce additional phase terms varying both in frequency and time. These errors are corrected for in the fringe fitting procedure. In first-order Taylor expansion, the interferometric phase is:

$$\Delta\phi\ (\nu, t) = \phi_0 + \left(\frac{\partial\phi}{\partial\nu}\Delta\nu + \frac{\partial\phi}{\partial t}\Delta t\right), \tag{4.19}$$

where $\frac{\partial\phi}{\partial\nu}$ is the delay and $\frac{\partial\phi}{\partial t}$ is the fringe rate. The effect of a non-zero residual delay can be seen as a slope when the phases are plotted versus frequency. Furthermore, a non-zero residual fringe rate produces a slope when the phases are plotted versus time. These errors should be removed. The reason behind this is that the data will be averaged in frequency later in the process. If the residual delay and rate are not removed, this leads to a lower signal-to-noise ratio, SNR, of the data.

Fringe-fitting is an algorithm which calculates the differences between the model applied by the correlator and the real interferometer we have used (Cotton 1995). The algorithm assumes that the target source is a point-like source located at the phase center. It tries to find the delay, phase and fringe rate which are necessary to apply to our data in order to satisfy this assumption. Fringe-fitting does a 2D Fast Fourier Transform (FFT) of the visibility, which is a function of frequency and time, to obtain the visibility as a function of the delay and rate. Then, it looks for the coordinates of the peak in the delay-rate space. These coordinates provide the values of delay and rate. After that, it performs a least-squares fit to the phases to find the visibility corrections corresponding to the the estimates of delay and rate obtained.

One of the most widely used fringe fitting algorithms is the Global Fringe Fitting (GFF) (Alef & Porcas 1986). This algorithm assumes that the values of delay and rate are antenna dependent and their values are then derived with respect to a reference antenna. That means that the phase corrections depend on the selection of the reference antenna.

4.3.1.d Bandpass calibration

To improve the data quality, frequency bandpasses at individual antennas also need to be corrected. Bandpass calibration is based on the correction of the frequency-dependent part of the gain. As described in section 4.2, the finite bandpasses cause a dependence of its response on frequency. Even though delay tracking is performed, small residual effects remain. Bandpass calibration is done by determining the variations of phase and amplitude with frequency and correcting for them.

4.3.2 Hybrid Mapping

After calibration, the source can be imaged. It is done using hybrid mapping with CLEAN algorithm (Högbom 1974), which describes structures as a sum of delta components. Section 4.1.1 showed that the visibilities are sampled and Fourier transformed. The Fourier transform of the sampling function represents the dirty beam, B. The Fourier transform of the visibility function provides the dirty image, I^D_ν. It was also shown that the dirty image can be understood as the convolution of the clean or true image, I^C_ν, with the dirty beam $I^D_\nu = B * I^C_\nu$. Therefore, the

CLEAN algorithm represents a deconvolution process to obtain a model of the source structure. The CLEAN algorithm can be described as follows:

1. The dirty map is created with a Fourier transform.
2. In the dirty map, the position of the maximum in intensity is located. In that position, the response of the dirty beam is subtracted, creating a clean component (CC), described by a delta function.
3. After subtraction, the resulting residual map shows a new intensity peak. The same steps are repeated for this peak and iterated further until no significant residual peak in the map is observed.
4. The clean map is created via convolution of the CC with the clean beam, an artificial beam function without side-lobe response. The size of this beam has to match the size of the dirty beam. The residual map is added to the final map.

If further improvement of the image is desired and feasible at this point, the data can be self-calibrated, and then subjected to a new round of hybrid imaging.

4.3.3 Self-calibration

The a priori calibration applied to the data before using the CLEAN algorithm is not perfect. This imperfection makes self-calibration necessary. If Eq. 4.12 is rewritten replacing the complex gain by its definition, $g_i(\nu,t) = a_i(\nu,t)e^{i\phi_i}$, and ignoring the noise, we obtain:

$$V'_{i,j}(\nu,t) = a_i(\nu,t)a_j(\nu,t)e^{i(\phi_i-\phi_j)}. \tag{4.20}$$

It is seen from Eq. 4.20 that the phases are additive and the amplitudes are multiplicative terms. These differences helps establishing self-calibration algorithms.

4.3.3.a Phase self-calibration

Residual calibration errors and unknown corruptions of the phases are corrected via phase self-calibration, which can only be applied if the data have sufficiently high SNR. The method assumes that the corrupted phases, ϕ_i, are antenna dependent and that their contribution to the measured visibility is written as follows:

$$\phi_{ij}^{\mathrm{m}} = \phi_{ij}^{\mathrm{real}} + \phi_i - \phi_j, \tag{4.21}$$

where ϕ_{ij}^{m} is the measured phase visibility and $\phi_{ij}^{\mathrm{real}}$ the real one. If true structure of the source is known (or can be approximated by its CLEAN model representation),

the real phases can be obtained. We obtain a system of $N(N-1)/2$ equations for a total of N telescopes.

If we consider the case of 3 antennas, Eq. 4.21 yields, for each individual baseline:

$$\begin{array}{l} \phi_{12}^{\mathrm{m}} = \phi_{12}^{\mathrm{real}} + \phi_1 - \phi_2 \\ \phi_{23}^{\mathrm{m}} = \phi_{23}^{\mathrm{real}} + \phi_2 - \phi_3 \\ \phi_{31}^{\mathrm{m}} = \phi_{31}^{\mathrm{real}} + \phi_3 - \phi_1. \end{array} \tag{4.22}$$

The result of adding the three formulas of Eq. 4.22 is:

$$C_{123} = \phi_{12}^{\mathrm{m}} + \phi_{23}^{\mathrm{m}} + \phi_{31}^{\mathrm{m}} = \phi_{12}^{\mathrm{real}} + \phi_{23}^{\mathrm{real}} + \phi_{31}^{\mathrm{real}}. \tag{4.23}$$

Equation 4.23 is called phase closure and it implies that the sum of the measured phases and the sum of the real visibility phases are the same. Due to the existence common antennas in different triangles not all the closure triangles are independent. An array of N antennas has $N-1$ independent closure triangles. Using these $N-1$ relations, the instrumental phases can be calculated by choosing a reference antenna and setting its instrumental phase value to zero.

To apply this algorithm, a model of the source is necessary, which is usually obtained from the CLEAN algorithm. After each run of CLEAN, a phase self-calibration can be applied and the corrected phases are used as input values for the next run of the CLEAN algorithm.

The only disadvantage of this method is that the true position of the source in the sky cannot be recovered from self-calibrated phases.

4.3.3.b Amplitude self-calibration

In the case of the amplitudes, the corrupting amplitudes are multiplicative terms. This makes amplitude correction more difficult to implement. Assuming that the corrupted amplitudes, A_i, are antenna dependent, their contribution to the measured visibility is:

$$A_{ij}^{\mathrm{m}} = A_{ij}^{\mathrm{real}} \times A_i A_j, \tag{4.24}$$

where A_{ij}^{m} is the measured amplitude visibility and A_{ij}^{real} the real one. For this case, a closure relationship is also found. If four antennas are combined, the final result is:

$$\Gamma_{1234} = \frac{A_{12}^{\mathrm{m}} A_{34}^{\mathrm{m}}}{A_{41}^{\mathrm{m}} A_{23}^{\mathrm{m}}} = \frac{A_{12}^{\mathrm{real}} A_{34}^{\mathrm{real}}}{A_{41}^{\mathrm{real}} A_{23}^{\mathrm{real}}}. \tag{4.25}$$

This equality can be used for self-calibrating visibility amplitudes in the same fashion as is done for the phases.

4.3.4 Model-fitting

Model-fitting is a technique that allows us to represent a source using specific analytical patterns, for instance 2D Gaussian components. As a result, the source is described by a simple model with few components for which different parameters can be extracted (e.g., the flux, size or distance to the map center). This model is obtained by minimizing the differences between the measured data and the model. It is done by minimizing the chi-squared, parameter that determines the fit likelihood:

$$\chi^2 = \sum_{i=1}^{N} \left(\frac{V(u_i, v_i) - F(u_i, v_i; a_1, ..., a_K)}{\sigma_i} \right)^2 , \tag{4.26}$$

where V is the observed distribution, F is the predicted distribution, σ, is the measurement errors and a_i model parameters. The typical methods used for the minimization are the Levenberg-Marquart method (Press et al. 1992) and the "grid search" (e.g., Bevington & Robinson 1992). The model is considered satisfactory when the value of reduced chi-squared, $\frac{\chi^2}{n}$ where n is the degrees of freedom of the model, approaches unity.

4.4 Data reduction in practice

To reduce the raw data after they are correlated, the Astronomical Image Processing System (`AIPS`) is commonly used (Greisen 1990). `AIPS` provides different tasks which allow full calibration of the data. Once the data are calibrated, they are exported and read with the differential mapping program or `difmap` (Shepherd et al. 1995). The CLEAN and self-calibration algorithms are applied in `difmap` until the final image is obtained. The next sections describe the basic calibration and imaging procedures.

4.4.1 Data reduction in `AIPS`: Calibration

The data are loaded in `AIPS` using the task `fitld`. Once the data are loaded, they need to be sorted with the task `msort`, which sorts them in time and baseline. The result is an organized data set that can be easily accesed. After the sorting, the data are indexed with the task `indxr`. If needed `indxr` also creates the calibration (CL) table, with the initial calibration values for the data. This table contains all the calibration parameters that may be required during the subsequent calibration.

Amplitude calibration

The amplitude calibration is performed with the tasks `antab`, `apcal`, and `clcal`. `Antab` reads in the measurements of the system temperature and the gain curves

of the participating antennas. It creates a system temperature (TY) table and a gain curve (GC) table containing all this information. The information from these tables is included in a solution (SN) table, which describes the corrections to be applied to the data. The SN table is generated with `apcal`, deriving its inputs from the TY and GC tables. This task allows us to do the opacity correction. To do this, `apcal` reads in the file with atmospheric information and requires initial guesses about the receiver temperatures and opacities at individual antennas. Then, `clcal` is applied to obtain a new CL table, which contains the results of the application of the amplitude calibration. The CL table can be examined using tasks `snplt` and `possm` (see Fig. 4.7).

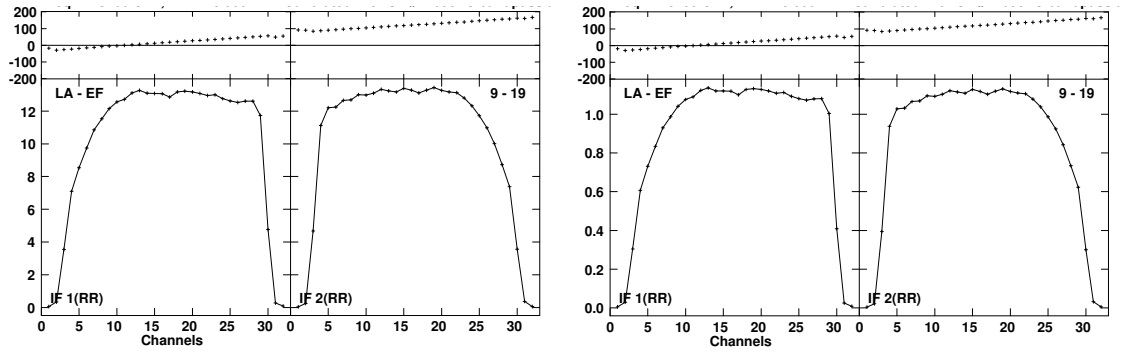

(a) (b)

Figure 4.7: Visibility (top: phase in degrees; bottom: amplitude) as a function of frequency channels in both IF for the baseline Los Álamos-Effelsberg of the 5 GHz observations of 0836+710 for the right hand polarization. a) No calibration applied. The amplitude is unitless. b) Same for CL table 2 obtained after amplitude calibration. The amplitude is in Janskys.

Parallactic angle calibration

The parallactic angle is corrected for antennas with the alt-azimuth mount with the task `clcor` using the `opcode 'PANG'`. Results of applying this correction can be checked using the task `snplt` or `vplot` with the new calibration table obtained from `clcor`.

Phase calibration

The fringe fitting algorithm is applied in `AIPS` with the task `fring`. To enable global fringe fitting, a reference antenna should be indicated. Usually it is chosen to be one of the best antennas of the array, which shows fringes in all or most of the cases and, if possible, located in the center of the array for avoiding fringe search at the longest (potentially lowest SNR) baseline. The task `fring` also has the possibility to choose another antenna indicated as potential reference for the situations where the main reference antenna has some problems. A solution

interval has to be given. It is the time interval used to determine calibration parameters. It should be a time in which delay and rate do not change significantly. If the solutions are good, they will be applied in a calibration table with the task `clcal`.

After applying the fringe-fitting solutions, the resulting baseline phases can be checked with the task `possm`, as shown in Fig. 4.8.

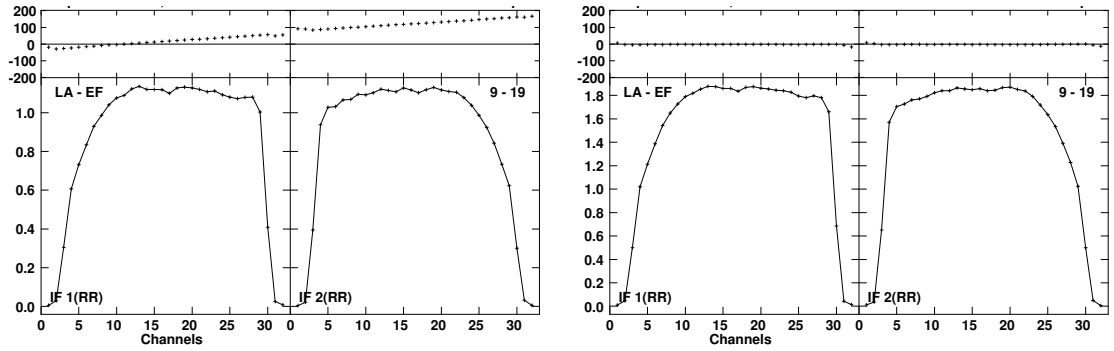

(a) (b)

Figure 4.8: Results of application of fringe fit solutions obtained for the baseline Los Álamos-Effelsberg of the 5 GHz observations of 0836+710 for the right hand polarization. a) Before fringe fit. We can see the slopes in phase for the two IFs, which indicates that delay and rate need to be corrected via fringe fitting. b) After fringe fitting. In this case, we can see that the delay is removed successfully because no slopes are observed in the phase. The change in the amplitude is because fringe fitting improves the SNR, which leads to a better amplitude determination.

Bandpass calibration

Bandpass calibration is applied in `AIPS` with the task `bpass`. A scan with a high SNR and with all antennas present is needed. It is necessary because bandpass, BP, tables in `AIPS` cannot be merged and only a single BP table can be applied to the data. As in `fringe`, a reference antenna has also to be chosen. Bandpass calibration can be performed before or after fringe fitting. However, to check the final solutions, the fringe-fitting should already be done. After applying the fringe-fitting, the solutions can be checked with the task `possm`.

Once this point is reached, the final calibration table is applied to the data in `split`. This task will apply the calibration and split the data on different sources into separated files. These resulting data sets can be exported into `difmap`.

4.4.2 Hybrid mapping in `difmap`

Once the data are read in `difmap`, they are averaged in time and a specific desired polarization is selected. The data are examined and edited using different built-in commands of `difmap`. For example, the flux amplitude of the data and phases can be seen with `radplot`. This task is useful to find antennas with a wrong

amplitude calibration (flux out-of-scale from the rest) or to compare the model with the measured data. The Högbom algorithm is applied with the task `clean` and phase self-calibration after each run of `clean` is applied with `selfcal`. After a model that provides a good representation of the visibility distribution of the source is obtained and not significant improvements with `clean` are achieved, one or more rounds of amplitude self-calibration with decreasing smoothing time can be performed. This has to be done carefully because amplitude self-calibration may adversely affect the visibility amplitudes, creating artifacts or removing parts of the real source structure. The amplitude self-calibration is done first with `gscale` and then with `selfcal true, true`.

Chapter 5

Source sample and data reduction

This Chapter is partially reproduced in Vega-García et al. submitted to A&A, Vega-García et al. a,b in prep.

This chapter describes the *RadioAstron* and ground-VLBI observations for all the sources together with their data reduction. We first introduce the sources in our sample, then describe the observations. We then describe the calibration details, mainly the fringe fitting and the imaging results. Lastly, we describe the model-fitting of the jet structure for each source and frequency.

5.1 0836+710

0836+710 (also known as 4C +71.07) is a powerful quasar located at a redshift of 2.17 (Stickel & Kuehr 1993). At this redshift, 1 miliarsecond (mas) corresponds to 8.4 pc. The source has a one-sided jet extending up to kiloparsec distances of $\sim$ 25 kpc. Otterbein et al. (1998) estimated the jet bulk Lorentz factor, $\gamma \approx 12$, and viewing angle, $\theta \approx 3.2°$, from VLBI monitoring at 8 GHz. Extended radio emission at Megaparsec scales has been observed in 0836+710 with MERLIN and VLA (Perucho et al. 2012b). Kappes et al. (in prep), observed the source at low frequencies with LOFAR and shows that the structure observed at these scales corresponds with a hot-spot. Its broadband spectral energy distribution (SED) is shown in Fig. 5.1. The SED clearly shows two humps, with the first peak at frequencies lower than 10^{14} Hz, which indicates that the spectrum is low-spectral peaked (LSP) (Tagliaferri et al. 2015). The authors also describe, besides these two peaks, a third one in the IR–UV band, $10^{14} - 10^{16}$ Hz, which can be identified as thermal emission coming from the accretion disk. Lister et al. (2013) report a proper motion of 240 ± 9 μas/yr corresponding to a superluminal speed of 21.08 c, based on kinematic study of 7 moving features observed in the jet with VLBI at 15 GHz.

Several authors have studied the development of plasma instability in 0836+710.

Krichbaum et al. (1990) observed several kinks in the source at 5 GHz and 326 MHz, which were associated with instability in the jet. The internal structure of the flow has been studied by Lobanov et al. (1998) with VSOP at 1.6 GHz and 5 GHz. They concluded that the jet ridgeline curvature was associated with Kelvin-Helmholtz instability (KHI) and variations of the angle of the velocity with respect to the line of sight. Krichbaum et al. (1990) and Otterbein (1996) measured a velocity of $\beta_{\rm app} \sim 14c$ near the core. At $\sim$ 3 mas, the apparent velocity decreased and further down increased again. This, together with the curvature of the jet, also indicates a clear existence of KHI. Perucho et al. (2012a) confirmed the presence of instability comparing the jet ridge-line at several frequencies and epochs. Observations at 1.6 GHz with MERLIN showed a large-scale structure situated around 1 arc-second and a gap of emission between 0.2−1.0 as Perucho et al. (2012b). The gap was explained as a product of the jet deceleration and expansion. A spine-sheath structure of the jet has been suggested by Asada et al. (2010). The authors suggested a spine-sheath structure where the spine has the emitting high-energy particles, the sheath surrounds the spine, and it contains non-magnetized plasma. The observed gradient in the Faraday rotation measure (RM) was explained with a helical magnetic field in the sheath.

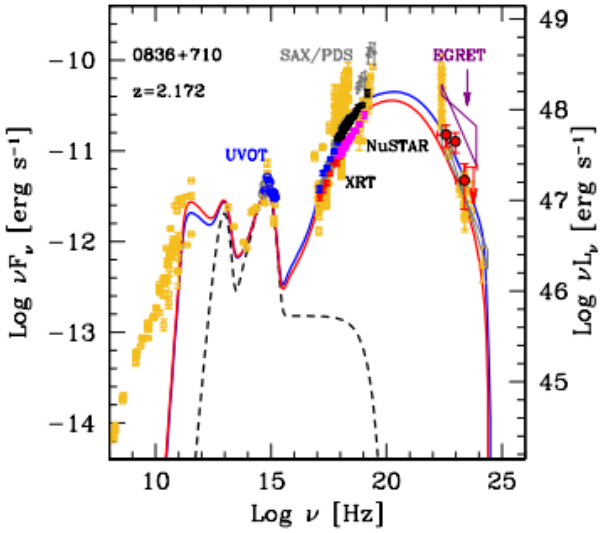

Figure 5.1: Spectral energy distribution of 0836+710 with fitted emission models, from Tagliaferri et al. (2015).

5.1.1 Observations

The jet in 0836+710 was observed within the *RadioAstron* Key Science Project on Strong AGN. Preliminary data reduction was made in an earlier work (Vega-García, 2015, MSc Dissertation). The data were reanlayzed for this work, and we summarize below the results of the observations and data reduction procedure.

RadioAstron observed 0836+710 at three different frequencies: 1.6 GHz (24th October 2013), 5 GHz (10th January 2014), and 22 GHz (10th January 2014). The observations at 1.6 GHz also led to the best *uv*-coverage up to date of the source, with a total of 22 antennas during a total observing time of 18h. The observations took place on the 24 and 25 October 2013. Simultaneously with the 5 GHz and 22 GHz observations, we also observed 0836+710 at 15 GHz and 43 GHz with the VLBA. We list all the participating antennas at each frequency in Table 5.1. Information about the observations is in Table 5.2.

Table 5.1: VLBI antennas participating in the observations of 0836+710 at different frequencies (in GHz). The plus sign means the antenna observed at a given frequency. No symbol means no participation.

Name	Code	Array	1.6	5	15	22	43
Green Bank	GB	-	+	+*	+*	+	+*
Brewster	BR	VLBA	+	+	+	+	+
Fort Davis	FD	VLBA		+	+	+	+
Hancock	HN	VLBA	+	+	+	+	+
Kitt Peak	KP	VLBA	+	+	+	+	+
Los Álamos	LA	VLBA		+	+	+	+
Mauna Kea	MK	VLBA	+	+	+	+	+
North Liberty	NL	VLBA	+	+	+	+	+
Owens Valley	OV	VLBA	+	+	+	+	+
Pie Town	PT	VLBA	+	+	+	+	+
St. Croix	SC	VLBA	+	+	+	+	+
Badary	BD	EVN	+				
Effelsberg	EF	EVN	+	+		+	
Jodrell Bank	JB	EVN	+	+			
Medicina	MC	EVN	+	+			
Noto	NT	EVN	+				
Onsala 25m	ON	EVN	+	+			
Sheshan	SH	EVN	+				
Svetloe	SV	EVN	+				
Torun	TR	EVN	+				
Urumqi	UR	EVN	+				
Westerbork	WB	EVN	+	+			
Yebes	YS	EVN				+	
Zelenchukskaya	ZC	EVN	+				
Kalyazin	KL	-	+*	+			
SRT	R1, R2	-	+	+		+	

* No fringes detected.

For the Space Radio Telescope (SRT), it was necessary to have on/off cycles to allow the system to cool down. For our observations at 1.6 GHz, the SRT needed

to cool down for 70 min for each 40 min of observing time. For the observations at 5 GHz and 22 GHz, the on/off cycle was of 30/95 min.

The data were recorded in dual circular polarisation mode at a rate of 128 megabits per second (Mbps), resulting in a total bandwidth of 2x16 MHz for each circular polarization channel (Andreyanov et al. 2014). The tracking stations at Puschino (Andreyanov et al. 2014) and Green Bank (Ford et al. 2014) received and recorded the SRT data and telemetry. The data from all participating telescopes were transferred to the VLBI correlator of the MPIfR.

Table 5.2: Summary of the observations for 0836+710

RadioAstron project code	global VLBI project code	Date	Observing time (UT)	$\nu_{\rm cent}$ [GHz]	on/off cycle [min]
raks05a	GL038A	2013/10/24	22:00–14:30	1.660	40/70
raks05b	GL038B/C	2014/01/10	04:10–10:00	4.828	30/95
raks05b	GL038B/C	2014/01/10	04:10–10:00	22.228	30/95

5.1.2 Calibration and imaging

In this section we describe the basic steps we took in the data reduction. The data were correlated using the DiFX correlator of the MPIfR at Bonn upgraded for *RadioAstron* data correlation (Bruni et al. 2015). Fringe searching for the SRT was performed separately for each individual observing scan. The correlation was performed by G. Bruni. After the data are correlated, we load them in `AIPS` to start the data reduction (see section 4.4 for general data reduction details). We sort the data by time and baseline, and then index them. Once we have the data ordered, the first step is to calibrate the amplitude using the gain curve and the system temperature for each antenna, as explained in section 4.4.1. For high frequencies, we also correct for the atmospheric opacity in this step. Then, we correct for the parallactic angle for alt-azimuth ground antennas. The next and most important step is the fringe fitting. We perform this in two steps: first, we fringe fit the ground data, and after we have a model of the source, we fringe fit the space antenna. For the ground-VLBI data of 1.6 GHz, 5 GHz and 22 GHz we choose Effelsberg as reference antenna for the fringe fitting with an SNR cutoff of 4.3. For the case of the 15 GHz and 43 GHz, Los Alamos was the reference antenna. The next step is to perform the hybrid imaging using the `CLEAN` algorithm in `difmap` for all the ground array images. We use natural weighting and perform phase and amplitude self-calibrations. For the *RadioAstron* observations, once the final image for each frequency is obtained, we use it in `AIPS` as a model for the `FRING` algorithm in order to find fringes with the space antenna. Effelsberg is again chosen to be the reference antenna for this process. The solution interval is 4 min for the 1.6 GHz data and 10 min (the entire scan length) for the 5 GHz and 22 GHz

data. After fringe-fitting, the data are smoothed. The imaging is performed in `difmap`, now using the uniform weigthing and we apply only phase self-calibration. Only the space-VLBI images were recalibrated and reimaged during the work of this thesis. However, we also show the ground images for completeness. Table 5.3 shows the map parameters for both ground and space-VLBI images. Figures 5.7, and 5.9 show the *RadioAstron* maps at 1.6 GHz and 22 GHz. The jet structure in the 1.6 GHz image is similar to the previous VSOP image presented by Lobanov et al. (2006). The 22 GHz image shows a strong asymmetry in the jet flow. The two main features observed outside the central region correspond to two moving features that are clearly identified in a modelfit of the ground data, and were traced with multi-epoch observations at 43 GHz (Chapter 6). This structure could be explained by jet rotation or limb-brightening.

Table 5.3: Parameters of the total intensity images of 0836+710.

ν	Array	$S_{\rm tot}$	$S_{\rm peak}$	$S_{\rm neg}$	$\sigma_{\rm rms}$	Beam		
						$\theta_{\rm max}$	$\theta_{\rm min}$	P.A.
[GHz]		[mJy]	[mJy/beam]	[mJy/beam]	[mJy/beam]	[mas]	[mas]	[°]
1.6	Space	3316	200	−5.4	1.30	1.20	0.21	−37
5	Space	3070	298	−15.0	1.50	0.146	0.056	−54
22	Space	1614	77	−7.9	1.03	0.035	0.016	77
1.6	Ground	3418	1160	−0.8	0.15	2.88	2.37	−34
5	Ground	3373	1700	−2.3	0.50	1.29	0.975	−22
15	Ground	2429	1330	−1.2	0.20	0.776	0.567	9
22	Ground	1658	603	−1.6	0.30	0.388	0.282	−6
43	Ground	1171	538	−3.4	0.60	0.349	0.214	−3

Notes: Column designation: ν: frequency; $S_{\rm tot}$: total flux density; $S_{\rm peak}$: peak flux density; $S_{\rm neg}$: maximum negative flux density in the image; $\sigma_{\rm rms}$: rms noise in the image; Beam: major axis, minor axis, position angle of major axis.

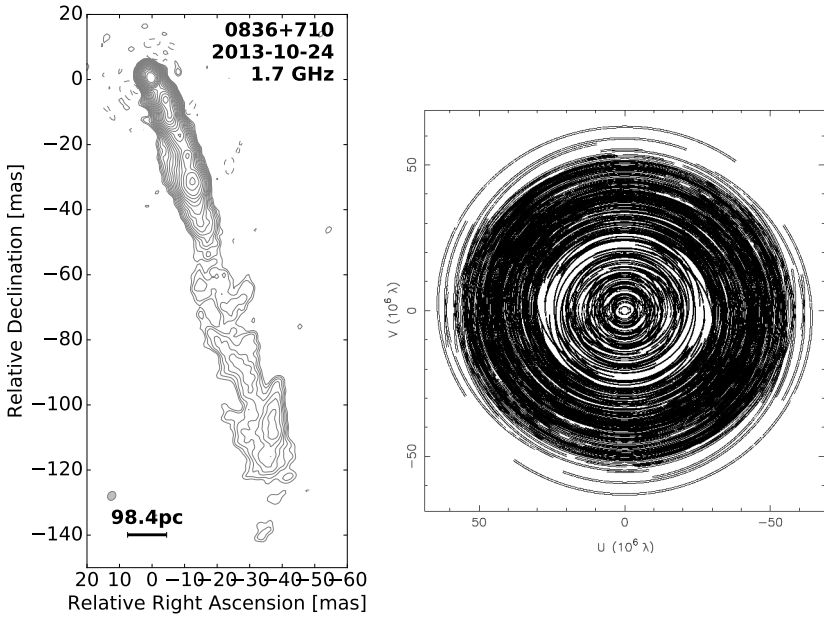

Figure 5.2: **Left panel:** Ground VLBI image of 0836+710 at 1.6 GHz. The contour levels are drawn at $(-1,\ 1,\ \sqrt{2},\ 2,\ \ldots\ )$ times 0.32 mJy/beam. **Right panel:** ground (u, v)-coverage plotted in units of Mλ of observations of 0836+710 at 1.6 GHz.

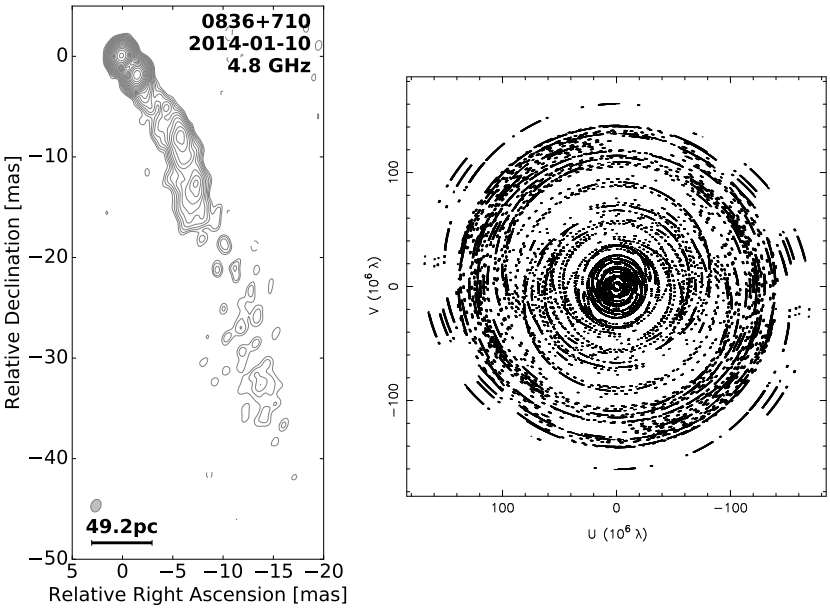

Figure 5.3: **Left panel:** Ground VLBI image of 0836+710 at 5 GHz. The contour levels are drawn at $(-1,\ 1,\ \sqrt{2},\ 2,\ \ldots\ )$ times 1.5 mJy/beam. **Right panel:** ground (u, v)-coverage plotted in units of Mλ of observations of 0836+710 at 5 GHz.

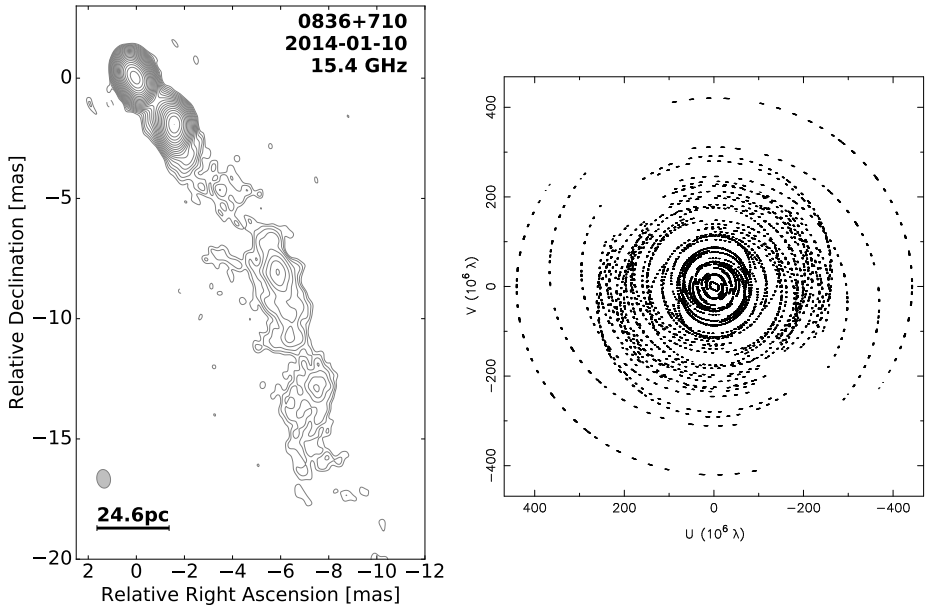

Figure 5.4: **Left panel:** Ground VLBI image of 0836+710 at 15 GHz. The contour levels are drawn at $(-1, 1, \sqrt{2}, 2, \ldots)$ times 0.75 mJy/beam. **Right panel:** ground (u, v)-coverage plotted in units of Mλ of observations of 0836+710 at 15 GHz.

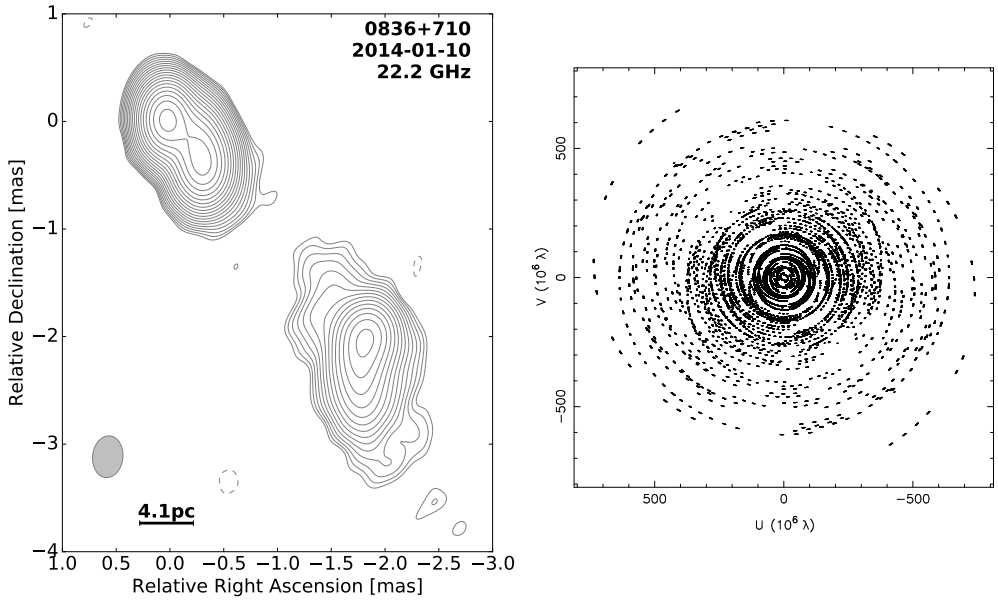

Figure 5.5: **Left panel:** Ground VLBI image of 0836+710 at 22 GHz. The contour levels are drawn at $(-1, 1, \sqrt{2}, 2, \ldots)$ times 1.0 mJy/beam. **Right panel:** ground (u, v)-coverage plotted in units of Mλ of observations of 0836+710 at 22 GHz.

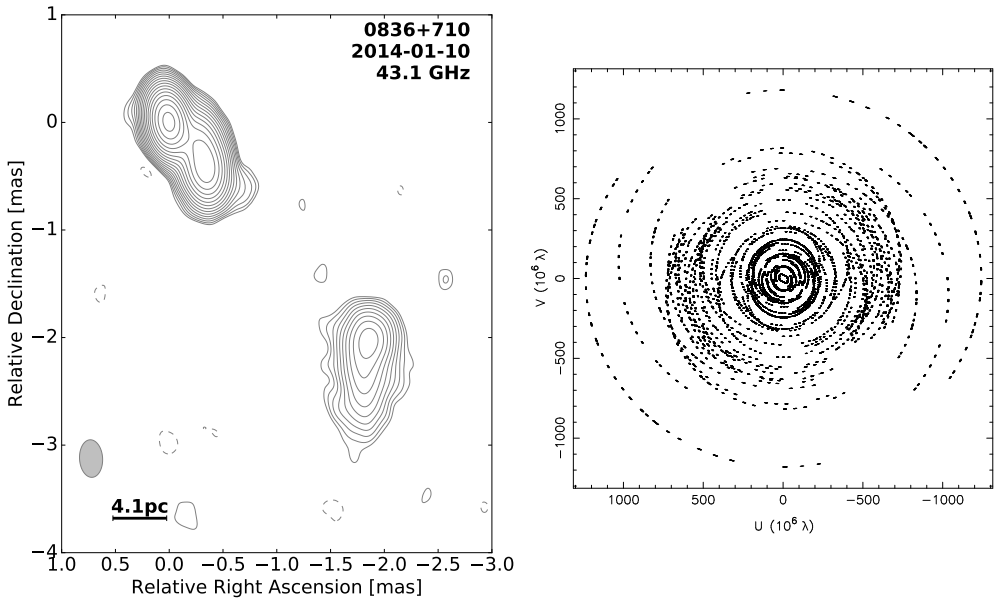

Figure 5.6: **Left panel:** Ground VLBI image of 0836+710 at 43 GHz. The contour levels are drawn at $(-1,\ 1,\ \sqrt{2},\ 2,\ \ldots\ )$ times 1.8 mJy/beam. **Right panel:** ground (u, v)-coverage plotted in units of MλMλ of observations of 0836+710 at 43 GHz.

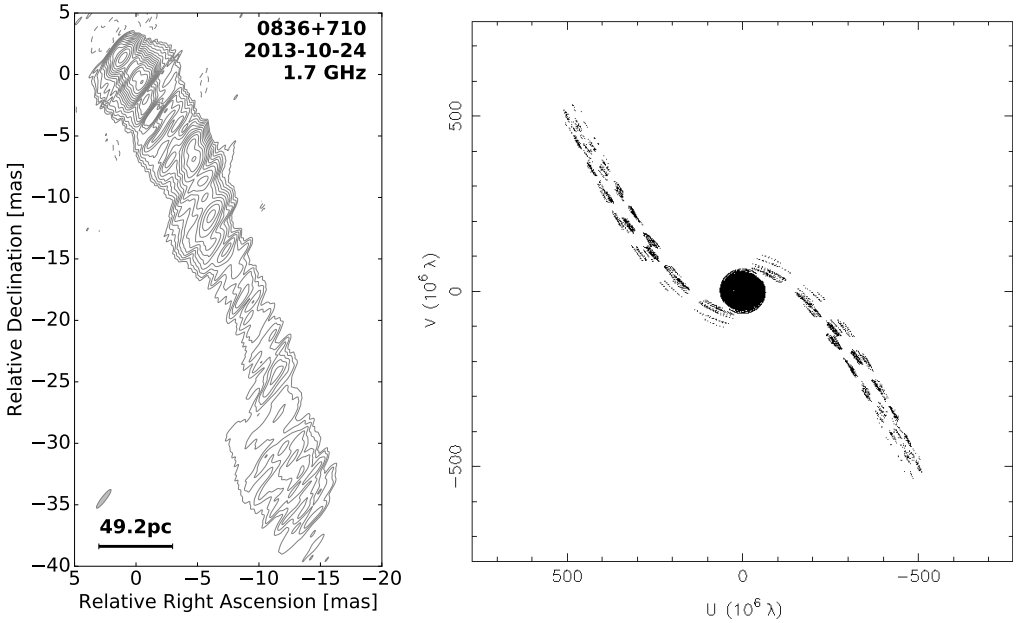

Figure 5.7: **Left panel:** *RadioAstron* image of 0836+710 at 1.6 GHz. The contour levels are drawn at $(-1,\ 1,\ \sqrt{2},\ 2,\ \ldots\ )$ times 0.10 mJy/beam. **Right panel:** (u, v)-coverage plotted in units of MλMλ of observations of 0836+710 at 1.6 GHz.

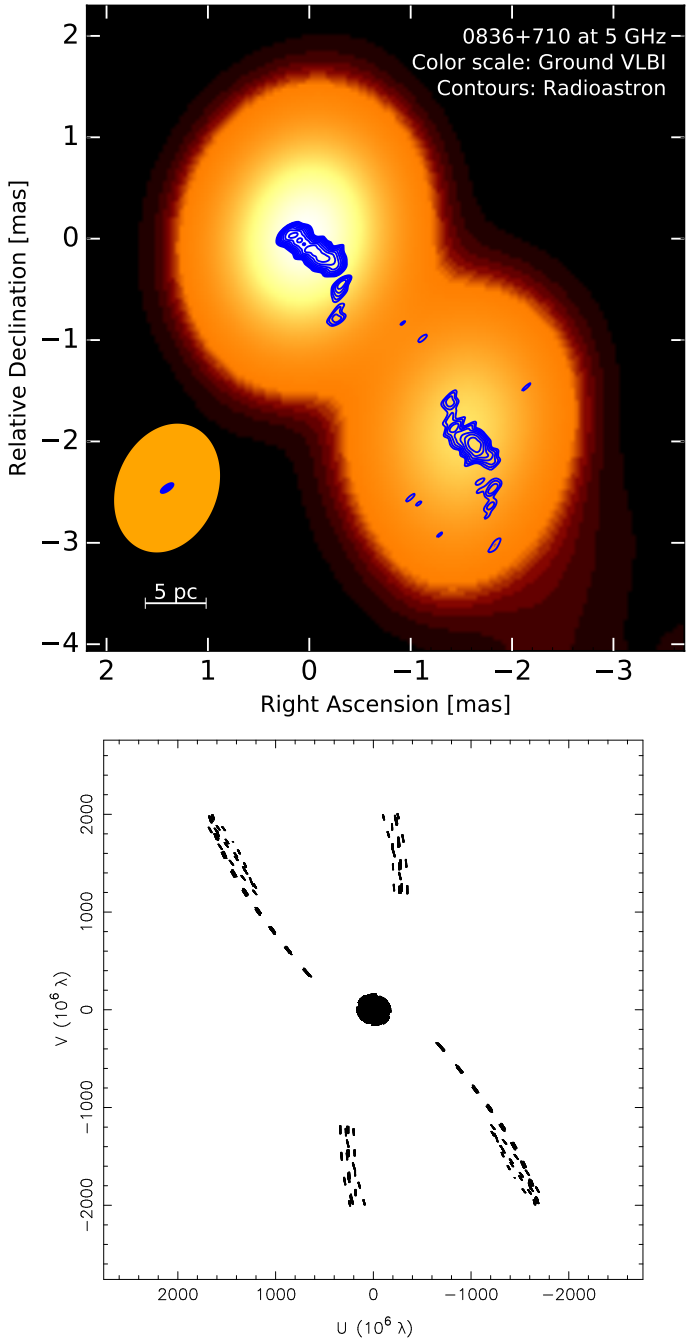

Figure 5.8: **Top panel:** *RadioAstron* image of 0836+710 at 5 GHz (contours) superimposed on the ground image of 0836+710 at 5 GHz (color scale). The contour levels are drawn at $(-1,\ 1,\ \sqrt{2},\ 2,\ \ldots)$ times 7.0 mJy/beam. **Bottom panel:** (u, v)-coverage plotted in units of Mλ of observations of 0836+710 at 5 GHz.

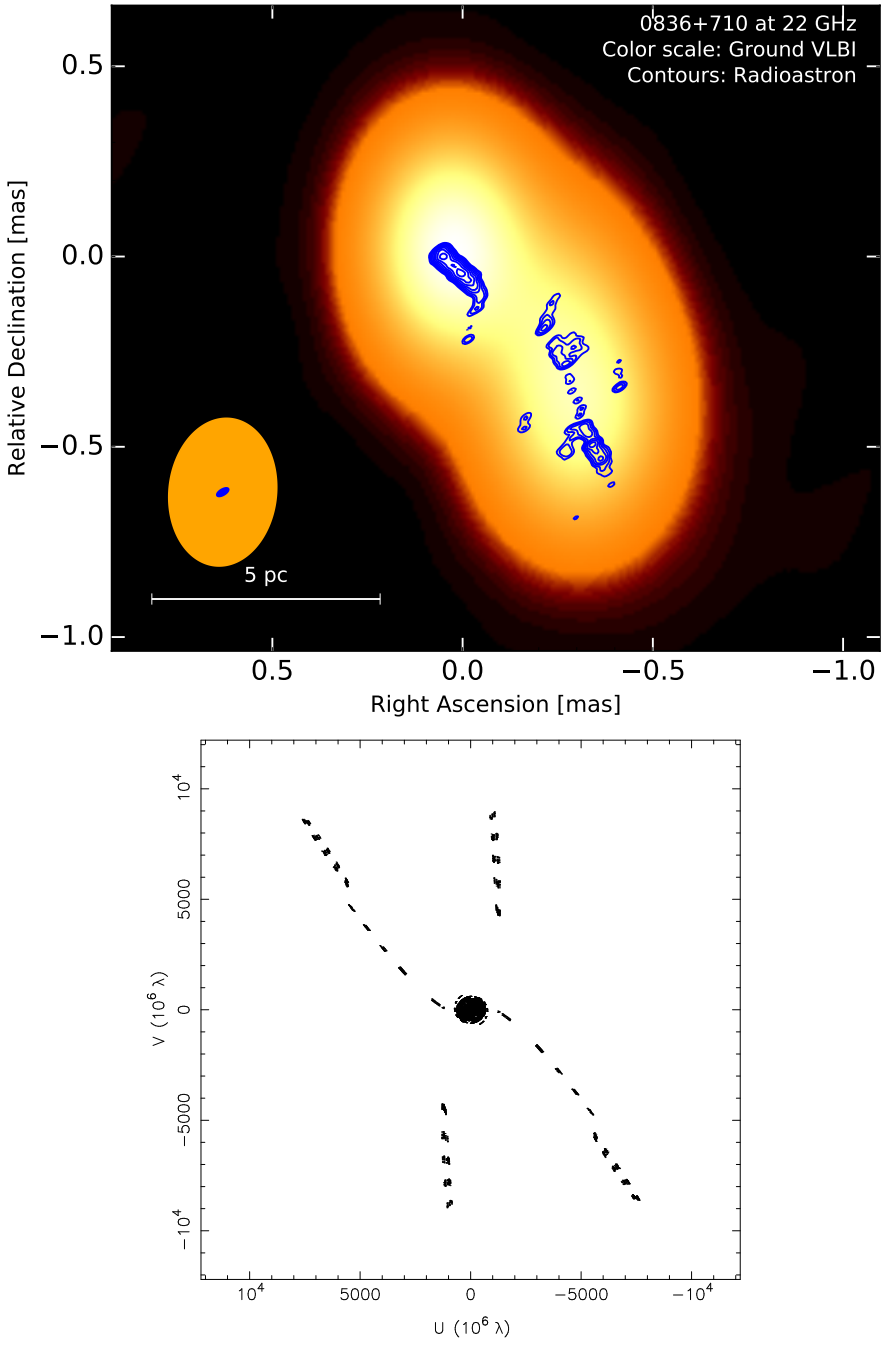

Figure 5.9: **Top panel:** *RadioAstron* image of 0836+710 at 22 GHz (contours) superimposed on the ground array image of 0836+710 at 22 GHz (color scale). The contour levels are drawn at $(-1, 1, \sqrt{2}, 2, \ldots)$ times 5.0 mJy/beam. **Bottom panel:** (u, v)-coverage plotted in units of Mλ of observations of 0836+710 at 22 GHz.

5.1.3 Model-fitting

We modelfit the *RadioAstron* and ground-VLBI visibility data using the `modelfit` task in `difmap`. The resulting modelfit components and their parameters are in Appendix C. Here we present as an example the results of the modelfit for 1.6 GHz for the ground array observations (Fig. 5.10 and Table 5.4). The tables show the polar (r,ϕ) and cartesian coordinates (x,y) for the center position of each component. The errors in the tables were obtained following Schinzel et al. (2012).

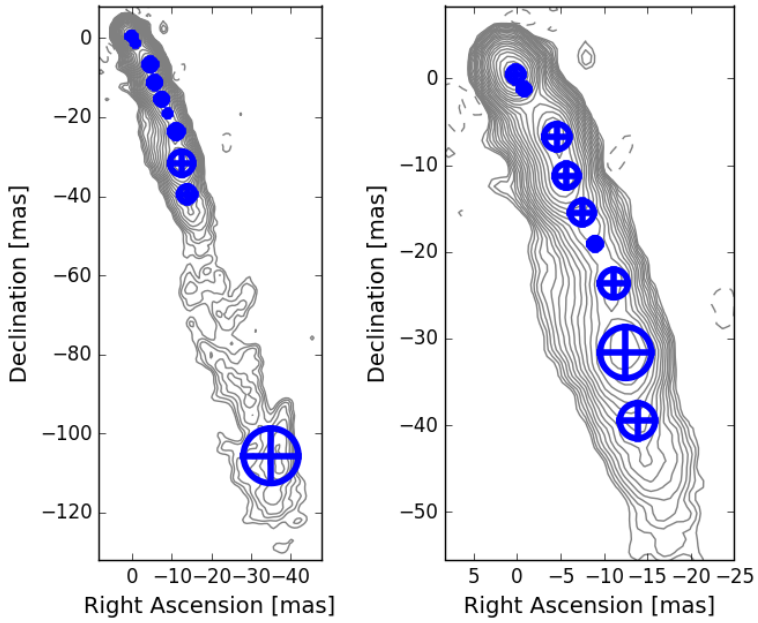

Figure 5.10: Modelfit components for the ground array observations of 0836+710 at 1.6 GHz. The contour levels are drawn at (-1, 1, $\sqrt{2}$, 2, ...) times 0.32 mJy/beam. **Left panel:** Whole map **Right panel:** Inner 60 mas

Table 5.4: Modelfit parameters for the ground VLBI image of 0836+710 at 1.6 GHz

	S_y [Jy]	r [mas]	ψ [°]	x [mas]	y [mas]	$\theta_{\rm g}$ [mas]	$\theta_{\rm lim}$ [mas]
c	1.55 ± 0.03	0.5 ± 0.5	20 ± 50	0.1 ± 0.5	0.5 ± 0.4	0.9 ± 0.5	0.695
c2.3	0.28 ± 0.08	1.5 ± 0.5	−150 ± 80	−0.8 ± 1.3	−1.2 ± 1.8	0.6 ± 0.6	2.426
c9	0.585 ± 0.02	8.1 ± 0.7	−146 ± 11	−4.6 ± 1.1	−6.7 ± 1.3	1.5 ± 0.5	0.895
c11	0.389 ± 0.01	12.6 ± 0.7	−153 ± 5	−5.7 ± 0.8	−11.2 ± 1.0	1.4 ± 0.5	0.798
c12	0.085 ± 0.006	17.2 ± 0.7	−154 ± 15	−7 ± 2	−15 ± 4	1.4 ± 0.5	1.280
c13	0.038 ± 0.003	21.1 ± 0.5	−155 ± 10	−9.0 ± 1.6	−19 ± 3	0.7 ± 0.5	1.296
c14	0.087 ± 0.002	26.2 ± 0.8	−155 ± 2	−11.2 ± 0.9	−23.7 ± 1.0	1.6 ± 0.5	0.751
c15	0.235 ± 0.004	34.0 ± 1.5	−158.4 ± 1.9	−12.5 ± 1.4	−31.6 ± 1.2	2.9 ± 0.5	0.631
c16	0.036 ± 0.002	41.9 ± 1.0	−161 ± 9	−14 ± 2	−39 ± 6	2.0 ± 0.5	1.272
c17	0.0475 ± 0.0017	111 ± 3	−162 ± 3	−35 ± 4	−106 ± 5	6.9 ± 0.5	0.912

Notes: Column designation: S_y: flux density; r: position of the component; ψ: position angle of the component; x: position of the component in RA; y: position of the component in DEC; θ_g: size of the gaussian component; $\theta_{\rm lim}$: limiting size of the gaussian component.

5.2 3C 345

3C 345 is a quasar located at a redshift of z=0.595 (Lynds et al. 1965) and for this redshift 1 mas corresponds to 6.5 pc. It is a core-dominated radio source in which the core contributes from 50% to 90% to its total flux density density. 3C 345 and has been monitored over the past 35 years with VLBI (see, e.g., Unwin et al. 1983; Lobanov 1996; Ros et al. 2000; Schinzel 2011, among others). The large scale of the source shows a strong jet to the northwest and a weaker counter-jet in the northeast (Kollgaard et al. 1989). Its black hole mass is of the order of $10^9 M_\bullet$ (Gu et al. 2001), based on the black hole mass estimator with the Hβ line width. The jet has a viewing angle of $\sim 5°$ (Unwin et al. 1983) and shows variable apparent speeds ranging from $\sim 1c$ to $20c$ (see Zensus et al. 1995; Lobanov & Zensus 1999; Schinzel et al. 2012). Schinzel et al. (2012) have found that the γ-ray emission is produced in the Compton-loss dominated zone extending to a deprojected length of 23 pc. They associated the superluminal knots in the flow with the optical and γ-ray flares in the source.

5.2.1 Observations

RadioAstron observed the source at two different frequencies: at 5 GHz and at 22 GHz on 21.-22. in April of 2014. Simultaneously, we also observed the source at 15 GHz and 43 GHz with the VLBA. We present all the participating antennas at each frequency in Table 5.5. Information about the observations is shown in Table 5.6. Again, for *RadioAstron*, it was necessary to have on/off cycles to let the system cool down. The on/off cycles were of 30/75 min. The data at a rate

of 128 megabits per second (Mbps), resulting in a total bandwidth of 2x16 MHz for each circular polarization channel (Andreyanov et al. 2014). The data from all participating telescopes were transferred to the VLBI correlator of the MPIfR.

Table 5.5: VLBI antennas participating in the observations of 3C 345 at different frequencies (in GHz). The plus sign means the antenna observed at a given frequency. No symbol means no participation.

Name	Code	Array	5	15	22	43
Brewster	BR	VLBA	+	+	+	+
Fort Davis	FD	VLBA	+	+	+	+
Hancock	HN	VLBA	+	+	+	+
Kitt Peak	KP	VLBA	+	+	+	+
Mauna Kea	MK	VLBA	+	+	+	+
Owens Valley	OV	VLBA	+	+	+	+
Pie Town	PT	VLBA	+	+	+	+
Badary	BD	EVN			+	
Effelsberg	EF	EVN	+		+	
Onsala 25m	ON	EVN	+			
Sheshan	SH	EVN	+			
Westerbork	WB	EVN	+			
Hartebeesthoek	HH	EVN	+		+	
Noto	NT	EVN	+			
Svetloe	SV	EVN			+	
Zelenchukskaya	ZC	EVN			+	
Yebes	YS	EVN			+	
Kalyazin	KZ,KL		+*		+	
SRT	R1, R2		+		+	

* No fringes detected.

Table 5.6: Summary of the observations of 3C 345

RadioAstron project code	global VLBI project code	Date	Observing time (UT)	$\nu_{\rm cent}$ [GHz]	on/off cycle [min]
raks05c	GL038D/E	2014/04/21	10:00–08:10	4.828	30/75
raks05c	GL038D/E	2014/04/21	10:00–08:10	22.228	30/75

5.2.2 Calibration and imaging

The data were correlated in the DiFX correlator in Bonn by G. Bruni. The calibration steps are nearly the same as described in section 5.1.2. The only difference is in the fringe parameters. For the 5 GHz data, the reference antenna is Effeslberg and we apply a solution interval of 4 min for ground baselines. For the 22 GHz

data, we also use Effeslberg as the reference antenna but the solution interval is 1 min. For the data at 15 GHz and 43 GHz Brewster is used as the reference, and we also apply a solution interval of 1 min. We image 3C 345 in `difmap` using uniform weighting with iterative phase and amplitude self-calibrations. We only find fringe solutions for the space baselines for one scan at 5 GHz. We attempt to improve the fringe detection rate by imaging the first scan and use that image as a starting model for the next *RadioAstron* scan. However, this did not improve the fringe detection. We also use an alternative fringe-fitting task `kring`, which is computationally faster and uses a different scan-breaking algorithm with respect to `fring`, and can in principle improve the solutions when the whole scan length is used. However, this did not improve the fringe detection rate and we did not find any fringes at 22 GHz for the space antenna. This can be due to the fact that the structure of the source is complex and highly resolved on the ground-space baselines, with several components close to the core region. This structure poses a problem when the fringe search method is dependent on the structure of the source. Using a baseline-based approach including the acceleration terms of the antenna with `PIMA` did not improve the number of solutions. We present the parameters of the images in Table 5.7.

We show the resulting maps from the ground array data in Fig. 5.11 through 5.14. The observed jet structure at 5 GHz shows a clear bending after 3 mas. At higher frequencies (22 GHz and 43 GHz), the inner structure of the jet is revealed with more detail. The 5 GHz core resolved in several components in those images. This was already described in earlier works, e.g., Schinzel et al. (2012).

The 5 GHz *RadioAstron* image shown in Fig. 5.15 hints at the presence of counter-jet emission. The existence of a counter-jet in this source was already mentioned in Kollgaard et al. (1989) based on VLA observations at 5 GHz with an A/B configuration. Apart from this, the source structure seen in the ground VLBI image made at 15 GHz.

Table 5.7: Parameters of the total intensity images of 3C 345.

ν	Array	$S_{\rm tot}$	$S_{\rm peak}$	$S_{\rm neg}$	$\sigma_{\rm rms}$	Beam		
						$\theta_{\rm max}$	$\theta_{\rm min}$	P.A.
[GHz]		[mJy]	[mJy/beam]	[mJy/beam]	[mJy/beam]	[mas]	[mas]	[°]
5	Space	5600	1100	−50	1.50	0.959	0.598	−24.5
5	Ground	5500	1500	−8	0.07	1.625	0.944	−0.01
15	Ground	4900	2600	−4	0.23	0.887	0.552	−23
22	Ground	3500	1500	−11	0.18	0.484	0.224	−3
43	Ground	2600	1600	−7	0.45	0.364	0.209	−32

Notes: Column designation: ν: frequency; $S_{\rm tot}$: total flux density; $S_{\rm peak}$: peak flux density; $S_{\rm neg}$: maximum negative flux density in the image; $\sigma_{\rm rms}$: rms noise in the image; Beam: major axis, minor axis, position angle of major axis.

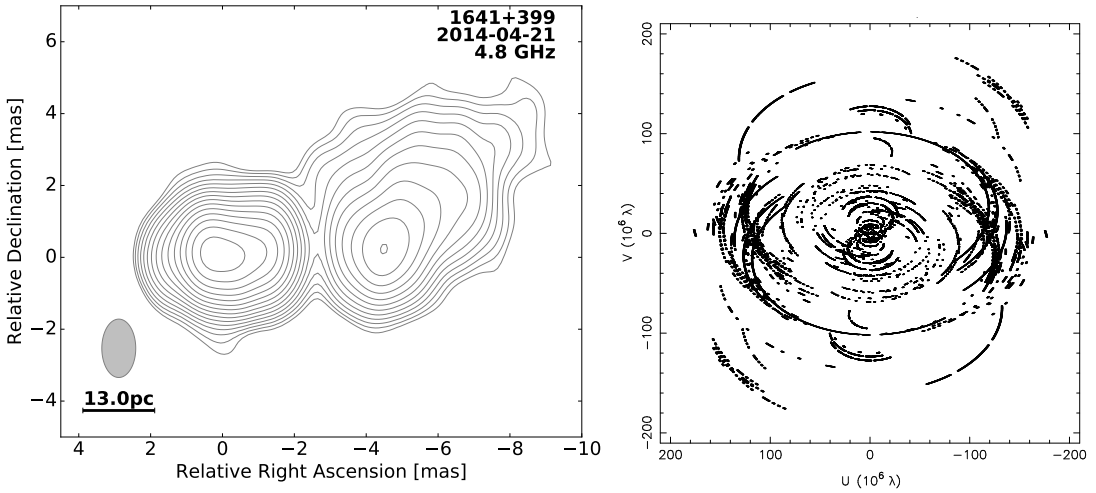

Figure 5.11: **Left panel:** Image of 3C 345 at 5 GHz. The contour levels are drawn at $(-1, 1, \sqrt{2}, 2, ...)$ times 10 mJy/beam. **Right panel:** (u, v)-coverage plotted in units of Mλ of the ground observations of 3C 345 at 5 GHz.

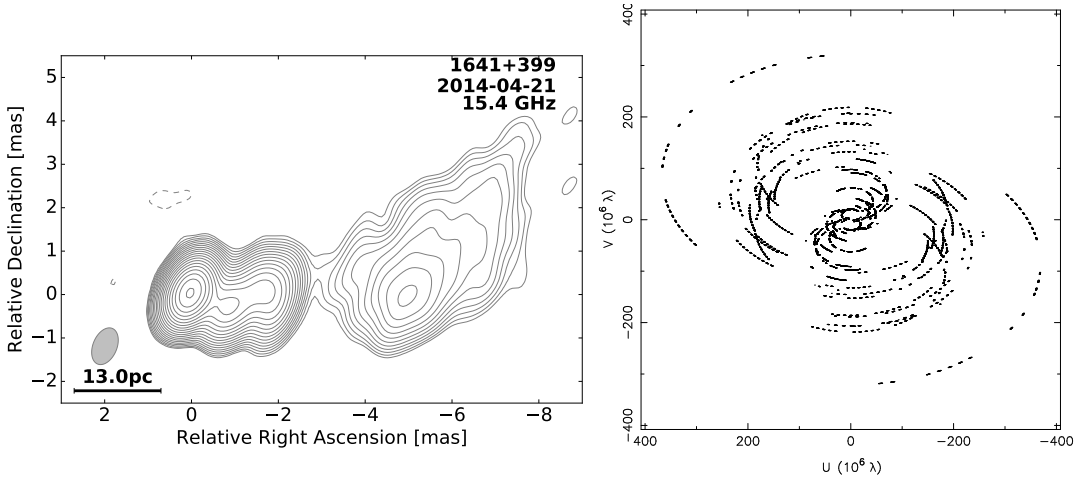

Figure 5.12: **Left panel:** Image of 3C 345 at 15 GHz. The contour levels are drawn at $(-1, 1, \sqrt{2}, 2, ...)$ times 3.5 mJy/beam. **Right panel:** (u, v)-coverage plotted in units of Mλ of the ground observations of 3C 345 at 15 GHz.

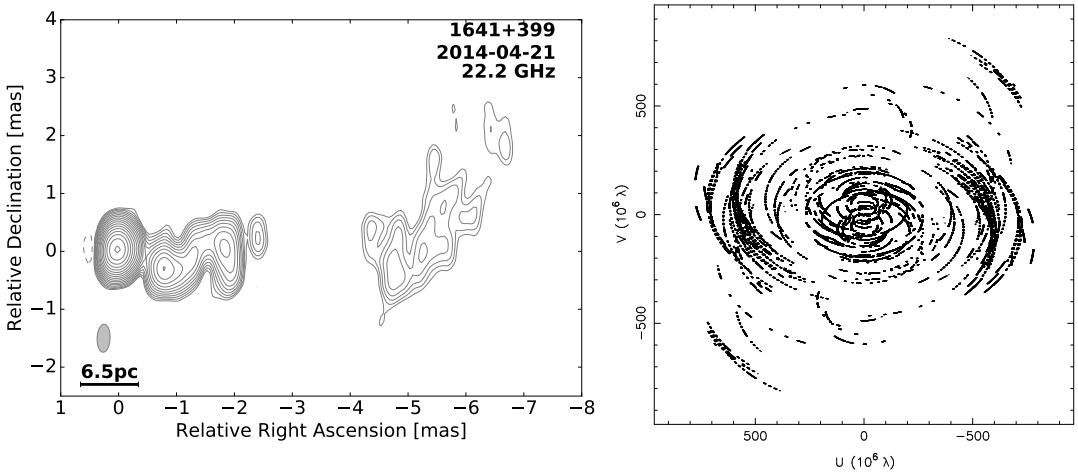

Figure 5.13: **Left panel:** Image of 3C 345 at 22 GHz. The contour levels are drawn at $(-1, 1, \sqrt{2}, 2, \ldots)$ times 5.4 mJy/beam. **Right panel:** (u, v)-coverage plotted in units of Mλ of the ground observations of 3C 345 at 22 GHz.

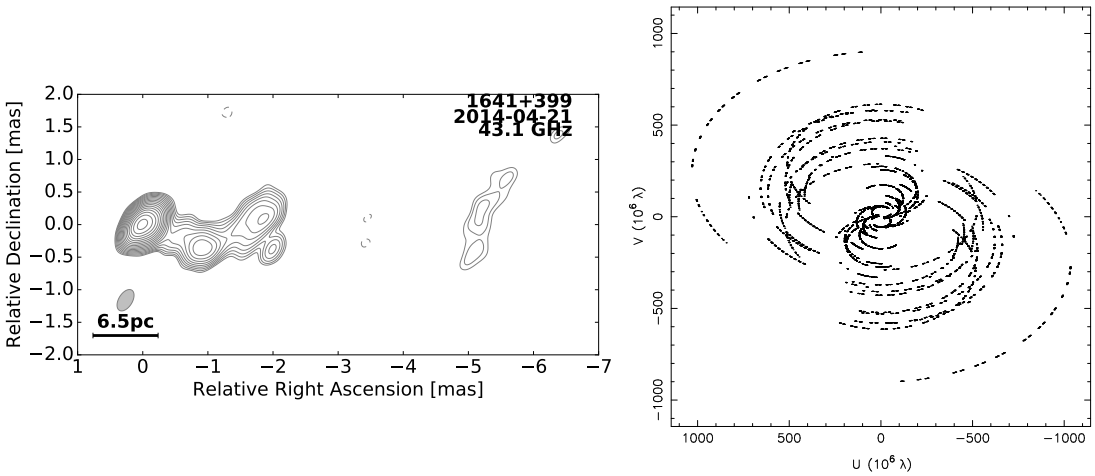

Figure 5.14: **Left panel:** Image of 3C 345 at 43 GHz. The contour levels are drawn at $(-1, 1, \sqrt{2}, 2, \ldots)$ times 5.5 mJy/beam. **Right panel:** (u, v)-coverage plotted in units of Mλ of the ground observations of 3C 345 at 43 GHz.

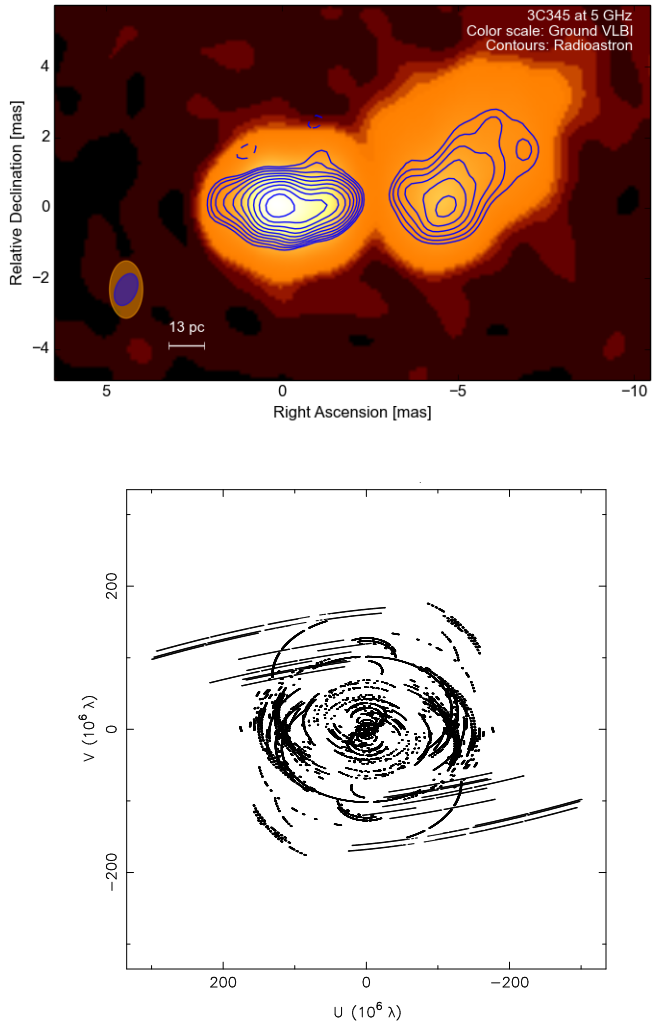

Figure 5.15: **Top panel:** *RadioAstron* image of 3C 345 at 5 GHz (contours) superimposed on the ground image at 5 GHz (color scale). The contour levels are drawn at $(-1,\ 1,\ \sqrt{2},\ 2,\ \ldots\ )$ times 38 mJy/beam. **Bottom panel:** (u, v)-coverage plotted in units of Mλ of observations of 3C 345 at 5 GHz.

5.2.3 Model-fitting

We perform a model-fitting using the same procedures as in the case of 0836+710. Here we present as an example the results of the modelfit of the ground data at 5 GHz (Fig. 5.16 and Table 5.8). The rest of the tables are in Appendix C.

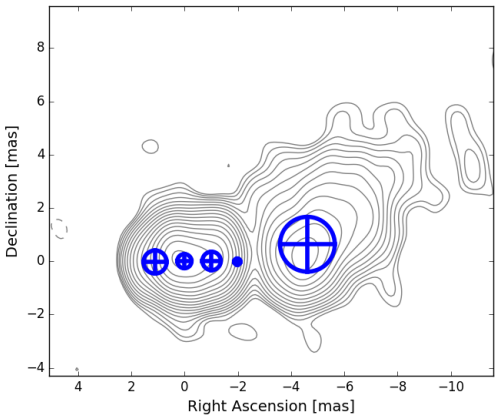

Figure 5.16: Modelfit components for the ground array observations of 3C 345 at 5 GHz. The contour levels are drawn at $(-1, 1, \sqrt{2}, 2, \ldots)$ times 10 mJy/beam.

Table 5.8: Modelfit parameters for the ground VLBI image of 3C 345 at 5 GHz

	S_y [Jy]	r [mas]	ψ [°]	x [mas]	y [mas]	$\theta_{\rm g}$ [mas]	$\theta_{\rm lim}$ [mas]
c	1.87 ± 0.04	0.0 ± 0.2	70 ± 90	0.01 ± 0.09	0.0 ± 0.2	0.3 ± 0.2	0.325
cj1	1.02 ± 0.06	1.1 ± 0.2	90 ± 60	1.1 ± 1.2	−0.0 ± 0.2	0.4 ± 0.2	0.552
c3	0.95 ± 0.04	1.0 ± 0.2	−90 ± 40	−1.0 ± 0.8	0.0 ± 0.2	0.3 ± 0.2	0.478
c4	0.133 ± 0.017	2.0 ± 0.2	−90 ± 50	−2.0 ± 1.9	−0.0 ± 0.2	0.1 ± 0.2	0.797
c5	0.99 ± 0.03	4.7 ± 0.5	−80 ± 20	−4.6 ± 1.9	0.6 ± 0.6	1.0 ± 0.2	0.426

Notes: Column designation: S_y: flux density; r: position of the component; ψ: position angle of the component; x: position of the component in RA; y: position of the component in DEC; θ_g: size of the gaussian component; $\theta_{\rm lim}$: limiting size of the gaussian component.

5.3 1642+690

The quasar 1642+690 has a redshift of 0.75 (Pearson et al. 1986), with the corresponding linear scale of 7.15 pc/mas. Pearson et al. (1986) investigated in detail the radio emission in 1642+690 on parsec to kilioparsec scales, with VLBI and MERLIN observations at 5 GHz. The MERLIN observations revealed an arsecond jet to the South, with a weak emission to the North. The 5 GHz VLBI observations showed a milliarsecond jet to the South with the opposite curvature to the arcsecond jet. The source flux density shows strong variability, decreasing by half in only 5 years. Venturi et al. (1997) also showed the variability of the source

with a 15 years monitoring, and revealed that the source has increased and further decreased. Both teams confirmed apparent superluminal speeds in the jet of $9c$.

Sambruna et al. (2004), performed a multi-wavelength study with Chandra, VLA and Hubble Space Telescope, did not find any optical emission from the jet. Optical emission was only detected in the inner knot of the source. The spatial size of the X-ray emission of 1642+690 was more compact than the detected radio emission. Georganopoulos & Kazanas (2004) proposed that the smaller size of AGN jets in X-rays in comparison with it extent in radio wavelengths can be due to jet deceleration. The source has not been detected in γ-rays yet.

5.3.1 Observations

RadioAstron observations of 1642+690 were made on 26-27 December 2014 at 22 GHz and on 20-21 April 2015 at 1.6 GHz and 5 GHz. We present all the participating antennas at each frequency in Table 5.9. Information about the observations is in Table 5.10.

Table 5.9: VLBI antennas participating in the observations of 1642+690 at different frequencies (in GHz). The plus sign means the antenna observed at a given frequency. No symbol means no participation.

Name	Code	Array	1.6	5	22
Brewster	BR	VLBA	+	+	+
Hancock	HN	VLBA	+	+	+
Kitt Peak	KP	VLBA	+	+	+
Los Álamos	LA	VLBA	+	+	+
Mauna Kea	MK	VLBA	+	+	+
Owens Valley	OV	VLBA	+	+	+
Pie Town	PT	VLBA	+	+	+
St. Croix	SC	VLBA	+	+	+
Badary	BD	EVN	+		
Jodrell Bank	JB	EVN	+		
Urumqi	UR	EVN	+		
Robledo	RO	EVN	+		
Effelsberg	EF	EVN		+	
Westerbork	WB	EVN	+	+	
Svetloe	SV	EVN		+	
Yebes	YS	EVN		+	
Zelenchukskaya	ZC	EVN		+	
Noto	NT	EVN			+
Green Bank	GB				+
SRT	R1, R2		+	+	+

* No fringes detected.

The on/off cooling cycles at the space antenna were 40/50 min for the 1.6 GHz

and 5 GHz observations and 50/80 for the 22 GHz observation. The data at a rate of 128 megabits per second (Mbps), resulting in a total bandwidth of 2x16 MHz for each circular polarization channel (Andreyanov et al. 2014). The data from all participating telescopes were transferred to the VLBI correlator of the MPIfR.

Table 5.10: Summary of the observations of 1642+690

RadioAstron project code	global VLBI project code	Date	Observing time (UT)	$\nu_{\rm cent}$ [GHz]	on/off cycle [min]
rags08b	GL042B	2015/01/20	21:00–11:00	1.660	40/50
rags08b	GL042B	2015/01/20	21:00–11:00	4.828	40/50
rags08a	GL042A	2014/12/26	23:00–07:00	22.228	50/80

5.3.2 Calibration and imaging

Data from the RadioAstron observations of 1642+690 were correlated in the Bonn DiFX correlator by G. Bruni and reduced with the same procedures as for the other objects except the fringe parameters. For the 1.6 GHz data, the reference antenna is Los Alamos and we apply a solution interval of 1 min for ground baselines. For the 5 GHz data, we use Effeslberg as the reference antenna and a solution interval of 1 min. For the 22 GHz data, the reference antenna is Green Bank, and we apply a solution interval of 1 min. We image the source in `difmap` using uniform weighting with phase and amplitude self-calibration.

For the space antenna, we only find fringes at 1.6 GHz and 5 GHz. To find fringes at 1.6 GHz and 5 GHz, we use the respective ground array images as the source model and set the solution intervals to 4 min and 10 min (full scan length), respectively. After failing to find fringes at 22 GHz with AIPS, we attempted to perform fringe search in `PIMA`, with the acceleration terms included. However, not fringes could be found with `PIMA` as well. Table 5.11 shows the map parameters for the different frequencies and arrays.

The resulting ground array images at 1.6 GHz, 5 GHz, and 22 GHz are shown in Figs. 5.17 through 5.19. The RadioAstron images are shown in Figs. 5.20 (1.6 GHz) and 5.21 (5 GHz). The 1.6 GHz and 5 GHz ground images show a feature at ∼5 mas from the core. This feature was already reported previously by Venturi et al. (1997), who concluded that this feature is probably due to strong energy dissipation in the jet. The 5 GHz image shows a feature downstream the core that outshines the core. This feature appears less bright in the ground array image at 22 GHz (Fig. 5.19). We study the nature of this component with in detail in Chapter 6.

Table 5.11: Parameters of the total intensity images of 1642+690.

ν	Array	$S_{\rm tot}$	$S_{\rm peak}$	$S_{\rm neg}$	$\sigma_{\rm rms}$	Beam		
						Chap8$\theta_{\rm max}$	$\theta_{\rm min}$	P.A.
[GHz]		[mJy]	[mJy/beam]	[mJy/beam]	[mJy/beam]	[mas]	[mas]	[°]
1.6	Space	1800	590	−15	1.30	0.993	0.373	16
5	Space	2200	620	−22	1.50	0.585	0.227	19
1.6	Ground	1700	1200	−1.9	0.15	3.22	2.76	7
5	Ground	2100	1100	−1.1	0.50	1.14	1.06	−41
22	Ground	1100	460	−3.5	0.30	0.316	0.218	72

Notes: Column designation: ν: frequency; $S_{\rm tot}$: total flux density; $S_{\rm peak}$: peak flux density; $S_{\rm neg}$: maximum negative flux density in the image; $\sigma_{\rm rms}$: rms noise in the image; Beam: major axis, minor axis, position angle of major axis.

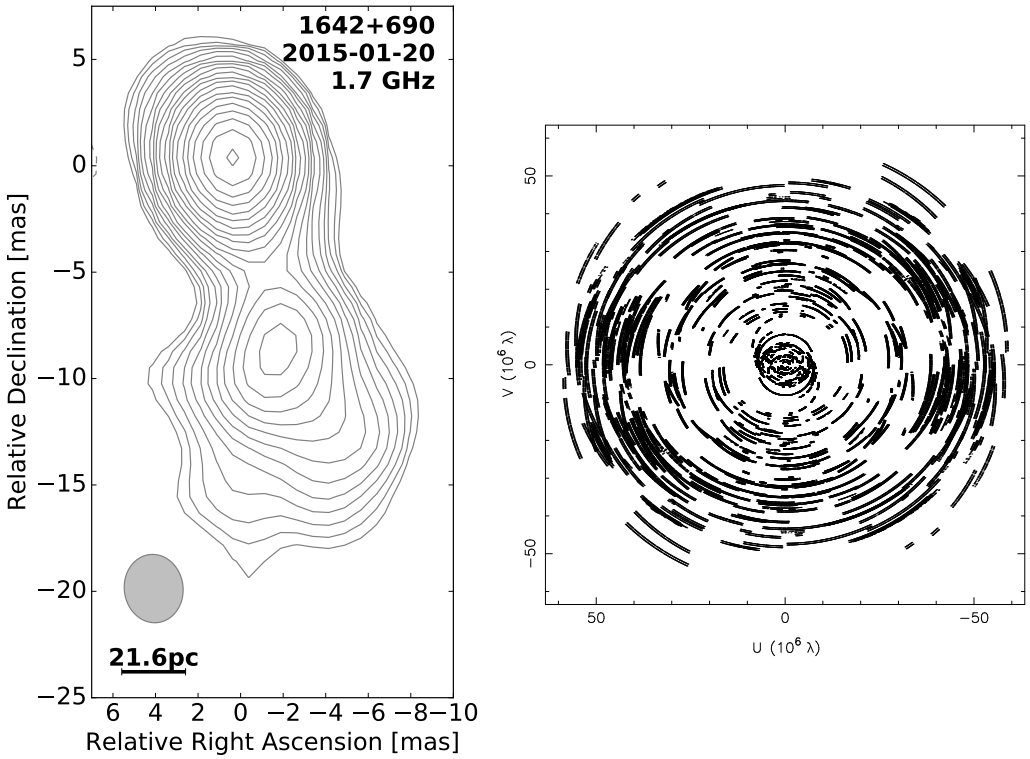

Figure 5.17: **Left panel:** Image of 1642+690 at 1.6 GHz. The contour levels are drawn at (-1, 1, $\sqrt{2}$, 2, ...) times 45 mJy/beam. **Right panel:** (u, v)-coverage plotted in units of Mλ of the ground observations of 1642+690 at 1.6 GHz.

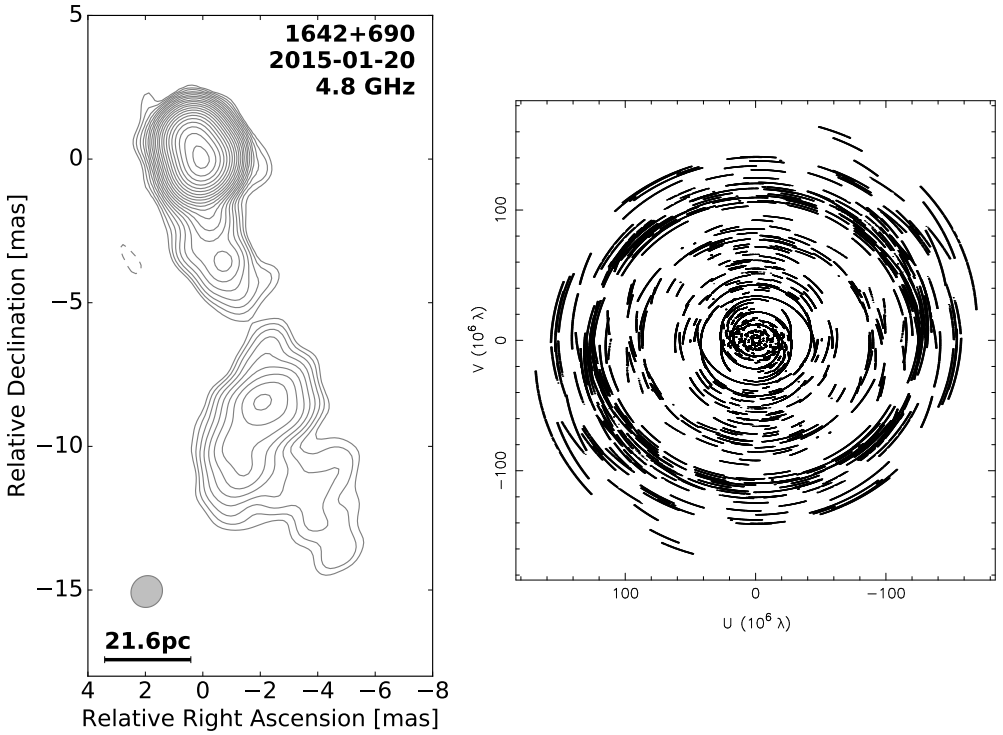

Figure 5.18: **Left panel:** Image of 1642+690 at 5 GHz. The contour levels are drawn at $(-1, 1, \sqrt{2}, 2, ...)$ times 80 mJy/beam. **Right panel:** (u, v)-coverage plotted in units of Mλ of the ground observations of 1642+690 at 5 GHz.

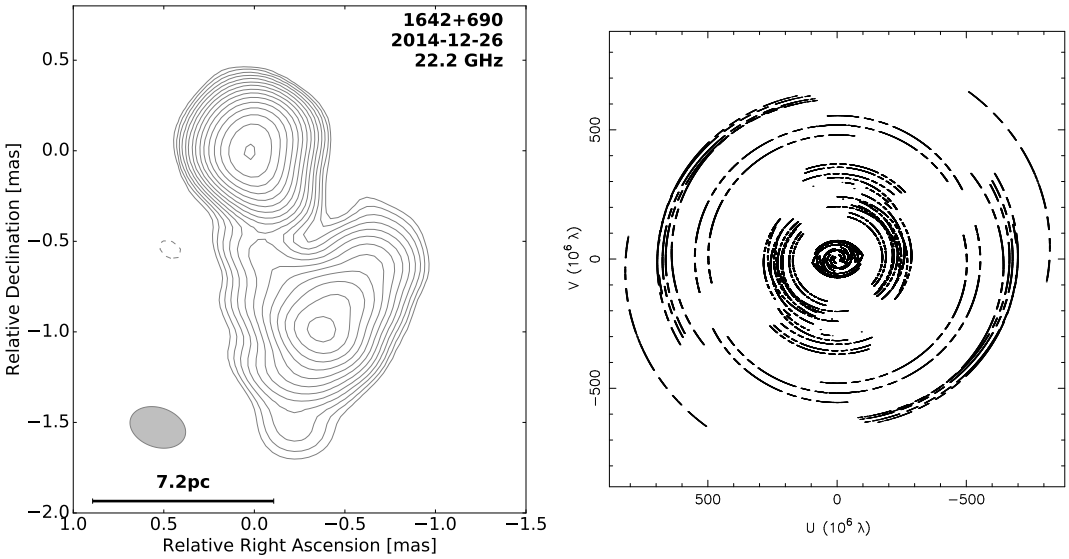

Figure 5.19: **Left panel:** Image of 1642+690 at 22 GHz. The contour levels are drawn at $(-1, 1, \sqrt{2}, 2, ...)$ times 9 mJy/beam. **Right panel:** (u, v)-coverage plotted in units of Mλ of the ground observations of 1642+690 at 22 GHz.

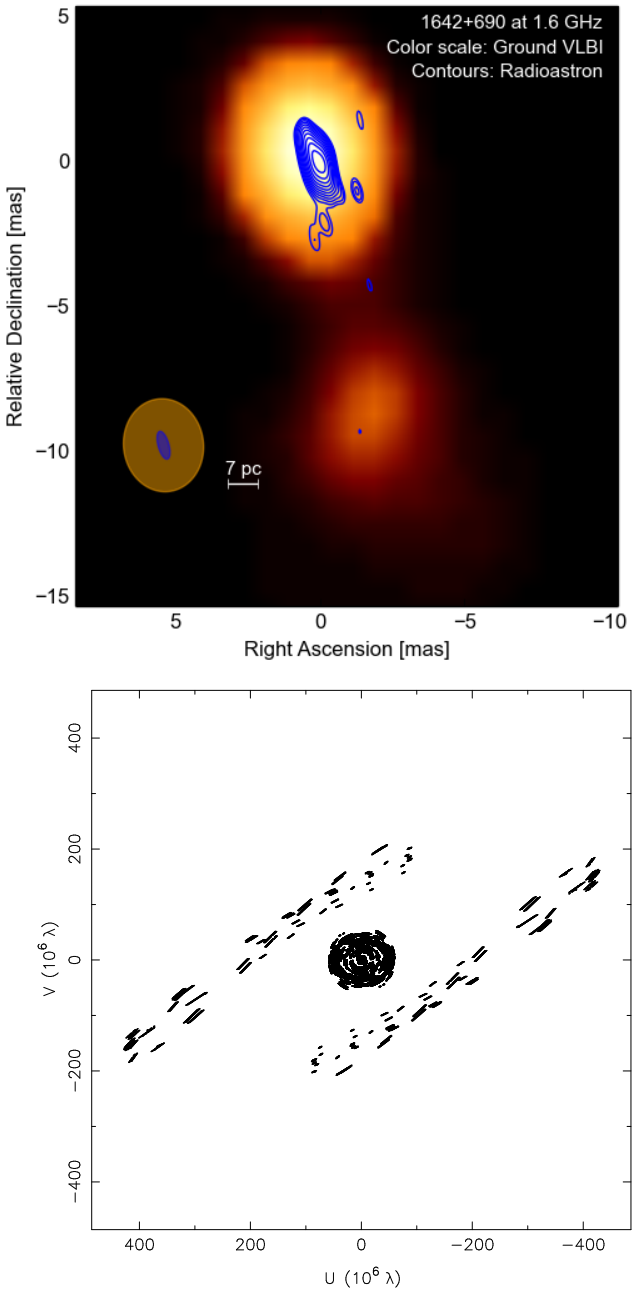

Figure 5.20: **Top panel:** *RadioAstron* image of 1642+690 at 1.6 GHz (contours) superimposed on the ground array image at 1.6 GHz (color scale). The contour levels are drawn at $(-1,\ 1,\ \sqrt{2},\ 2,\ \ldots\ )$ times 20 mJy/beam. **Bottom panel:** (u, v)-coverage plotted in units of Mλ of observations of 1642+690 at 1.6 GHz.

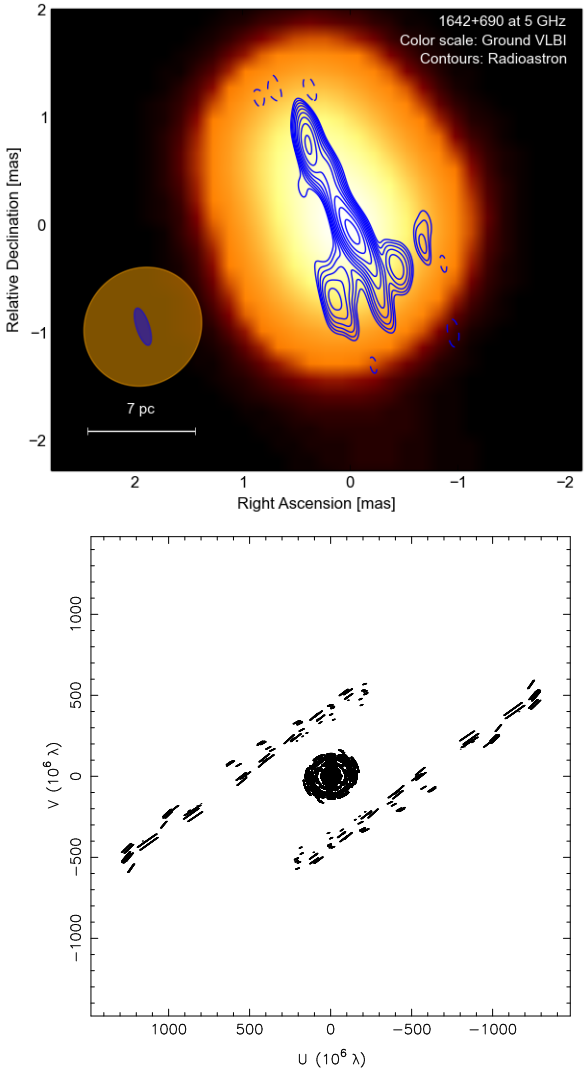

Figure 5.21: **Top panel:** *RadioAstron* image of 1642+690 at 5 GHz (contours) superimposed on the ground array image at 5 GHz (color scale). The contour levels are drawn at $(-1, 1, \sqrt{2}, 2, \ldots)$ times 23 mJy/beam. **Bottom panel:** (u, v)-coverage plotted in units of Mλ of observations of 1642+690 at 5 GHz.

5.3.3 Model-fitting

Model-fitting of the source structure is performed using the same procedure as for the other targets. Here we present as an example the results of the modelfit of the ground data at 1.6 GHz (Fig. 5.22 and Table 5.12). The rest of the tables are in Appendix C.

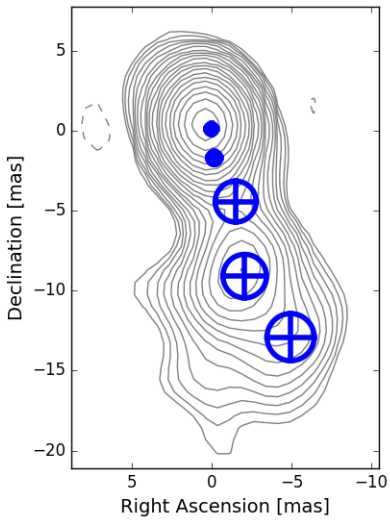

Figure 5.22: Modelfit components for the ground array observations of 1642+710 at 1.6 GHz. The contour levels are drawn at $(-1,\ 1,\ \sqrt{2},\ 2,\ \ldots\ )$ times 45 mJy/beam.

Table 5.12: Modelfit parameters for the ground VLBI image of 1642+690 at 1.6 GHz

	S_y [Jy]	r [mas]	ψ [°]	x [mas]	y [mas]	$\theta_{\rm g}$ [mas]	$\theta_{\rm lim}$ [mas]
c	1.27 ± 0.004	0.1 ± 0.6	3 ± 17	0.0 ± 0.6	0.11 ± 0.04	0.3 ± 0.6	0.324
c4	0.13 ± 0.002	1.7 ± 0.6	-174 ± 16	-0.2 ± 0.6	-1.7 ± 0.5	0.4 ± 0.6	0.770
c5	0.049 ± 0.002	4.7 ± 0.6	-160 ± 40	-1.5 ± 1.1	-4 ± 3	1.3 ± 0.6	1.163
c6	0.161 ± 0.006	9.3 ± 0.7	-167 ± 15	-2.1 ± 0.9	-9 ± 2	1.4 ± 0.6	1.030
c8	0.041 ± 0.003	13.8 ± 0.7	-160 ± 30	-5 ± 2	-13 ± 6	1.5 ± 0.6	1.372

Notes: Column designation: S_y: flux density; r: position of the component; ψ: position angle of the component; x: position of the component in RA; y: position of the component in DEC; θ_g: size of the gaussian component; $\theta_{\rm lim}$: limiting size of the gaussian component.

5.4 3C 273

3C 273 is one of the brightest quasars. It is the first quasar discovered and is located at a redshift of $z = 0.158$, at which 1 mas corresponds to 2.7 pc (Schmidt 1963). It is also the first quasar in which the γ-ray emission was detected (Swanenburg et al. 1978). The viewing angle of the jet in 3C 273 is estimated to be in the $5° - 11°$ range (Liu & Shen 2009). The jet has been observed with VLBI (see, e.g., Pearson et al. 1981; Abraham et al. 1996; Krichbaum et al. 2000; Lister et al. 2013, among others) and space VLBI (see, e.g., Lobanov & Zensus 2001; Asada et al.

2002). Lister et al. (2013) obtained a median apparent speed of $\beta_{\rm app} \sim 8.5$ and a maximum apparent speed of $\beta_{\rm app} \sim 15$. Lobanov & Zensus (2001) observed a double helical structure in the source and explained it with the presence of elliptical Kelvin Helmholtz instability modes. They inferred a jet Lorentz factor of ~ 2 and a Mach number of ~ 3.5. Asada et al. (2002) also suggested the presence of helical magnetic fields to interpret the observed helical structure. The variability observed in 3C 273 in radio, millimiter, and γ-ray band is dominated by strong and frequent flares (Türler et al. 2000; Abdo et al. 2010).

5.4.1 Observations

RadioAstron observations of 3C 273 were made on 30th April 2014 at two different frequencies of 5 GHz, and 22 GHz. We show all the participating antennas at each frequency in Table 5.13. Information about the observations is in Table 5.14. The on/off cycles for *RadioAstron* were 40/65 min, at all three observing frequencies. The data at a rate of 128 megabits per second (Mbps), resulting in a total bandwidth of 2x16 MHz for each circular polarization channel (Andreyanov et al. 2014). The data from all participating telescopes were transferred to the VLBI correlator of the MPIfR.

Table 5.13: VLBI antennas participating in the observations of 3C 273 at different frequencies (in GHz). The plus sign means the antenna observed at a given frequency. No symbol means no participation.

Name	Code	Array	5	22
Ceduna	CD	LBA	+	
Hobart	HO	LBA	+	
ATCA	AT	LBA		+
Mopra	MO	LBA		+
Mauna Kea	MK	VLBA	+	
Effelsberg	EF	EVN	+	+
Hartebeesthoek	HH	EVN	+	+
Kalyazin	KZ,KL		+	+
Badary	BD	EVN		+
Zelenchukskaya	ZC	EVN		+
Westerbork	WB	EVN	+	
Noto	NT	EVN	+	
Yebes	YS	EVN	+	
Onsala 25m	ON	EVN	+	
Torun	TR	EVN	+	
SRT	R1, R2		+	+

* No fringes detected.

Table 5.14: Summary of the observations of 3C 273

RadioAstron project code	global VLBI project code	Date	Observing time (UT)	$\nu_{\rm cent}$ [GHz]	on/off cycle [min]
raks05d	GL038F	2014/04/30	10:00–22:00	4.828	40/65
raks05d	GL038F	2014/04/30	10:00–22:00	22.228	40/65

5.4.2 Calibration and imaging

Data from the *RadioAstron* observations of 3C 273 were correlated in the Bonn DiFX correlator by G. Bruni and reduced with the same procedures as for the other objects except the fringe parameters. For the 5 GHz data, the reference antenna is Onsala and we apply a solution interval of 2 min for ground baselines. For the 22 GHz data, we use Badary as reference antenna and adopt a solution interval of 1 min. We use uniform weighting with phase and amplitude self-calibration in `difmap` to perform the hybrid imaging.

For the space VLBI data, we only find fringes at 5 GHz for half of the experiment (where the EVN antennas were participating). The second half of the experiment had mostly LBA antennas, and we were not able to find fringes for the space antenna for this time interval. The reference antenna at 5 GHz is Onsala, and the solution interval is 4 min. The reference antenna for the 22 GHz data is Effelsberg, and we use a 4 min solution interval. Finding fringes at 22 GHz resulted to be quite challenging due to the few available antennas and high frequency. Table 5.15 shows the map parameters for the different frequencies and observing arrays.

The ground array images are in Figs. 5.23 and 5.24 and the space VLBI images in Figs. 5.25 and 5.26. The *RadioAstron* image of 3C 273 at 5 GHz traces the brightest regions in the jet and it could be tracing the brightest of the two ridges described in Lobanov & Zensus (2001).

Table 5.15: Parameters of the total intensity images of 3C 273.

ν	Array	$S_{\rm tot}$	$S_{\rm peak}$	$S_{\rm neg}$	$\sigma_{\rm rms}$	Beam		
						$\theta_{\rm max}$	$\theta_{\rm min}$	P.A.
[GHz]		[mJy]	[mJy/beam]	[mJy/beam]	[mJy/beam]	[mas]	[mas]	[°]
5	Space	25000	950	−15.0	1.50	0.632	0.270	18
22	Space	2900	990	−1.6	0.30	0.226	0.147	62
5	Ground	20000	2900	−2.3	0.50	2.88	1.86	−82
22	Ground	2000	1000	−1.6	0.30	0.260	0.246	32

Notes: Column designation: ν: frequency; $S_{\rm tot}$: total flux density; $S_{\rm peak}$: peak flux density; $S_{\rm neg}$: maximum negative flux density in the image; $\sigma_{\rm rms}$: rms noise in the image; Beam: major axis, minor axis, position angle of major axis.

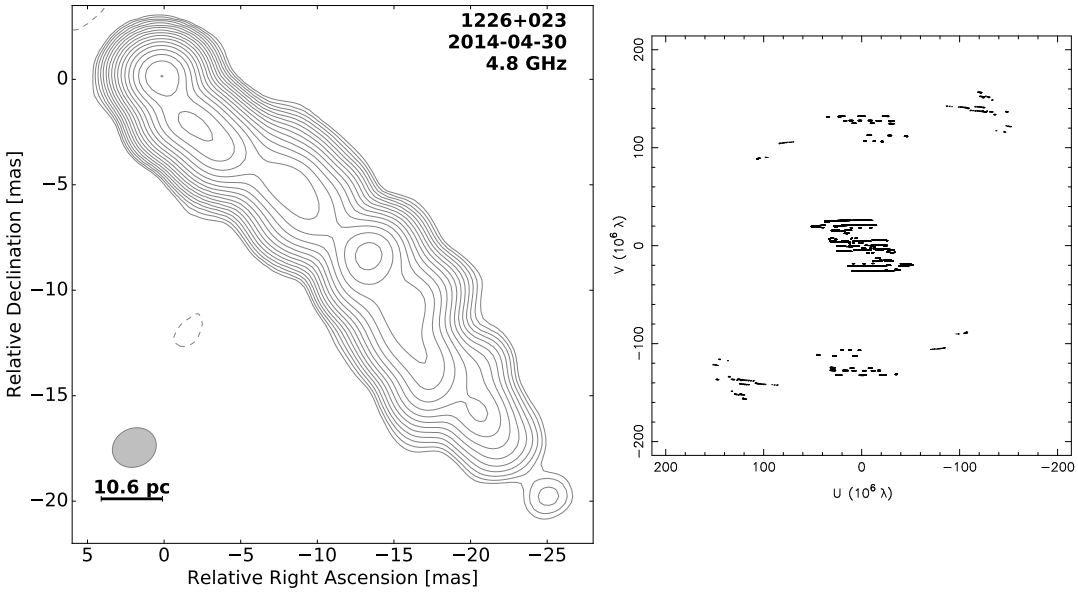

Figure 5.23: **Left panel:** Image of 3C 273 at 5 GHz. The contour levels are drawn at $(-1, 1, \sqrt{2}, 2, \ldots)$ times 65 mJy/beam. **Right panel:** (u, v)-coverage plotted in units of Mλ of the ground observations of 3C 273 at 5 GHz.

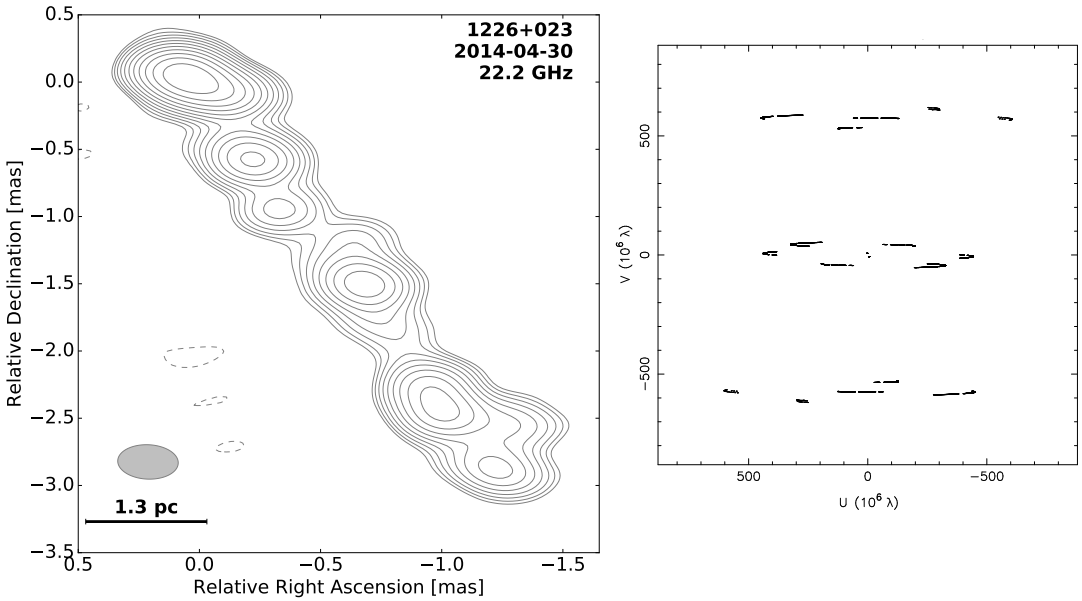

Figure 5.24: **Left panel:** Image of 3C 273 at 22 GHz. The contour levels are drawn at $(-1, 1, \sqrt{2}, 2, \ldots)$ times 1.2 mJy/beam. **Right panel:** (u, v)-coverage plotted in units of Mλ of the ground observations of 3C 273 at 22 GHz.

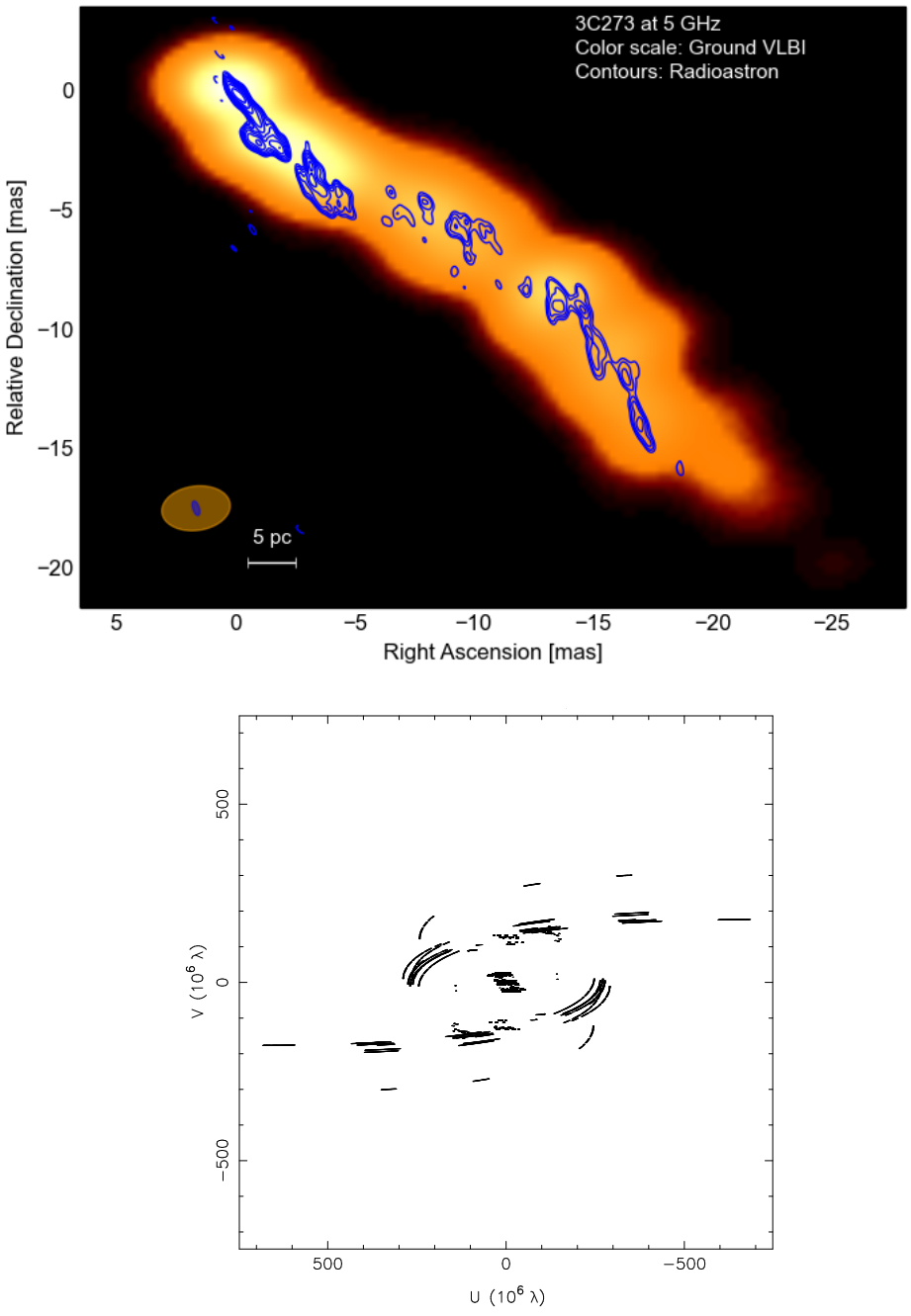

Figure 5.25: **Top panel:** *RadioAstron* image of 3C 273 at 5 GHz (contours) superimposed on the ground array image at 5 GHz (color scale). The contour levels are drawn at $(-1,\ 1,\ \sqrt{2},\ 2,\ \ldots\ )$ times 42 mJy/beam. **Bottom panel:** (u, v)-coverage plotted in units of Mλ of observations of 3C 273 at 5 GHz.

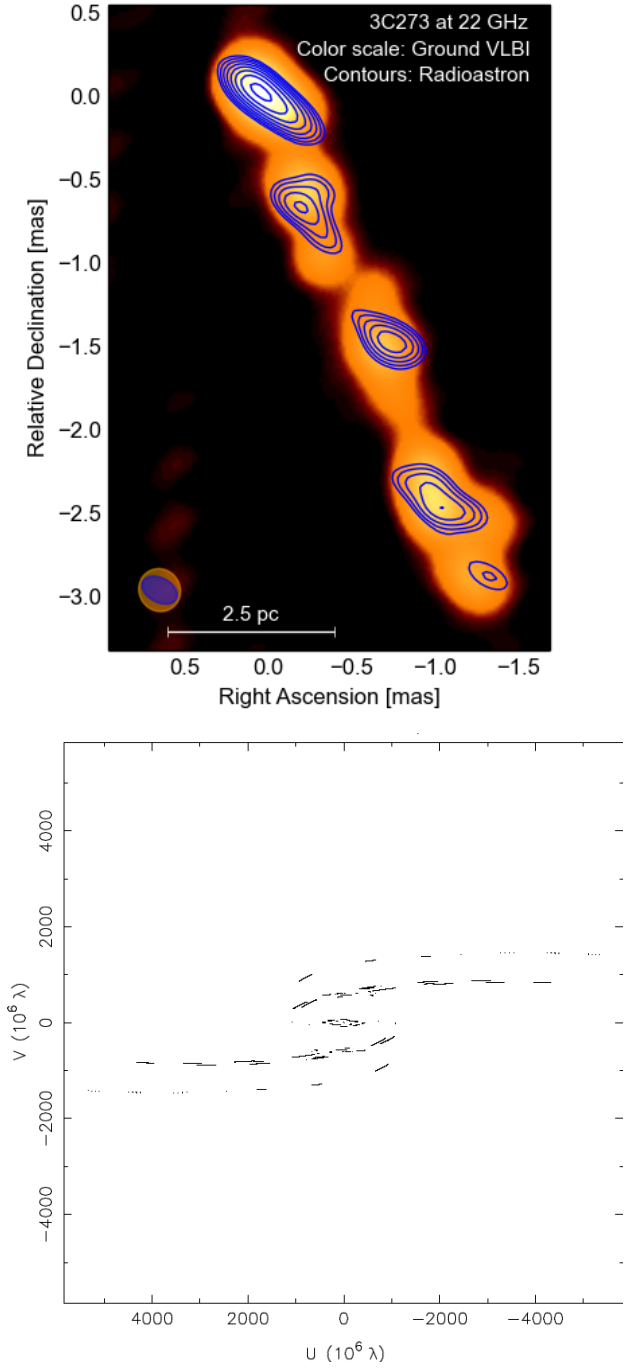

Figure 5.26: **Top panel:** *RadioAstron* image at 22 GHz (contours) superimposed on an image obtained using only the ground array data at 22 GHz (color scale) of 3C 273. The contour levels are drawn at $(-1,\ 1,\ \sqrt{2},\ 2,\ \ldots\ )$ times 40 mJy/beam. **Bottom panel:** (u, v)-coverage plotted in units of Mλ of observations of 3C 273 at 22 GHz.

5.4.3 Model-fitting

Model-fitting of the source structure is performed using the same procedure as for the other targets. We do not apply the model-fitting analysis for the 22 GHz data due to the bad data quality. Here we present as an example the results of the modelfit of the ground data at 5 GHz (Fig. 5.27 and Table 5.16). The rest of the tables are in Appendix C.

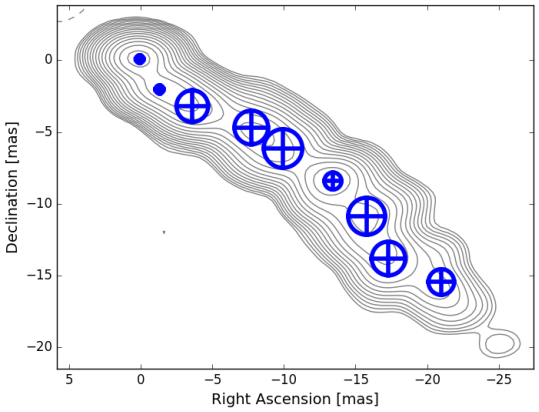

Figure 5.27: Modelfit components for the ground array observations of 3C 273 at 5 GHz. The contour levels are drawn at (-1, 1, $\sqrt{2}$, 2, ...) times 65 mJy/beam.

Table 5.16: Modelfit parameters for the ground VLBI image of 3C 273 at 5 GHz

	S_y [Jy]	r [mas]	ψ [°]	x [mas]	y [mas]	$\theta_{\rm g}$ [mas]	$\theta_{\rm lim}$ [mas]
c	3.6 ± 0.3	0.1 ± 0.5	40 ± 90	0.1 ± 0.4	0.1 ± 0.3	0.3 ± 0.5	1.129
c1	2.4 ± 0.15	2.4 ± 0.5	−150 ± 50	−1.3 ± 1.2	−2.0 ± 1.7	0.3 ± 0.5	1.061
c2	3.49 ± 0.11	4.8 ± 0.6	−132 ± 18	−3.6 ± 1.2	−3.2 ± 1.1	1.1 ± 0.5	0.779
c3	1.68 ± 0.07	9.0 ± 0.6	−121 ± 14	−7.7 ± 1.9	−4.7 ± 1.2	1.2 ± 0.5	0.867
c4	1.63 ± 0.08	11.7 ± 0.7	−122 ± 15	−10 ± 3	−6.1 ± 1.7	1.3 ± 0.5	0.970
c5	2.0 ± 0.06	15.8 ± 0.5	−122 ± 4	−13.4 ± 1.0	−8.4 ± 0.7	0.6 ± 0.5	0.741
c6	1.9 ± 0.06	19.2 ± 0.6	−125 ± 5	−15.8 ± 1.3	−10.9 ± 1.0	1.3 ± 0.5	0.748
c7	1.01 ± 0.08	22.1 ± 0.6	−129 ± 13	−17 ± 4	−14 ± 3	1.2 ± 0.5	1.192
c8	0.39 ± 0.04	26.1 ± 0.5	−126 ± 15	−21 ± 6	−15 ± 4	0.9 ± 0.5	1.428

Notes: Column designation: S_y: flux density; r: position of the component; ψ: position angle of the component; x: position of the component in RA; y: position of the component in DEC; θ_g: size of the gaussian component; $\theta_{\rm lim}$: limiting size of the gaussian component.

Chapter 6

Multifrequency and multiepoch study

This Chapter is partially reproduced in Vega-García et al. a,b,c in prep.

In this chapter we will discuss the kinematic and spectral properties of relativistic jets for the sources from the *RadioAstron* KSP of strong AGNs, presenting the results from ground and space observations for each source.

6.1 Kinematic analysis

In this section we discuss the results from a kinematic analysis of 0836+710 at 43 GHz using Boston University data, and relate them to high-energy flaring episodes in the same source.

6.1.1 0836+710

We introduce the kinematics analysis at 43 GHz for epochs between 2012 and the end of 2017. We use data from the Boston University (BU) blazar monitoring program, that provides 43 GHz VLBA observations of 0836+710 with a regular cadence. These high frequency observations are more sensitive to the structure close to the jet base, which we are mainly interested in. The analysis was preformed using *kinepy*, a newly developed software for kinematic analysis of multi-epoch VLBI data, which will be presented briefly in the appendix B.

We modeled 38 images of 0836+710 from the BU blazar monitoring program, by fitting Gaussian components to the jet using the task `modelfit` in `difmap`. In order to perform a kinematics analysis, we first need to reference all the component positions to the same point. The procedure is to identify the core component in each epoch, since it is the dynamical center of the jet, and shift all maps so that it is always at the (0,0) position. Then, we associate the components across all

the available epochs, and obtain their angular speed, μ through a linear fit. We do this for the two components of the velocity vector, performing a fit in right ascension and declination (see, e.g., Schinzel et al. 2012; Fromm et al. 2013a):

$$\begin{aligned} x(t) &= \mu_x \left(t - t_{x,0}\right) + \frac{\dot{\mu_x}}{2} \left(t - t_{\rm mid}\right)^2 \\ y(t) &= \mu_y \left(t - t_{y,0}\right) + \frac{\dot{\mu_y}}{2} \left(t - t_{\rm mid}\right)^2 , \end{aligned} \tag{6.1}$$

where $t_{x,0} = t_{\rm mid} - x(t_{\rm mid})/\mu_x$, $t_{y,0} = t_{\rm mid} - y(t_{\rm mid})/\mu_y$, and $t_{\rm mid} = (t_{\rm max} + t_{\rm min})/2$. We only perform a linear fit, excluding the second order terms, because we do not observe a clear acceleration of components. This allows us to obtain the apparent speed of the components, as:

$$\beta_{\rm app} = \frac{\langle \mu \rangle \, D_L}{1+z}. \tag{6.2}$$

The resulting apparent speed values and ejection dates are listed in Table 6.1. The modelfit parameters for the identified components can be found in Appendix D.

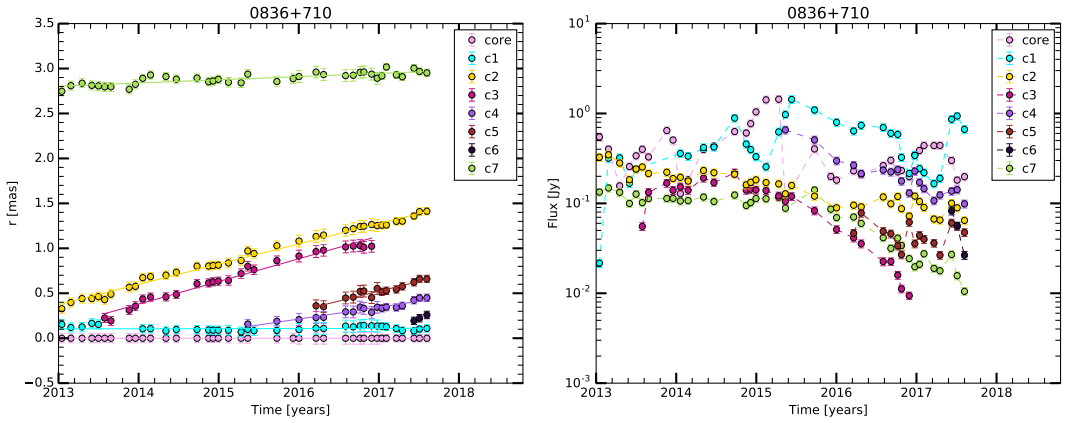

Figure 6.1: Multiepoch component analysis of 0836+710 at 43 GHz. **Left panel:** Evolution of the component distance with respect to the core with time. **Right panel:** Evolution of the component flux with time.

Figure 6.1 shows the results of our kinematics analysis: on the left panel, we show the core separation of identified components as a function of time; on the right panel, we show their flux evolution as a function of time. A standing feature, c7, is observed between 2.5 and 3 mas, seen in the upper part of the left panel. Krichbaum et al. (1990) and Hodgson (2015) also reported the existence of non moving features at this distance. Some discrepancies in the exact location of the component between our results and previous works might be caused by the difference in resolution, which can lead to one component being resolved into two in different epochs. This might cause a systematic error in the position which

can bias possible conclusions, since in some cases we will be model-fitting one component instead of two. This can be the cause of an apparent slow motion of this feature. Since component c7 is resolved into two in some epochs, we do not report an apparent speed for this feature. In addition to c7, we also see a standing feature, c1, at around 0.12 mas from the core region. This indicates the presence of a recollimation shock close to the jet base. We can see a wiggling of the recollimation shock when moving components are nearby, for example after the ejection of component c6 in mid 2017. This was also observed in the case of CTA 102 (Fromm 2015) and analyzed with numerical simulations. The reason behind this behavior is the interaction between a standing and moving shock (Fromm et al. 2016). It might also cause a temporary disappearance of the recollimation shock, or its wandering, as it is perturbed by the violent event of a moving shock passing through it.

We describe the results for each component dividing them in different groups. On the one hand, we have the recollimation shock, component c1, which is located at a distance of 0.11 ± 0.06 mas. The speed of the component is consistent with zero with an apparent speed of $\beta_{\rm app} = 0.1 \pm 0.2$. Therefore, we can consider the component to be stationary, consistent with our interpretation of the component as a recollimation shock. On the other hand, the components c2 and c3, ejected at 2011.4 and 2012.6 respectively, show quite high apparent speed, with $\beta_{\rm app} \sim 20$. It would appear as if the two components merged, at the end of the analyzed time interval, due to the slightly higher speed of component c3 (see Tab 6.1). The third group consists of components c4 and c5, which were ejected within the same year, in 2014.4 and 2014.7, respectively. The apparent speed of the two components is $\beta_{\rm app} \sim 11$ and $\beta_{\rm app} \sim 20$, respectively. The non detection of component c5 between the ejection time and the beginning of 2016 might be due to lack of resolution at this frequency, with c4 being resolved into two components at later epochs. Alternatively, this might be due to an interaction between the two components, with only one being detected until the end of the interaction. Around mid 2017 another component, c6, is ejected, but we do not have enough data to perform a fit on this feature and measure its apparent speed.

Table 6.1: Component speed and ejection times for the 43 GHz multiepoch analysis of 0836+710.

label	μ [mas/yr]	$\beta_{\rm app}$	t_0 [yr]	$\theta_{\rm crit}$ [°]	$\delta_{\rm crit}$	$\theta_{\rm max}$ [°]
c2	0.225 ± 0.008	19.0 ± 0.7	2011.4 ± 0.1	3.00 ± 0.07	19.1 ± 0.6	6.0 ± 0.2
c3	0.253 ± 0.015	21.4 ± 1.3	2012.6 ± 0.1	2.68 ± 0.11	21.4 ± 1.3	5.4 ± 0.3
c4	0.13 ± 0.03	11 ± 2	2014.4 ± 0.2	5.1 ± 0.8	11 ± 2	10.4 ± 1.9
c5	0.22 ± 0.05	19 ± 4	2014.7 ± 0.2	3.1 ± 0.5	19 ± 4	6.0 ± 1.3

The kinematics analysis also allows us to obtain estimates of the Doppler factor and an upper limit of the viewing angle, since we do not observe any counter jet. For the Doppler factor, we have two different definitions: the critical Doppler factor

and the variability Doppler factor. However, it is only possible to calculate the latter if we observe an exponential decrease of the flux density during different time periods for one or several components. For the critical Doppler factor, as already stated in Chapter 1, the maximum apparent speed of a travelling component is given at a critical angle, $\theta_{\rm crit}$, and the corresponding Doppler factor is $\delta_{\rm crit}$. Both parameters are calculated as (solving for $\theta_{\rm crit}$ in Eq. 1.7):

$$\theta_{\rm crit} = \arccos\sqrt{\frac{\beta_{\rm app}^2}{1+\beta_{\rm app}^2}}, \qquad \delta_{\rm crit} = \sqrt{1+\beta_{\rm app}^2}. \tag{6.3}$$

The calculation of the variability viewing angle and variabilty Doppler factor is described in Jorstad et al. (2005). To obtain these parameters, we need to calculate first the variability timescale, $\Delta t_{\rm var} = dt/\ln(S_{\rm max}/S_{\rm min})$, where $S_{\rm max}$ and $S_{\rm min}$ are the maximum and minimum flux density of the component in the considered time interval (where its flux density decreased exponentially), and dt is the time difference between the epoch in which the component was at its maximum flux-density and its minimum flux-density (Jorstad et al. 2005). Using these quantities, the variability Doppler factor is defined as:

$$\delta_{\rm var} = \frac{d_{\rm eff} D_L}{c\Delta t_{\rm var}(1+z)}, \tag{6.4}$$

where $d_{\rm eff}$ is the effective size of the gaussian, defined by $d_{\rm eff} = 1.8 \times$ FWHM (Marscher 1983) where the FWHM is the full width half maximum of the component at the time when its flux density was maximum. This quantity allows us to also calculate the variability Lorentz factor, $\Gamma_{\rm var}$, and variability viewing angle, $\theta_{\rm var}$:

$$\Gamma_{\rm var} = \frac{\beta_{\rm app}^2 + \delta_{\rm var} + 1}{2\delta_{\rm var}}, \qquad \theta_{\rm var} = \arctan\frac{2\beta_{\rm app}}{\beta_{\rm app}^2 + \delta_{\rm var}^2 - 1}. \tag{6.5}$$

It is also possible to give an upper limit of the viewing angle for each component. To do this, we use the formula of the apparent speed, Eq. 1.7. We assume the maximum value of the intrinsic speed, $\beta = 1$, and solve the equation for the viewing angle. The lower limit of the apparent speed will be corresponding to the maximum viewing angle:

$$\theta \leq \arccos\frac{\beta_{\rm app}^2 - 1}{\beta_{\rm app}^2 + 1}. \tag{6.6}$$

We present the results of the critical angle and critical Doppler factor, together with the maximum viewing angle in Table 6.1. For the components that are moving with an apparent speed of ~ 20, the critical angle is 3°, while for the component moving at $\beta_{\rm app} \sim 10$, the critical angle is $\theta_{\rm crit} = 5°$. The faster components have a critical angle similar to the source viewing angle, $\theta \sim 3°$ (Otterbein et al. 1998). The literature value for the viewing angle falls below the upper limit calculated using Eq. 6.6, i.e., $\theta < 6°$.

For the variability Doppler factor, there are only two possible components whose flux density decreases exponentially during some time segments. The results are in Table 6.2. Even though components c2 and c4 show this kind of behaviour for some intervals, we have excluded those components because they show hints of acceleration. Therefore we only studied this effect for component c3, between 2015.4 and 2016.6, and component c5 between 2016.3 and 2016.8. The variability Doppler factor is around $\delta_{\rm var} = 22 \pm 5$ in both cases, which hints at the absence of acceleration or deceleration in the flow between 0.5 mas and 1.0 mas.

To complement the analysis at larger scales, we have considered the kinematics results from 15 GHz VLBA observations from the MOJAVE monitoring program (Lister et al. 2013). Figure 6.2 shows the core separation as a function of time for the MOJAVE kinematics. Component 4, between 2006.7 and 2010.8, component 6 between 2003.2 and 2010.8, and component 7 between 2004.7 and 2010.8, show time periods where their flux decreases exponentially, and it is therefore possible to calculate jet parameters from variability for these features. The resulting variability Doppler factors are $\delta_{\rm var} \sim 13$ at distances of $r \sim 1.5$ mas, $\delta_{\rm var} \sim 11$ at $r \sim 2.1$ mas and $\delta_{\rm var} \sim 8.5$ at $r \sim 3.5$ mas, respectively (see Table 6.3). This could indicate a deceleration of the flow between 1.5 and 3.5 mas. It could also mean that the components are moving away from our line of sight following a helical structure, which would lead to an apparent deceleration of the flow. Since the variability Doppler factor at r$\sim$1.5 mas is double than the one at r$\sim$3.5 mas, we can see which changes in the viewing angle or the speed of the flow are needed to explain this difference. Using, $\delta_1 = 2\delta_2$ with δ_1 corresponding at distances of r$\sim$1.0 mas and δ_2 to r$\sim$3.5 mas, we obtain that, assuming a constant jet speed and a viewing angle of 3° for the innermost region, the viewing angle should be smaller at larger distances, dropping to $\theta \sim 2.1°$. If we now assume the viewing angle to be constant, we have the following relationship between the jet Lorentz factor at the two distances, $\gamma_1 = 2\gamma_2$, implying a deceleration of the flow.

Table 6.2: Variability Doppler factor and angle from c3 and c5 of the Boston University dataset for 0836+710.

label	$d_{\rm eff}$	$\Delta t_{\rm var}$ [yr]	$\delta_{\rm var}$	$\Gamma_{\rm var}$	$\theta_{\rm var}$ [°]
c3	0.12 ± 0.02	0.47 ± 0.06	22 ± 5	9.6 ± 3	2.6
c5	0.19 ± 0.02	0.72 ± 0.08	22 ± 3	9.5 ± 4	2.6

Table 6.3: Kinematics parameters from the MOJAVE public archive of 0836+710.

number	$\beta_{\rm app}$	$d_{\rm eff}$	$\Delta t_{\rm var}$ [yr]	$\delta_{\rm var}$	$\Gamma_{\rm var}$	$\theta_{\rm var}$ [°]	$\theta_{\rm crit}$ [°]
4	16.8 ± 0.4	1.04 ± 0.02	10.43 ± 0.06	8.5 ± 5	17 ± 5	5.44	3.41 ± 0.06
6	17.7 ± 0.6	0.47 ± 0.02	3.61 ± 0.08	11 ± 3	15 ± 4	4.68	3.23 ± 0.08
7	21.1 ± 0.8	0.29 ± 0.02	1.93 ± 0.08	13 ± 3	18 ± 5	4.00	2.71 ± 0.07

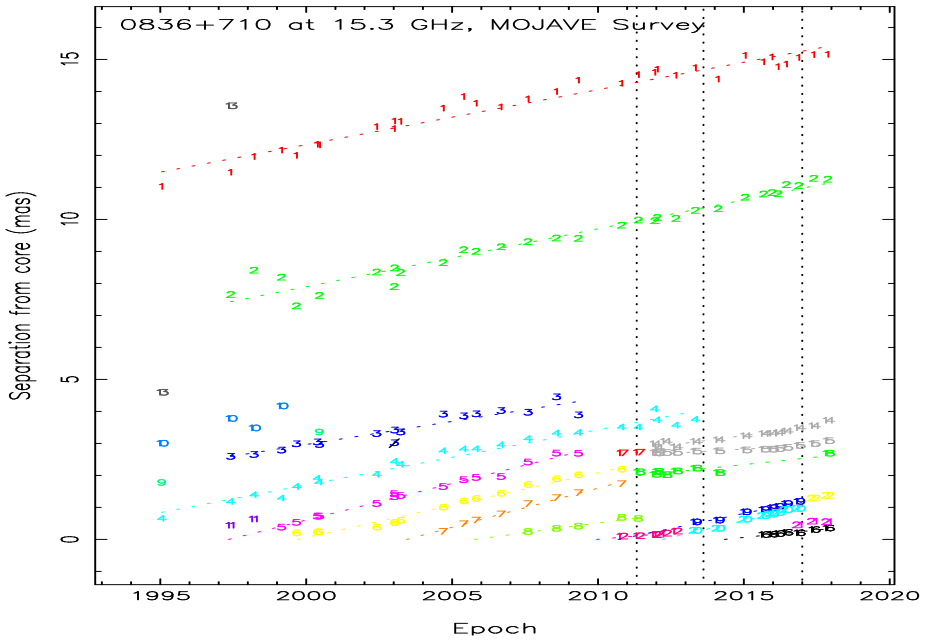

Figure 6.2: Evolution of the component distance with respect to the core with time for the MOJAVE data set for 0836+710 (Lister et al. 2013).

0836+710 is a well-known γ-ray source showing strong variability. We can attempt to relate the behavior of pc-scale jet components with the γ-ray state of the source, which is monitored by the *Fermi*-LAT space telescope. The *Fermi*-LAT collaboration provides public light curves of flaring sources on daily and weekly time scales[1]. It is interesting to note that γ-ray flaring states of the source in three different epochs might be related to pc-scale jet components, as seen in Fig. 6.3. The figure shows the source's flux as a function of time. After the launch of *Fermi*-LAT, a γ-ray flare was first observed in the second half of 2011 (Akyuz et al. 2013), at a time consistent with the ejection of component c2. Later, at the end of 2011 the source had a brighter flare which is temporally consistent (within

[1]URL: https://fermi.gsfc.nasa.gov/ssc/data/access/lat/msl_lc/

the errors) with the moment in which component c2 passed through the recollimation shock, c1. A smaller γ-ray flaring event was observed at the beginning of 2013, at a time consistent with the passage of component c3 through the standing feature. Following episodes of high-energy activity appeared in 2014. The two peaks in the γ-ray emission are consistent with the ejection of components c4 and c5 respectively. In August 2015, 0836+710 underwent the brightest γ-ray flare observed up to date. This is also temporally coincident with the interaction of component c4 and c5 with the recollimation shock. However, several concurrent processes were happening close to the time of the flare. First, the recollimation shock brightened by a factor of five with respect to its average flux level. This could be due to the standing shock-travelling shock interaction. Furthermore, the source was active in γ-rays (at lower flux levels with respect to the main peak) until mid 2016. This extended flaring period could be due to the interaction between the two travelling shocks, before they divided their trajectory. All these effects could have contributed to the 2015 γ-ray flare being significantly brighter than the previous episodes.

Jorstad et al. (2013) discussed a γ-ray flaring state of 0836+710 in 2012, and concluded, studying the optical polarization behavior of the source, that there is a connection between such flares and the properties of the innermost jet region when a travelling knot was within 0.2 mas. This constraint is consistent with the position of the recollimation shock and strengthens the argument that the flares can be related to the interaction of moving shocks with it.

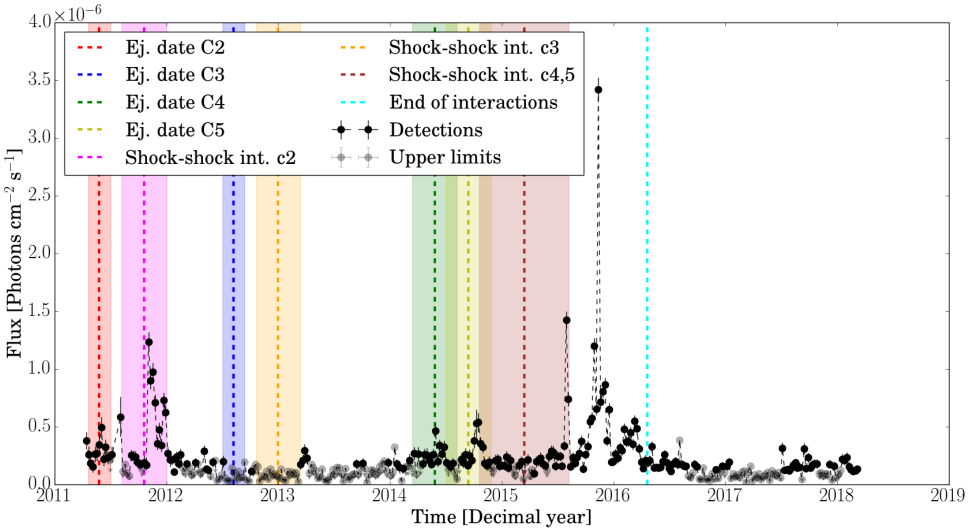

Figure 6.3: Public γ-ray light curve of 0836+710 with weekly binning from *Fermi*-LAT data (URL: https://fermi.gsfc.nasa.gov/ssc/data/access/lat/msl_lc/source/S5_0836p71). The colored vertical lines and shaded areas indicate interactions occurring in the pc-scale jet of 0836+710, according to the figure legend.

6.2 Spectral analysis

The spectral analysis of VLBI jets is divided in several steps in order to perform a consistent analysis. Before describing the analysis and results for each of the sources, we describe the steps followed. Then, we proceed to describe the obtained results.

6.2.1 Procedure

The main steps through which it is possible to obtain physical jet properties with a spectral analysis are image alignment, spectral index calculation between adjacent frequencies, and, if possible, computing the turnover frequency and flux density. These quantities, together with the coreshift, allow us to estimate the magnetic field in the jet. For this analysis I have developed a software which is described in Appendix B.

6.2.1.a Coreshift and image alignment

The first step is to align the images with respect to an image at a chosen reference frequency, since the absolute position of the source is lost during the imaging process. As we need to align two images made at two different frequencies, we select an optically thin region or component of the jet, because its position does not change with frequency. There are two possible methods for image alignment using an optically thin region at the jet: a) the 2D-cross correlation on an optically thin region of the jet or b) comparing the position with respect to the core of one or more optically thin components obtained from model-fitting. Both approaches have been performed, and their results compared. The alignment is done pairwise for adjacent frequencies, since it is difficult to select the same optically thin region at frequencies that are too far apart. It is also necessary for the map parameters at the two frequencies (i.e. beam, cellsize and mapsize) to be the same. The beam size and mapsize are chosen to be the ones of the lower frequency image. The cellsize is that of the higher frequency image. These parameters will guarantee that no information is lost.

(a) **2D-cross correlation**. A typical manner to perform this analysis is to mask the optically thick core region and to perform the cross-correlation with the rest of the image. However, as there might be some other optically thick regions along the jet, which should not be considered when computing the cross-correlation, we manually select a specific optically thin region in both images. The same region is selected in the maps at both frequencies and one of them is shifted in right ascension, Δx, and declination, Δy. The cross correlation coefficient is calculated for each shift. The best values for (Δx,Δy) will

be the those that maximizes this coefficient. The cross-correlation coefficient, $cc(a,b)$, is given by (Lewis 1995):

$$cc(a,b) = \frac{\sum_{x,y}\left(f(x,y) - \overline{f}_{a,b}\right)\left(t(x-a,y-b) - \overline{t}\right)}{\left(\sum_{x,y}\left(f(x,y) - \overline{f}_{a,b}\right)^2 \sum_{x,y}\left(t(x-a,y-b) - \overline{t}\right)^2\right)^{\frac{1}{2}}}, \tag{6.7}$$

where x and y are the different positions in the window that contains the selected optically thin region, f is the image, t is the feature to identify, which is situated at coordinates (a,b), $\overline{f}_{a,b}$ is the mean of the image, $f(x,y)$, in the region where the feature is, and $\overline{t}$ is the mean of the feature. The denominator represents a normalization factor. It is necessary because the flux level at different frequencies is typically not the same, and therefore, if the correlation coefficient is not normalized correctly, the algorithm would simply attempt to match regions with similar fluxes. Furthermore, it is necessary to subtract the mean value in the above formula, $\overline{f}_{a,b}$, in order to avoid bright regions in one map to match with equally bright (but opposite sign) negative flux regions in the map at the second frequency. The error on the shift is assumed to be equal to the pixel size (see Fromm et al. 2013b).

(b) **Alignment using optically thin modelfit components**. For this method, we use the gaussian components obtained from model-fitting. We select one or more optically thin components and compare their positional offsets from the core component at each individual frequency. The difference in the positions of these components is assumed to be caused by the frequency dependence of the position of the radio core. The resulting coreshift is calculated by subtracting the positions of the components with respect to the core between the two frequencies. The error is calculated with error propagation.

6.2.1.b Spectral index

The next step is to calculate the spectral index using the two images in each of the frequency pairs. The spectral index, α, is defined as:

$$\alpha = \frac{\ln\left(S_1/S_2\right)}{\ln\left(\nu_1/\nu_2\right)}, \tag{6.8}$$

where $S_{1,2}$ are the flux densities in the given pixel, and $\nu_{1,2}$ are the frequencies of each map. A cut along the spectral index is also done in order to highlight spectral index changes downstream of the core, which could indicate the presence of shocks (Mimica et al. 2009). We see these regions as zones where the spectral index becomes flatter or even inverted.

6.2.1.c Turnover analysis

It is also possible to study the synchrotron spectrum of the source at different locations, i.e., make a map of turnover frequency and flux (Lobanov 1998a). This is only possible if the data set includes at least three different frequencies and if both the optically thin and optically thick parts of the spectrum are seen. If not, the only information that is possible to extract is the spectral index of the source, through a linear fit of the optically thin part of the spectrum. In order to not lose information, as in the case of the image alignment, it is desirable to use the beam of the lowest frequency image and the cell size of the high frequency image. Then, we shift all the images with respect to the high frequency image with the shifts calculated using image pairs and perform a fitting of the spectrum pixel-by-pixel with Eq. 2.22.

6.2.1.d Magnetic field

At last, we can obtain the magnetic field using the coreshift approach (Lobanov 1998b), and the turnover approach (Lobanov 1998a; Fromm et al. 2013c).

If we use the turnover approach, we need to apply Eq. 2.35, and we can only do this if we have a turnover frequency and turnover flux-density map.

If we estimate the magnetic field using the coreshift, we need at least four frequencies, unless we assume that k_r is equal to unity. In this case, two frequencies are sufficient. It is preferable, however, to derive the value of k_r instead of assuming the jet shape. Because the measurements of the coreshift are made relative to a reference frequency, the relationship of the coreshift with the frequency is (O'Sullivan & Gabuzda 2009; Fromm et al. 2013b):

$$\Delta r = A \left(\nu^{-1/k_r} - \nu_{\rm ref}^{-1/k_r} \right) . \tag{6.9}$$

Performing a fit using the previous equation will give us a value for k_r. After, the magnetic field is calculated using $k_r = 1$ and the k_r obtained directly from the fit. For that, we use Eq. 2.48 (if $k_r = 1$) or Eq. 2.46 (if $k_r \neq 1$) to calculate the magnetic field at 1 pc from the core. Its value in the core region is calculated with Eq. 2.47. We can also calculate an estimate of the particle density at a distance of 1 pc with Eq. 2.49 (see Chapter 2 for more details).

6.2.2 0836+710

6.2.2.a Coreshift and image alignment

We have observed this source at five different frequencies, 1.6 GHz, 5 GHz, 15 GHz, 22 GHz, and 43 GHz, observed mainly in 2014. We obtain the coreshift for each frequency with respect to the core position at 43 GHz. The coreshift values obtained

from using the 2D cross-correlation approach are given in Table 6.4. Table 6.5 gives the respective shift obtained by using modelfit components.

Table 6.4: Coreshift measured with respect to the core position at 43 GHz in 0836+710. 2D cross correlation approach.

ν [GHz]	x [mas]	ϵ_x [mas]	y[mas]	ϵ_y [mas]	Δr [mas]	$\epsilon_{\Delta r}$ [mas]
22	-0.030	$\pm$ 0.010	-0.0003	$\pm$ 0.010	0.030	$\pm$ 0.014
15	-0.160	$\pm$ 0.010	-0.093	$\pm$ 0.010	0.185	$\pm$ 0.014
5	-0.16	$\pm$ 0.05	-0.093	$\pm$ 0.05	0.19	$\pm$ 0.07
1.6	-1.19	$\pm$ 0.15	-1.8	$\pm$ 0.15	2.2	$\pm$ 0.2

Table 6.5: Coreshift measured with respect to the core position at 43 GHz in 0836+710. Modelfit components approach.

ν [GHz]	x [mas]	ϵ_x [mas]	y[mas]	ϵ_y [mas]	Δr [mas]	$\epsilon_{\Delta r}$ [mas]
22	-0.03	$\pm$ 0.05	-0.05	$\pm$ 0.020	0.06	$\pm$ 0.05
15	-0.24	$\pm$ 0.15	-0.15	$\pm$ 0.11	0.28	$\pm$ 0.19
5	-0.28	$\pm$ 0.18	-0.18	$\pm$ 0.18	0.3	$\pm$ 0.2
1.6	-1.7	$\pm$ 0.9	-2.2	$\pm$ 0.9	2.8	$\pm$ 1.3

The coreshifts obtained with the two methods are similar, with a slight tendency towards higher coreshifts when using the modelfit approach. We can see this by comparing the spectral index maps obtained with each method, and performing a transversal cut on the spectral index. This is shown in Figs. 6.4 and 6.5 for the spectral index maps between 5 GHz and 15 GHz. If we compare the spectral index maps we can see that the 2D cross correlation is a more reliable approach, yielding to a more homogeneous map. Even though the values of the spectral index along the jet are similar in both cases, the modelfit approach shows a gradient in the transversal direction (right panel of Fig. 6.4) which is not seen in the case of the shifting performed using the 2D cross correlation, which has a smoother spectral index (right panel of Fig. 6.5). We ignore the larger discontinuities at the edges as the error on the spectral index in these regions are quite large. Therefore, we will use the 2D cross correlation for all further analysis.

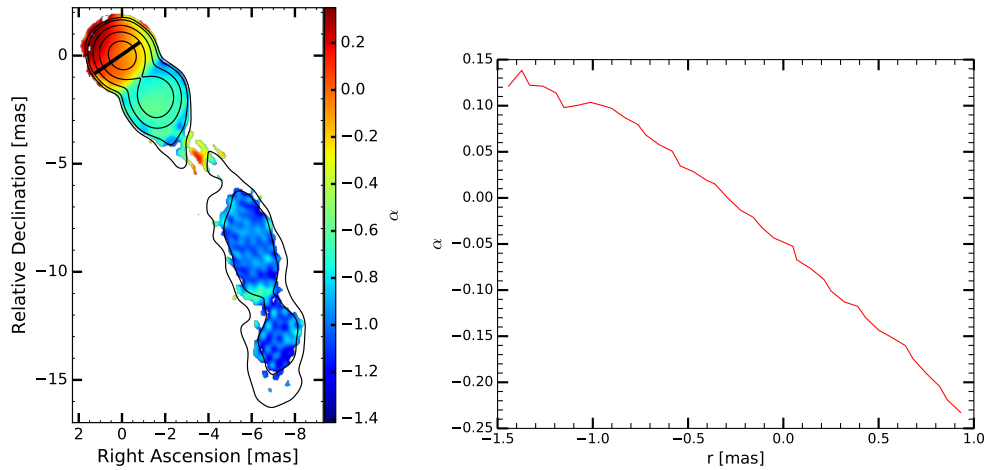

Figure 6.4: **Left Panel:** Spectral index map between 5 GHz and 15 GHz using the ground images of 0836+710 and the modelfit approach. **Right Panel:** Transverse cut of the spectral index in the core region. It shows a gradient.

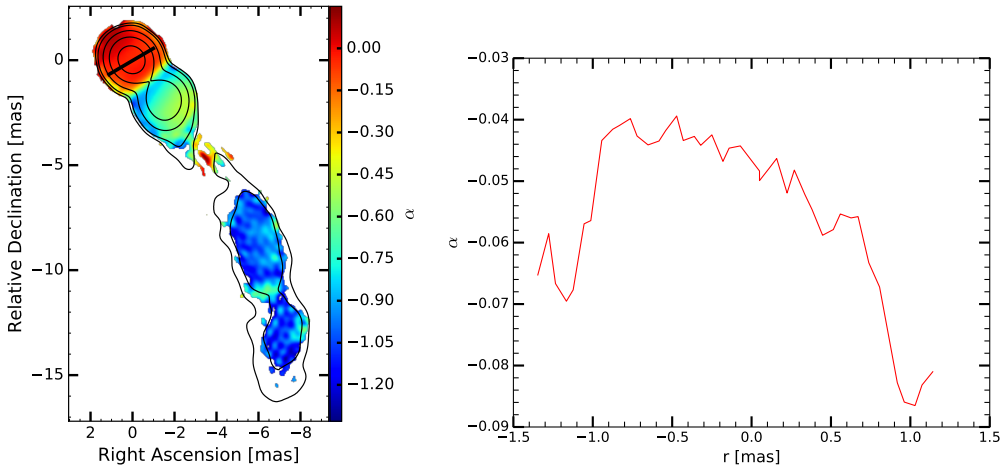

Figure 6.5: **Left Panel:** Spectral index map between 5 GHz and 15 GHz using the ground images of 0836+710 and the 2D cross correlation approach. **Right Panel:** Transverse cut of the spectral index in the core region. It is fairly constant. Notice the different scale with respect to Fig. 6.4.

We also study how the coreshift changes with frequency. We can see its behaviour in Fig. 6.6. The red solid line shows the result of the fit applying Eq. 6.9. The blue dashed line shows the same fit but with a fixed $k_r = 1$.

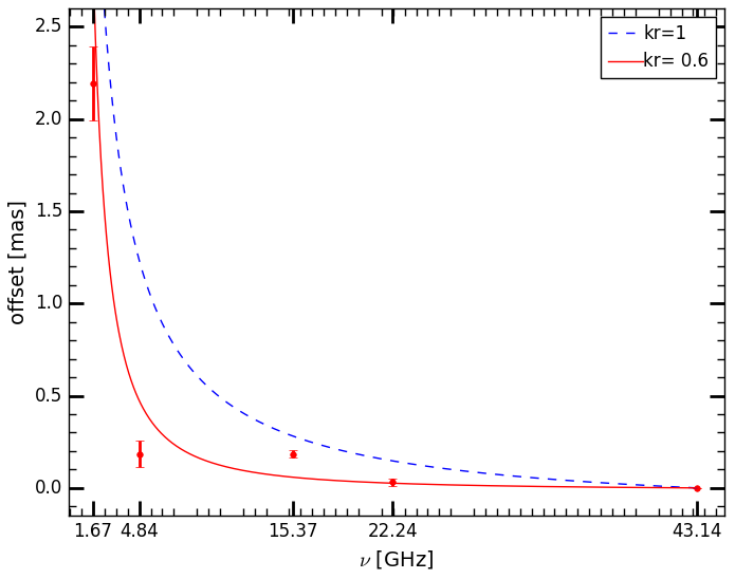

Figure 6.6: Measured coreshifts in 0836+710 as a function of the observing frequency. A plateau seen between 5 GHz and 15 GHz might be an indicative of a recollimation shock.

We see that the coreshift in 0836+710 fitted with the red line does not follow the expected behavior as a function of frequency, and does not show the typical decay $\propto 1/\nu$. In the case of a conical jet in equipartition we expect $k_r = 1$ (blue dashed line) (Lobanov 1998b). We see a plateau between 5 GHz and 15 GHz. One of the possibilities that can explain this kind of behaviour is the existence of recollimation shocks (Fromm et al. 2018) at the distance where we observe the plateau. This has only been observed for high frequencies (between 43 GHz and 86 GHz) and was related to the nature of the VLBI core at millimiter wavelenghts with a recollimation shock (Dodson et al. 2017). Recollimation shocks produce a local flux peak, in the same way as the radio core does. The position of these shocks is frequency independent, therefore a plateau is produced in the coreshift. What we also see in the curve is that this plateau disappears at higher frequencies. This is due to the fact that the upstream emission of the shocks becomes optically thin at those frequencies, which creates a new local flux density maximum further upstream. You can distinguish the presence of recollimation shocks with a kinematic analysis. They are recognized as stationary features. We presented this analysis in section 6.1 for the Boston University monitoring program at 43 GHz. The analysis showed the presence of a stationary feature at a distance of $\sim 0.11 \pm 0.06$ mas, which is consistent with the position of the plateau. This tells us that the plateau in the coreshift is real and related to the presence of a recollimation shock, rather than resulting from an error in the measurement.

6.2.2.b Spectral index maps

We now introduce the spectral index maps between adjacent frequencies, for ground and *RadioAstron* images. In order to better visualize the behavior of the spectral index, we cut the spectral index map along its brightest points. Figures showing the exact location where the spectral index maps are cut can be found in Appendix E. We do not show them here for clarity of the image. Local maxima in these cuts have been reported as hints for the existence of moving and standing shocks at that position (Mimica et al. 2009).

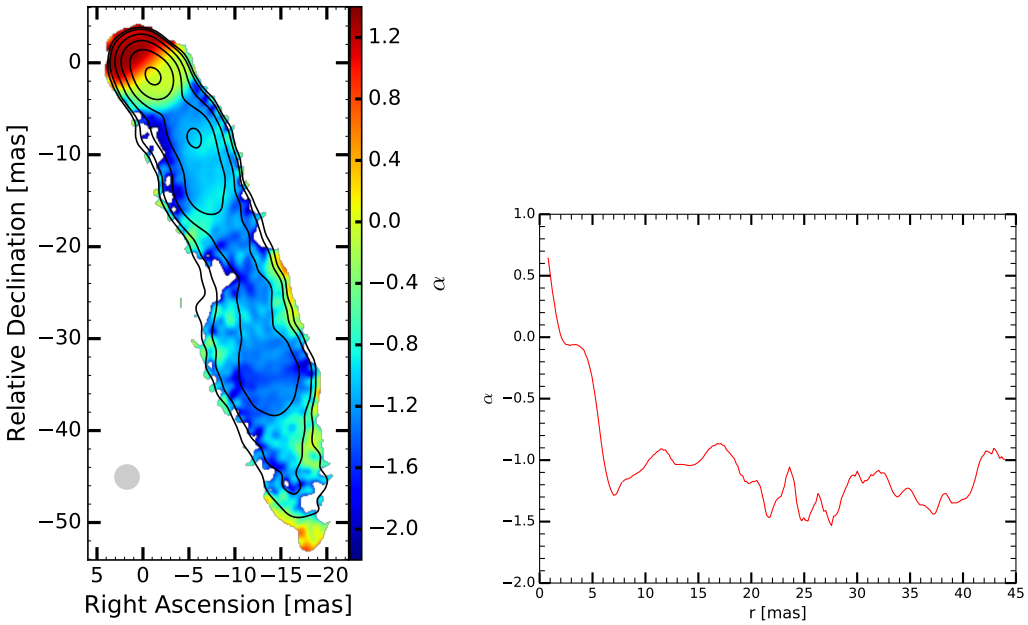

Figure 6.7: **Left Panel:** Spectral index map between 1.6 GHz and 5 GHz using the ground images of 0836+710. **Right Panel:** Cut along the spectral index. We can observe a fast steepening followed by a constant value between 5 mas and 45 mas.

The spectral index map and its cut at 1.6/5 GHz are presented in Fig. 6.7. The core region is optically thick and shows a highly inverted spectrum. Between 2 mas and 3.5 mas the spectral index flattens. At this distance, the existence of standing components has been previously reported (e.g. Krichbaum et al. 1990). This is also confirmed by our kinematics analysis (section 6.1.1). Looking at other peaks in the plot, for instance, the local maxima observed around 10 mas and 15 mas can be related to a moving shock, as indicated by a kinematic analysis performed by the MOJAVE team at 15 GHz (Figure 6.2). We also see that the spectral index stops decreasing at 6 mas and it remains fairly constant beyond that distance. This means that the flux ratio remains unchanged between the two frequencies and hence there are no strong radiation losses. This could be due either to the presence of re-acceleration, or indicate that the synchrotron cooling

time is larger than size of the jet divided by the speed of light, which would lead to electrons radiating at 1.6 GHz and 5 GHz in the same proportion. The latter explanation allows us to obtain a value of the magnetic field (see, e.g., Rybicki & Lightman 1979; Baczko et al. 2016), and can help to distinguish which of the two options is more plausible. To do this, we first need to estimate an upper limit on the synchrotron cooling time, using:

$$t_{\rm sync} \geq \frac{d}{c},$$

where d is the maximum distance at which we see the constant spectral index: $d \sim 40$ mas.

We can then calculate the magnetic field using Eq. 2.7, where we insert the critical frequency assuming plasma with random pitch angle distribution. This leads to the following expression for the synchrotron cooling time:

$$t_{\rm sync} = 3\sqrt{3\pi}\sqrt{\frac{m_e e c}{\nu_c}}\frac{B^{-3/2}}{\sigma_T \beta^2}. \tag{6.10}$$

We can now derive the magnetic field from Eq. 6.10. This equation will give us a lower limit on the magnetic field, since the synchrotron cooling time that we obtain is an upper limit because it has to be larger than the jet size. Then:

$$B \leq \left(\frac{t_{\rm sync}\sigma_T \beta^2}{3\sqrt{3\pi}\sqrt{\frac{m_e e c}{\nu_c}}} \right)^{-2/3}. \tag{6.11}$$

Considering the frequency of 5 GHz, because it gives us the stricter constraint on the jet size, this leads to $B \leq 0.01$ G. From the coreshift analysis, we can make an estimate of the distance of the VLBI core to the black hole. With this estimate, the 40 mas region at weakly variable spectral index corresponds to $\sim 400\,$pc , i.e. $\sim 7.6 \times 10^5 R_g$ from the central engine. If we assume that the magnetic field is mainly toroidal, we can estimate the magnetic field close to the black hole, which results to be $B \sim 1.5 \times 10^4$ G. This magnetic field is of a similar order of magnitude as the one found in Baczko et al. (2016) for the case of NGC 1052. With this, it is also possible to calculate the magnetic power of the jet, using:

$$L_B \leq \frac{1}{4\pi} B_\phi^2 v_j \pi R_j^2, \tag{6.12}$$

where $R_j \sim 20$ pc, is the radius of the jet at half of extent of the region with nearly constant spectral index. The reason to choose that position is that the upper limit of B estimated earlier represents an average value of the magnetic field in the whole region. In Eq. 6.12, v_j is the speed of the jet, and B_ϕ^2 is the

toroidal magnetic field estimated using Eq. 6.11. This leads to a magnetic power of 0.28×10^{46} erg/s.

If the total jet power, L_j, can be estimated using low frequency observations, we can estimate the ambient medium density, ρ_a, using:

$$L_j = L_B \left(7.2 \frac{\rho_a}{1\mathrm{p/cm}^3} + 1 \right). \tag{6.13}$$

Furthermore, it is also worth noting the arc-like structure we can observe in the spectral index map between 10 mas and 20 mas (light blue). This structure correspond to the jet ridgeline. Being the flux higher in this region, it can be considered as the reason why we see a slight increase of the spectral index. This supports that ridgeline traces regions of enhanced pressure in the jet, (see, e.g., Perucho et al. 2012a). These aspects will be discussed in more detail in the Chapter 7.

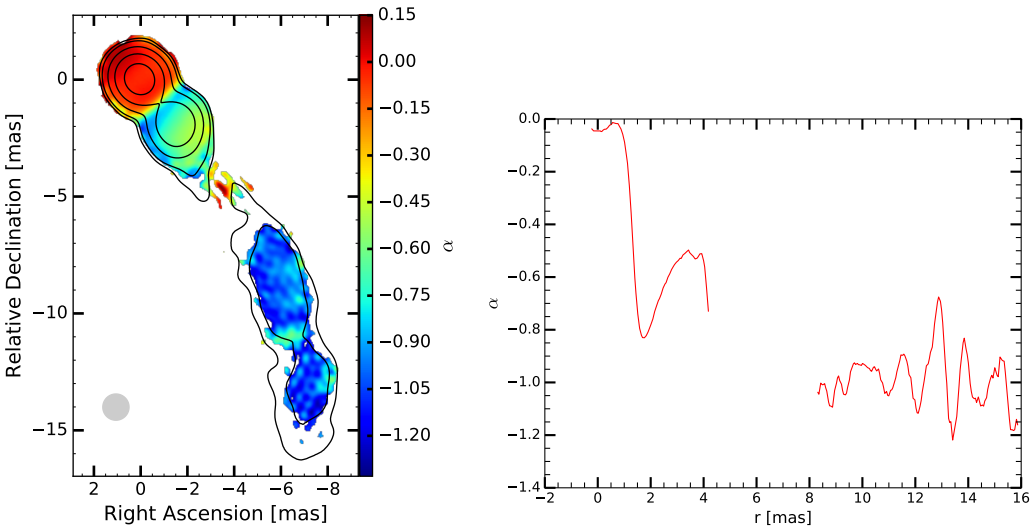

Figure 6.8: **Left Panel:** Spectral index map between 5 GHz and 15 GHz using the ground images of 0836+710. **Right Panel:** Cut along the spectral index. We can observe a flat core after which the spectral index also decreases fast. We also see a peak at 2.5 mas corresponding to a stationary feature.

The 5 GHz - 15 GHz spectral index map (Fig. 6.8) shows the expected flattening at spectral indices in the core region. A second region showing a flattening in the spectral index is observed between 2 mas and 4 mas. The 1.6/5 GHz image already showed this peak, which is probably caused by a standing component since it is the location is where a stationary component was present in the kinematics analysis performed at 43 GHz (Fig. 6.1). After the gap in the spectral index image, between 5 mas and 8 mas, we can see that it also remains constant up to the largest distances at which the jet emission at 15 GHz is detected, as observed in Fig. 6.7.

The spectral index between 15 GHz and 22 GHz (Fig. 6.9) shows an almost flat distribution in the upstream core region of the jet. The spectral index goes through a remarkably decrease and increase at around 1.5 mas. This can indicate an expansion of the jet at this position, possibly taking place before a shock. After this region the spectral index remains relatively flat between 2 mas and 3.5 mas, that can again be related to the standing shocks, as can also be seen in Fig. 6.1. The spectral index between 22 GHz and 43 GHz (Fig. 6.10) does not give us extra information with respect to the previous figures. Two distint components are seen there as well, one at around 2.7 mas and another around 3.1 mas.

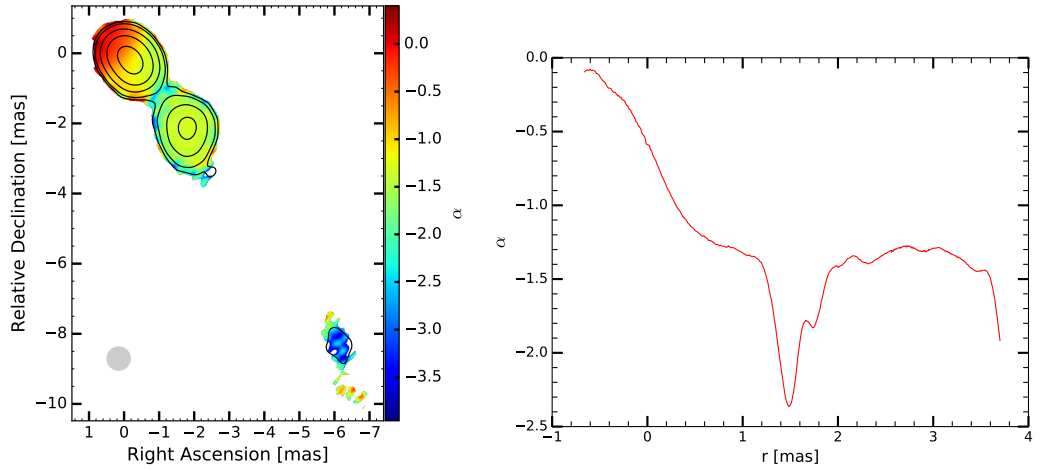

Figure 6.9: **Left Panel:** Spectral index map between 15 GHz and 22 GHz using the ground images of 0836+710. **Right Panel:** Cut along the spectral index. It shows an expansion region at around 1.5 mas.

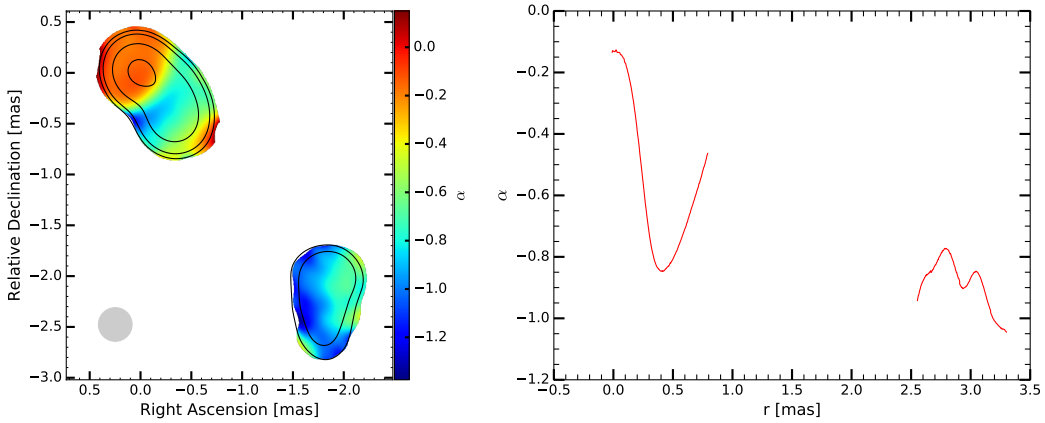

Figure 6.10: **Left Panel:** Spectral index map between 22 GHz and 43 GHz using the ground images of 0836+710. **Right Panel:** Cut along the spectral index. It shows two peaks equivalent with two possible stationary features at distances 2.5 mas and 3 mas.

Since our data set at 1.6 GHz, and 22 GHz include also space-VLBI baselines, it is interesting to compare the spectral index maps obtained with the ground with those obtained using the space VLBI images. This is of particular interest also since the scales observed with the 1.6 GHz *RadioAstron* observations are comparable with the scales observed with 1.6 GHz image with VSOP in 1997 (even though *RadioAstron* image is slightly smaller) and the two images can be directly compared.

The resolution of the *RadioAstron* observations at 1.6 GHz matches the resolution of the ground observations at 5 GHz, and therefore these two maps are ideal for studying the morphology of the spectral index. We plot the resulting spectral index image in Fig. 6.11 and we compare it with the ground array result shown in Fig. 6.12. The structures observed in the two maps are consistent. We can see that the increase of resolution using the space array reveals more substructure, that remained unresolved in the ground map. Some of the flux peaks in the spectral index cut with *RadioAstron* are more pronounced but the locations are consistent. In the *RadioAstron* image, we can see a drop in the spectral index, at around 6 mas. We can interpret this as another jet expansion region. This part coincides with the gap in the spectral index map between 5 GHz and 15 GHz with the ground array, shown in Fig. 6.9. The farthest peak seen, at 16 mas, is consistent with a moving component in the MOJAVE kinematics. The spectral index map between the 1.6 GHz VSOP image and the 5 GHz ground array image is shown in Fig. 6.13. The spectral index values are similar to those of the *RadioAstron* observations.

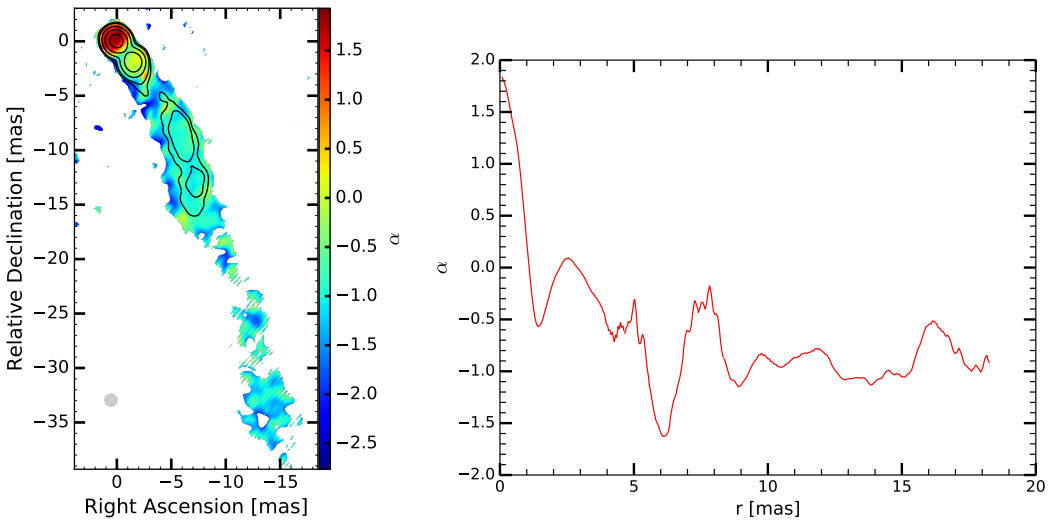

Figure 6.11: **Left Panel:** Spectral index map between the 1.6 GHz *RadioAstron* image and the 5 GHz ground VLBI image of 0836+710. **Right Panel:** Cut along the spectral index. It shows an expansion region at 6 mas consistent with the gap seen in the spectral index between 5 GHz and 15 GHz.

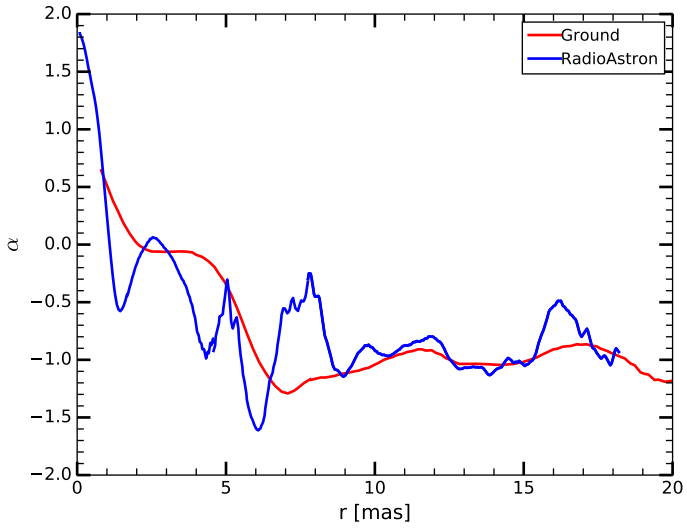

Figure 6.12: Comparison between the cut of the spectral index maps of 0836+710 between 1.6 GHz and 5 GHz using ground images at both frequencies (red) and *RadioAstron* image at 1.6 GHz (blue). Notice the increase of resolution.

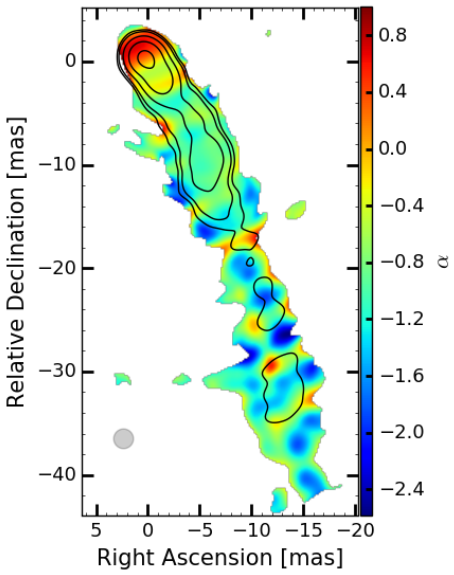

Figure 6.13: Spectral index map between the 1.6 GHz VSOP image and the 5 GHz ground array image of 0836+710.

We also compute the spectral index between the 22 GHz *RadioAstron* image and the 43 GHz ground array image (Fig. 6.14). The resolution is not sufficient to distinguish any possible recollimation shock present at ∼0.10 mas, hinted by the coreshift curve (Fig. 6.6) and present in the kinematics at 43 GHz (Fig. 6.1).

It is possible to distinguish one peak at $\sim$ 0.45 mas. It is consistent with the existence of a travelling component at around 0.5 mas during the observation time (Fig. 6.1). The values of the spectral index in the core region are consistent with those obtained with the ground array images.

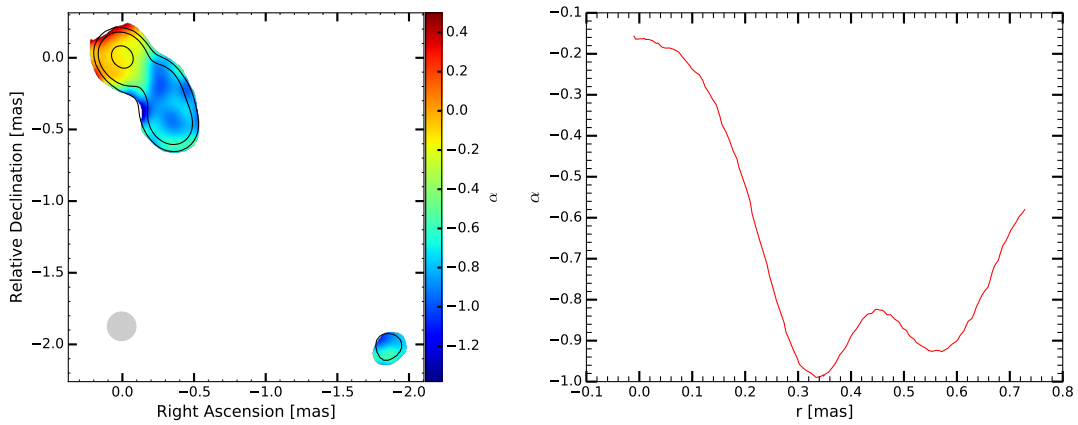

Figure 6.14: **Left Panel:** Spectral index map between the 22 GHz *RadioAstron* image and the 43 GHz ground array image of 0836+710. **Right Panel:** Cut along the spectral index. We see a peak at 0.45 mas.

6.2.2.c Spectral analysis of the 2003 data set

Now, in order to check if the behaviour of the coreshift is repeated in other epochs, we perform the same analysis for an archive multifrequency dataset from 2003. The calibration of this data set was performed by I. Agudo as part of a study of the blazar 0716+714 (Gupta et al. 2012). This data includes 1.6 GHz, 5 GHz, 22 GHz, and 43 GHz. Since it does not include 15 GHz, we use the closest MOJAVE epoch for our the analysis. However, that addition might introduce a bias on the values and estimations of the coreshift due to the time difference. It should be noted that the resolution in the two epochs, 2003 and 2014, is not comparable, since the 2003 data only included the VLBA, and therefore the resolution is better in the 2014 data at 1.6 GHz, 5 GHz and 22 GHz.

We first calculate the coreshift with respect to the core position at 43 GHz with the 2D cross correlation method and compare it with the values obtained for the 2014 observations.

Table 6.6: Coreshift measured with respect to the core position at 43 GHz in 0836+710 for the observations in 2003

ν [GHz]	x [mas]	ϵ_x [mas]	y[mas]	ϵ_y [mas]	Δr [mas]	$\epsilon_{\Delta r}$ [mas]
22	−0.010	± 0.015	−0.000	± 0.015	0.01	± 0.02
15	−0.06	± 0.05	−0.06	± 0.05	0.08	± 0.07
5	−0.16	± 0.1	−0.17	± 0.1	0.23	± 0.14
1.6	−1.19	± 0.2	−1.87	± 0.2	2.2	± 0.3

The values in Table 6.6 show some differences with respect those in Table 6.4. These differences are mostly affecting the coreshift between 15 GHz and 22 GHz and 5 GHz and 15 GHz, and can be caused by the temporal difference, the different resolutions, and the fact that small variations within the error can be induced by calibration (as seen with the *RadioAstron* images, where there is a shift between ground and space images at the same frequency).

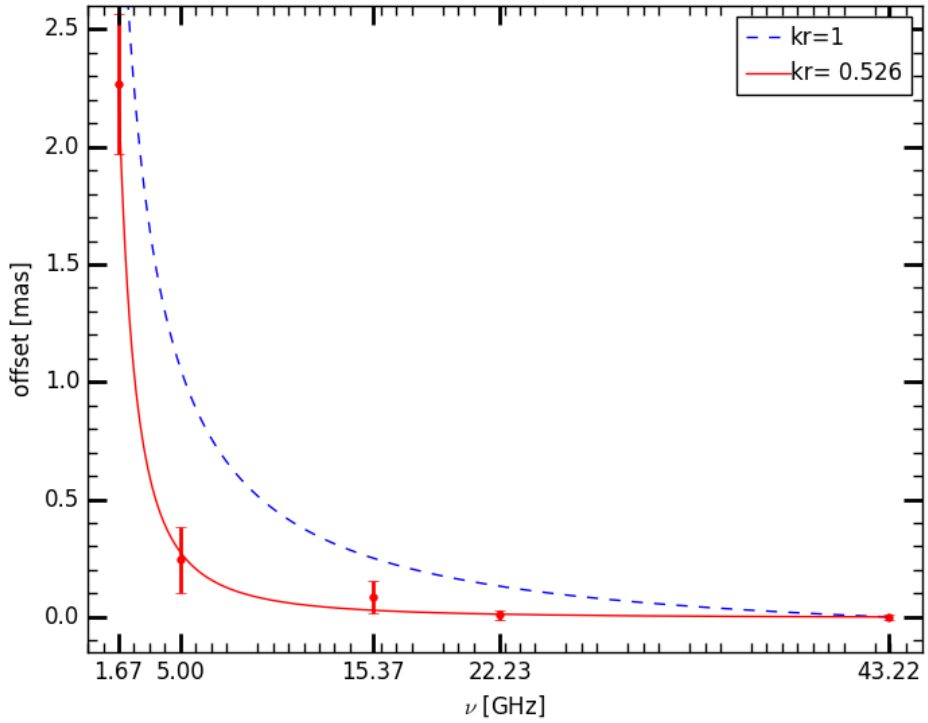

Figure 6.15: Coreshift values of 0836+710 in function of the observing frequency. The exponential decrease breaks between 5 GHz and 15 GHz even though the coreshift between both frequencies is not exactly zero.

Looking at the coreshift curve (Fig. 6.15), we can see that the plateau between 5 GHz and 15 GHz, observed in our observations, is not so evident. However, we

see that increase of the coreshift value of the 5 GHz data point in comparisson with the value at 15 GHz does not follow the same trend, causing a decrease in the measured k_r, as was observed in 2014 (see Fig. 6.16). In the case of 2014, the deviation from the trend of that data point is more evident. If we now exclude the 5 GHz point, in the case of the observations of 2014, we obtain $k_r \sim 1$, in line with expectations for a conical jet in equipartition. For 2003, this effect is not as clear, but we can see that the point is around two times lower than what we would expect if it would follow the fit parameters (red line in the left panel in Fig. 6.16). Since the data from the 2003 observations show slightly lower coreshift values, the fitted k_r is around 0.7. However, if we try to compare the value of the data point at 5 GHz with the value it would take in the case $k_r \sim 1$ (dashed blue line), we can clearly see the difference with respect to the trend. Looking first at the coreshift value corresponding to 15 GHz and 22 GHz, we see that they are agreement with the general trend within the errors. Therefore, it is clear that there is something happening between the core positions of 5 GHz and 15 GHz. However, if the recollimation shock would be located at a distance of around 0.1 mas from the core of 43 GHz a plateau between 5 GHz and 15 GHz would not be expected, since the coreshift between 15 GHz and 22 GHz would be smaller and therefore farther away from the location of this standing feature. Furthermore, recollimation shocks can wiggle Fromm et al. (2016), for example, due to moving components passing by, and this can cause small differences in the location from epoch to epoch. To determine this, a more exhaustive analysis is needed and it is out of the scope of this thesis.

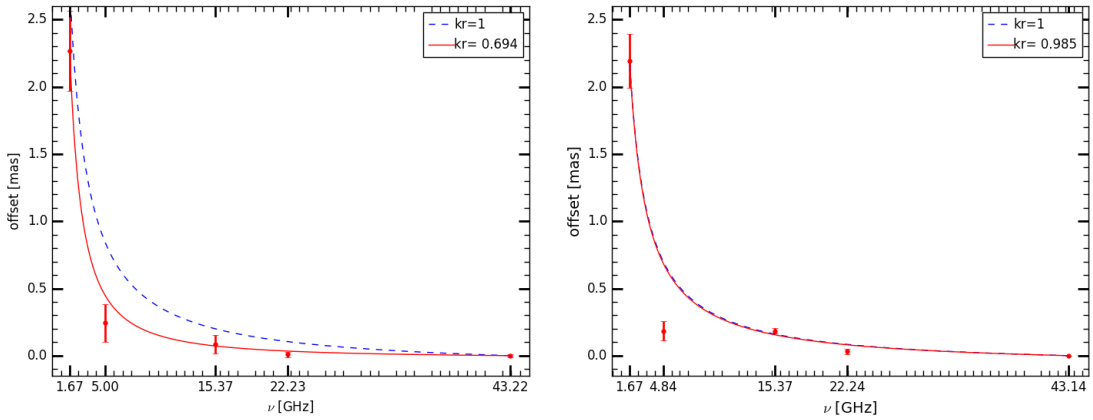

Figure 6.16: Coreshift values of 0836+710 in function of the observing frequency excluding the value at 5 GHz. This lead to a more consistent tendency between the different values. **Left panel:** 2003 observations. **Right panel:** Our observations.

We can describe now the spectral index maps and compare them with the results of the 2014 observations. We plot them in Fig. 6.17 through 6.10. The

structure shown by the spectral index images in 2003 is quite consistent with the one obtained for the 2014 epoch. The only spectral index map providing additional information is the one between 15 GHz and 22 GHz (Fig. 6.19). Here, we see a peak at around 1.3 mas that shows an enhanced value of the spectral index. A moving shock is at the same position at the same epoch (see Fig. 6.2), and it is probably the cause of this spectral index peak as components can have a high influence on the opacity of the region.

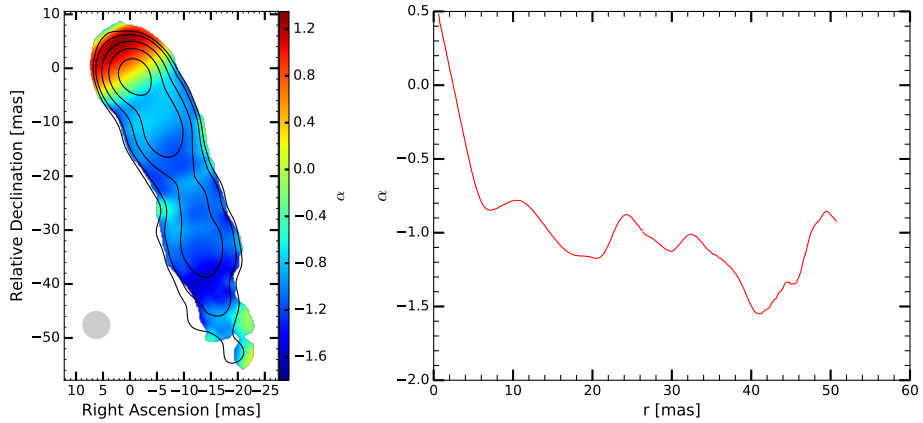

Figure 6.17: **Left Panel:** Spectral index map between the 1.6 GHz and the 5 GHz ground VLBI images of 0836+710 from the 2003 observations. **Right Panel:** Cut along the spectral index. It shows an inverted core and a fairly constant region between 10 mas and 40 mas.

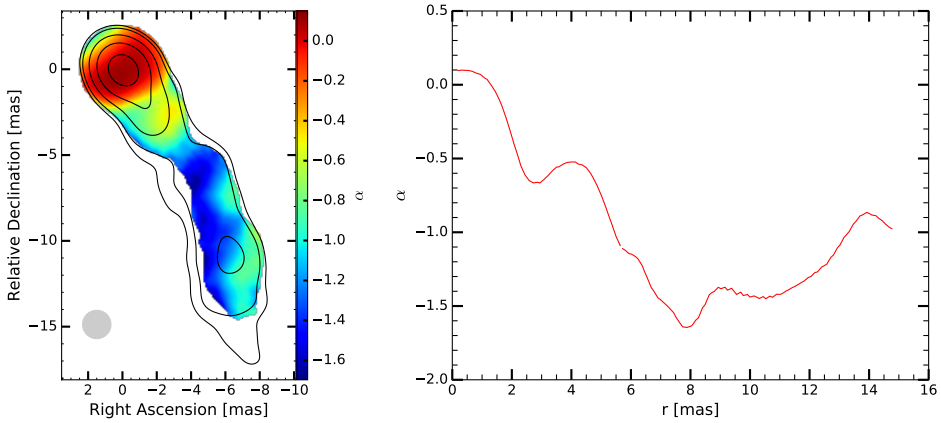

Figure 6.18: **Left Panel:** Spectral index map between the 5 GHz and the 15 GHz ground VLBI images of 0836+710 from the 2003 observations. **Right Panel:** Cut along the spectral index. It shows an flat core followed by a decay up to $\sim$ 8 mas.

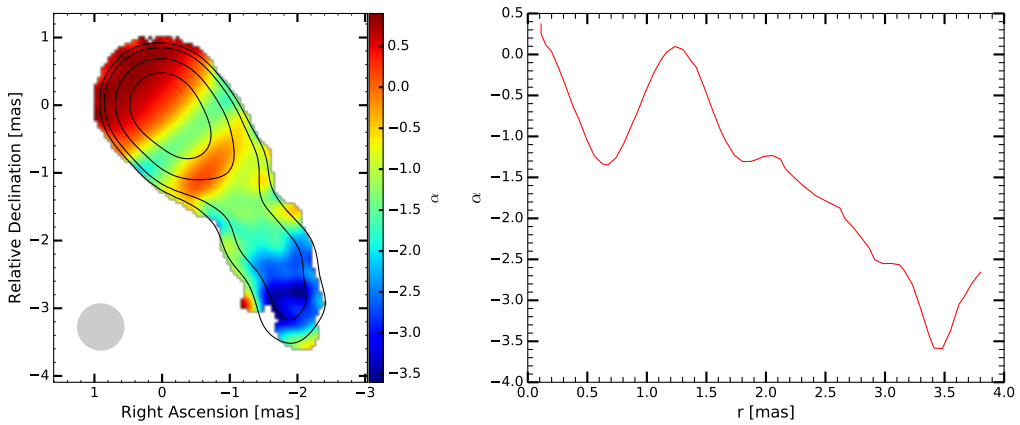

Figure 6.19: **Left Panel:** Spectral index map between the 15 GHz and the 22 GHz ground VLBI images of 0836+710 from the 2003 observations. **Right Panel:** Cut along the spectral index. It shows the presence of a component with a flat spectral index between 1 mas and 2 mas.

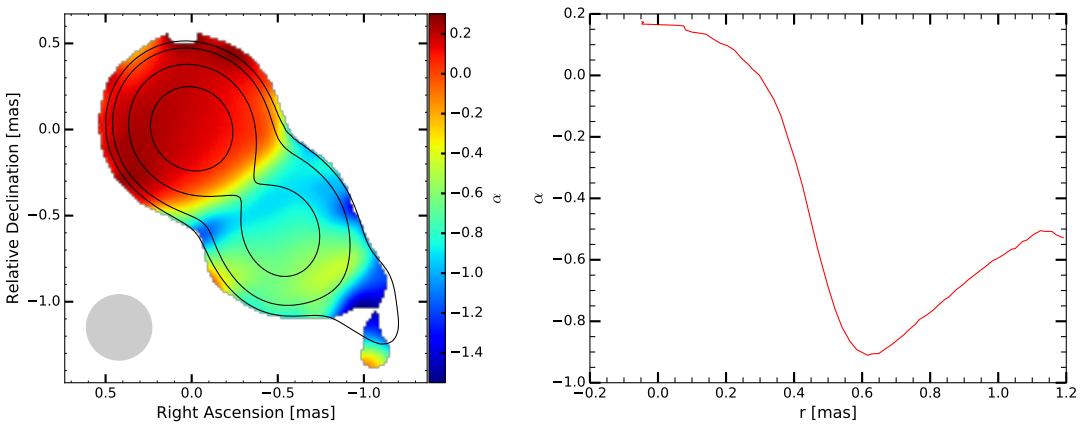

Figure 6.20: **Left Panel:** Spectral index map between the 22 GHz and the 43 GHz ground VLBI images of 0836+710 from the 2003 observations. **Right Panel:** Cut along the spectral index. It shows an flat core.

6.2.2.d Turnover frequency and turnover flux density

The ground array data includes five frequencies, which are sufficient to perform a study of the synchrotron spectrum. The approach is explained in section 6.2.1. We used the beam at 5 GHz instead of the beam at 1.6 GHz, because the latter would only be sufficient to study the core region. No information was lost using the beam at 5 GHz at these scales. Figure 6.21 shows an example of the synchrotron spectrum in one of the pixels corresponding to the core, showing a turn between 5 GHz and 15 GHz. The analysis was restricted to the central region, where the observed spectrum is most reliable. The turnover flux density in the core (see left

panel in Fig. 6.22) ranges from 1.2 Jy to 3 Jy, while the turnover frequency (right panel in Fig. 6.22) falls between 7 GHz and 9.6 GHz. No turnover was observed outside of the core region, showing an optically thin spectrum.

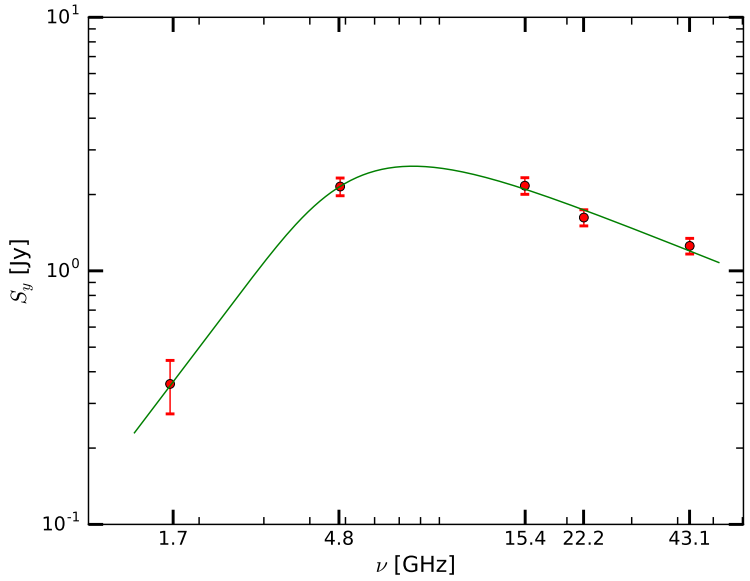

Figure 6.21: Core spectrum for 0836+710. It shows a turnover frequency at 7 GHz and a turnover flux density of 2 Jy.

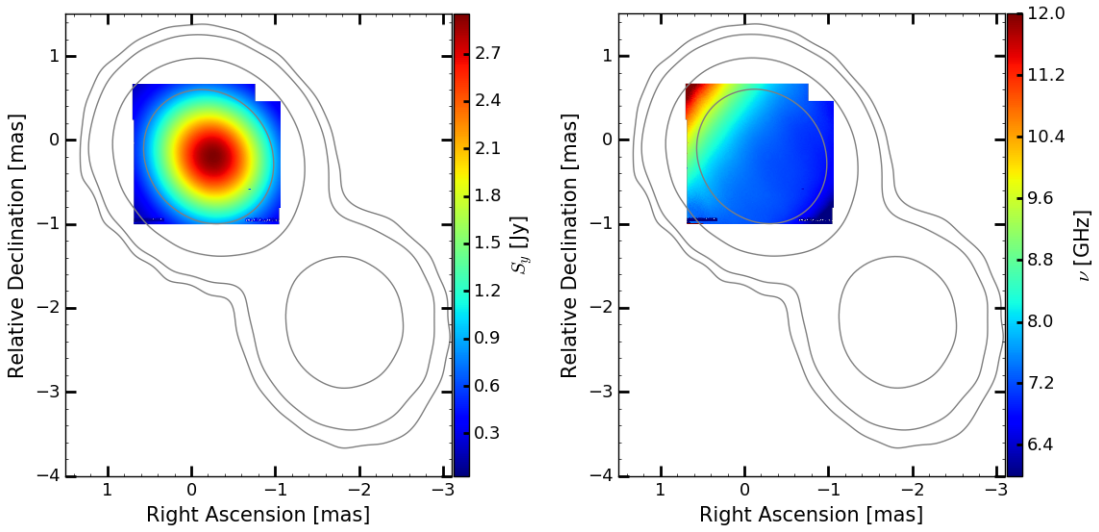

Figure 6.22: **Left panel:** Turnover flux density. **Right panel:** Turnover frequency. For both images the contours correspond to the ground array image of 0836+710 at 15 GHz.

6.2.2.e Magnetic field estimate

Coreshift approach

We can now calculate the magnetic field. First we use the coreshift method. If we consider $k_r = 1$, we can use Eq. 2.48 to calculate the magnetic field at 1 pc from the core. However, since the fitted k_r is not equal to one, we also use Eq. 2.46 to calculate the magnetic field at 1 pc. We use Eq. 2.47 to compute its value in the core region. Furthermore, we calculate an estimate of the particle density at a distance of 1 pc using Eq. 2.49.

The first step is to calculate the coreshift measurement using Eq. 2.39. In principle, this quantity should be approximately constant between all the frequencies, but in practice it can change if k_r changes along the jet, which could happen due to changes in the absorption coefficient (Lobanov 1998b). The coreshift measurement used for our calculations is an average value using frequency pairs that are not affected by the flattening of the curve (Fig. 6.6). In the case of $k_r = 1$, we obtain $\Omega_{r\nu} = 24$ and in the case where $k_r = 0.6$, we get $\Omega_{r\nu} = 57$.

The resulting values of the magnetic field in the core region for the different frequencies are listed in Table 6.7.

The values of the magnetic field in the core are similar using the two approaches ($k_r = 1$ and $k_r = 0.6$). It should be noted, however, that the distance to the central engine is different in the two cases. In the case of 1.6 GHz and 5 GHz the magnetic field is an order lower when $k_r = 0.6$. However, the corresponding distance of the core to the central engine is also larger. One of the possible reasons for these differences on distance where the core is located, and therefore in the magnetic field strength, are all the assumptions that have been made to obtain the main formula for the coreshift, which were discussed in Chapter 2. The main assumptions that could have affected our result are a constant viewing angle, a small and constant half opening angle and a constant Lorentz factor. Furthermore, the formulae assume a uniform magnetic field distribution and approximate equipartition between particle energy and magnetic field energy. Additionally, assuming $k_r = 1$ implies that the jet should be conical and the magnetic field only has a toroidal component.

Since archival data from 2003 are also available, we repeat the same analysis for this epoch as well. The values are listed in Table 6.8. The magnetic field in this epoch is slightly larger than the one obtained from our 2014 observations. However, due to the fast decrease of the magnetic field with distance, the value obtained at larger distances (for example for the core at 1.6 GHz) is similar between the two epochs.

The particle density at 1 pc has a similar order of magnitude in the two cases. For its calculation we have used a minimum particle Lorentz factor of 10, as relativistic jets in blazars cannot have a value for $\gamma_{\rm min}$ lower than this (Mimica

et al. 2009). We obtain a particle density of $N_1 \sim 190$ cm^{-3} for the 2003 epoch, while in our 2014 observations we find $N_1 \sim 80$ cm^{-3}, which is two times lower. If we take $k_r = 1$, the order of magnitude the particle density is higher, reaching 10^3 cm^{-3}. It should be noted that this calculation is strongly dependent on the assumption on the value of $\gamma_{\rm min}$, which is not known a priori.

Table 6.7: Magnetic field using the coreshift approach for the 2014 observations of 0836+710.

ν [GHz]	k_r	$\Omega_{r\nu}$ [pcGHz]	B_1 [G]	B_c [G]	r_c [pc]	N_1 [cm^{-3}]	$\gamma_{\rm min}$
43	1.0	24 ± 8	1.7	0.33	5	1400	10
22	1.0	24 ± 8	1.7	0.17	10	1400	10
15	1.0	24 ± 8	1.7	0.12	15	1400	10
5	1.0	24 ± 8	1.7	0.04	46	1400	10
1.6	1.0	24 ± 8	1.7	0.013	135	1400	10
43	0.6	57 ± 7	0.4	0.16	2.4	76	10
22	0.6	57 ± 7	0.4	0.05	7.4	76	10
15	0.6	57 ± 7	0.4	0.03	14	76	10
5	0.6	57 ± 7	0.4	0.0043	94	76	10
1.6	0.6	57 ± 7	0.4	0.00072	550	76	10

Table 6.8: Magnetic field using the coreshift approach for the 2003 observations of 0836+710.

ν [GHz]	k_r	$\Omega_{r\nu}$ [pcGHz]	B_1 [G]	B_c [G]	r_c [pc]	N_1 [cm^{-3}]	$\gamma_{\rm min}$
43	1.0	34 ± 8	2.2	1.5	1.5	2400	10
22	1.0	34 ± 8	2.2	0.77	2.9	2400	10
15	1.0	34 ± 8	2.2	0.5	4.2	2400	10
5	1.0	34 ± 8	2.2	0.17	13	2400	10
1.6	1.0	34 ± 8	2.2	0.06	40	2400	10
43	0.7	50 ± 6	0.6	0.03	20	190	10
22	0.7	50 ± 6	0.6	0.017	37	190	10
15	0.7	50 ± 6	0.6	0.011	55	190	10
5	0.7	50 ± 6	0.6	0.0037	170	190	10
1.6	0.7	50 ± 6	0.6	0.0012	500	190	10

Synchrotron spectrum approach

Another method to obtain the magnetic field of the source is to use the synchrotron spectrum using the turnover values shown in Fig. 6.22. In order to calculate it, we use Eq. 2.35. The result is shown in Fig. 6.23. Since the convolution is done using the 5 GHz beam, the magnetic field strenght in the core region corresponds to the value in the core obtained with the coreshift approach at this frequency. The magnetic field is of the order of 0.03 G, which is comparable with the core value at 5 GHz when $k_r = 1$. This could suggest that the value of k_r should be close to unity, rather than to the value obtained from fitting the coreshift curve. Further support to this conclusion is that when the data point at 5 GHz is not

considered in the fit, since it is presumably affected by the recollimation shock (see Fig. 6.16), the fitted value of k_r results to be quite close to unity.

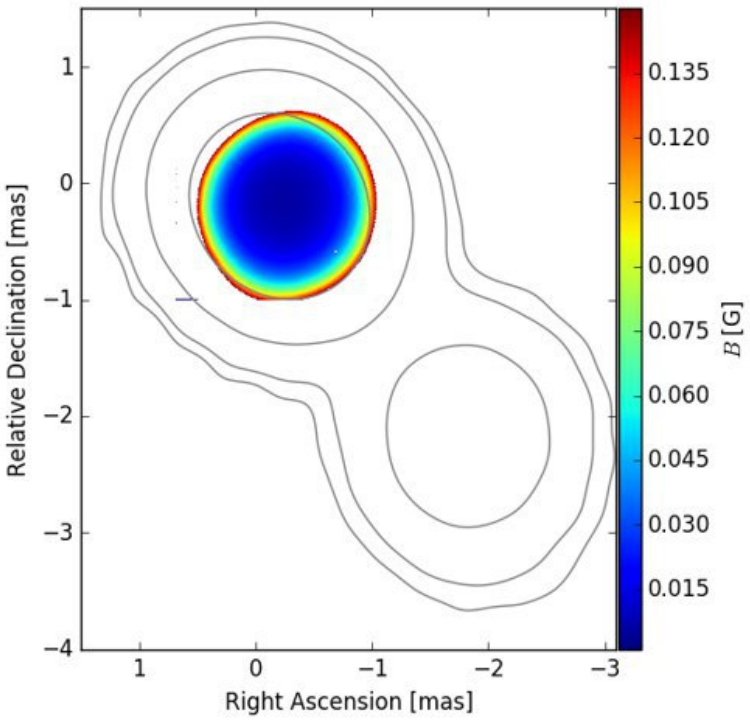

Figure 6.23: Magnetic field obtained using the synchrotron spectrum for 0836+710. The value in the core is around 0.03 G.

6.2.3 3C 345

6.2.3.a Image alignment

Our data set for 3C 345 includes four frequencies: 5 GHz, 15 GHz, 22 GHz, and 43 GHz. We align the images using the 2D cross correlation, taking 43 GHz as reference frequency. We choose this methode since our analysis with 0836+710 (section 6.2.2.a) showed that the 2D cross correlation leads to better results. Table 6.9 shows the results of the coreshift for all the frequencies with respect to the core position at 43 GHz.

Table 6.9: Coreshift measured with respect to the core position at 43 GHz for 3C 345. 2D cross correlation approach.

ν [GHz]	x [mas]	ϵ_x [mas]	y[mas]	ϵ_y [mas]	Δr [mas]	$\epsilon_{\Delta r}$ [mas]
22	−0.018	± 0.010	−0.012	± 0.010	0.022	± 0.014
15	−0.026	± 0.05	−0.013	± 0.05	0.03	± 0.07
5	−0.48	± 0.07	−0.08	± 0.07	0.49	± 0.10

The coreshift as a function of frequency is shown in Fig. 6.24. We fit the coreshift curve in order to estimate the value of k_r, obtaining $k_r = 0.8$. However, the errors on the spectral points are quite large, and therefore we chose not to use this method to estimate the magnetic field. Schinzel (2011) calculated the coreshift of 3C 345 for different epochs, and found that it varies with time. This can be explained by travelling components, which can affect the apparent core position as they pass through it. The values we obtained for the coreshift for our observations are in agreement with Schinzel (2011).

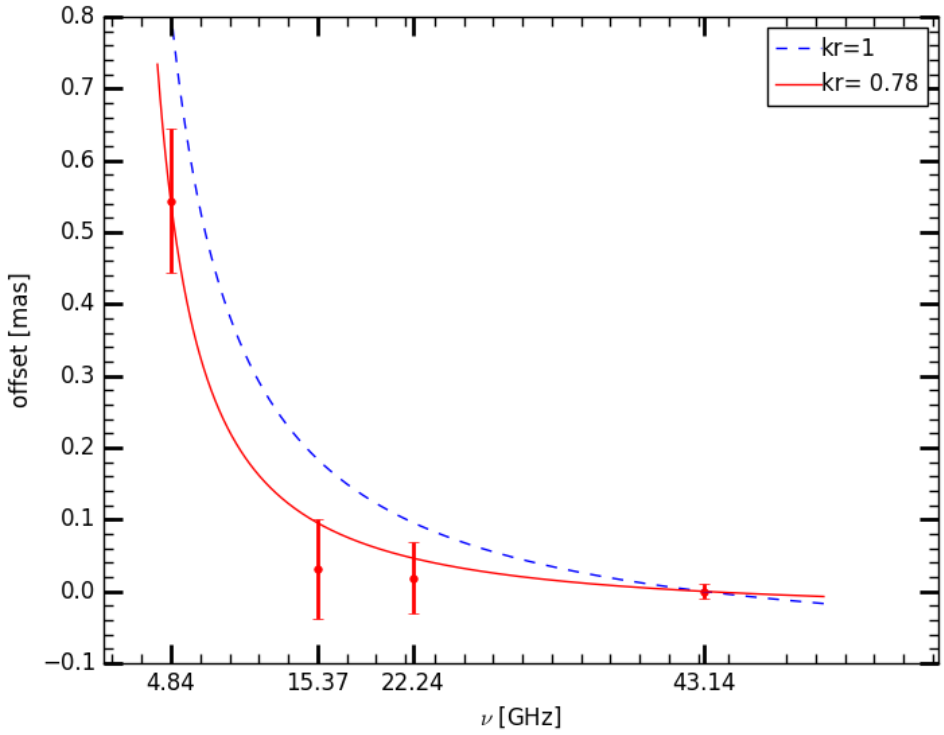

Figure 6.24: Coreshift values of 3C 345 as a function of the observing frequency.

6.2.3.b Spectral index maps

In the same way as with 0836+710, we calculate the spectral index map between the different adjacent frequencies and cut them along its brightest points. Appendix E shows the exact location where this cuts are made. We do not show them here for a better clarity in the spectral index image. The analysis also hints at the presence of a counter jet, as the spectral index for the 5/15GHz spectral index map steepens upstream the core. The *RadioAstron* image also showed indications for this (Fig. 5.15).

In the spectral index map obtained using 5 GHz and 15 GHz (Fig. 6.25) we see an inverted core ($\alpha \sim 0.6$). The spectral index decreases until 1 mas. After these distances, we see two peaks, one between 1 mas and 3 mas and another between 5 mas and 8 mas. They are consistent with the position of moving components in the kinematics analysis performed by the MOJAVE team (Lister et al. 2013).

The spectral index between 15 GHz and 22 GHz (Fig. 6.26) shows again a decrease downstream the core, along the jet direction. Beyond the gap, we see that the region between 4 mas and 8 mas shows three different peaks instead of the one seen between 5 GHz and 15 GHz, due to the increased resolution. The peaks are also consistent with the position of moving components in the MOJAVE analysis.

In the case of the spectral index between 22 GHz and 43 GHz (Fig. 6.27), we see two peaks at distances of 0.5 mas and 1 mas. After this last peak, we see a dip of the spectral index that indicates the presence of an expansion region.

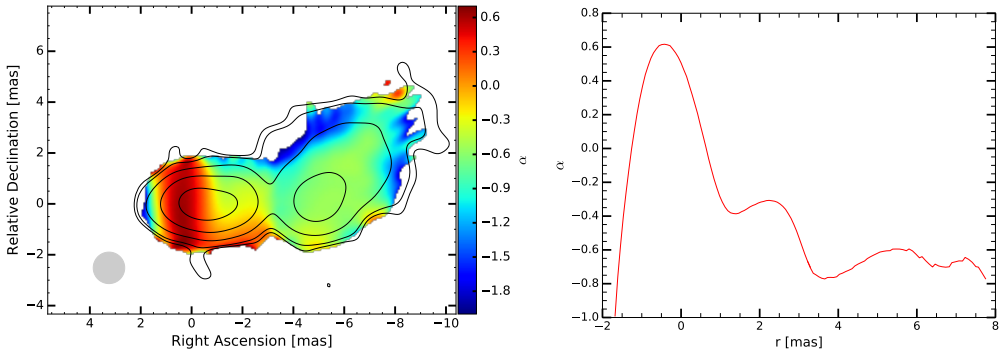

Figure 6.25: **Left Panel:** Spectral index map between 5 GHz and 15 GHz using the ground images for 3C 345. **Right Panel:** Cut along the spectral index. We can observe an inverted core followed by a fast steepening. Two components are situated at around 2.5 mas and 6 mas.

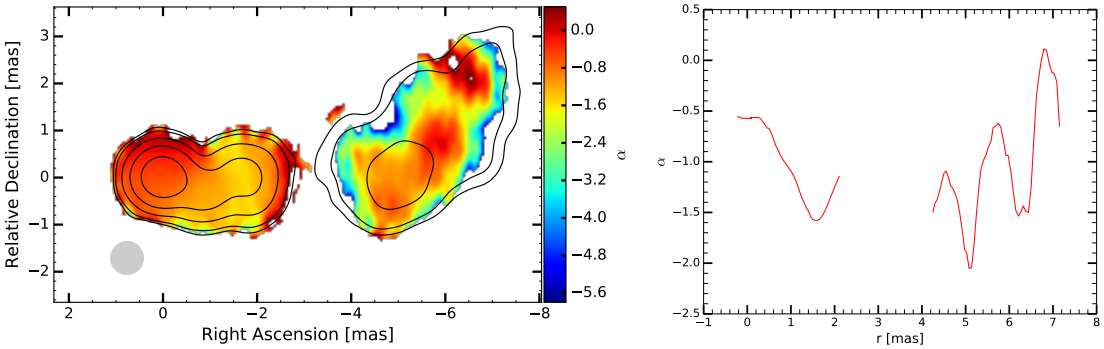

Figure 6.26: **Left Panel:** Spectral index map between 15 GHz and 22 GHz using the ground images for 3C 345. **Right Panel:** Cut along the spectral index. The same component that was seen in the previous image is seen at around 6 mas.

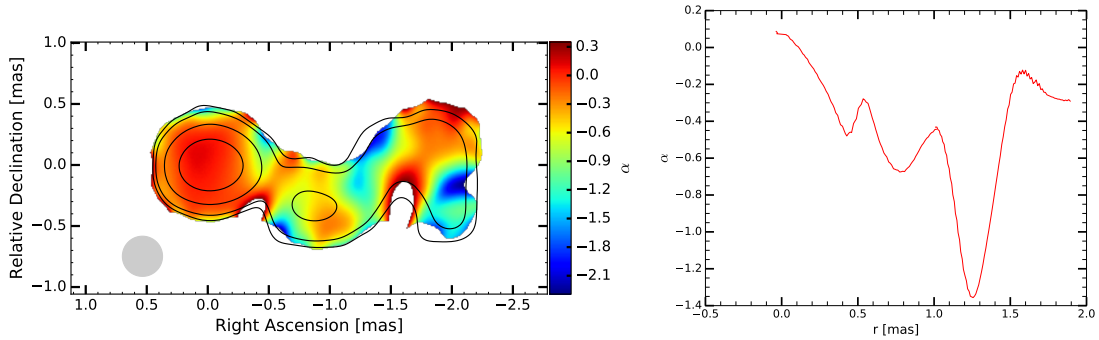

Figure 6.27: **Left Panel:** Spectral index map between 22 GHz and 43 GHz using the ground images for 3C 345. **Right Panel:** Cut along the spectral index. We observe an expansion region at around 1.3 mas.

Since our data set at 5 GHz includes space-VLBI baselines, we can compare the spectral index maps obtained with the ground with those obtained using the space VLBI images. The resolution of the *RadioAstron* observations at 5 GHz matches the resolution of the ground observations at 15 GHz. We plot the spectral index image between these two images in Fig. 6.28 and we compare it with the ground array result in Fig. 6.29. The structures observed in the two maps are consistent. The core has a harder spectral index in the map obtained using the 5 GHz space-VLBI image. We can also notice that the increase of resolution using the space array reveals additional substructure, showing two components in the region between 4 mas and 7 mas. The peaks in the spectral index profile obtained using the ground image are broader because of the lower resolution. However, the position of the peaks is consistent between the two maps.

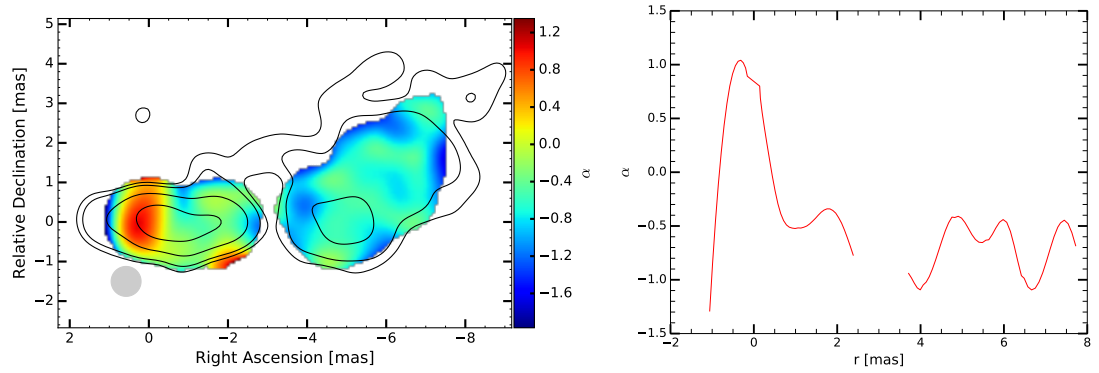

Figure 6.28: **Left Panel:** Spectral index map between the 5 GHz *RadioAstron* image and the 25 GHz ground VLBI image of 3C 345. **Right Panel:** Cut along the spectral index. It shows an inverted core and three components seen as regions with a flatter spectral index value.

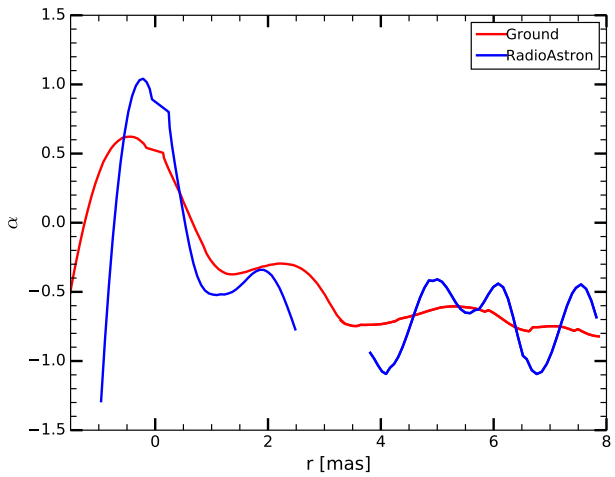

Figure 6.29: Comparison between the cut of the spectral index maps of 3C 345 between 5 GHz and 15 GHz using ground images at both frequencies (red) and *RadioAstron* image at 5 GHz (blue). Notice the increase of resolution, which allows us to distinguish two shocked regions instead of one between 4 mas and 6 mas.

6.2.3.c Turnover frequency and turnover flux density

Our data set includes a sufficient number of frequencies to perform a turnover analysis for 3C 345, following section 6.2.1. We convolve all the maps using the beam of the 5 GHz image. We only see a turnover in the core region and within the first milliarcsecond from the core. At the core, the turnover frequency is ~ 10 GHz, with a corresponding flux density of 5 Jy. Figure 6.30 shows an example of the spectrum in the selected region.

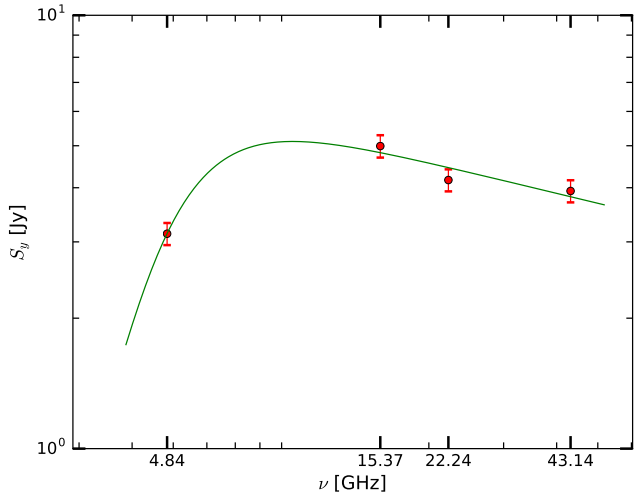

Figure 6.30: Synchrotron spectrum for 3C 345. It shows a turnover frequency at 8 GHz and a turnover flux density of 4 Jy.

The turnover flux density map of the central region (top panel in Fig. 6.31) ranges from 2.4 Jy to 5.4 Jy, while the turnover frequency (bottom panel in Fig. 6.31) ranges between 8 GHz and 11 GHz.

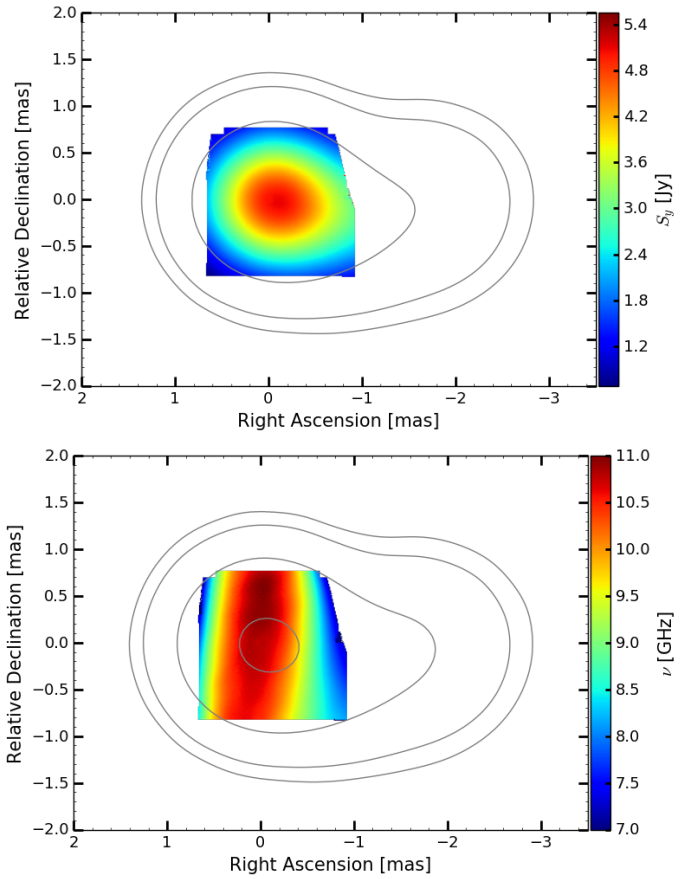

Figure 6.31: **Top panel:** Turnover flux density. **Bottom panel:** Turnover frequency. For both images the contours correspond to the ground array image of 3C345 at 15 GHz.

6.2.3.d Magnetic field estimate

Synchrotron spectrum approach

We do not perform a calculation of the magnetic field using the coreshift method for 3C 345 due to the large errors in the fit while estimating k_r. The estimated k_r led to high variations on the coreshift measurement and therefore we decide to exclude this method from our anaylsis. We calculated the magnetic field using the turnover frequency. The result is shown in Fig. 6.32. This leads to a magnetic field of ~ 0.07 G in the core of 5 GHz. For the 5 GHz core, Schinzel (2011) reported a value of 0.04 G, consistent with our result.

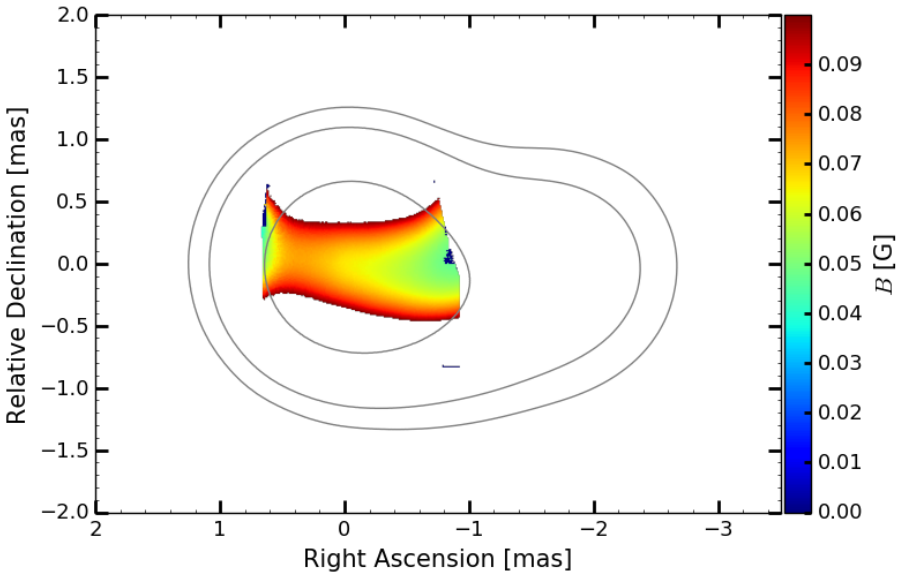

Figure 6.32: Magnetic field in 3C 345. The value corresponding to the core is 0.07 G.

6.2.4 1642+690

6.2.4.a Image alignment

Our data set for 1642+690 includes three frequencies: 1.6 GHz, 5 GHz and 22 GHz. As in the previous cases, we choose the 2D cross correlation to align the image pairs. We present the resulting coreshift values, referenced to the core position at 22 GHz, in Table 6.10. We see that the coreshift value between the reference frequency and 1.6 GHz and 5 GHz is quite similar, and is relatively high. The reason why the coreshift between the two frequencies and the reference frequency is similar might be due to the presence of a recollimation shock (Fromm et al. 2018), as argued for the case of of 0836+710 (Section 6.2.2.a). If we now look at the kinematics analysis performed for 1642+690 by the MOJAVE team (Lister et al. 2016, see Fig. 6.33), we see two static components around the region where this flattening in the curve is observed. This is another hint that the flattening observed in the coreshift curve in 1642+690 can be related to the presence of stationary features.

Table 6.10: Coreshift measured with respect to the core position at 22 GHz for 1642+690. 2D cross correlation approach.

ν [GHz]	x [mas]	ϵ_x [mas]	y[mas]	ϵ_y [mas]	Δr [mas]	$\epsilon_{\Delta r}$ [mas]
5	−0.32	± 0.04	−0.65	± 0.04	0.72	± 0.06
1.6	−0.28	± 0.15	−0.63	± 0.15	0.69	± 0.2

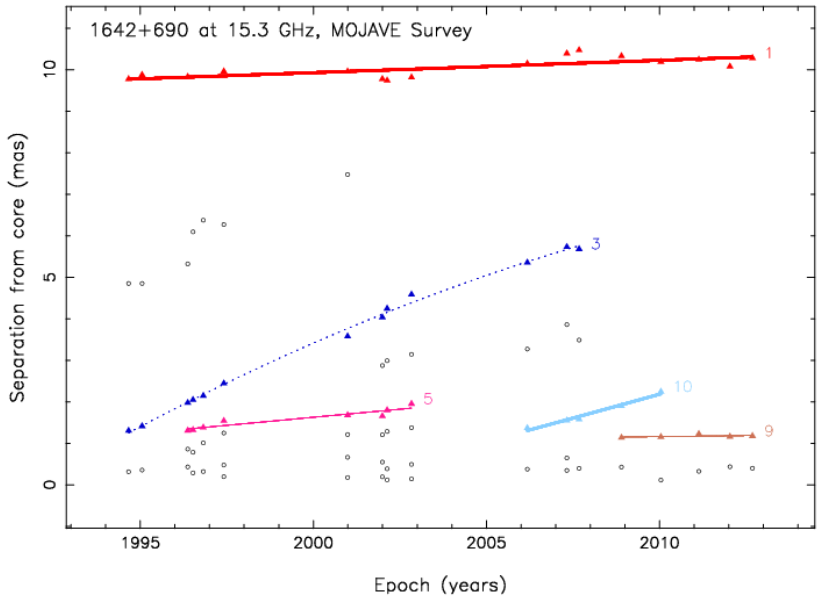

Figure 6.33: Evolution of the component distance with respect to the core with time for the MOJAVE data set for 1642+690 (Lister et al. 2016).

6.2.4.b Spectral index maps

After the frequency alignment, we introduce the spectral index maps and cut along its brightest points.

We start describing the results obtained for the frequency pair 1.6 GHz and 5 GHz (Fig. 6.34). In this case we see a flat core, with the spectral index decreasing slowly up to distances of 2 mas. Then, the spectral index value decreases faster up to 6 mas. After these distances, it flattens slightly and remains quite constant until 14 mas where it decreases again. If we look again at the kinematics performed by MOJAVE (see Fig. 6.33) and extrapolate its components 3 and 9 until the date of our observation, we see that two components are at the distances where we observe an increase in the spectral index. The dip in spectral index up to distances ~ 7 mas can be understood as an expansion region upstream a standing or moving shock, in this case, most probably a moving component.

The spectral index map between 5 GHz and 22 GHz (Fig. 6.35) also shows a flat core with an initial slow decrease followed by a fast steepening. Further downstream we observe a small increase at a distance of 2 mas. This agrees with the distances up to which the plateau in the spectral index map between 1.6 GHz and 5 GHz is observed

We also obtain the spectral index map between 1.6 GHz *RadioAstron* image and the 5 GHz ground array map (Figure 6.36). It is worth noting the peak in the

spectral index downstream the jet, with its highest point at a position between 0.7 mas and 0.8 mas. This position is consistent with the coreshift value obtained for both frequencies pairs and hints the presence of a recollimation shock since it is located at the same distance where the plateau is present.

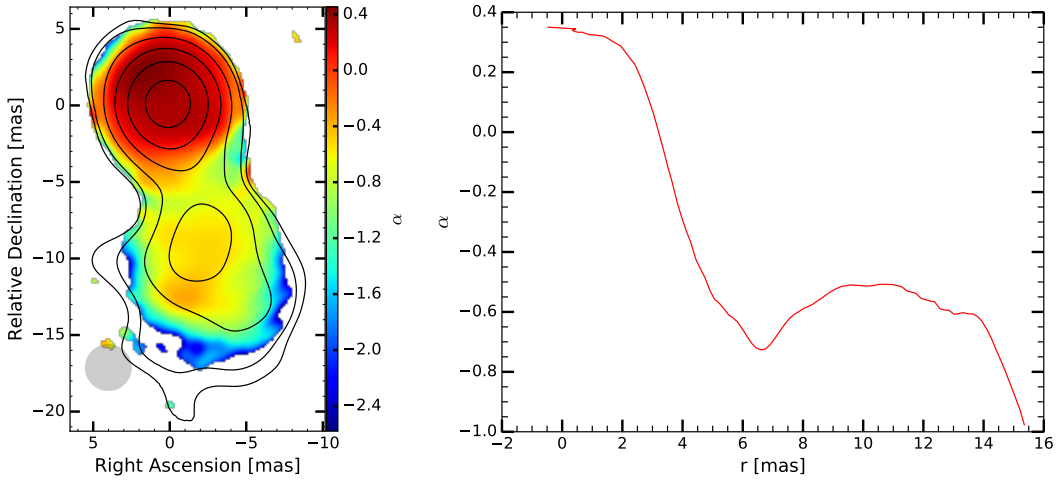

Figure 6.34: **Left Panel:** Spectral index map between 1.6 GHz and 5 GHz using the ground images for 1642+690. **Right Panel:** Cut along the spectral index. We can observe a flat core followed by a steepening. An increase in the spectral index at distances of 8 mas and 14 mas is consistent with the position of two moving components.

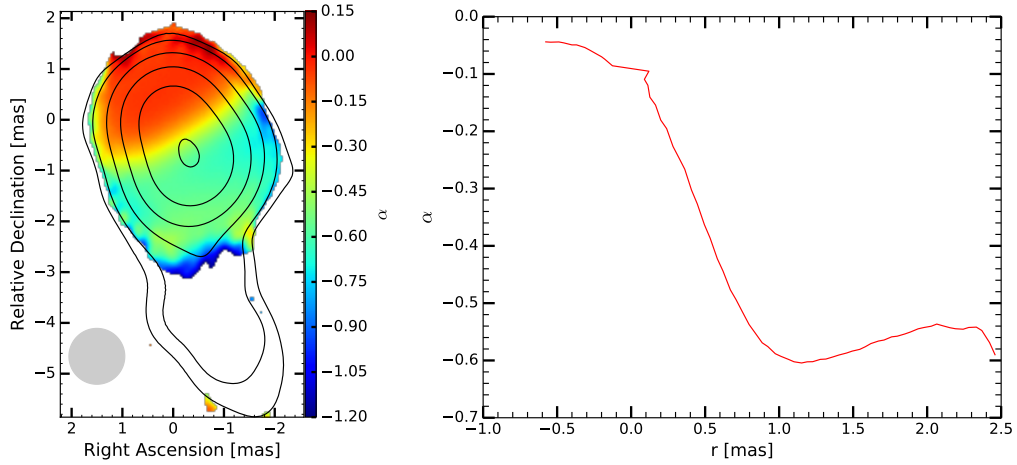

Figure 6.35: **Left Panel:** Spectral index map between 5 GHz and 22 GHz using the ground images for 1642+690. **Right Panel:** Cut along the spectral index. We can observe a flat core followed by a decrease of the quantity. There is a bump between 1.5 mas and 2.5 mas.

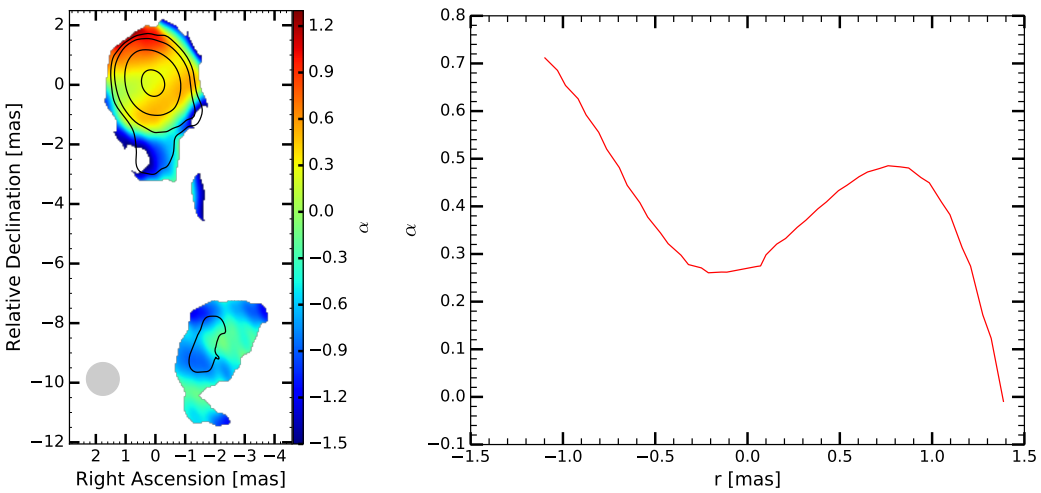

Figure 6.36: **Left Panel:** Spectral index map between 1.6 GHz space-VLBI image and 5 GHz using the ground images for 1642+690. **Right Panel:** Cut along the spectral index. We can observe a peak with its center around 0.7 mas.

6.2.4.c Turnover frequency and turnover flux density

We perform a turnover analysis for 1642+690 as well. Although our data set includes only three frequencies, it is possible to observe the turnover. We used the beam at 1.6 GHz as common beam for the analysis. Figure 6.37 shows an example of the synchrotron spectrum in one of the pixels corresponding to the core region and another further down in the jet. We can see that the turnover is observed in the core at frequencies larger than 5 GHz while further down in the jet it appears at frequencies lower than 5 GHz. We plot the turnover frequency in the right panel of Fig. 6.38. Its value in the core is around 7.2 GHz, whereas further down in the jet it ranges between 2.4 GHz and 4.2 GHz. An increase of the frequency is observed at the southern edge of the jet, which also corresponds to a region where the spectral index value increases (see Fig. 6.35). The structure observed with *RadioAstron* at 5 GHz (Fig. 5.21), showing a component downstream the jet brighter than the core, is in agreement with the turnover flux density image, as seen in the left panel of Fig. 6.38, showing the turnover flux density map. It can be seen that the peak in flux density does not correspond to the core position, but is found further downstream. The projected distance of this brighter component is consistent with the position of the possible recollimation shock indicated by the

coreshift values. No turnover is observed beyond the region shown in the map.

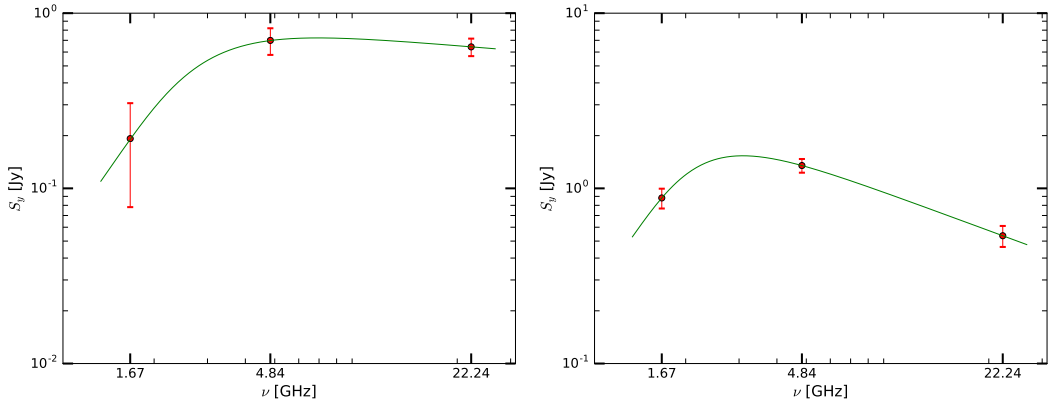

Figure 6.37: **Left panel:** Synchrotron spectrum in the core region of 1642+690. It shows a flat spectral index. **Right panel:** Synchrotron spectrum in the jet of 1642+690. It shows an steep spectral index value.

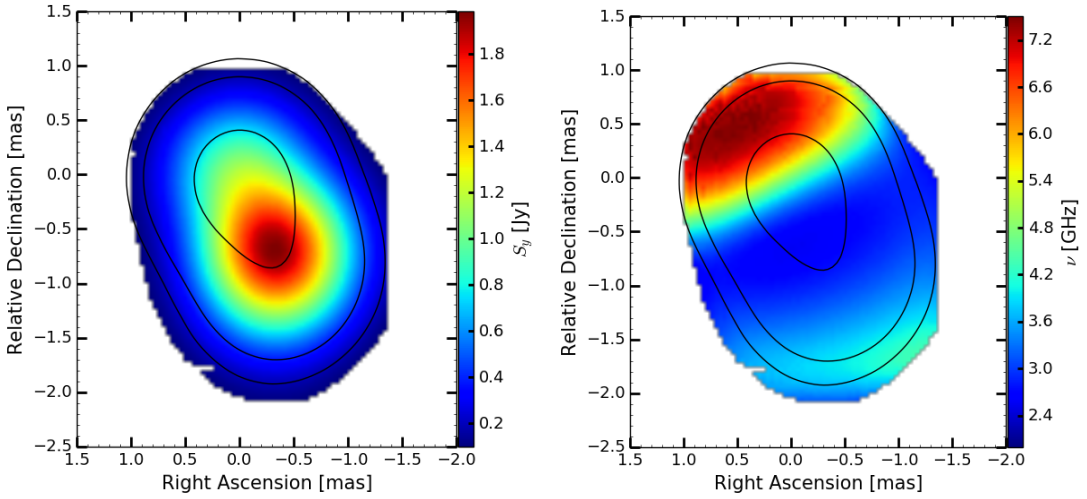

Figure 6.38: **Left panel:** Turnover flux density. **Right panel:** Turnover frequency. For both images the contours correspond to the ground array image of 1642+690 at 22 GHz.

We show the spectral index distribution obtained with the spectral fit in Fig. 6.39. We see that the spectral index distribution is in agreement with the one showed in Fig. 6.35.

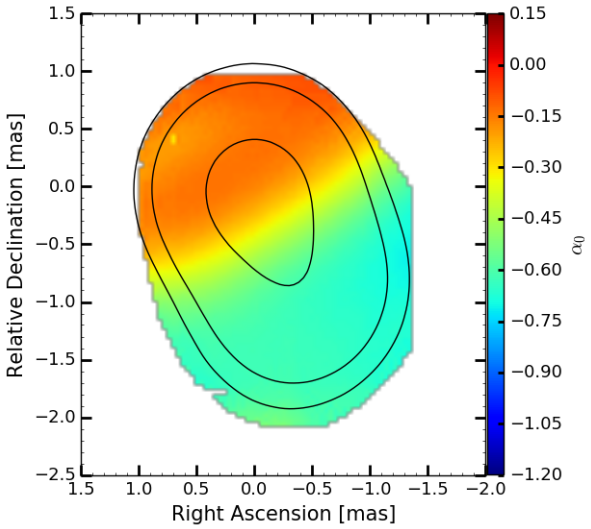

Figure 6.39: Spectral index of 1642+690 obtained after the fitting of the synchrotron spectrum. It is equivalent to Fig. 6.35.

6.2.4.d Magnetic field estimate

In the case of 1642+690 we calculate the magnetic field using the coreshift method and the turnover method.

Coreshift approach

Since we only have two frequency pairs, we use $k_r = 1$ to perform an estimation of the magnetic field in the core region using the coreshift approach. The resulting coreshift measurement is $\Omega_{r,\nu} = 35 \pm 5$. This leads to a value of the magnetic field at 1 pc from the core of 62 G. With this value, we obtain a magnetic field in the core region at the three frequencies of $B_{\mathrm{c},1.6} \sim 0.4$ G, $B_{\mathrm{c},5} \sim 1.3$ G, and $B_{\mathrm{c},22} \sim 5.5$ G, respectively.

Synchrotron spectrum approach

We use the values of the synchrotron spectrum to calculate the magnetic field as we did for the previous two sources. In this case it was also possible to estimate the magnetic field for regions other than the core, so we report values corresponding to two different features: the core at 1.6 GHz, and the recollimation shock. We only present the result in these regions since they are the regions with smaller errors in the fit. The value corresponding to the core is B_c 5 G and in the recollimation shock $B_{\mathrm{RCS}} \sim 0.2$ G.

6.2.5 3C 273

Given the difficulties encountered in the observations of 3C 273, it was only possible to use the 5 GHz image for further analysis. We selected the 15 GHz MOJAVE epoch closer to our observations.

6.2.5.a Image alignment

As in the previous cases, we calculate the shift between the two images using the 2D cross correlation. The resulting coreshift value between 5 GHz and 15 GHz is -0.50 ± 0.10 mas in R.A. and $-0.63 \pm$ mas in Dec.

6.2.5.b Spectral index maps

The spectral index map (Fig. 6.40) shows an inverted core with the spectral index value decreasing slowly until 8 mas. There, it shows a small peak followed by a fast steepening that might indicate an expansion region at 10 mas. At larger distances, we see two other peaks at 12 mas and 19 mas.

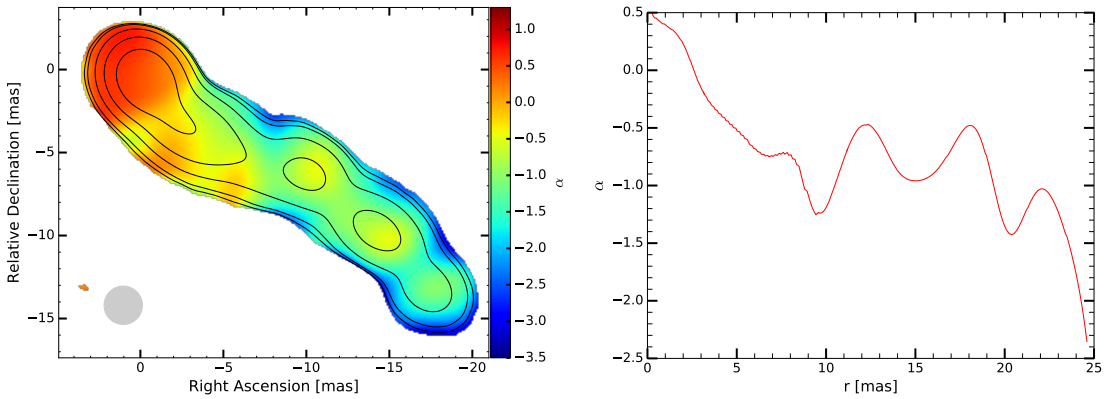

Figure 6.40: **Left Panel:** Spectral index map between 5 GHz (our observations, end of April 2014) and 15 GHz (MOJAVE, end of May 2014) using the ground images for 3C 273. **Right Panel:** Cut along the spectral index. We can observe an inverted core. It also shows three peaks at 12 mas, 19 mas and 23 mas.

6.3 Brightness temperature

In this section we calculate the brightness temperature for the core region for the different sources. We calculate the brightness temperature using Eq. 2.25, correcting for the redshift. To calculate the upper limit for the magnetic field, which can be compared with the previous estimates, we solve Eq. 2.26 and consider the proper corrections :

$$B < \frac{2\pi}{9}\frac{m_e^3 c^5}{k^2 e}\frac{\nu}{T_b}\frac{\Gamma\delta}{1+z}. \tag{6.14}$$

We also calculate the equipartition brightness temperature for each of these components in order to evaluate whether the core is dominated by particles or by the magnetic field. We follow the approach in Singal (2009):

$$T_{\rm B,eq} = t(\alpha)10^{11}\left[\left(\frac{s}{\rm pc}\right)\left(\frac{\nu_m}{\rm GHz}\right)^{1.5+\alpha}\right]^{1/8}, \tag{6.15}$$

where s is the linear size of the emitting region, that we assume as 1.8× FWHM the core size (Marscher 1983), $t(\alpha)$ is a parameter which depends on the spectral index, α, and ν_m is the turnover frequency.

The ratio of kinetic energy density (u_k) to magnetic energy density (u_B) is given by (Readhead 1994):

$$\frac{u_k}{u_B} = \left(\frac{T_{\rm B,eq}}{T_{\rm B}}\right)^{-17/2}. \tag{6.16}$$

6.3.1 Ground array images

We derive the aforementioned quantities for the core of the ground array images. The results are listed in Table 6.11

Table 6.11: Core brightness temperature for *RadioAstron* images.

source	ν	$T_{b_{\rm core}} \times 10^{11}$ [K]	$T_{b_{\rm eq}} \times 10^{11}$ [K]	$B_{\rm max}$ [G]
0836+710	1.6	30.85	0.96	0.006
0836+710	5	51.20	0.82	0.007
0836+710	15	24.22	0.71	0.09
0836+710	22	0.85	0.74	110.89
0836+710	43	0.60	0.56	435.00
3C 345	5	16.7	0.82	0.18
3C 345	15	20.0	0.73	0.39
3C 345	22	6.87	0.75	4.8
3C 345	43	4.10	0.69	18.16
1642+690	1.6	91.0	0.80	0.0006
1642+690	5	48.0	0.68	0.009
1642+690	22	1.5	0.71	41.00
3C 273	5	1.9	-	-

The brightness temperature in the core is higher than its equipartition value for all sources and frequencies, indicating that in the core region, the jet is dominated by particle energy. The upper limits for the magnetic field are in agreement for frequencies larger or equal to 22 GHz. In the case of 0836+710, the upper limits

obtained at 1.6 GHz, 5 GHz, and 15 GHz are below the actual value obtained with the coreshift approach and turnover frequency. This is the case for 1642+690 as well, however, in this case the upper limit is much lower and not included within the errors of any other estimate. Furthermore, 1642+690 is the source with higher brightness temperature, which would imply that its jet is more particle dominated. However, at least for the case of 1.6 GHz, the modelfit was not able to clearly resolve the brighter recollimation shock downstream the jet, which could have led to higher brightness temperatures in the core region with respect to its true value.

6.3.2 RadioAstron images

We derive the aforementioned quantities for the core of the ground array images. The results are in the Table 6.12.

Table 6.12: Core brightness temperature for *RadioAstron* images.

source	ν	$T_{b_{\rm core}} \times 10^{11}$ [K]	$T_{b_{\rm eq}} \times 10^{11}$ [K]	$B_{\rm max}$ [G]
0836+710	1.6	20.9	1.11	0.0134
0836+710	22	88.5	0.81	0.010
1642+690	1.6	35.6	1	0.0056
1642+690	5	15.6	0.8	0.085
3C 273	5	4.0	-	-
3C 273	22	1.9	-	-

The brightness temperature in the core is higher than its equipartition value for all cases. Therefore, the core region of all the sources at these frequencies with *RadioAstron* is particle dominated. The brightness temperatures for 1642+690 are lower than those obtained with the ground, in contrast with the recent findings based on *RadioAstron* observations (Kovalev 2014). The reason for this discrepancy could be that in the *RadioAstron* image, the bright recollimation shock downstream the jet at 1.6 GHz is clearly resolved, whereas in the ground array image it is not. This would lead to a higher brightness temperature with *RadioAstron* than the one corresponding to the core itself in the ground array images. For the case of 5 GHz, this difference between ground and space baselines estimates is included within the errors.

For the space-VLBI observations of 0836+710, we have also calculated the minimum brightness temperature using the visibility data (Eq. 2.30). At 1.6 GHz, it is measured at a baseline of 0.64 Gλ, leading to a brightness temperature of $T_{\rm B,min} = 5 \times 10^{13}$ K. For the image at 22 GHz, the brightness temperature is calculated at a baseline of 11.2 Gλ, resulting on a brightness temperature of $T_{\rm B,min} = 1.2 \times 10^{13}$ K. The error is 20% of the measurement. The minimum brightness temperature is slightly higher than that obtained with the modelfit,

probably due to residual structure in the source, which could not be resolved using model-fitting.

It is also worth noting that in all cases, for ground and space VLBI observations, the VLBI core is not in equipartition but particle dominated. Since in the estimations obtained with the coreshift approach we have assumed that the jet was in equipartition, the deviation from this state could affect the values obtained by this method. The only method that does not uses this assumption is described in Lobanov (1998b). However, in order to calculated it we need to know the particle density at 1 pc beforehand, which is usually not the case.

Chapter 7

Internal jet structure

This Chapter is partially reproduced in Vega-García, Perucho and Lobanov submitted to A&A, Vega-García et al. in prep.

This chapter describes the internal structure of the jets in 0836+710 and 3C 273, as revealed by the ridgeline. First, we define the jet ridgeline and describe the method used to derive it. Then we introduce the work performed for 0836+710. This was complemented with a stability analysis, solving the dispersion relation for the case of helical modes and assuming different jet parameters, which yields to an estimate of jet physical parameters, such as the jet classical Mach number and density ratio with respect to the ambient medium. Finally, in 3C 273 the ridgeline analysis is performed with the primary objective to study jet rotation and the influence of moving jet components on the flow.

7.1 Ridgeline and internal structure of the jet

We study the internal structure of jets using transverse cuts made perpendicular to the jet main direction of propagation. We fit the resulting profiles by one gaussian component, and the position of its peak traces the so-called ridgeline. We use the parameters of the fitted component (position, peak flux density and width of the gaussian) for further investigation. The ridgeline gives information about the position of maximum flux density at each radial distance from the core. In some cases, however, one single gaussian might not be enough to fit the observed structure, so more than one gaussian components are used, providing additional information about the jet structure.

To perform the ridgeline analysis, I developed a code in `Python` to produce the transverse profiles and fit them with one to three gaussians, based on user input. In this case, the code does not have a graphical interface and is used from command line. The code implements the following algorithm:

- First, we need to determine the number of cuts and the distance between them. These are functions of the beam and the cell size of the map. The smaller the beam, and therefore the cell size, the smaller will be the step between the slices. This leads to a larger number of cuts. We also have to define a slice width, which is then given as input to the `AIPS` task `slice`. This task calculates the brightness profiles between the start and end point of the cuts calculated. The resulting profiles are exported and analyzed in `Python`.

- As `AIPS` defines each point in the slice as an offset with respect to the center position of the cut, we need to express these offsets with respect to the center of the map. The result of this transformation will be the RA and DEC coordinates in the map. The `AIPS` output gives us two offsets: an offset for the RA-axis, and another for the DEC-axis. The brightness profiles are completely identical in both directions. Hence, we do a linear regression fit to obtain the parameters of the gaussian: the peak flux density, $S_{\rm p}$, the center position of the gaussian, r, and the fitted size or full width half maximum (FWHM) of the gaussian. The FWHM measured from the profile is a result of the convolution of the intrinsic size of the gaussian, $d_{\rm dec}$, with the restoring beam of the image. We first perform a fit to obtain the gaussian parameters in the RA-axis. As the profiles are identical in the two directions, we use the RA position, $x_{\rm obs}$, and calculate the position of the DEC, $y_{\rm obs} = mx_{\rm obs} + b$, where the slope m and the coordinate in the origin b are calculated independently for each slice. If more than one gaussian is fitted, we perform the same analysis that we just described for the case of one gaussian profile including the extra gaussians.

- The fitting process is iterative, using the results of the fit to a given slice as initial guesses for the next slice. We also applied specific constraints to the gaussian parameters to avoid nonphysical parameters. These constraints are: $S_p > 0$, $b < x < e$, where b and e are the beginning and the end position of the slice, and FWHM$< 2w_{\rm slice}$, where $w_{\rm slice}$ is the width of the slice. Furthermore, we require continuity conditions to the different fit parameters, because the separation between the adjacent slices is quite small, and therefore the change between the parameters for each pair of slices should not be large. Moreover, the jet is modeled as a plasma, where continuity conditions must be fulfilled. The conditions are: the value of the amplitude in the next fit has to differ by not more than 30% from the value of the previous slice. The value of the FWHM has to differ by not more than 20% from the value of the last cut. Finally, the value of the center position cannot vary more than a fourth of the beam.

- The fitting algorithm was based in minimizing χ^2 using the Minuit package[1].

The uncertainties on the fitted parameters have been calculated using the approach based on the analysis of SNR of the fit (Fomalont 1999; Schinzel et al. 2012):

1. We first have to determine the intrinsic (deconvolved) estimated size of the gaussian. This process includes two steps:

   i. The calculation of the limiting size of the gaussian, $d_{\rm lim}$, with (Lobanov 2005) :

   $$d_{\rm lim} = \frac{4}{\pi}\, b_{\rm eff} \sqrt{\pi\, \ln(2)\, \ln\left(\frac{\rm SNR+1}{\rm SNR}\right)} = \frac{4}{\pi}\, b_{\rm eff} \sqrt{\pi\, \ln(2)\, \ln\left(\frac{S_{\rm p}+\sigma_{\rm p}}{\sigma_{\rm p}}\right)}\,, \tag{7.1}$$

   where $\rm SNR = S_p/\sigma_p$, σ_p is the rms noise along the jet, and $b_{\rm eff} = \sqrt{b_{\rm bmaj} b_{\rm bmin}}$. This quantity refers to the true (deconvoled) size of the gaussian, which implies the measured width of the gaussian has to be deconvolved as well.

   ii. We calculate the deconvolved size of the gaussian component, $d_{\rm dec}$, using the fitted size, d, and the beam size, $b_{\rm eff}$, with:

   $$\begin{aligned} d_{\rm dec} &= \sqrt{d^2 - b_{\rm eff}^2} \quad \text{if } d > b_{\rm eff}\,, \\ d_{\rm dec} &= 0 \quad \text{if } d \le b_{\rm eff}\,. \end{aligned} \tag{7.2}$$

   iii. The final estimated size of the gaussian component, $d_{\rm g}$, is then:

   $$d_{\rm g} = \max(d_{\rm dec}, d_{\rm lim})\,.$$

2. Once we know the estimated size of the gaussian, the error estimation is performed following the approach developed in Fomalont (1999) and Schinzel et al. (2012):

   - The error of the peak flux density, σ_p is calculated by deriving the rms noise in several areas along the jet (centered on the jet axis used for obtaining the slices) and interpolating between the values derived. This results in a dependence, $\sigma_p(z)$, as a function of the distance from the map center (z).
   - The error of the position is calculated using Schinzel et al. (2012):

   $$\sigma_{\rm r} = \frac{1}{2\sqrt{2}}\, \frac{\sigma_{\rm p}}{S_{\rm p}}\, d_{\rm g}\, (1 + \frac{d_{\rm g}}{d_{\rm lim}})^{1/2} \tag{7.3}$$

[1] https://pypi.python.org/pypi/iminuit

- The error of the size is calculated using Schinzel et al. (2012):

$$\sigma_{\rm d} = \sigma_{\rm r}\sqrt{2(1+\frac{d_{\rm g}}{d_{\rm lim}})} = \frac{1}{2}\frac{\sigma_{\rm p}}{S_{\rm p}}\,d_{\rm g}\,(1+\frac{d_{\rm g}}{d_{\rm lim}}) \tag{7.4}$$

7.2 0836+710

To study the jet structure in 0836+710 we perform cuts perpendicular to the direction of propagation of the jet. We see that the flux density peak does not follow the straight line along which the jet is propagating. We first compare the jet profile at different frequencies and then study how moving components can affect the flow. We then perform a modelling of the ridgeline at 1.6 GHz in order to obtain jet parameters. At last, we study the existence of a multiple ridgeline structure in some regions in the jet.

7.2.1 Calculation of the jet ridgeline at different frequencies

We calculate the ridgeline as described in section 7.1. The number of slices and step size are listed in Table 7.1. The higher the resolution, the higher the number of slices and the smaller the step size. In some cases, one single gaussian is not describing all the observed structure, and we perform double or triple gaussian fits. Figure 7.1 shows an example for each kind of fit. We see a double gaussian structure in the case of the 5 GHz ground VLBI image and a triple gaussian structure in the region at distances larger than 60 mas for the ground VLBI image at 1.6 GHz. The resulting single ridgelines are plotted in Figures 7.2 to 7.4. Figures 7.2- 7.4 show that the ridge line is oscillating around the mean propagation direction of the jet. The double and triple ridgeline are shown in Figures 7.5 and 7.6.

Table 7.1: Number of slices and step size used to obtain transverse profiles from 0836+710 observations.

ν [GHz]	Array	Number slices	Step [mas]
1.6	Ground-VLBI	809	0.155
1.6	Space-VLBI	1005	0.038
5	Ground-VLBI	259	0.076
15	VLBA	395	0.046
22	Ground-VLBI	161	0.024
43	VLBA	171	0.020

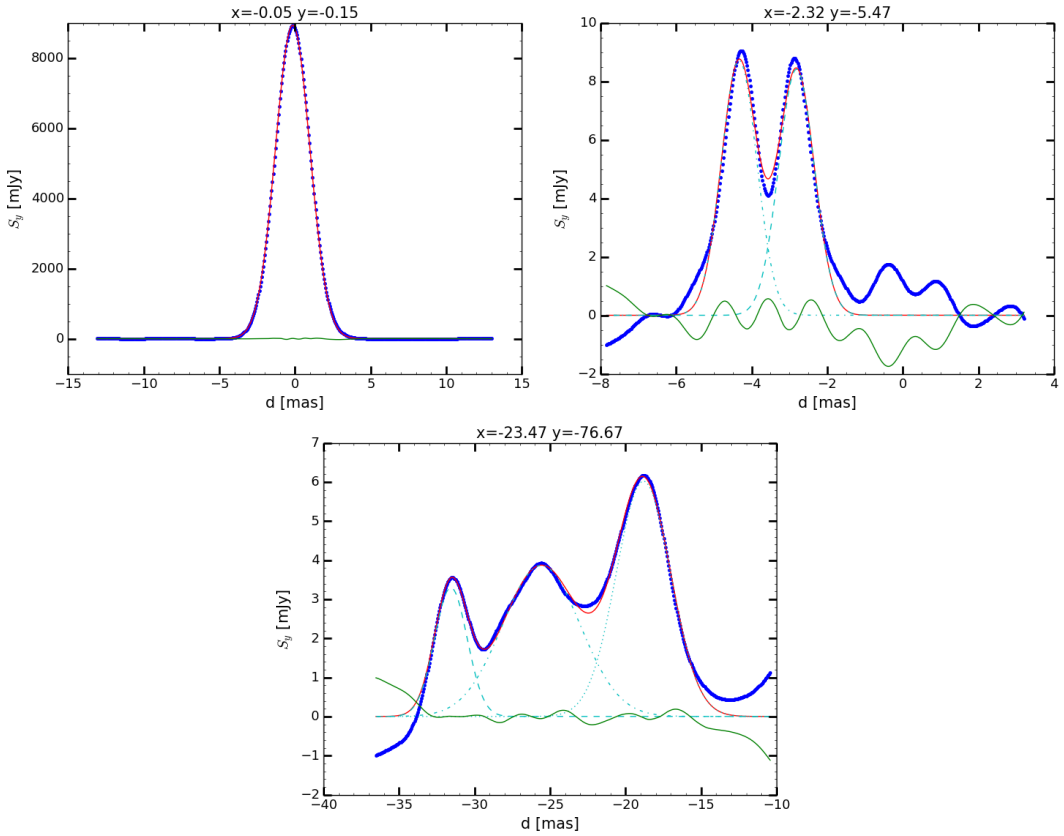

Figure 7.1: Different gaussian profiles obtain studying the transverse structure of 0836+710. The dark blue line is the data, the red line is the total fit, and the green line the residuals. **Upper left panel:** single gaussian fit at 1.6 GHz. **Upper right panel:** double gaussian profile at 5 GHz. **Bottom panel:** triple gaussian fit at 1.6 GHz.

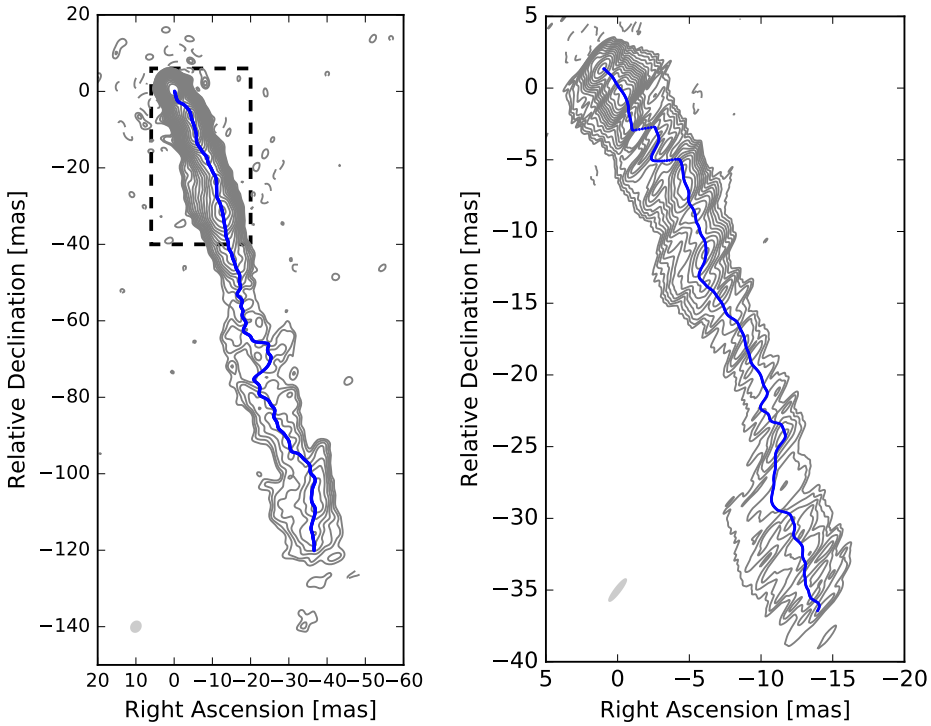

Figure 7.2: Ridgeline (blue) for ground-VLBI observations (**Left panel**) and for space-VLBI observations (**Right panel**) at 1.6 GHz of 0836+710. The contour levels are drawn at $(-1, 1, \sqrt{2}, 2, \ldots)$ times 0.32 mJy/beam for the global array image and times 10 mJy/beam for the *RadioAstron* map. The dashed box in the left panel corresponds to the coordinate range of the map in the right panel.

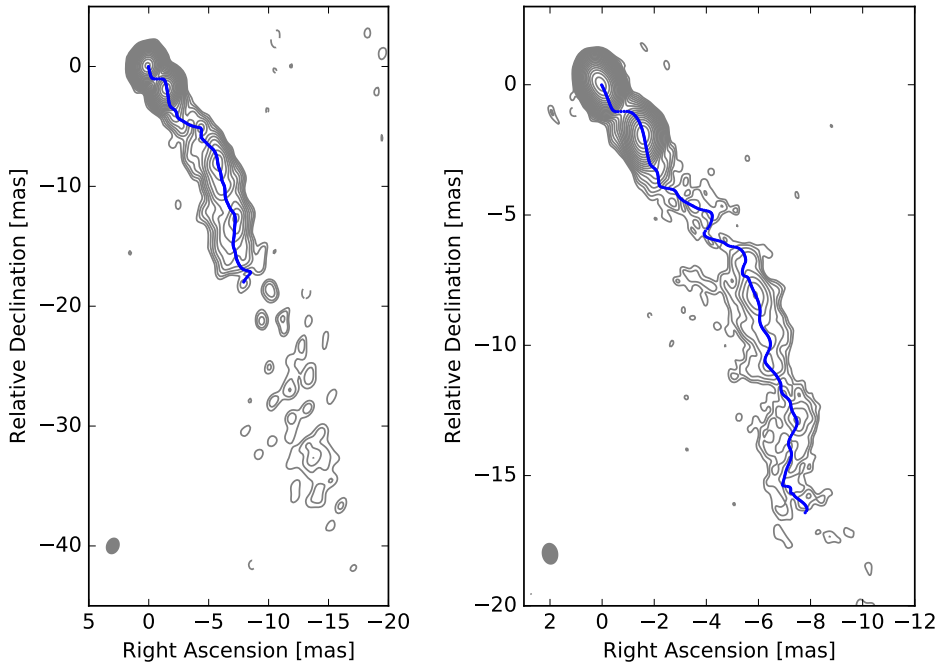

Figure 7.3: **Left panel:** Ridgeline (blue) for ground-VLBI observations at 5 GHz of 0836+710. The contour levels are drawn at $(-1, 1, \sqrt{2}, 2, \ldots)$ times 1.5 mJy/beam. **Right panel:** Ridgeline (blue) for ground-VLBI observations at 15 GHz. The contour levels are drawn at $(-1, 1, \sqrt{2}, 2, \ldots)$ times 0.75 mJy/beam.

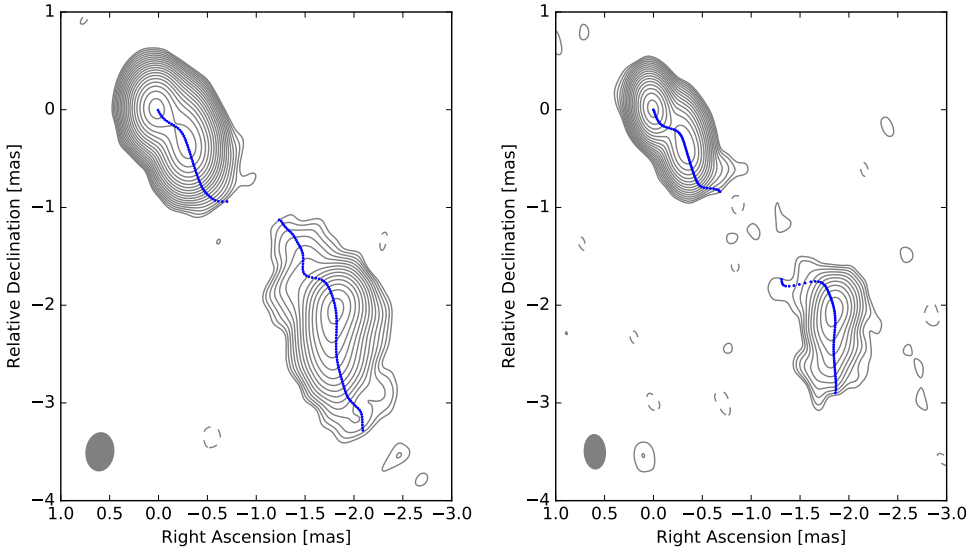

Figure 7.4: **Left panel:** Ridgeline (blue) for ground-VLBI observations at 22 GHz of 0836+710. The contour levels are drawn at $(-1, 1, \sqrt{2}, 2, \ldots)$ times 1.0 mJy/beam. **Right panel:** Ridgeline (blue) for ground-VLBI observations at 43 GHz. The contour levels are drawn at $(-1, 1, \sqrt{2}, 2, \ldots)$ times 1.8 mJy/beam.

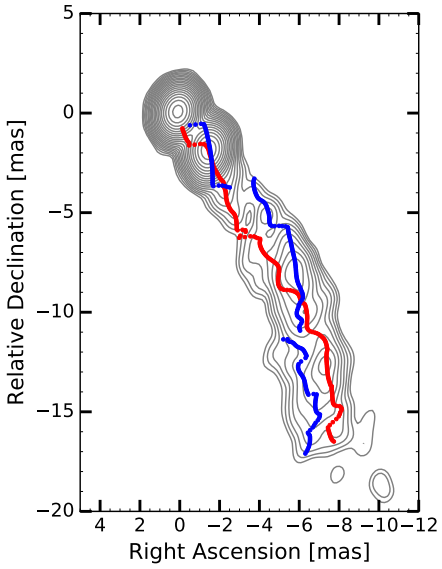

Figure 7.5: Double ridgeline for ground-VLBI observations at 5 GHz of 0836+710. The contour levels are drawn at $(-1, 1, \sqrt{2}, 2, \ldots)$ times 1.5 mJy/beam.

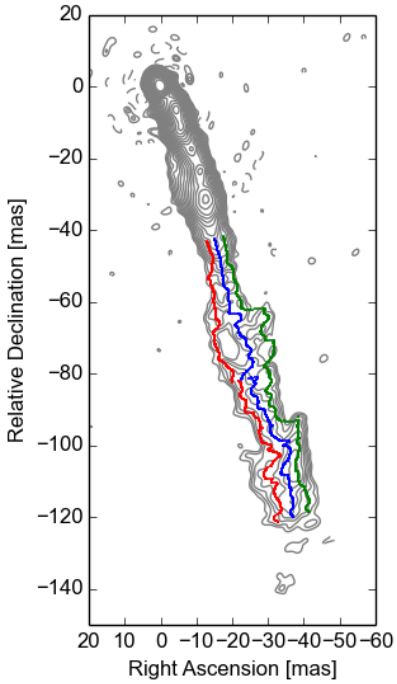

Figure 7.6: Triple ridgeline for ground-VLBI observations at 1.6 GHz of 0836+710. The contour levels are drawn at $(-1, 1, \sqrt{2}, 2, \ldots)$ times 0.32 mJy/beam

7.2.2 Comparison of the ridgelines at different frequencies

To compare the measurements of the ridgeline obtained in the ground array images at different frequencies, all fitted positions of the gaussian profiles are referred to a mean jet direction, at a position angle of $-162°$. This angle corresponds to the average propagation direction of the jet, i.e., the axis along which the jet should propagate without any perturbation present. We do this applying the following equation (Perucho et al. 2012a):

$$\begin{aligned} \text{Axial distance} &= x_{\text{obs}} \cos(2\pi - \chi) - y_{\text{obs}} \sin(2\pi - \chi) \\ \text{Axial displacement} &= x_{\text{obs}} \sin(2\pi - \chi) + y_{\text{obs}} \cos(2\pi - \chi), \end{aligned} \tag{7.5}$$

where x_{obs} and y_{obs} are the coordinates in DEC and RA of the ridge line in the map respectively and χ is the position angle. The different ridgelines are shown in Fig. 7.7.

We see some deviation if we compare the ridgeline at 1.6 GHz with the ridgeline at higher frequencies. The ridgelines at frequencies above 1.6 GHz all clearly trace the same structure as their offset with respect to the propagation direction is similar. To understand the difference between the ridgelines, we consider the individual fits for the regions where we see this different behaviour. In figure 7.8 and 7.9 we plot two different slices at the projected distances of ~ 1.3 mas and ~ 7.6 mas, respectively. The figures illustrate that the position of the single gaussian fit in the low frequency image is close to the center of those two gaussians. However, in the case of the high frequency image, the peak is closer to the brightest of both features, with the exception of the regions where both peaks become similar. In that case, the single gaussian fit also peaks between the two gaussians (Fig. 7.9).

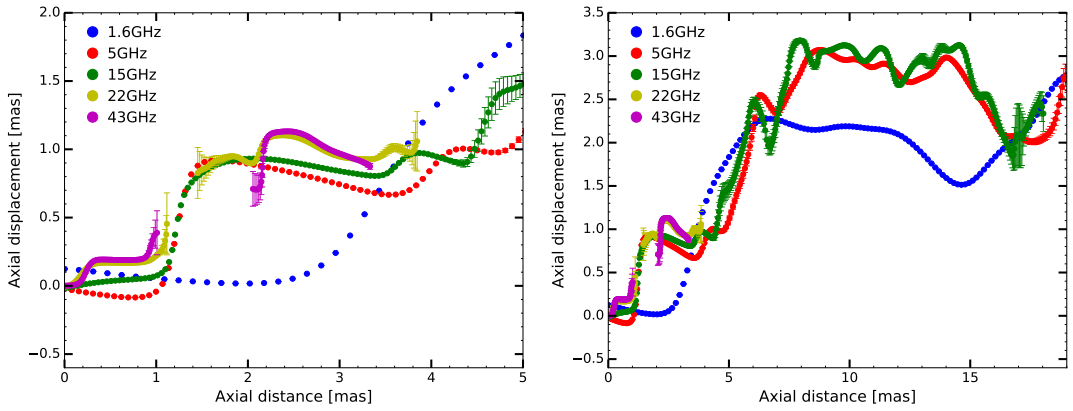

Figure 7.7: Ridgelines of 0836+710 for ground images. **Left panel:** Distances up to 5. mas. **Right panel:** Distances up to 19. mas.

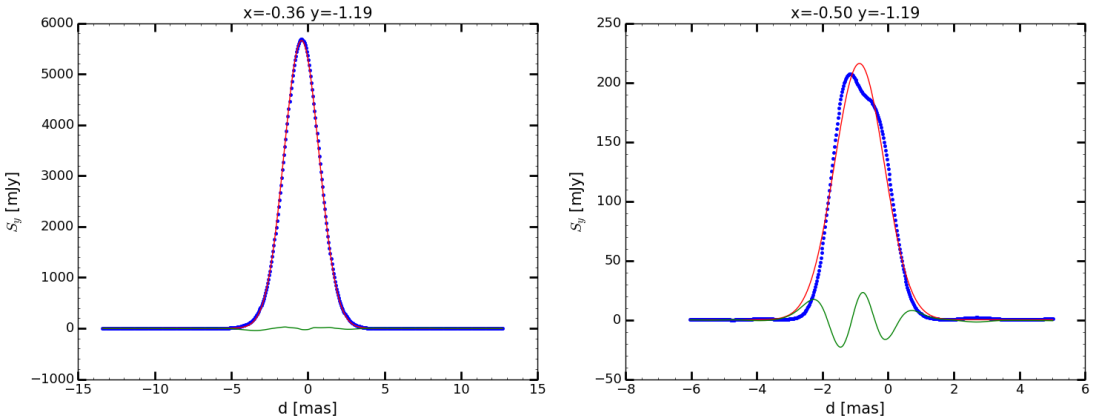

Figure 7.8: **Left panel:** Gaussian fit at a projected distance of 1.24 mas for the 1.6 GHz observations of 0836+710. The center of the gaussian is at ~ -0.6 mas. **Right panel:** Gaussian fit at a projected distance of 1.29 mas for the 5 GHz observations of 0836+710. The center of the gaussian is at ~ -1 mas. The middle point between both gaussians is located at a distance of ~ -0.6 mas.

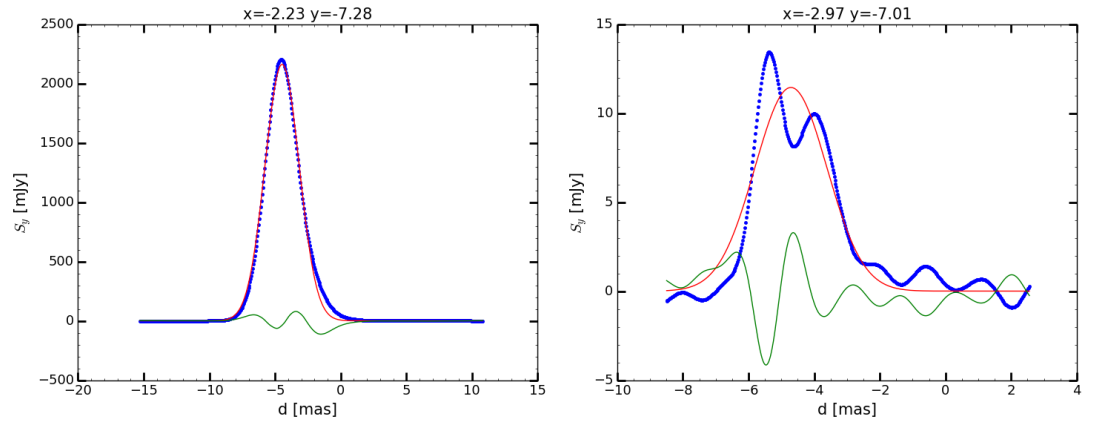

Figure 7.9: **Left panel:** Gaussian fit at a projected distance of 7.61 mas for the 1.6 GHz observations of 0836+710. The center of the gaussian is at ~ -5 mas. **Right panel:** Gaussian fit at a projected distance of 7.61 mas for the 5 GHz observations of 0836+710. The center of the gaussian is at ~ -5 mas. The middle point between both gaussians is located at a distance of $\sim$ -5 mas.

7.2.3 Effect of the components on the ridgeline structure

The study of the flux density profiles of the ridgeline also gives us some hints on how the components travelling in the plasma might affect the underlying structure. First, focusing on the 43 GHz ridgeline flux density profile (shown in Fig 7.10), we see a peak almost as bright as the core at a distance of $\sim$ 0.07 mas (the core corresponds to the first point of the ridge line). This is consistent, within the errors, with the position of the recollimation shock already mentioned in Chapter 6. Furthermore, we can see a small increase in the flux density at distances of $\sim$ 0.5 mas, which is consistent with the presence of a travelling component located at this position at this epoch. We can also observe this at 22 GHz at the same distance (Right panel on Fig. 7.11). Looking now at distances between 2 mas and 3 mas, in this case at frequencies between 15 GHz (Left panel on Fig. 7.11) and 43 GHz, we see that, at the position of the peak in flux density, we have a slow or standing component. This increase on the flux density at this location appears consistently in several epochs of MOJAVE data (see Fig. 7.12 for January 1995 and October 2010). Perucho et al. (2006) mentions that the presence of a moving shock can disturb the equilibrium state of the underlying structure. In our case, we can see how the presence of components affects the ridgeline and it implies that the structure of the flow can be affected by shocks or travelling components, which can cause a small increase of the offset at those distances (clearly visible in the case of 22 GHz at distances between 2-5 mas, right panel on Fig. 7.11). Furthermore, this tells us that the modelling at small scales requires special care, as small variations of the ridgeline can be caused by the presence of components. The way these components affect the ridgeline should depend on their brightness, which would explain why some of them are less bright and create a lower offset than others.

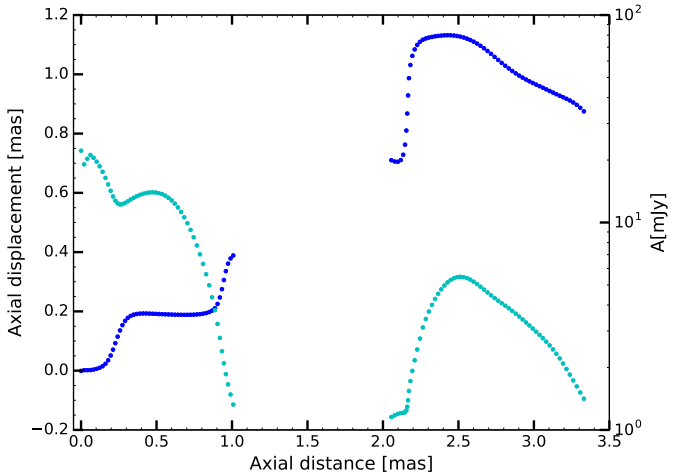

Figure 7.10: Offset (dark blue) and flux density (light blue) in the jet of 0836+710 as a function of the (projected) distance at a frequency of 43 GHz.

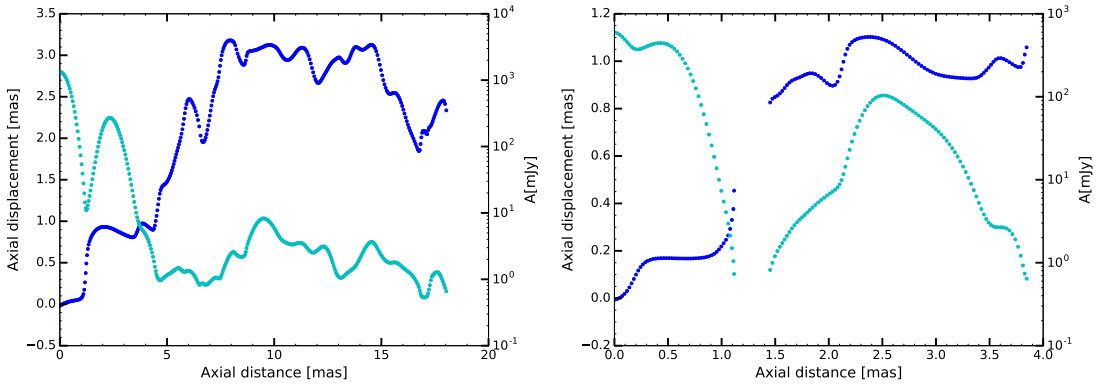

Figure 7.11: Offset (dark blue) and flux density (light blue) in the jet of 0836+710 as a function of the (projected) distance. **Left panel:** at a frequency of 15 GHz. **Right panel:** at a frequency of 22 GHz.

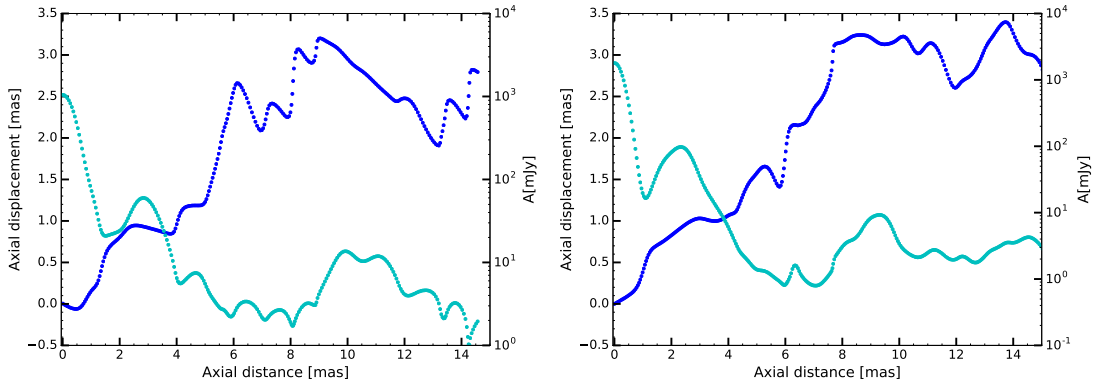

Figure 7.12: Offset (dark blue) and flux density (light blue) in the jet of 0836+710 as a function of the (projected) distance at a frequency of 15 GHz for MOJAVE data from different epochs. **Left panel:** January 1995. **Right panel:** October 2010.

7.2.4 1.6 GHz ridgeline modelling

We perform a ridgeline modelling for the 1.6 GHz images obtained using the ground and space-VLBI array, which allows us to compare the value of the resulting parameters between two separate and independent fits. We show the ridgelines for the 1.6 GHz images in Fig. 7.2. We model the ridgelines by fitting them with oscillatory patterns of the form:

$$\Delta r(z) = \sum_{i=1}^{N_{\mathrm{mod}}} a_i \sin\left(\frac{2\pi}{\lambda_i} x_i + \psi_i\right) , \tag{7.6}$$

where $\Delta r(z)$ is the observed offset of the ridgeline from the jet axis, a_i, ψ_i, and λ_i are the amplitude, phase and wavelength corresponding to the i-th mode.

We performed the modelling with two different methods:

1. Fitting the first wavelength and subtracting it from the original ridgeline. Then, a second periodic structure is fitted and again subtracted. The process was iterated until the addition of a new oscillation did not provide any improvement to the fit.

2. Fitting all periodic structures at the same time. This method has a higher dependence on the initial guess parameters.

We applied this for the space and ground VLBI 1.6 GHz ridgelines obtaining consistent results in the two cases. The results are plotted in Fig. 7.13 and the fit parameters listed in Tables 7.2 and 7.3 for the ground array and space ridgeline, respectively. The errors listed in the table correspond to the method yielding the largest uncertainty.

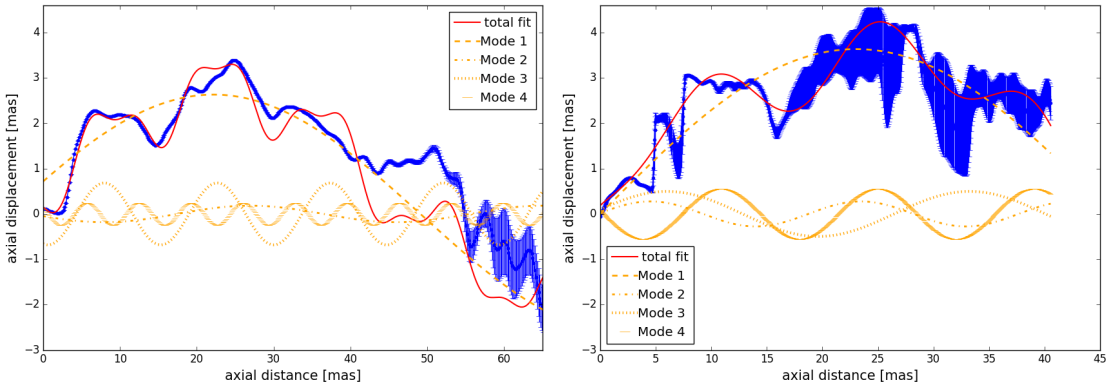

Figure 7.13: Fits by oscillatory structures to the jet ridgelines in the ground (left) and space (right) VLBI images of 0836+710 at 1.6 GHz. In each plot, the red line is the multi-mode fit and the orange lines represent contributions from the individual oscillatory modes as described in the legend. The dark blue line is the ridgeline resulting from the data.

Table 7.2: Results of the modelling to the single Gaussian ridgeline of the ground array L band image of 0836+710 ($\chi^2 = 21$), using four wavelengths. See the left panel Fig. 7.13.

Mode	λ [mas]	a [mas]	ψ [°]
1	102 ± 6	2.9 ± 0.2	15 ± 8
2	35 ± 5	0.21 ± 0.03	195 ± 50
3	16.5 ± 1.5	0.55 ± 0.16	-105 ± 30
4	6.6 ± 0.2	0.30 ± 0.05	146 ± 11

We can see four different modes that are consistent in both VLBI images. The only mode that is significantly different in the two fits is the shortest wavelength oscillation (mode 4). However, it is important to note that accurately measure the shortest modes can be challenging, as the VLBI images are affected by factors such as the *uv*-coverage, the quality of the data and the image noise. This can lead

Table 7.3: Results of the modelling to the single Gaussian ridgeline of the space-VLBI array L band image of 0836+710 ($\chi^2 = 1.4$), using four wavelengths. See the right panel of Fig. 7.13.

Mode	λ [mas]	a [mas]	ψ [°]
1	97 ± 4	3.7 ± 0.2	0 ± 10
2	44 ± 8	0.42 ± 0.04	82 ± 14
3	16.9 ± 1.4	0.50 ± 0.12	-106 ± 7
4	8.84 ± 0.12	0.23 ± 0.07	54 ± 6

to a non robust measurement of the shortest wavelength. Due to this, together with the influence of multiple gaussian structure at short scales in the source, we exclude this oscillatory structure in our further analysis of the instabilities in the source.

In order to verify the consistency of our results, we now compare them with earlier works. Lobanov et al. (1998) reported ridgeline oscillations with wavelengths of $\simeq 100$, ~ 8, and ~ 5 mas based on space VLBI observations of 0836+710 with VSOP. The first wavelength can be identified with our longest mode, while the two shortest wavelengths likely correspond to the shortest oscillatory structure in our ground and space-VLBI results. Perucho et al. (2012a) reported a long wavelength of 80 mas in the jet of 0836+710, based on VLBA images. The authors also reported shorter wavelengths of 10 mas and 20 mas up to distances of 40 mas, that grow to a wavelength of 40 mas. Therefore, all fitted structures have been detected in previous works.

Identification of the modes

Since the ridgeline deviates from the observed mean jet direction, we can relate the flux maxima with pressure maxima in the jet, since no large changes in speed are observed in 0836+710, and therefore these deviations cannot be caused by differential Doppler boosting (Perucho et al. 2012a). Given the scales we are considering in the jet (up to ~ 500 pc from the central engine), if we interpret the ridgeline as the trace of pressure maxima accross the jet, the maximum of pressure is most probably caused by the presence of Kelvin Helmholtz instabilities in the flow (Perucho et al. 2012a). Therefore, in order to know which instability modes are affecting the plasma, we first identify the oscillatory structures using a linear analytic description of Kelvin-Helmholtz instability (Hardee 2000). Following Lobanov & Zensus (2001), we define a characteristic wavelength $\lambda^* = \lambda_i(n_i + 2m_i + \frac{1}{2})$, where λ_i is the observed wavelength and n_i and m_i are the two transverse wavenumbers. n describes waves with similar azimuthal characteristics (pinch, helical,...) (Birkinshaw 1991), m indicates if the mode of a given n is surface ($m = 0$) or j-order body mode ($m \geq 1$). We also apply a second method, based on a numerical solution of the differential equation relating k and ω which is obtained for a perturbed hydrodynamical plasma with a shear layer (Eq. 3.14). This gives us an intrinsic

wavelength that can be converted into the observed wavelength and compared to the observations.

7.2.4.a Jet parameters using the characteristic wavelength

The longest-wavelength mode has the largest amplitude, and it is clearly reflecting a displacement of the jet flow. This favours its identification with a helical surface mode.

We perform a first tentative identification of the other modes using the characteristic wavelength, λ^*. If we assume that the observed wavelengths correspond to modes excited at their maximum growth rates, the characteristic wavelength should have a similar value for the different instability modes (Lobanov & Zensus 2001). We calculate λ^* for different m and n for each mode and compare its values, taking into account that our identification of mode 1 ($\lambda \simeq 100$ mas) with an helical surface mode implies that $n = 1$ and $m = 0$. We therefore obtain that the second-longest wavelength (mode 2) should be identified as the first helical body mode, H_{b1}, whereas the third longest wavelength (mode 3) could be either the second, H_{b2}, or the third helical body mode, H_{b3}. We exclude the fourth mode due to its small wavelength since it complicates its identification. If we identify the third mode as the second helical body mode, the average characteristic wavelength is 119 ± 12 mas. If we identify it instead as the third body mode, the average characteristic wavelength takes a value of 130 ± 12 mas.

Following Hardee (2000) and references therein, some basic physical parameters of the plasma, as the jet classical Mach number, M_j, and the jet density ratio, η can be calculated from the identification of the different modes, using the linear analysis of Kelvin-Helmholtz instability. The formulae to calculate M_j and η are:

$$M_\mathrm{j} = \frac{\lambda^*(1-\beta_w\cos\theta_\mathrm{j})}{8R_\mathrm{j}\gamma_\mathrm{j}(1-\beta_w/\beta_\mathrm{j})\sin\theta_\mathrm{j}}\,, \qquad \eta = \frac{M_\mathrm{j}^2}{M_\mathrm{x}^2}, \tag{7.7}$$

where the external jet Mach number, M_x, and the intrinsic jet speed, β_j, and the instability pattern speed, β_ω, are obtained from:

$$M_\mathrm{x} = \frac{\lambda^*\beta_\mathrm{j}(1-\beta_w\cos\theta_\mathrm{j})}{8R_\mathrm{j}\beta_w\sin\theta_\mathrm{j}}\,, \tag{7.8}$$

$$\beta_w = \frac{\beta_{w_\mathrm{app}}}{\sin\theta_\mathrm{j}+\beta_{w_\mathrm{app}}\cos\theta_\mathrm{j}}\,, \tag{7.9}$$

and

$$\beta_\mathrm{j} = \frac{\beta_\mathrm{app}}{\sin\theta_\mathrm{j}+\beta_\mathrm{app}\cos\theta_\mathrm{j}}. \tag{7.10}$$

where $\beta_{\omega_{\rm app}}$ is the wave apparent pattern speed, $\beta_{\rm app}$ is the jet apparent speed, θ_j the viewing angle, and R_j the jet radius. These formulae assume that $M_j \gg 1$ (Hardee 1987, 2000) and a vortex sheet.

As a value for λ^*, we use the previously calculated characteristic wavelengths ($\lambda^* = 119$ mas, and $\lambda^* = 130$ mas). For the viewing angle, θ_j, and apparent speed, $\beta_{\rm app}$ we assume the values $\theta_{\rm j} = 3^\circ$ and $\beta_{\rm app} = 10.7$ (or $\gamma_{\rm j} = 12$) reported in Otterbein et al. (1998). We measure the jet radius at the point where the jet brightness drops to 1% of the peak brightness (Wehrle et al. 1992). In practice, we choose the first slice with a peak flux density 1% of the flux density of brightest point of the jet (first slice). Then, the measurement of jet width is the full width half maximum, $\theta_{\rm FWHM}$, of the corresponding Gaussian fit for the selected slice. As the latter is affected by the convolution with the clean beam, we deconvolve it, using the relation $R_{\rm j}[{\rm mas}] = 0.5\sqrt{\theta^2_{\rm FWHM} - b^2}$, where b is the beam size. This yields a jet radius of 2 mas or 16 pc.

Finally, we estimate the apparent pattern speed by comparing the ridgeline at different epochs at 15 GHz, obtained with the public data from the MOJAVE monitoring program, since our observations include only one epoch. To avoid systematic errors, we use the region with highest SNR, which corresponds to the inner $1 - 4$ mas. We also choose two epochs that are distant enough in time (1995 and 2014) and in which no component was detected at the distance used for calculating the speed ($3.8 - 4.3$ mas). The measured speed is $v_{\rm app} = 0.35 \pm 0.25c$. Due to the short scales in which we obtain the speed, this velocity is corresponding to a mode with a short wavelength. The other modes could be moving at different pattern speeds, typically smaller since the shorter wavelength modes typically propagate faster (Perucho & Lobanov 2007; Perucho et al. 2012a).

Applying these estimates in Eq. 7.7, we obtain a Mach number of $M_{\rm j} = 12 \pm 3$ and a density ratio of $\eta = 0.33 \pm 0.08$. We should notice the effect of the pattern speed on the density ratio is also relevant. If we consider different values of the wave pattern speed within the range allowed by the error, for example assuming a pattern speed of $\beta_{w_{\rm app}} = 0.10$, the density ratio changes by an order of magnitude, to $\eta \sim 0.02$. Nevertheless, this does not affect the value of the jet Mach number, which is consistent with the validity range of the parameters in order to used these equations.

7.2.4.b Numerical analysis

Taking into account that the presence of a shear layer surrounding the jet (defined by Eq. 3.15) in 0836+710 has been suggested in earlier works (Perucho & Lobanov 2007, 2011), we solve the second-order differential equation expressed in Eq. 3.14 using the shooting-method (see, e.g., Perucho et al. 2005, 2007, for details), which provides us with values for frequency, ω, and the wavenumber, k, that satisfy the equation. This method consist in choosing values for the frequency (in the spatial

approach) and obtain the wavenumbers that satisfy the relation to solve. It is done integrating, using the Ruge-Kutta method, from the central axis of the jet until an external point in the ambient medium. If the solution of the integral does not satisfy the boundary conditions, a new pair of points is chosen using the Muller method (Press et al. 1992) and the integration is repeated. The process is iterated until the pair of points satisfy the conditions.

Furthermore, since we want to study how the perturbations evolve as a function of distance along the jet, we use the spatial approach, which assumes that the unstable modes grow in distance. The resulting parameters are complex wavenumbers and real frequencies. The real part of the wavenumber corresponds to the wavelength of the perturbation, $\lambda_{\rm int}$, and the imaginary part to the growth length, $\lambda_{\rm e}$. The relationship is:

$$\lambda_{\rm int} = \frac{2\pi}{\Re(k)}\,, \tag{7.11}$$

$$\lambda_{\rm e} = -\frac{1}{\Im(k)}. \tag{7.12}$$

Our calculations assume an infinite cylindrical jet, and a dynamically negligible magnetic field. In order to solve Eq. 3.14 we need to assume a value for the shear layer width, m, jet specific internal energy density, $\varepsilon_{\rm j}$, and jet rest-mass density. In the calculations, we use units of $\rho_a = 1$, $c = 1$ and $R_j = 1$ (jet radius). Therefore, the jet density in the equations represents the density ratio, η, between the jet and the ambient medium. We investigated a spectrum of broad and narrow shear layer widths, from ≤ 10 % of the jet radius ($m = 16$ and $m = 12$) to $\simeq 20$ % of the jet radius ($m = 8$ and $m = 4$). In order to include cold and hot jets, the values of the jet specific internal energy density range from $0.001c^2$ to c^2. The values of the density ratio range from 10^{-5} to 0.1. Finally, we considered Lorentz factors from 5 to 17, including $\gamma_{\rm j}$=12 as derived from VLBI observations at 8 GHz (Otterbein et al. 1998), $\gamma_{\rm j}$=17 from VLBI observations at 15 GHz (Lister et al. 2013) and $\gamma_{\rm j}$=5 to study the option of a slower layer of plasma surrounding a fast inner spine. We only solve Eq. 3.14 for helical modes, since the three longest modes are displacing the ridgeline. Furthermore, the crossing observed between the double ridgeline morphology observed in the 5 GHz image, that might be related to the existence of elliptical modes, is produced after ~ 6 mas, which excludes any other longer wavelength to be the cause of such structure.

In this case, we calculate the value of the Mach number from its definition, $M_{\rm j} = v_{\rm j}/c_{\rm sj}$, where $c_{\rm sj}$ is the jet sound speed, which can be calculated as:

$$c_{\rm sj}^2 = \frac{\Gamma p}{h} = \frac{\Gamma(\Gamma-1)\epsilon_{\rm j}}{1+\Gamma\epsilon_{\rm j}}, \tag{7.13}$$

where h is the entalphy, p the pressure and Γ the adiabatic index.

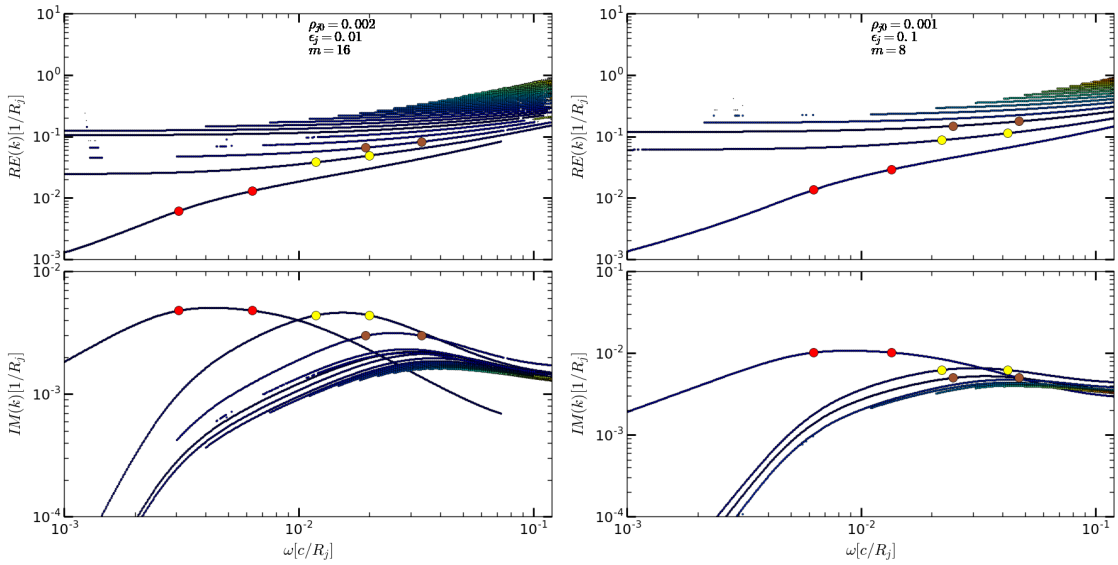

Figure 7.14: Solutions of the dispersion relation for helical modes applied to the jet of 0836+710. The upper panel represents the wavenumber and the lower panel the growth length in function of the frequency. The colored dots represent the values for which the maximum value of the imaginary part of the wavenumber is reduced by 5%, i.e., the interval where the growth length is minimized. The red dots corresponds to the helical surface mode, the yellow dots to the first body mode and the brown ones to the second body mode. **Left panel:** Solutions for a shear layer of $m = 16$, jet internal energy of 0.01 and jet density of 0.002. **Right panel:** Solutions for a shear layer of $m = 8$, jet internal energy of 0.01 and jet density of 0.001.

For illustrative purposes, Figure 7.14 shows the solutions of the helical instability modes for the case of $m = 16$, $\varepsilon_{\rm j} = 0.01c^2$ and $\eta = 2 \times 10^{-3}$ (left panel) and $m = 8$, $\varepsilon_{\rm j} = 0.01c^2$ and $\eta = 10^{-3}$ (right panel). Since the differential equation could only be solved numerically and not analytically due to its complexity, we only have solution pairs and not its correspondence with a specific mode, and thus they need to be identified. We perform this identification using the clustering algorithm `DBSCAN` (Ester et al. 1996). Since the number of solutions obtained for each mode was high, in order to identify a mode we required a small enough separation between consecutive points (the exact separation value varies for each set of parameters) and a minimum number of ten points to identify them as belonging to the same mode. This method successfully identifies the modes resulting from the different solutions through to the interest range. We only focus on the helical surface mode, and the two first helical body modes because they correspond to the longest unstable wavelengths. Since the upper panel of both plots in Fig. 7.14 corresponds to the wavelength, we use it to identify the different modes. As we stated previously, the mode with a longer wavelength (a lower wavenumber) is the helical surface mode, the mode with the second longest wavelength corresponds to the first body mode, and the following body modes have shorter wavelengths.

The modes of interest are identified in Fig. 7.14 with color dots (red, yellow, and brown).

The intrinsic wavelength is calculated by finding the minimum growth length, defined in Eq. 7.12, for each mode. To do this, we look for the maximum in $\Im(k)$ for each mode. Since we have plateau-like maxima instead of sharp maxima, we consider as lower and upper bounds the points where the maximum value of the imaginary part of the wavenumber is reduced by 5% for each mode. As we are working in units of jet radii, we need to account for this in the conversion. Therefore, we convert the distance unit used in the calculations (jet radius, R_j) into milliarcseconds using the jet radius, $R_{\rm j} = 16$ pc, that was used in the analytical method. Since the solutions are found by assuming that the jet is infinitely cylindrical, but it has an opening angle, this introduces a source of error in our solutions. However, taking into account that the opening angle is very small ($< 1°$, see Perucho et al. 2012a) and that, in principle, the jet expansion introduces an increase of the peak wavelengths (e.g., Hardee 1982, 1984, 1986), we conclude that our solutions will provide us the jet parameters within the plausible order-of-magnitude.

We derive the deprojected wavelength from the intrinsic wavelength, using the viewing angle, $\theta_{\rm j}$, and the intrinsic wave speed, β_ω, as follows:

$$\lambda_{\rm obs} = \lambda_{\rm int} \frac{\sin\theta}{1 - \beta_\omega \cos\theta}. \tag{7.14}$$

The intrinsic wave speed has been estimated using the values of the complex k and real ω from the calculations using:

$$\beta_\omega = \frac{\omega}{k} \simeq \Re\left(\frac{\omega}{k}\right), \tag{7.15}$$

taking into account that $\Re(k) \gg \Im(k)$.

The values of observed wavelengths corresponding to each solution of the dispersion relation and its corresponding Mach number can be found in the Table 7.4 and in the tables in the Appendix F.

To evaluate which model is closer to our observational results, we calculate the dispersion between the observed wavelengths and the values obtained with the numerical calculations, in order to see which set of parameters describes best the observed wavelengths. Figure 7.15 illustrates how the predicted observed wavelengths change with the shear layer width and the jet density. In the plots, the horizontal lines and shaded areas indicate the observed wavelengths and their formal errors. Each *family* of three points in the y direction represents the wavelengths at the maxima in growth rate of the fundamental, first and second body modes for each different model (defined by the given set of physical parameters). The most likely model is thus the one for which the points lie closer to the observed wavelengths (horizontal lines) within the error given by the shaded areas. We plot the wavelengths obtained for the relevant modes, as a function of rest-mass den-

Table 7.4: Solutions of the dispersion relation for $m = 16$, $\gamma_j = 12$, and $\epsilon_j = 0.01$

Mode	m	$\varepsilon_{\rm j}$	η	$M_{\rm j}$	ω $[c/R_{\rm j}]$	$\Re(k)$ $[1/R_{\rm j}]$	λ [mas]
H_s	16	0.01	10^{-4}	12.53	0.0015−0.0041	0.0042−0.0092	121.71−211.18
H_{b_1}	16	0.01	10^{-4}	12.53	0.0050−0.010	0.0200−0.0260	39.00−41.94
H_{b_2}	16	0.01	10^{-4}	12.53	0.0054−0.010	0.0320−0.0390	22.68−24.73
H_s	16	0.01	10^{-3}	12.53	0.0024−0.0055	0.0054−0.0122	89.69−166.25
H_{b_1}	16	0.01	10^{-3}	12.53	0.0110−0.0190	0.0340−0.0450	25.14−28.41
H_{b_2}	16	0.01	10^{-3}	12.53	0.0160−0.0310	0.0600−0.0760	14.61−14.95
H_s	16	0.01	2×10^{-3}	12.53	0.0030−0.0060	0.0060−0.0130	85.19−157.74
H_{b_1}	16	0.01	2×10^{-3}	12.53	0.0120−0.0200	0.0330−0.0490	22.55−31.01
H_{b_2}	16	0.01	2×10^{-3}	12.53	0.0190−0.0330	0.0660−0.0830	13.14−13.99
H_s	16	0.01	6×10^{-3}	12.53	0.0045−0.0084	0.0078−0.0152	85.60−140.39
H_{b_1}	16	0.01	6×10^{-3}	12.53	0.0150−0.0250	0.0440−0.0570	20.47−22.59
H_{b_2}	16	0.01	6×10^{-3}	12.53	0.0210−0.0360	0.0720−0.0890	12.40−12.89
H_s	16	0.01	0.01	12.53	0.006−0.011	0.01−0.018	84.37−126.43
H_{b_1}	16	0.01	0.01	12.53	0.019−0.033	0.049−0.066	19.86−21.85
H_{b_2}	16	0.01	0.01	12.53	0.025−0.045	0.079−0.100	11.95−12.18
H_s	16	0.01	0.1	12.53	0.015−0.022	0.020−0.029	87.23−114.63
H_{b_1}	16	0.01	0.1	12.53	0.047−0.078	0.077−0.111	19.85−21.84
H_{b_2}	16	0.01	0.1	12.53	0.070−0.120	0.125−0.180	10.94−11.94

sity ratio for each value of the shear layer and jet internal energy. The figure only shows the best result given by the most probable set of jet parameters (top left panel), another example with a different jet internal energy density, and other two examples with different shear layer widths (the lower panels). Additional figures can be found in the Appendix F.

We will first consider the effect of the shear layer on the simulated wavelengths. If we look at the separation between the different modes, in Fig. 7.15, we see that the broader the shear layer is, the larger is the distance between the peaks of fundamental mode and the first body mode. The separation between body modes remains unchanged. This excludes wide shear-layers (e.g., $m \geq 4$) since the separation between first body mode and fundamental mode is larger than the observed, and it is the reason why we did not perform more calculations for these cases. In addition, the predicted wavelength for the surface mode for the highest considered density ratios for $m = 4$ was already larger than the highest observed wavelength, including the same models that for other shear layers widths would have implied larger predicted wavelengths than those observed. The ratio between the wavelengths of the fundamental and body modes indicates that the most likely scenario is a rather narrow shear layer with $m = 16$. The resulting best models are the ones with $\eta = 2 \times 10^{-3}$ and $\varepsilon_{\rm j} = 0.01c^2$, and $\eta = 10^{-3}$ and $\varepsilon_{\rm j} = 0.01c^2$. Both cases correspond to a jet Mach number of $M_j \sim 12$. This value is in good

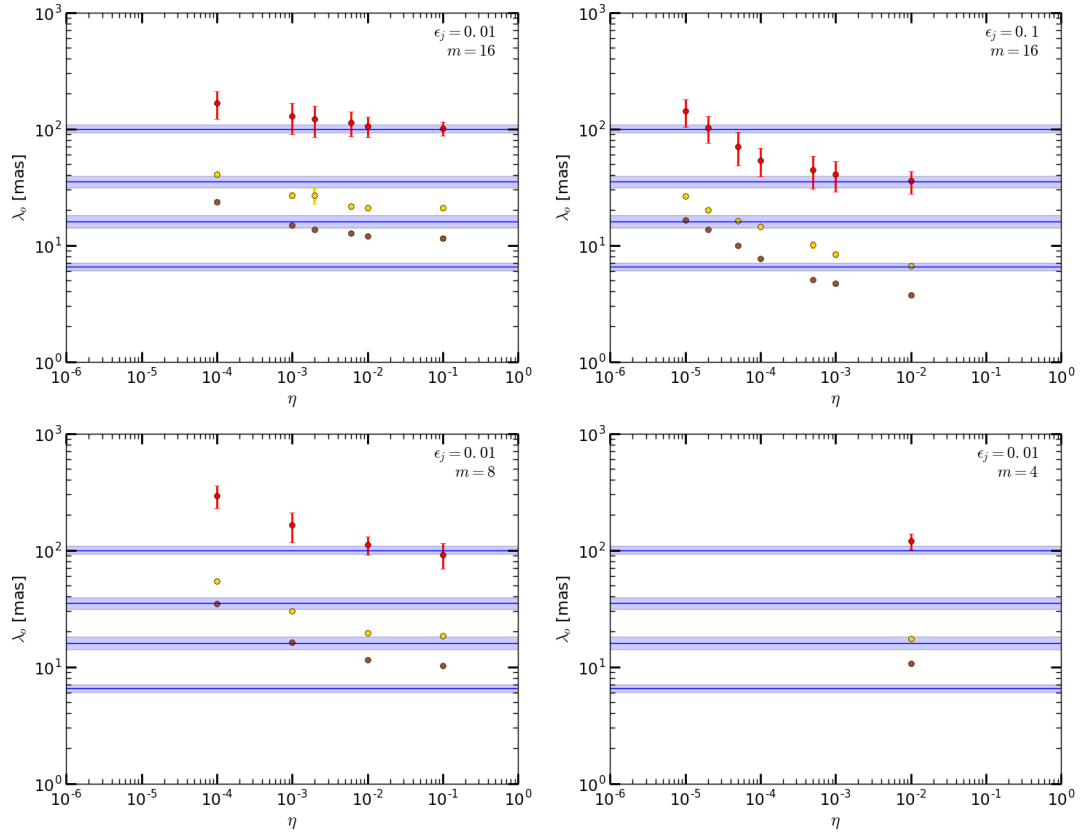

Figure 7.15: Observed wavelengths and their errors (blue lines and shades) compared to the wavelengths of different instability modes (symbols) obtained from the linear stability analysis. The color scheme used for representing the calculated wavelengths is the same as the one used in Fig 7.14. The $x-$axis represents the density ratio and the $y-$axis the corresponding observed wavelength. **Upper left panel:** Results for a shear layer of steepness $m = 16$ and jet internal energy of 0.01. **Upper right panel:** Results for a shear layer of steepness $m = 16$ and jet internal energy of 0.1. **Lower left panel:** Results for a shear layer of steepness $m = 8$ and jet internal energy of 0.01. **Lower right panel:** Results for a shear layer of steepness $m = 4$ and jet internal energy of 0.01.

agreement with the value obtained independently with the analytic method. The specific internal energy of the jet for those models is lower than one (c^2) and therefore it corresponds to a cold jet, which is possibly kinetic energy dominated. Furthermore, the jet has a density ratio of $\eta \sim 10^{-3}$, much lower than the value obtained with the method described in section 7.2.4.a.

We have also computed the solutions for different jet Lorentz factors values, $\gamma_j = 5$ and $\gamma_j = 17$, for the best fitting values of ε_j and η. We found that the case of $\gamma_j = 17$ results in peak wavelengths that are compatible with the observed wavelengths for each of the helical modes proposed (surface, and first and second body modes), whereas the $\gamma_j = 5$ models systematically result in lower peak wavelengths for each of the modes. Comparing the results given by Lorentz

factors 12 and 17, we see that although both models could still be compatible, the dispersion between the calculated wavelengths and the observed ones is lower for the Lorentz factor of 12 (see the Tables in the Appendix). It is noteworthy that the parameter sets that give the lowest dispersion for Lorentz factor 17 include options with larger values of $\varepsilon_{\rm j}$ ($0.01-0.1\,c^2$) and smaller η ($10^{-5}-10^{-4}$). Finally, although we found a relatively small dispersion values for paremeter sets with $\gamma_{\rm j}=12$ and higher values of $\varepsilon_{\rm j}$ ($1-10\,c^2$), the density ratios are extremely small ($10^{-7}-10^{-6}$), and still the dispersion is larger than for the aforementioned parameter sets. Our results thus allow us to confirm that the Lorentz factor of the jet at the scales revealed by the 1.6 GHz jet is probably in the range $12-17$, i.e., in agreement with the estimated value by Otterbein et al. (1998), $\gamma_{\rm j}=12$ from jet kinematics at 8 GHz and that derived by Lister et al. (2013) from 15 GHz observations. For this values of the Lorentz factor, we find that the jet is remarkably underdense with respect to its environment ($\eta\sim10^{-5}-10^{-3}$) and relatively cold ($\varepsilon_{\rm j}\sim0.01-0.1\,c^2$). This results in a relativistic jet Mach number, $\mathcal{M}_{\rm j}\simeq\gamma_{\rm j}M_{\rm j}$, range of $60-144$.

Because we model the observed jet structures along 100 mas, representing ~10 kpc, and the jet flow may change considerably along this distance, we have to discuss the validity of our results as estimates of mean jet parameters. On the one hand, taking into account that the analysis pictures a cold and fast jet, and that our estimate of the Lorentz factor coincides with that derived by Otterbein et al. (1998) from jet kinematics at 8 GHz, we can infer that any kind of Bernoulli acceleration (internal energy conversion into kinetic energy) must have taken place upstream and that no further acceleration takes place along the observed jet at 1.6 GHz. This argumentation consolidates the value of the Lorentz factor of $\gamma_{\rm j}\simeq12$ for the jet in 0836+710. In addition, since MOJAVE reports a Lorentz factor of $\gamma_{\rm j}=20$ Lister et al. (2013) on scales up to 15 mas the jet has probably gone through a mild deceleration. On the other hand, both the values of the specific internal energy and density ratio can be regarded as an order of magnitude estimate because 1) jet expansion leads to a drop in both parameters, and 2) these values are estimated from a stability analysis that gives the most unstable modes for a jet that has these parameters along the whole observed region. Regarding this second statement, the initial jet parameters are essential in the determination of the growing wavelengths. This could lead to the idea that the density ratio and specific internal energy derived are probably closer to the jet values around the 1.6 GHz core. However, the observed wavelengths that we use for comparison are developing along the whole observed jet, and could thus be growing with distance (Hardee 1982), so that the jet properties far from the core also influence the calculation.

We can also use the solutions of the stability problem to perform a sanity check of the characteristic wavelength relation discussed in Section 7.2.4.a. In order to do this, we introduce our parameter sets to derive the corresponding characteristic wavelengths in each case. On the one hand, we found that the body modes give

similar values for λ^* at the peak wavelengths from the numerical solutions. On the other hand, the characteristic wavelengths obtained for the fundamental mode has a much longer value in comparison. This tells us that the mode identification using the approximations leads to similar results to those obtained from numerical solutions for the body modes. In addition, once the first body mode has been identified, any obviously longer wavelength corresponds necessarily to the fundamental mode, so this identification can also be taken as accurate even though the characteristic wavelength obtained from the approximation is much longer than that from the numerical solutions. Interestingly, both independent approaches result in similar Mach numbers of the jet, albeit with very different density ratios.

7.2.5 Implications of the presence of a double ridgeline

Figure 7.5 shows the double Gaussian structure of the jet in 0836+710 and Fig. 7.16 plots the structure with respect to the mean jet direction. It is worth noting that the jet structure is not smooth, and therefore the fit needed to be restarted several times in order to converge. We perform the fit by choosing a slice where both Gaussians have sufficient amplitudes to be fitted reliably, and use this fit as a starting point for the adjacent slices in both directions, until a point is reached where the fit is not reliable. It can be noticed that in regions where the ridgeline varies sharply, the errors are larger for one of the two paths. This corresponds to the less bright Gaussian which has a quite low SNR. Because of this, the two lines are consistent with each other within the errors. However, this makes a further modelling of the structure more challenging. The projected distance of the clear crossing in the middle of the observed structure is ~ 7 mas, which compares well with the shortest measured wavelength in the modelling of the single ridgeline at 1.6 GHz (corresponding to a wavelength of 6.6 mas for the case of the ground image and 8.8 mas for the case of the *RadioAstron* image). This could tentatively identify the wavelength as an elliptical mode.

However, this is not the only reason that can lead to such a jet structure. The presence of a double ridgeline has two possible explanations:

1. The presence of elliptical modes in the jet (see, e.g., Lobanov & Zensus 2001, for the case of 3C 273).

2. A limb-brightened flow due to the interaction of the plasma with the ambient medium (see, e.g., Walker et al. 2018, for the case of M 87) as the jet oscillates. In this case the side that is brighter will be the region of the plasma interacting with the medium.

More detailed analysis would be necessary in order to discriminate between the two possibilities. However, this is an effort that goes beyond the scope of this thesis.

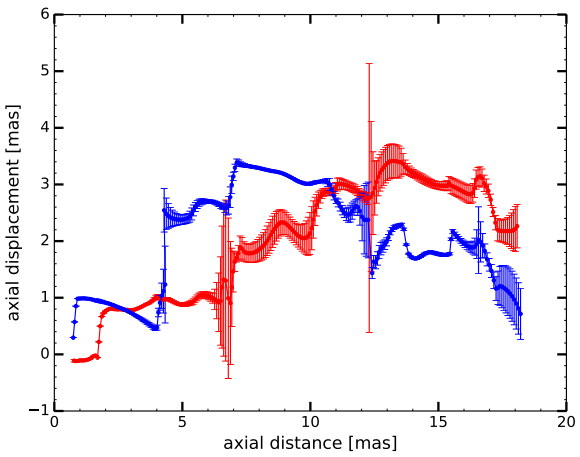

Figure 7.16: Double ridgelines for the 5 GHz ground array image of 0836+710 rotated with respect to the propagation direction, at a position angle of $-162°$.

7.2.6 Changes on the 1.6 GHz transversal structure

Beyond 60 mas, we observed a three-peaked profile (see Fig. 7.6). This is right after a jet region of low brightness and the beginning of a plateau in brightness and can be explained as a result of post linear growth of the instability mode. This is suggested by the fast and large variations of the the ridgeline offset at these distances. Furthermore, it can be seen that the flux density starts increasing again beyond $\sim$ 60 mas, looking at the flux density profiles (see top panel of Fig. 7.17), and that, looking at the width profiles, the jet becomes broader (see bottom panel of Fig. 7.17). This can be an indication of a change in the viewing angle, which allows us to see other regions on the jet, such as the shear layer, that were not visible in shorter scales. Furthermore, it may indicate an increase of the energy dissipation in the jet, probably due to the interaction of the plasma with the ambient medium as the instability grows. We can quantify this looking at the collimation profiles, which relates the deconvolved jet width with the distance as:

$$d \propto r^k,$$

where k defines different regimes on the jet and it depends on the plasma internal energy. If $k < 1$, the jet is in a collimation regime. If $k = 1$, the jet has a conical shape. And if $k > 1$ the jet expands freely. d is the deconvolved jet width.

As seen in Fig. 7.17, we have two different trends, when $r < 60$ mas and when $r > 100$ mas. We exclude the low SNR region between 60 mas and 100 mas. If we perform a fit in the two regions, we obtain:

$$\begin{aligned} d &\propto r^{0.37 \pm 0.11} && \text{if } r < 60\,\text{mas} \\ d &\propto r^{1.5 \pm 0.4} && \text{if } r > 100\,\text{mas}. \end{aligned}$$

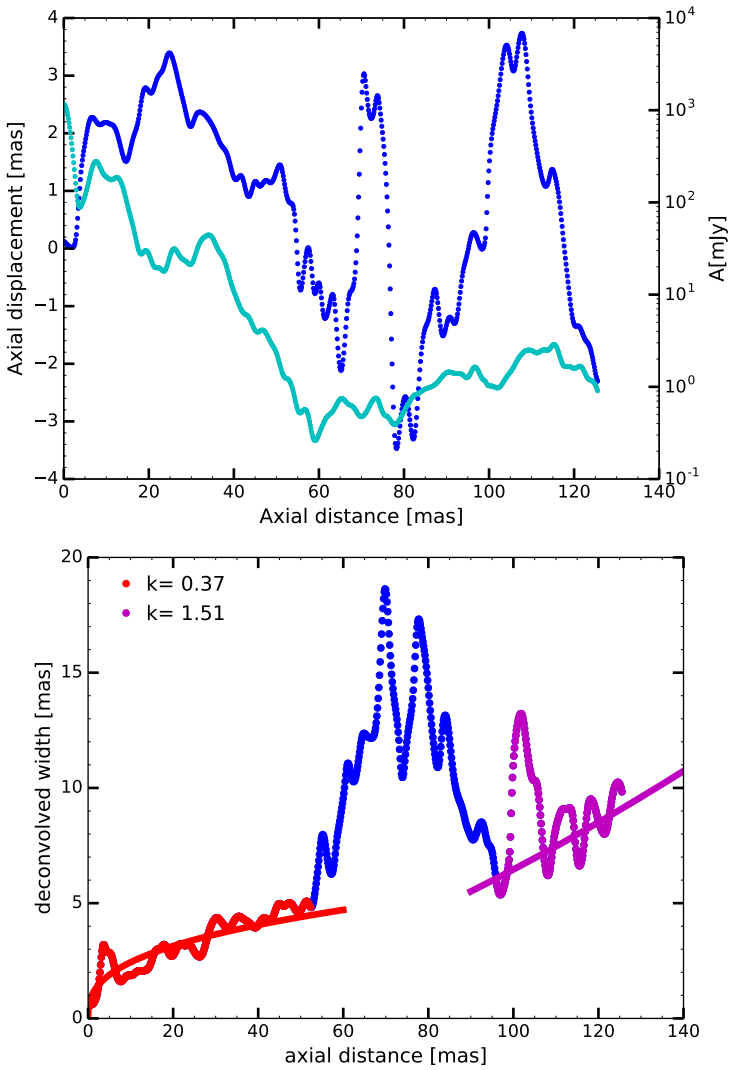

Figure 7.17: **Upper panel:** Offset (dark blue) and flux density (light blue) in the jet of 0836+710 as a function of the (projected) distance. **Lower panel:** Jet width in function of the (projected) distance. The red points indicate the inner region (< 60 mas) and its fit. The magenta points correspond to the region > 100 mas and its fit. The blue points correspond to the width that we did not consider for any of the fitting.

This allows us to calculate the average apparent opening angle, $\alpha_{\rm app}$, and average intrinsic opening angle, $\alpha_{\rm int}$, as follows:

$$\alpha_{\rm app} = 2 \arctan\left(\frac{0.5d}{r}\right), \qquad \alpha_{\rm int} = \alpha_{\rm app} \sin\theta. \tag{7.16}$$

For the region where $r < 60$ mas we obtain an average apparent opening angle of $\alpha_{\rm app} = 6.54°$ and $\alpha_{\rm int} = 0.37°$, while at distances $r > 100$ mas, we obtain an average apparent opening angle of $\alpha_{\rm app} = 3.43°$ and $\alpha_{\rm int} = 0.19°$. It can be seen that the apparent opening angle is lower by a factor of two in the outer region. This implies two possibilities for the behavior in the intrinsic opening angle. The first one is that it has also reduced by half. The second is that it remained constant, which implies a roughly twofold increase of the viewing angle at distances > 60 mas.

7.3 3C 273

In this section we describe the analysis perform for 3C 273. We first obtain the rotational and propagation speed of the source. Then, we study the source at different epochs using MOJAVE and Boston university data.

7.3.1 Rotational and propagation speeds of the instability patterns

The presence of instabilities and a double helical pattern in the flow were reported previously in this source (Lobanov & Zensus 2001). As we have more recent observations, we want to study the evolution of such structures. Thus, we calculate the jet ridgeline as explained in section 7.1. Since the RadioAstron image at 5 GHz showed only the brightest parts of the jet due to low sensitivity, we use the ground array image for our calculations. The ground array image at 5 GHz does not resolve the jet transversally, hence we can only compare the structure of the earlier 5 GHz VSOP image (Lobanov & Zensus 2001) by comparing the respective ridgelines obtained for both images from single gaussians fits to transverse brightness profiles. Figure 7.18 shows the location of the two ridgelines overploted on the ground array map (color scale) and the *RadioAstron* map (contours) from our observations. The figure shows that the jet ridgeline has changed over the 17 years between these observations. As the differences are large, this cannot be explained by the speed of the plasma alone, and significant jet rotation should be present.

The rotation of the flow direction can be measured by comparing the displacement in the $y-$direction after the ridgelines have been rotated. Since the data points of both ridgelines are not exactly in the same position for the axial distance and that corresponding to the VSOP observations has less data points than that of the *RadioAstron* observations, we fit a line is first fitted between to adjacent points for that of 2014, and then we take the value for the axial distance corresponding to the data point of that of 1997. Then, we calculate the difference in offset between the two ridgelines and calculate the speed. The result is shown in Fig. 7.19. A constant velocity is assumed for the propagation and it is represented by the straight line in the left panel. The residual variations once this line is subtracted correspond to the rotational velocity and are shown in the right

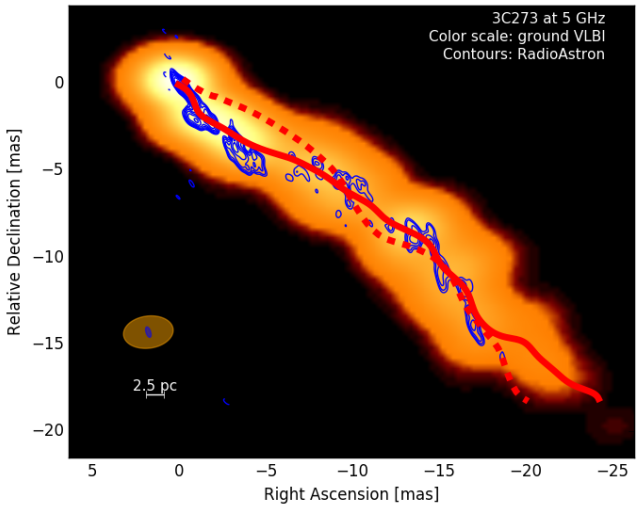

Figure 7.18: Ground array image (color scale) and *RadioAstron* map (contours) of 3C 273 at 5 GHz for the 2014 observations. Overplotted in red are the ridgelines from the ground array observations in 2014 (continous line) and from the VSOP image in 1997 (dashed line).

panel. The slope of the fitted line corresponds to the propagation speed and, given that the light speed at the redshift of 3C273 is $c = 0.103$ mas/yr, we obtain the pattern speed as:

$$v_p = 0.070 \pm 0.016c.$$

Looking now at the right panel of Fig. 7.19, we see a wave-like angular speed which maximum value is $0.5c$.

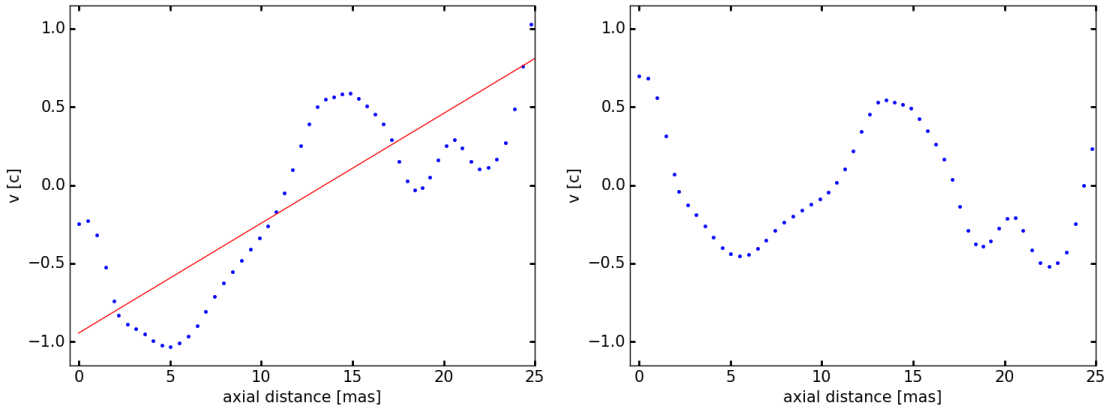

Figure 7.19: **Left panel :** Velocities for each axial distance in 3C 273. The line corresponds to the fit of the propagation speed. **Right panel :** rotational speed in 3C 273 after the linear fit related to the propagation velocity is substracted.

We can also calculate the value of the rotational speed with an alternative method, using the modelling of the ridgeline in the two epochs. Since the flow is rotating, we modify Eq. 7.6, taking into account a difference of phase in the most recent observations considering that the underlying modes have the same wavelengths at those distances in the two epochs:

$$\Delta\, r(z) = \sum_{i=1}^{N_{\rm mod}} a_i \sin\left(\frac{2\pi}{\lambda_i} x_i \;+\; \left(\psi_i + \frac{2\pi v \Delta t}{\lambda_i}\right)\right). \tag{7.17}$$

where Δt is the time interval.

Therefore, we use Eq. 7.6 and Eq. 7.17 for the fit of the 1997 and 2014 observations respectively. We first fit the ridgeline corresponding to the old VSOP observations and for the modelling of the 2014 data, we perform the fit using as guess parameters the wavelength, initial phase and amplitude of the modes obtained for the fit of the image from 1997. Figure 7.20 shows the fit results, while the obtained wavelengths are listed in Table 7.5. The wavelength of 19 mas is in complete agreement with one of the values obtained in Lobanov & Zensus (2001). The one of 49 mas is not reported in the paper, since the authors only modelled short scales which are not sensitive to the longest wavelengths. This method gives us a rotation speed of:

$$v = 0.43 \pm 0.02c.$$

This value is in agreement with the rotation curve found with the previous method. We do not calculate the propagation speed with this method, since we are only comparing the instability modes in the jet.

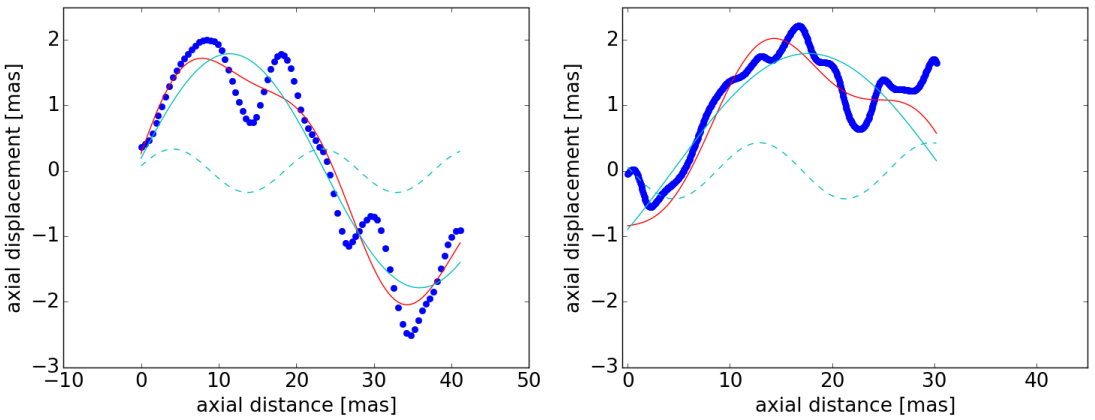

Figure 7.20: Fits by oscillatory structures to the jet ridgelines for the 1997 observations (left) and 2014 obaservations (right) of 3C 273 at 5 GHz. In each plot, the red line is the multi-mode fit and the blue lines represent contributions from the individual oscillatory modes. The dark blue line is the ridgeline resulting from the data.

Table 7.5: Results of the modeling of the Gaussian ridgeline of the 3C 273 ridgeline at 5 GHz ($\chi^2 = 2.4$) using two modes. See Fig. 7.20.

Mode	λ [mas]	a [mas]	ψ [°]
1	49 ± 4	1.8 ± 0.2	6 ± 10
2	19 ± 2	0.33 ± 0.16	13 ± 14

7.3.2 Effect of the components on the ridgeline structure

In this section we will report the effect on moving knots in a ridgeline performing a multiepoch analysis using public MOJAVE data ($\sim$ 90 epochs) and calculate the ridgeline for all of them. We observe, as in the case of 0836+710, the effect of moving components along the plasma on the underlying jet structure. Comparing the ridgeline for different epochs (Fig. 7.21), we can clearly see a feature disturbing its structure (for example between 2.5 mas and 5 mas in 1995). If we observe its behaviour with time, we can see that its position moves. However, its apparent speed is superluminal, and the plasma cannot move faster than c. Therefore, we check the position of all MOJAVE fitted components for the first epoch. We find that the position of this disturbance in the ridgeline was consistent with the position of one MOJAVE component. Following its position with time, we can see that the location of the component follows perfectly the location of the disturbance of the ridgeline (Fig. 7.21). We already saw in the case of 0836+710 (section 7.2.3) that a violent event, such as the interaction with of a moving shock, can disturb the equilibrium state of the ridgeline structure (Perucho et al. 2006). This is exactly what we observe in 3C 273 on a larger scale, with quite large offsets in the ridgeline caused by the existence of a component. Furthermore, we can see that once the component disappears, the underlying structure reverts back to its previous state before being disturbed by the component. This indicates that the jet flow can revert back to an equilibrium oscillatory state after a disturbance. Figure 7.22 shows the ridgeline for several epochs where the component is no longer affecting these scales, where it can be seen that the ridgelines have a consistent structure along the years. The component shown in Fig. 7.21 is the clearest example of this behaviour. The reason why other components are not seen to have such a clear effect could be their differences in brightness. Furthermore, this analysis shows how the component dissipates part of its energy as it moves in the flow, since this effect is stronger when it is closer to the core at this frequency. This is clearly visible in the last plot of Fig. 7.21, where the offset caused by the component is lower than that seen in the first plot.

Since monitoring of the source at 43 GHz is also available, we analyze all the epochs observed by the Boston University program as well ($\sim$ 100). Since the resolution is higher, the scale is much smaller than at 15 GHz. We also see in some cases a small disturbance on the underlying structure due to the moving

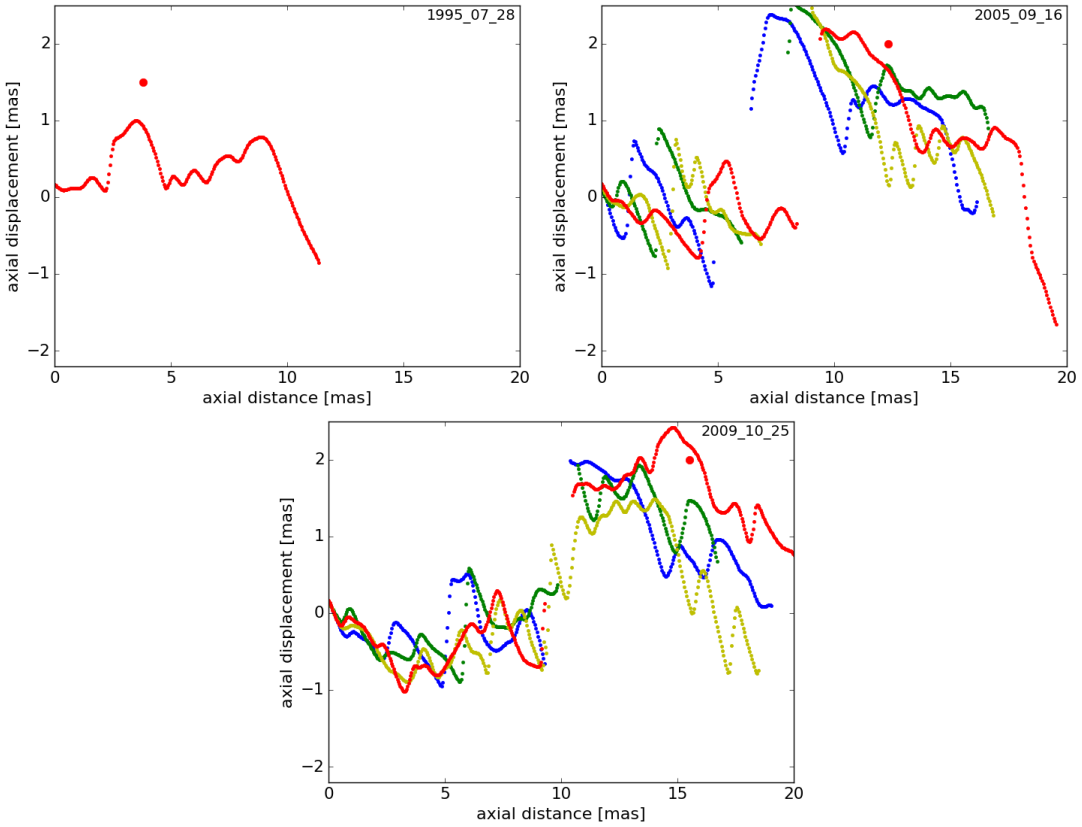

Figure 7.21: Ridgeline of 3C 273 at different epochs at 15 GHz. The epoch indicated in the legend corresponds to the red line. The red dot above the ridgeline corresponds to the location of a moving knot in the modelfiting made by the MOJAVE team (Lister et al. 2013). **Upper left panel:** Ridgeline corresponding to the July 1995 data. We can see a disturbance in the ridgeline between 2.5 mas and 5 mas. **Upper right panel:** Ridgeline corresponding to the July 1995 data (blue), September 1996 data (green), and August 1997 (red) . We can see that the disturbance in the ridgeline has moved and in the last epoch is between 5 mas and 6.5 mas. **Bottom panel:** Ridgeline corresponding to the September 2007 data (blue), September 2008 data (green), and October 2009 (red). The disturbance is now between 14 mas and 16 mas.

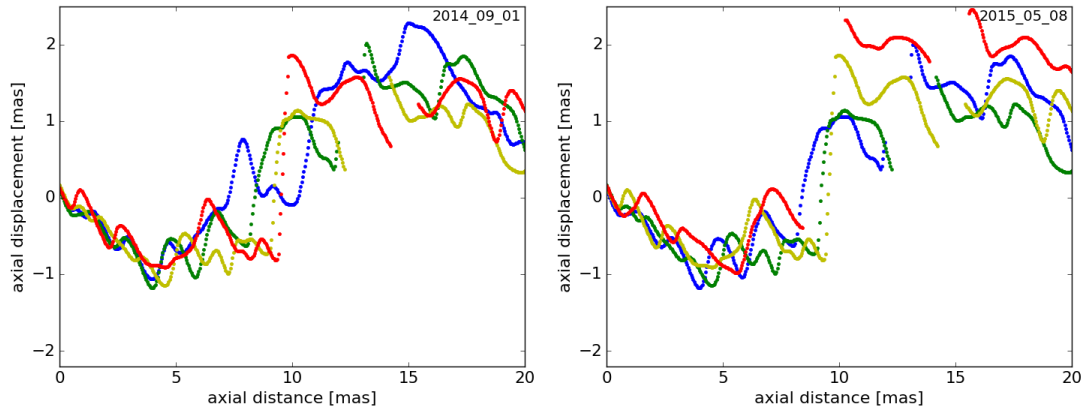

Figure 7.22: Ridgeline of 3C 273 at different epochs at 15 GHz. The epoch indicated in the legend corresponds to the red line. No clear disturbations in the flow are visible comparing the red lines between both plots. **Left panel:** Ridgeline corresponding to the April 2012 data (blue), February 2013 data (green), and September 2014 (red). **Right panel:** Ridgeline corresponding to the February 2013 data (blue), September 2014 data (green), and May 2015 (red).

components. Figure 7.23 shows this behaviour. However, due to the short scale, the components cannot be tracked for more than a few months as they away from the observed scales. This shows us that weaker components can also create small offsets, since with higher resolutions, we can see the disturbance of less strong components in the flow that we could not appreciate at low frequencies.

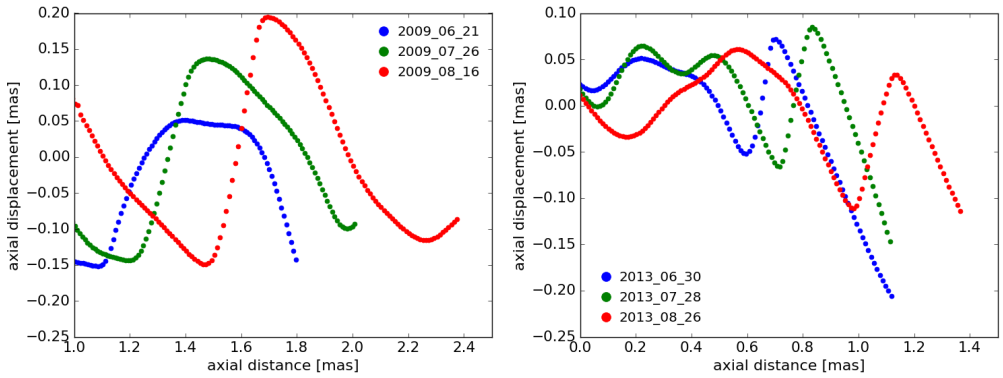

Figure 7.23: Ridgeline of 3C 273 at different epochs at 43 GHz. **Left panel:** Ridgeline corresponding to the June 2009 data (blue), July 2009 data (green), and August 2009 (red). Fast Displacements of the ridgeline are observed. **Right panel:** Ridgeline corresponding to the June 2013 data (blue), July 2013 data (green), and August 2013 (red). Fast Displacements of the ridgeline are observed.

7.3.3 Verification of the rotation speed using archival data

To prove that this rotating pattern is real, we consider all the ridgelines we calculated for the MOJAVE data. The observation of disturbances of the ridgeline due

to passing components has to be taken into account before obtaining any kind of rotation speed. First, the rotation of the flow is evident already at a visual inspection, since the direction of the ridgeline has clearly changed with time within the first 4-5 mas. Choosing a location in the first few milliarseconds, where the SNR is higher and the jet is always well detected, we can obtain the rotation speed of the flow in order to confirm the observed rotation at 5 GHz. Using the first method described for the case of the 5 GHz images, which consists in compare the offset positions of the ridgeline at two dates, and selecting epochs in which components had a weaker effect, we calculate an angular speed. We remark that in order to do this calculation we need to select epochs with large enough time difference, since this leads to better results. The resulting rotation speed ranges between -0.45c and 0.5c (Fig. 7.24). It is worth noting that the speed calculation performed at distances larger than 5 mas may be affected by the presence of a component. Due to this, we reduce the studied interval to the inner 5 mas leading to the peak of the rotation speed at ~ -0.45c. This value is in agreement with the value obtained for the 5 GHz images in section 7.3.1. We did not repeat the analysis for the Boston University data since their scales are much smaller, of only a few milliarseconds.

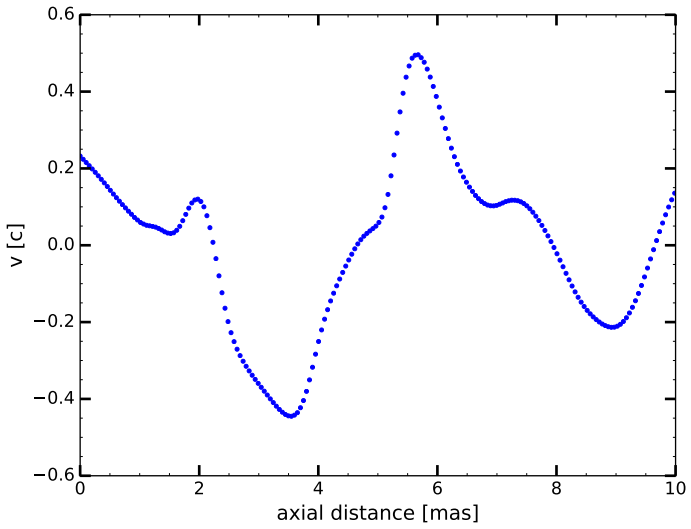

Figure 7.24: Rotational speed from the MOJAVE images of 3C 273 calculated using the images from 1996 and 2013. The peak at 6 mas is partly influenced by a component. The corresponding propagation speed is $v_p = 0.05 \pm 0.02$c.

7.3.4 Double peaked structure at 1.6 GHz

Besides the data analyzed in this thesis, we also look to the data analyzed by Gabriele Bruni et al. at L Band as part of the RadioAstron polarization Key Science Program. We perform transversal cuts of the jet as described in section 7.1. The transversal structure of the source shows a clear double peaked profile at almost all distances, as seen in Fig.7.26. We perform the cuts starting at a distance of ~ 2.5 mas as the SNR of the second peak is not high enough before this point. The resulting double ridgeline in the contour map is shown in Fig. 7.25. As in the case of 0836+710, we have two possible explanations for the existences of such profiles. The first one is the existence of a limb-brightened flow, produced due to the interaction of the jet with the ambient medium. The second could be the existence of elliptical modes in the jet as suggested by Lobanov & Zensus (2001) and caused by the presence of Kelvin-Helmholtz instability.

It is also worth noting the different structures observed between the 1.6 GHz image and the 5 GHz image. While in the 5 GHz image we seem to be detecting the jet spine, in the 1.6 GHz image we observe the limbs. Another possible explanation would be that the filament observed at the high frequency corresponds to the brightest of the two peaks.

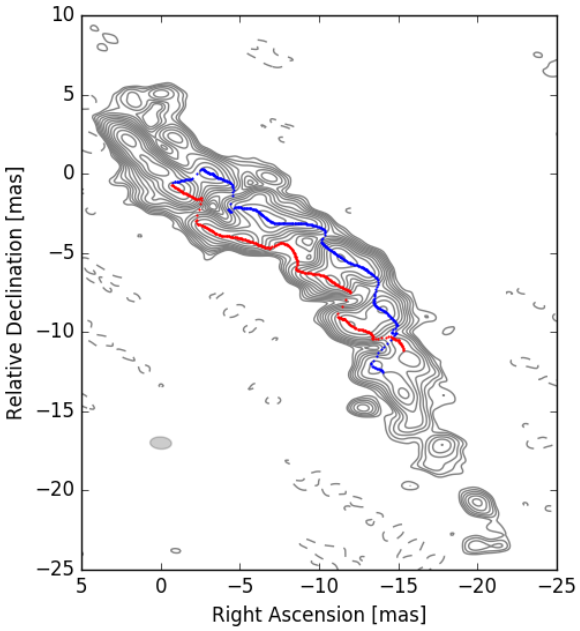

Figure 7.25: *RadioAstron* image of 3C 273 at 1.6 GHz performed by Bruni, the contour levels are drawn at $(-1, 1, \sqrt{2}, 2, \ldots)$ times 15 mJy/beam. Overplotted in the map are the peaks of the double gaussian profile existent in the data.

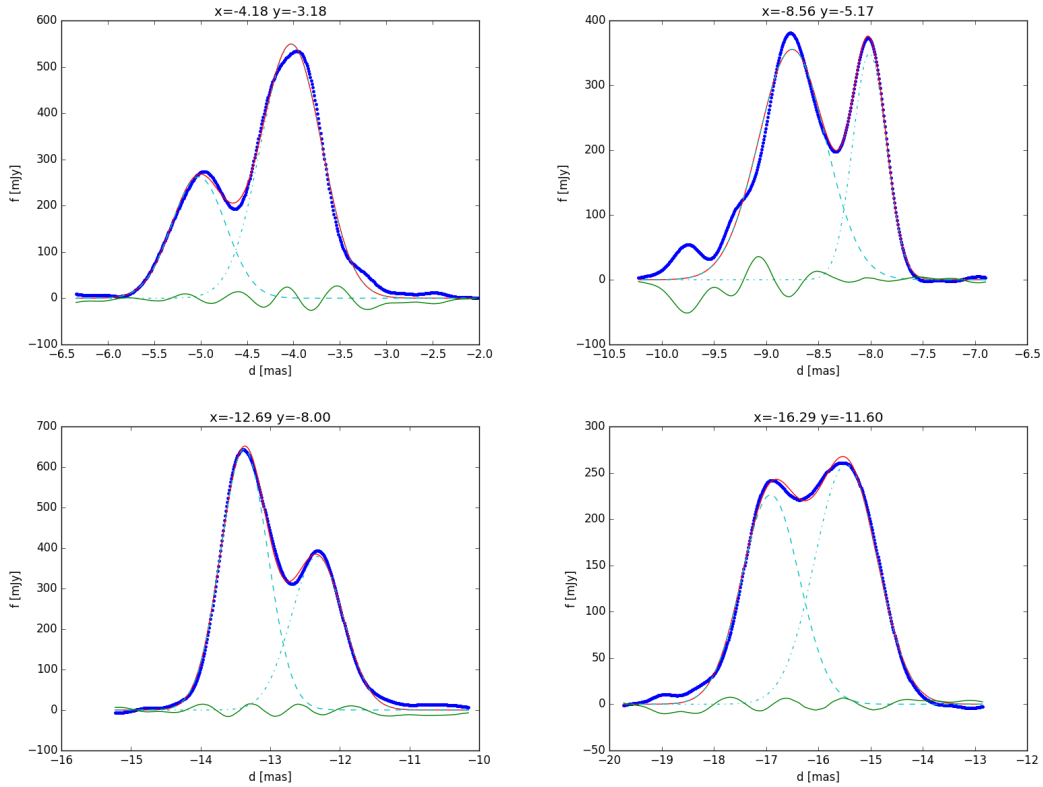

Figure 7.26: Double gaussian fits of the L Band observations of 3C 273. The double gaussian structure of the source is clearly present in all of them. **Top left panel:** cut at a projected distance of 5 mas. **Top right panel:** cut at a projected distance of 10 mas. **Bottom left panel:** cut at a projected distance of 15 mas. **Bottom right panel:** cut at a projected distance of 20 mas.

Chapter 8

Numerical simulations

This Chapter is partially reproduced in Vega-García et al. a submitted to A&A.

This chapter focuses on physical modelling of the asymmetric structure observed in the *RadioAstron* image at 22 GHz of 0836+710 (Fig. 5.9). First, we discuss the possible origin of these asymmetries. This discussion is complemented by magnetohydrodynamical numerical simulations in order to try to reproduce the observed structure.

8.1 Asymmetries

The 22 GHz image of 0836+710 presented in Fig. 5.9 shows an apparent, strongly asymmetric transverse structure of the flow. This appearance may, in part, be due to the limited dynamic range (estimated to be about 75:1) of the images, or result from differential Doppler boosting of the flow within the jet. Following Rybicki & Lightman (1979) (see also Aloy et al. 2000; Lyutikov et al. 2005; Clausen-Brown et al. 2011), the bright side of the jet changes from top to bottom at a critical viewing angle given by $\cos(\theta_{\rm r}) = \beta_{\rm j}$, for a helical magnetic field at its maximum asymmetry, achieved with a pitch angle of 45°. In the case of 0836+710, this corresponds to $\theta_r = 4°$. Therefore, the top side of the jet should be brighter at the source viewing angle of $3° < \theta_{\rm r}$. This is actually the case, as observed in Fig. 5.9, where we see a change of dominant brightness, from the bottom side in the beginnig to the top side at larger distances, implying a helical field oriented counterclockwise (e.g. Aloy et al. 2000). The maximum asymmetry is obtained at $\theta^{'} = \phi_B$, with $\theta^{'}$ the viewing angle in the jet reference frame and $\phi_B = \arctan B^{\phi}/B^{z}$, the pitch angle in the fluid's frame (Aloy et al. 2000). Fixing the viewing angle to 3° and $\beta_{\rm j}$ to that corresponding to Lorentz factor $\gamma = 12$ ($\beta_{\rm j} = 0.99652$), we obtain $\phi_B \simeq 64°$ for a maximum asymmetry. This pitch angle implies the presence of a helical field with a slightly dominating toroidal component. Nonetheless, the asymmetry in emission could also indicate a physical asymmetry in the jet properties, revealing

the presence of distinct regions, varying across the jet channel with time. This has been revealed by a number of VLBI observations that show components only partially filling the jet cross-section, where the jet is only observed in its full width in stacked images over many epochs (e.g. Lister et al. 2013; Beuchert et al. 2018).

We can take the dynamic range of the 22 GHz image as a lower limit of the difference in brightness across the jet. Asymmetries in the transverse structure of the jet emission could be caused by compression due to jet oscillation or by pressure difference across the flow (Perucho et al. 2007, 2012b). However, this effect alone cannot explain such a difference in brightness, if the perturbation is still developing in the linear regime (Perucho et al. 2005, 2006), and the effect of the magnetic field orientation in the jet frame on the synchrotron emissivity needs to be taken into account. Non-linear effects such as large instability amplitudes, are not expected so close to the jet base, unless they respond to the development of short-wavelength, fast-growing modes (e.g., Perucho & Lobanov 2007). However, in that case, we would expect a persistently symmetric emissivity profile across the flow. We thus exclude the option of instability patterns generating this strong asymmetry in brightness.

We focus our discussion on the possibility that the asymmetry (of the order of the dynamic range of the observation), is produced by differential Doppler boosting. The observed flux density is given by

$$S_\nu \propto \delta^{2-\alpha}\, B'^{1-\alpha}\, \sin(\theta'_B), \tag{8.1}$$

where D is the Doppler factor, B' and θ'_B are the intensity of the magnetic field and the angle between the magnetic field and the line of sight in the fluid frame, respectively, and α is the spectral index ($S_\nu \propto \nu^\alpha$). In this expression, we ignore the dependence on the particle energy distribution (in particular, on the Lorentz factor cutoffs of this distribution, $\gamma_{\rm min}$ and $\gamma_{\rm max}$, which introduce dependencies on other parameters, such as the particle number density). Recalling that the inner jet region has a flat spectral index, $\alpha \simeq 0$, and assuming that the total magnetic field intensity (as given by both the toroidal and poloidal components of the field) does not change much with the toroidal angle (implicitly assuming axisymmetry), we obtain the following expression for the brightness ratio between the top, brighter part of the jet (indicated with the superscript t), and the bottom part of the jet (superscript b) in terms of the differential Doppler factors, δ:

$$\frac{S^{\rm t}_\nu}{S^{\rm b}_\nu} \simeq \frac{(\delta^{\rm t})^2 \sin(\theta'_B)^{\rm t}}{(\delta^{\rm b})^2 \sin(\theta'_B)^{\rm b}} \sim 100\,. \tag{8.2}$$

Taking into account that $\sin(\theta'_B) = \delta\, \sin(\theta_B)$ (the primed value refers to the jet rest frame), we obtain:

$$\frac{S^{\rm t}_\nu}{S^{\rm b}_\nu} \simeq \frac{(\delta^{\rm t})^3 \sin(\theta_B)^{\rm t}}{(\delta^{\rm b})^3 \sin(\theta_B)^{\rm b}} \sim 100\,. \tag{8.3}$$

$\delta^{\rm t}$ and $\delta^{\rm b}$ can be different only if there is a toroidal component of the velocity and henceforth the velocity vector changes across the jet.

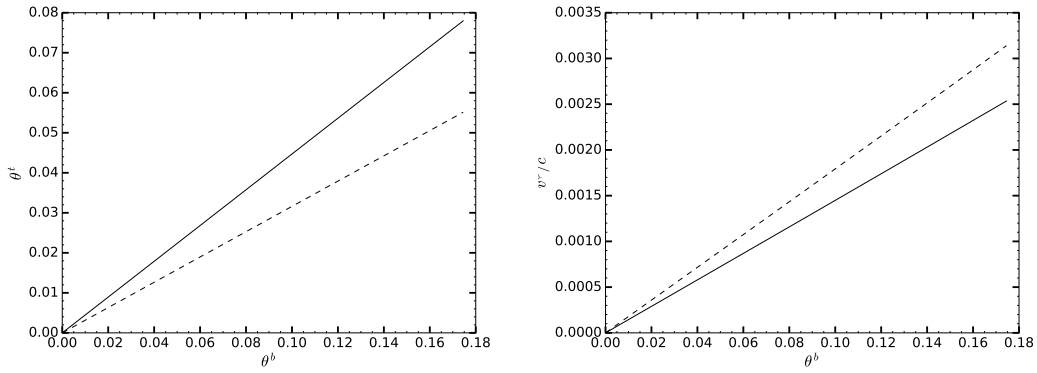

Figure 8.1: **Left panel:** $\theta^{\rm t}$ versus $\theta^{\rm b}$ required to explain a Doppler factor ratio of 5 (solid line) and 10 (dashed line). **Right panel:** Relative azimuthal velocity versus $\theta^{\rm b}$ for Doppler factor ratio of 5 (solid line) and 10 (dashed line).

Assuming that the axial velocity component $v_z \simeq c$ is constant across the jet, the brightness asymmetry can be ascribed to the top-to-bottom change of the angle $\theta_{\rm v}$ between the velocity vector and the line of sight, so that, from Eq. 8.3:

$$\frac{\delta^{\rm t}}{\delta^{\rm b}} \simeq \frac{1-cos(\theta_{\rm v}^{\rm b})}{1-cos(\theta_{\rm v}^{\rm t})} \simeq 5\left(\frac{\sin(\theta_B)^{\rm b}}{\sin(\theta_B)^{\rm t}}\right)^{1/3}, \tag{8.4}$$

which allows us to derive $\theta_{\rm v}^{\rm t}$ in terms of $\theta_{\rm v}^{\rm b}$ if we approximate $\left(\sin(\theta_B)^{\rm b}/\sin(\theta_B)^{\rm t}\right)^{1/3} \sim 1$. The result is shown in the left panel of Fig. 8.1 for the Doppler factor ratios of 5 (solid line) and 10 (dashed line). In the plot, $\theta_{\rm v}^{\rm b}$ spans from 0° to 10° in the observer's frame. The required changes in the viewing angle can give estimates of the relative values of the toroidal velocity component, v_ϕ, as $v_\phi/v_z = \tan(\psi)$, with ψ defined as the deprojection of the half-angle formed by the velocity vectors on both sides of the jet.[1] This ratio is plotted in the right panel of Fig. 8.1 for the same Doppler factor ratios. The plots show that small toroidal velocities can result in sufficiently large changes in the Doppler factor of different regions in the flow.

If, on the contrary, we assume that $\delta^{\rm t} \simeq \delta^{\rm b}$, then the brightness asymmetry has to be given by:

$$\frac{S_\nu^{\rm t}}{S_\nu^{\rm b}} \simeq \frac{\sin(\theta'_B)^{\rm t}}{\sin(\theta'_B)^{\rm b}} \simeq 100\,. \tag{8.5}$$

Taking into account that this ratio $\sin(\theta'_B)^{\rm t}/\sin(\theta'_B)^{\rm b} \simeq \sin(\theta_B)^{\rm t}/\sin(\theta_B)^{\rm b}$ ($\delta^{\rm t} \simeq \delta^{\rm b}$) and that $0 \leq \sin(\theta_B) \leq 1$, the fraction can only give a value $\simeq 100$ if one

[1] We have assumed a mean viewing angle of 3° to deproject the half-angle between the velocity vectors.

or both values of θ_B are very close to 0°, where the sine can take values differing in several orders of magnitude. We find this coincidence of both angles aligned to such an accuracy less probable than the presence of small toroidal velocities. Furthermore, a toroidal component of velocity has been shown to naturally arise in RMHD simulations of expanding jets, due to the Lorentz force (Martí 2015). Finally, the required azimuthal velocities are compatible with the fitted axial velocity (Lorentz factor) given in previous works for this jet, in terms of causality. We can conclude that a small toroidal velocity has to be present in the jet flow to explain the brightness asymmetry.

8.2 1D MHD simulations

Our objective is to verify if the structure observed in the 22 GHz *RadioAstron* image of 0836+710 can be explained with the existence of azimuthal velocity component in the jet, as described in the previous section. To this end, we perform numerical simulations using the 1D-MHD approximation of Martí (2015). This is a radial-cylindrical, time dependent, second-order conservative, finite-volume code based on high-resolution shock-capturing techniques. The main characteristics of the code are:

1. cell reconstruction using a MC limiter.

2. computation of numerical fluxes using a HLLC Riemann solver (Mignone & Bodo 2006) taking in account an hypothetical shock formation (since shocks are reflected by discontinuities in the solution)

3. time advance. It is performed with the third-order TVD-preserving Runge-Kutta algorithm (Shu & Osher 1988, 1989) with CFL = 0.3.

The numerical code considers a magnetized and axisymmetric jet, described using cylindrical coordinates (r, z, ϕ), that is propagating through a non-magnetized ambient medium. Since the jet is assumed to be axisymmetric, there will be no dependence on the azimuthal cylindrical coordinate. A slab geometry is also assumed. This implies that $B^r = 0$, and, together with the assumption of a stationary flow, $v^r = 0$. The conditions of the ambient medium are: for the velocity $v_a^r = v_a^\phi = v_a^z = 0$, for the magnetic field $B_a^r = B_a^\phi = B_a^z = 0$, for the density $\rho_a = 1$, and for the pressure $p_a =$ct, i.e., we will not consider an ambient medium with a pressure profile.

The models are computed using the approach of Komissarov et al. (2015). It is based on one-dimensional time-dependent equations where the axial coordinate is considered as the temporal coordinate, since for highly relativistic jets $z \approx ct$. As mentioned in section 3.2, this approximation is valid if the radial dimension is much smaller in comparison with the axial dimension. Furthermore, the radial

and azimuthal components of the velocity should be much smaller than the axial speed ($v^r, v^\phi \ll v^z \simeq c$) and the radial component of the magnetic field should be much smaller than its azimuthal and axial components ($B^r \ll B^\phi, B^z$). In order to perform the simulations, we use the steady-state configuration of a jet which has given injection parameters at the base of the grid and propagates through the ambient medium, programmed around it. Since we are using a 1D approach, the boundary conditions from 2D simulations need to be modified accordingly. In particular, as we replace the axial coordinate with time, we need to impose time-dependent conditions. In order to do this, we need to track the point that separates the jet from the external medium and reset the ambient gas parameters at each computational time step. To track the jet surface, the code uses a version of the level-set method (Osher & Sethian 1988) consisting in introducing a passive scalar satisfying the continuity equation.

As in the case discussed in Martí (2015); Martí et al. (2016), we can find the equilibrium profile of one variable, in our case gas the pressure, p, as a function of the others, in our case ρ, v^ϕ, v^z, B^ϕ, and B^z, by introducing below the equation of transversal equilibrium. For the density, axial magnetic field and axial velocity, we use top-hat profiles.

$$\rho(r) = \begin{cases} \rho_j, & 0 \le r \le 1, \\ 1 & r > 1. \end{cases} \tag{8.6}$$

$$v^z(r) = \begin{cases} v^z_j, & 0 \le r \le 1, \\ 1 & r > 1. \end{cases} \tag{8.7}$$

$$B^z(r) = \begin{cases} B^z_j, & 0 \le r \le 1, \\ 1 & r > 1. \end{cases} \tag{8.8}$$

For the azimuthal magnetic field we assume the profile:

$$B^\phi(r) = \begin{cases} \dfrac{2B^\phi_{j,m}\left(r/R_{B^\phi_{,m}}\right)}{1+\left(r/R_{B^\phi_{,m}}\right)^2} & 0 \le r \le 1, \\ 0 & r > 1. \end{cases} \tag{8.9}$$

where the parameter $R_{B^\phi_{,m}}$ is the value for which the linearly growing toroidal magnetic field (when $r \ll R_{B^\phi_{,m}}$) reaches its maximum, $B^\phi_{j,m}$. The magnetic field decreases as $1/r$ when $r \gg R_{B^\phi_{,m}}$, reaching zero at the boundary.

We modify the code to account for a small value of the rotation speed. In order to do that, we violate the assumptions used by the 1D code (see Section 3.2) in v^ϕ, assumed to be zero. However, we will only consider $v^\phi \ll v^z \simeq c$. We contemplate three different models for v^ϕ:

1. without rotation, $v^{\phi}(r) = 0$
2. with rigid rotation,

$$v^{\phi}(r) = \begin{cases} v^{\phi}_{j,m} r, & 0 \leq r \leq 1, \\ 0 & r > 1. \end{cases} \tag{8.10}$$

3. with differential rotation. We consider a smooth transition between inner jet core with rigid rotation and a sheath with a Keplerian rotation profile for $R_{v^{\phi}_{,m}} \ll 1$.

$$v^{\phi}(r) = \begin{cases} \dfrac{3 v^{\phi}_{j,m} \left(r / R_{v^{\phi}_{,m}} \right)}{1 + 2 \left(r / R_{v^{\phi}_{,m}} \right)^{3/2}} & 0 \leq r \leq 1, \\ 0 & r > 1. \end{cases} \tag{8.11}$$

Then, the equation of equilibrium can be written as:

$$\frac{dp^*}{dr} = \frac{\rho h^* \gamma_j^2 (v^{\phi})^2 - (B^{\phi})^2}{r} \tag{8.12}$$

where h^* is the specific entalphy including the magnetic field and p^* is the total pressure.

We solve Eq. 8.12 for the cases with and without rotation.

We consider different jet models consistent with the jet structure in 0836+710. The common parameters are the pitch angle $\phi_B = 45°$, the radial position at maximum of the toroidal field, $R_{\mathrm{B}^{\phi}_{,\mathrm{m}}} = 0.37$ (Martí 2015), and the Lorentz factor, $\gamma_{=}12$. We consider initial rotational velocities of $v^{\phi}_{j,m} = 0.001$ and of $v^{\phi}_{j,m} = 0.01$. The jet radius used is 0.6 mas. We also consider different overpressure factors, namely $d_k = 1, 1.2, 1.4$, and 2, to force jet expansion. When we use the third model for the rotation profiles, the junction radius is $R_{v^{\phi}_{,m}} = 0.25$ (Martí 2015). Unlike Martí et al. (2016), we use a narrow shear layer with $m = 16$, as obtained in Chapter 7.2.4.b. Table 8.1 shows the different considered parameters for the different simulations. We consider that both the jet and the ambient medium are a perfect gas. The adiabatic index in each model, Γ, is given in Table 8.1. We run the simulations considering the three different kinds of rotation speed.

We calculate the jet magnetosonic Mach number, M_{ms}, using Eq. 3.16 and the jet internal energy with $\epsilon_j = \frac{p}{(\Gamma - 1)\rho}$. We plot each model in the $M_{\mathrm{ms}} - 1/\epsilon_j$ plane (Martí 2015; Martí et al. 2016). This plane allows to identify several jet regimes: kinetically dominated, magnetically dominated or hot jets. Kinematically dominated jets have $\epsilon_j \beta_m < c^2$ and $\epsilon_j < c^2$, where $\epsilon_j \beta_m$ is the specific magnetic energy. Magnetically dominated jets fall into the region where $\beta_m > 1$ and $\epsilon_j \beta_m > c^2$ and

Table 8.1: Initial parameters defining the different simulation models

Model	ρ_j [g/cm^3]	Γ	p_a	$B^{\phi}_{,m}$	B^z
JL01	10^{-26}	1.36	111.856	4.551	3.704
JL02	10^{-27}	1.336	111.856	14.371	11.697
JL03	10^{-26}	1.36	5.593	1.971	1.604
JL04	10^{-27}	1.336	55.928	6.186	5.034
JL05	10^{-25}	1.56	0.559	0.946	0.770

$\epsilon_j > c^2$. Finally, hot jets are those with $\epsilon_j > c^2$ and $\beta_m < 1$. We show the corresponding parameters in of each model in Table 8.2, Table 8.3, and Table 8.4. The corresponding $M_{\rm ms} - 1/\epsilon_j$ plots are shown in Fig. 8.2 for each of the simulations, grouped according to the different values of the adiabatic index. In the plot it is only possible to distinguish one data point per model instead of three, since the values of the magnetosonic Mach number and jet internal energy are quite close for the three different rotation models. If we consider all models together, we can see that they sample different regions in this plane, but fall predominantly in the region of hot jets. The models JL01, JL02, JL03, and JL04 correspond to this region. The model JL05 is kinetically dominated.

We also show, as an example, some of the maps of the physical variables obtained from the simulations for the kinematically dominated model JL05 and the hot jet JL02. We plot first the maps, only for the model JL05, for the case of pressure equilibrium between the jet and the ambient medium (Fig. 8.3) and an overpressure factor of 1.2 and 2, in the case of non rotation in the flow (Fig. 8.3 and 8.5 respectively), to show how the overpressure factor affects the jet. Looking at Fig. 8.3 we can see that if there is pressure equilibrium between the ambient medium and the jet, recollimation shocks do not form and the shape of the jet does not change. Adding an overpressure factor (Figs. 8.4 and 8.5), and therefore breaking the equilibrium between the ambient and the plasma, allows recollimation shocks to form and the shape of the jet changes, being slightly wider at the end of the simulated length. Figures 8.5 through 8.14 show the jet models JL05 and JL02, both with an overpressure factor of 2.

We describe now the differences between a kinetically dominated jet (JL05, see Figs. 8.5, 8.6 and 8.7) and a hot jet (JL02, see Figs. 8.10, 8.11 and 8.12). Looking at the Lorentz factor, we see larger differences along the jet for the hot jet than for the kinetically dominated jet. In the case of the hot jet, the Lorentz factor increased by a factor of 3 in each of the three models with different rotation speeds. In the case of a kinetic flux dominated jet, this factor is reduced to two, because there is less magnetic or internal energy to be converted into kinetic energy, whereas in the case of a hot jet larger changes in the Lorentz factor are produced by variations of the jet internal energy (Martí 2015; Martí et al. 2016). This proves that the jet dynamics are controlled by v^z and since $v^{\phi} \ll 1$ they are not affected

significantly by this velocity component.

At last, if we consider the azimuthal velocity, our main parameter of interest, we can see that even those models without initial rotation show azimuthal speeds of the order of those required to explain the observed asymmetries, i.e., $v^{\phi} \sim 0.001$ (see section 8.1), or even larger, which naturally arise from our setups. This is due to the Lorentz force (see Chapter 2 and also Martí et al. (2016), whose azimuthal component in cylindrical coordinates and for an axisymmetric flow is:

$$F_L^{\phi} = B^z \frac{\partial B^{\phi}}{\partial z} + \frac{B^r}{r} \frac{r \partial B^{\phi}}{\partial r} + \left(v^r B^z + v^z B^r\right) \rho_e \tag{8.13}$$

where ρ_e is the electric charge density.

Equation 8.13 shows that azimuthal speeds will grow in the flow when the jet expands and $B^r \neq 0$. The values of the azimuthal speed in the flow are larger for the cases where a rotation model has been considered (rigid or differential rotation). In the case of JL05D, the model which shows higher azimuthal speed is the model with differential rotation, showing maximum velocities a factor of 4 higher than those of the model without including rotation at the inlet, whereas the model with rigid rotation shows a maximum speed a factor of 2 higher. We see the same for the model JL02D, which shows slightly larger maximum azimuthal speeds. To better compare the models, we calculate the Doppler factor taking in account the rotation. Since the rotation effects are better seen in the case where the initial rotation speed was $v^{\phi}_{j,m} = 0.01$, we center on those cases for the models JL02D and JL05D (Figs. 8.13, 8.14,8.8, and 8.9), since the differences are much less visible when $v^{\phi}_{j,m} = 0.001$. The Doppler factor value is similar for the hot jet (JL02) and the kinetic flux dominated jet (JL05). We can appreciate clear differences between the evolution of the Doppler factor for the different models of rotational speeds considered. For the case of the rigid rotation, we see a slow spine, with the Doppler factor increasing towards the boundary. At the boundary, the Doppler factor drops fast. For the case of differential rotation, we can see a slow spine, surrounded by faster flow, which then decelerates to an intermediate speed between the one of the spine and that of the faster region. At the boundary, again, its value decreases fast.

More detailed simulations including the emission will have to be performed in order to check if the considered rotation models can reproduce the actual brightness asymmetry observed in the VLBI image of 0836+710 at 22 GHz with *RadioAstron*. In those simulations, we will use the jet parameters of 0836+710, such as the synchrotron spectrum we obtained in section 6.2.2.d. We will consider different jet viewing angles around the $\theta = 3°$ value reported in the literature (Otterbein et al. 1998) to check if we obtain a similar asymmetry (see section 8.1). For the best jet model, we will produce a synthetic map using the details of the *RadioAstron* observations of 0836+710.

Table 8.2: Parameters defining the jet models without rotation

Model	d_k	$M_{\rm ms}$	β_m	ϵ_j [c^2]	$\beta_m\epsilon_j$ [c^2]
JL01A	1.0	15.29	0.066	292.55	19.24
JL01B	1.2	15.41	0.054	354.88	19.24
JL01C	1.4	15.49	0.046	417.22	19.24
JL01D	2.0	15.64	0.032	604.21	19.24
JL02A	1.0	9.20	1.58	129.35	204.46
JL02B	1.2	10.53	1.04	195.95	204.63
JL02C	1.4	11.45	0.78	262.55	204.73
JL02D	2.0	13.05	0.44	462.36	204.88
JL03A	1.0	13.93	0.301	12.00	3.61
JL03B	1.2	14.26	0.239	15.11	3.61
JL03C	1.4	14.50	0.198	18.23	3.61
JL03D	2.0	14.93	0.131	27.58	3.61
JL04A	1.0	14.07	0.30	128.77	37.96
JL04B	1.2	14.52	0.23	162.08	37.97
JL04C	1.4	14.84	0.19	195.38	37.97
JL04D	2.0	15.43	0.13	295.28	37.98
JL05A	1.0	13.71	1.13	0.47	0.53
JL05B	1.2	13.30	0.79	0.67	0.53
JL05C	1.4	12.98	0.61	0.87	0.53
JL05D	2.0	12.36	0.36	1.47	0.53

Table 8.3: Parameters defining the jet models with rigid rotation

Model	d_k	$M_{\rm ms}$	β_m	ϵ_j [c^2]	$\beta_m\epsilon_j$ [c^2]
JL01A	1.0	15.29	0.066	292.55	19.26
JL01B	1.2	15.40	0.054	354.88	19.26
JL01C	1.4	15.49	0.046	417.22	19.26
JL01D	2.0	15.64	0.032	604.21	19.26
JL02A	1.0	9.20	1.58	129.35	204.65
JL02B	1.2	10.53	1.05	195.95	204.81
JL02C	1.4	11.44	0.78	262.55	204.90
JL02D	2.0	13.05	0.44	462.36	205.03
JL03A	1.0	13.93	0.301	12.00	3.61
JL03B	1.2	14.26	0.239	15.11	3.61
JL03C	1.4	14.50	0.198	18.23	3.61
JL03D	2.0	14.93	0.131	27.58	3.61
JL04A	1.0	14.07	0.30	128.77	37.99
JL04B	1.2	14.52	0.23	162.08	38.00
JL04C	1.4	14.84	0.20	195.38	38.00
JL04D	2.0	15.43	0.13	295.28	38.01
JL05A	1.0	13.71	1.13	0.47	0.53
JL05B	1.2	13.29	0.80	0.67	0.53
JL05C	1.4	12.98	0.61	0.87	0.53
JL05D	2.0	12.36	0.36	1.47	0.53

Table 8.4: Parameters defining the jet models with differential rotation

Model	d_k	$M_{\rm ms}$	β_m	ϵ_j [c^2]	$\beta_m\epsilon_j$ [c^2]
JL01A	1.0	15.29	0.066	292.55	19.27
JL01B	1.2	15.41	0.054	354.88	19.27
JL01C	1.4	15.49	0.046	417.22	19.27
JL01D	2.0	15.64	0.032	604.21	19.27
JL02A	1.0	9.20	1.58	129.35	204.77
JL02B	1.2	10.53	1.05	195.95	204.92
JL02C	1.4	11.44	0.78	262.55	205.01
JL02D	2.0	13.05	0.44	462.36	205.13
JL03A	1.0	13.92	0.301	12.00	3.61
JL03B	1.2	14.26	0.239	15.11	3.61
JL03C	1.4	14.50	0.198	18.23	3.61
JL03D	2.0	14.93	0.131	27.58	3.61
JL04A	1.0	14.06	0.30	128.77	38.02
JL04B	1.2	14.52	0.24	162.08	38.02
JL04C	1.4	14.84	0.20	195.38	38.02
JL04D	2.0	15.43	0.13	295.28	38.02
JL05A	1.0	13.70	1.13	0.47	0.53
JL05B	1.2	13.29	0.80	0.67	0.53
JL05C	1.4	12.97	0.61	0.87	0.53
JL05D	2.0	12.36	0.36	1.47	0.53

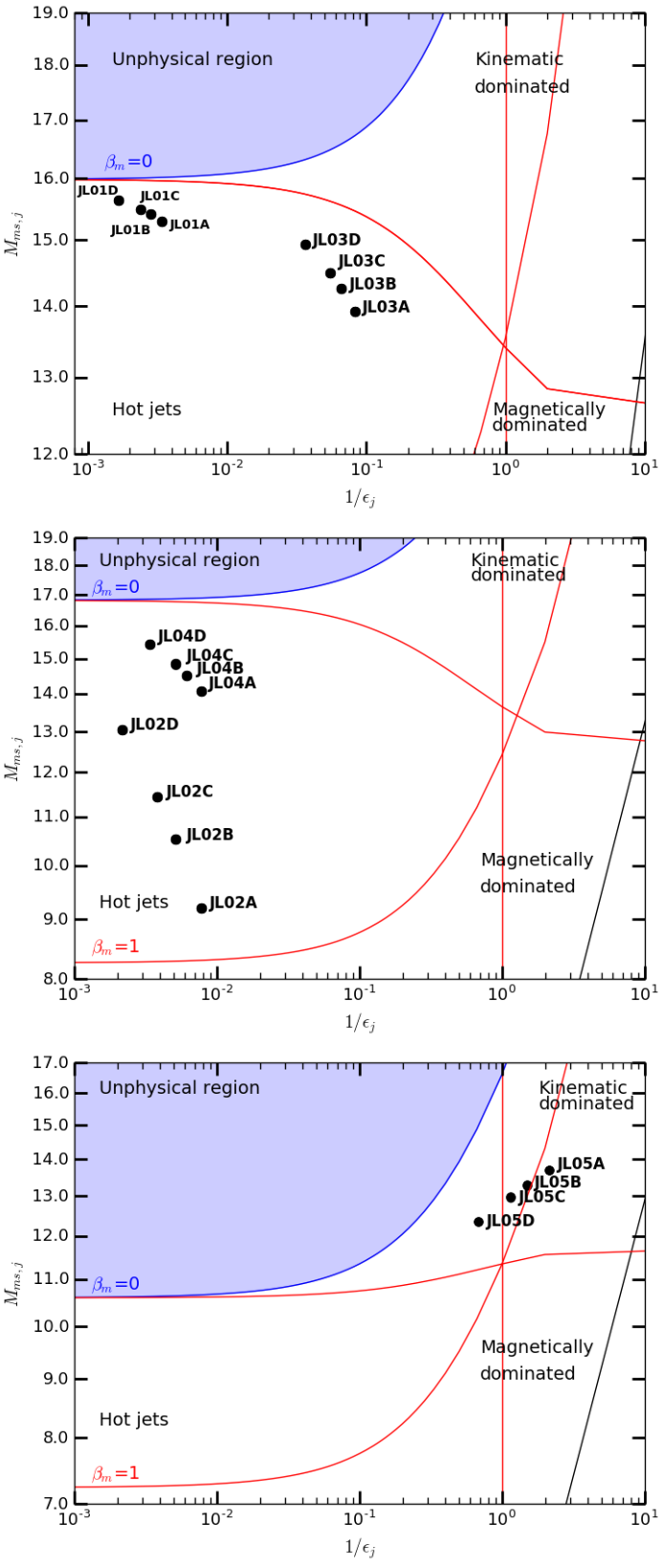

Figure 8.2: Run models in the $M_{\rm ms} - 1/\epsilon_j$ for a jet with 0836+710 speed, $v_j = 0.9965$. Drawn are lines of constant magnetization (0, 1, 10). The three red lines correspond to$\rho_j = \rho_j\epsilon_j$, $b_j^2 = \rho_j\epsilon_j$ and $b_j^2 = \rho_j$ and help us to distinguish different kind of jets: kinetically dominated jets, magnetically dominated jets, cold, and hot jets. The unphysical models with negative magnetic energies are in the blue region, above the $\beta_m = 0$ line. **Top panel:** Models with adiabatic index $\Gamma = 1.36$. **Middle panel:** Models with adiabatic index $\Gamma = 1.336$. **Bottom panel:** Models with adiabatic index $\Gamma = 1.56$.

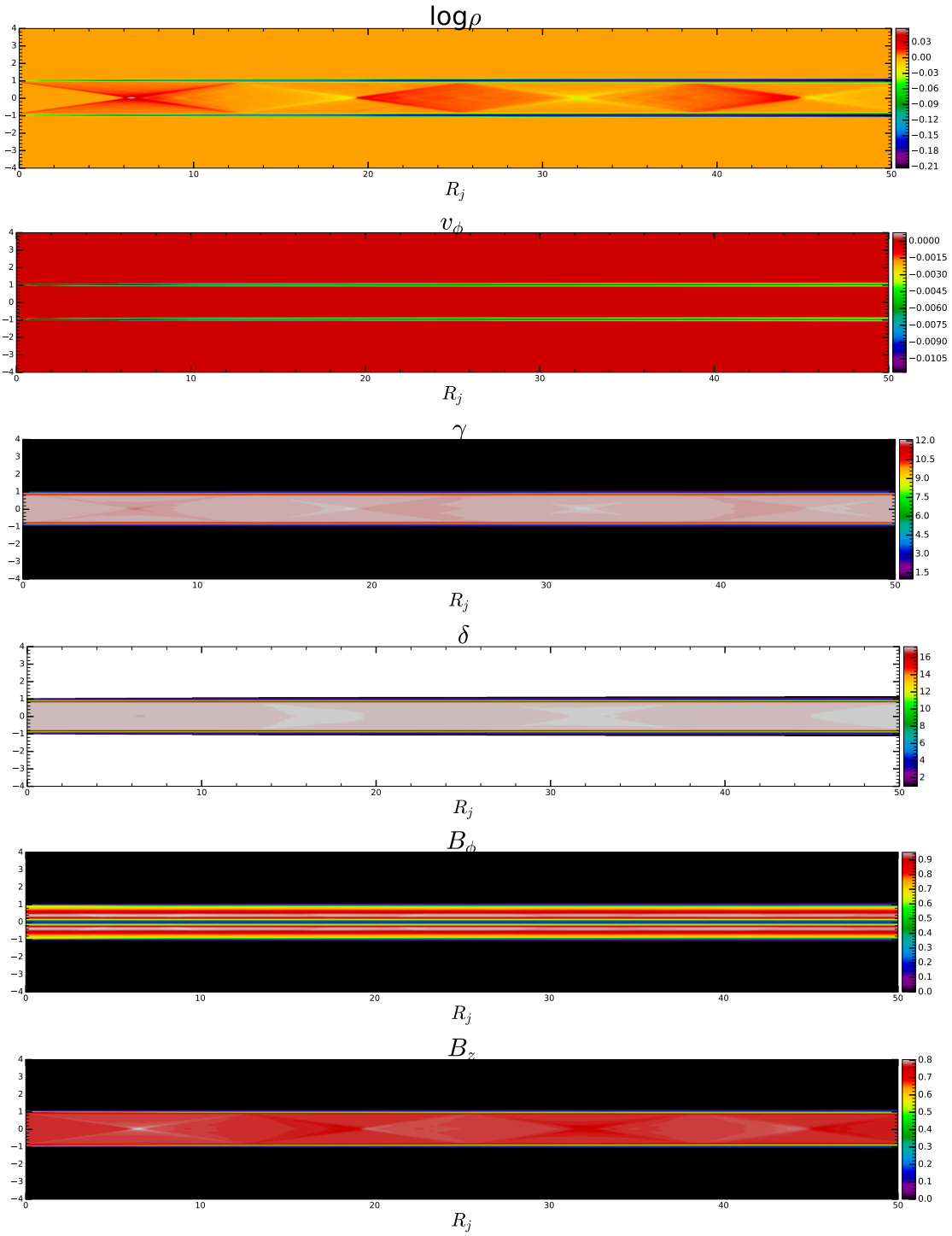

Figure 8.3: Steady structure of the jet model JL05 with $d_k = 1$ and no rotation. From top to bottom, distributions of rest-mass density, toroidal flow velocity, flow Lorentz factor, flow Doppler factor, and toroidal and axial magnetic field components. Notice the different scales between the x and y axis. Models are expressed in units of the ambient medium density and pressure, ρ_a, p_a, and the jet radius at injection, R_j.

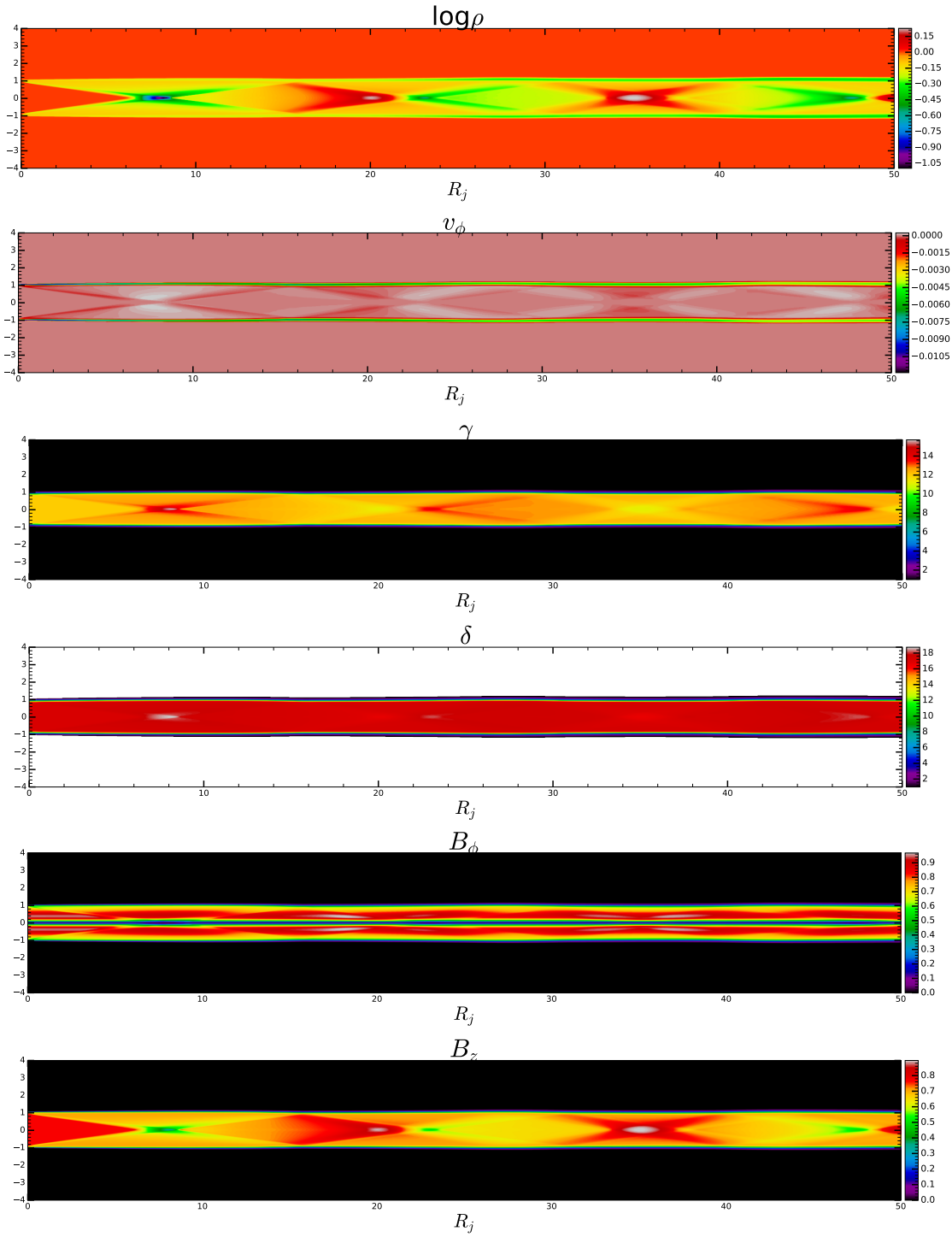

Figure 8.4: Steady structure of the jet model JL05 with $d_k = 1.2$ and no rotation. From top to bottom, distributions of rest-mass density, toroidal flow velocity, flow Lorentz factor, flow Doppler factor, and toroidal and axial magnetic field components. Notice the different scales between the x and y axis. Models are expressed in units of the ambient medium density and pressure, ρ_a, p_a, and the jet radius at injection, R_j.

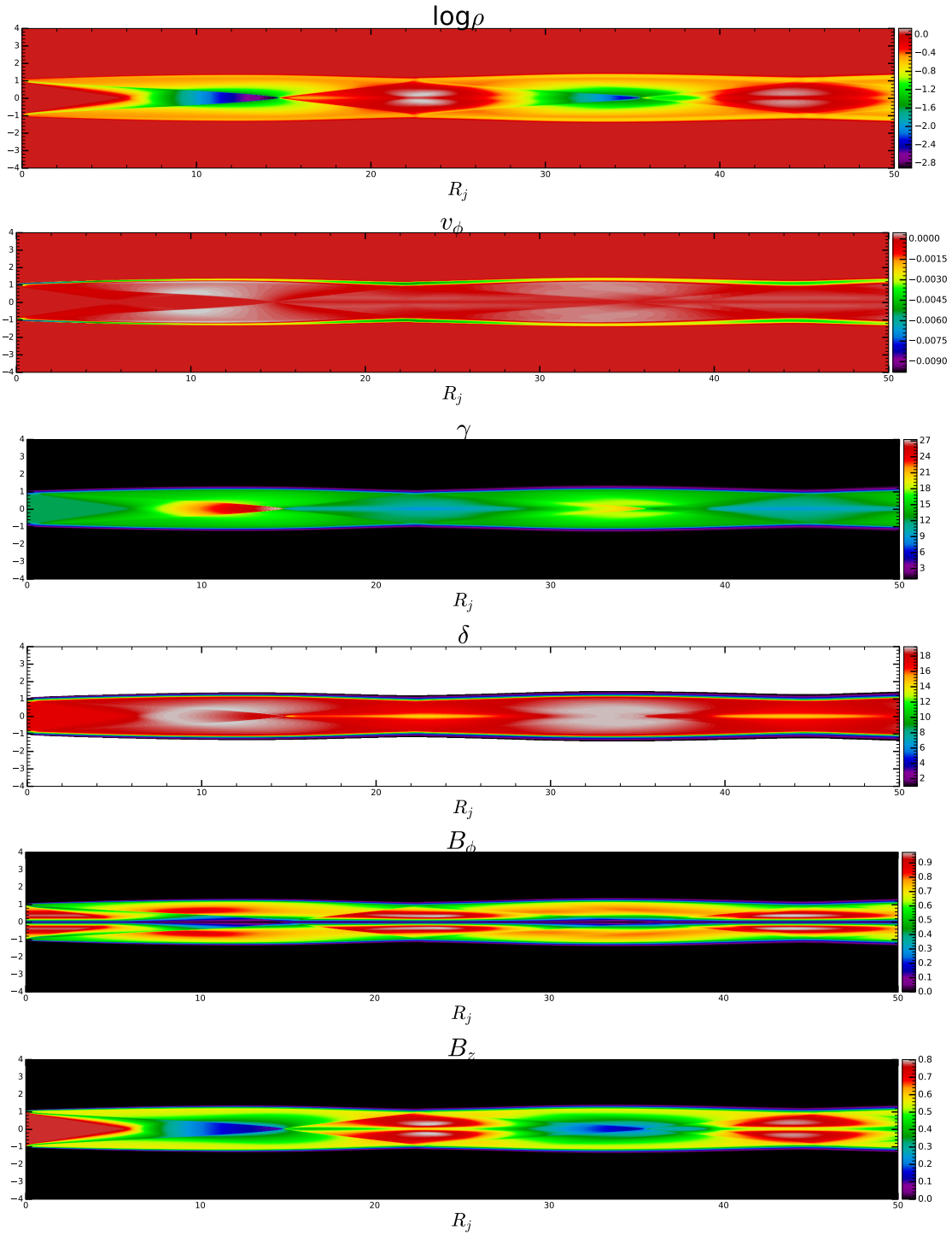

Figure 8.5: Steady structure of the jet model JL05 with $d_k = 2$ and no rotation. From top to bottom, distributions of rest-mass density, toroidal flow velocity, flow Lorentz factor, flow Doppler factor, and toroidal and axial magnetic field components.

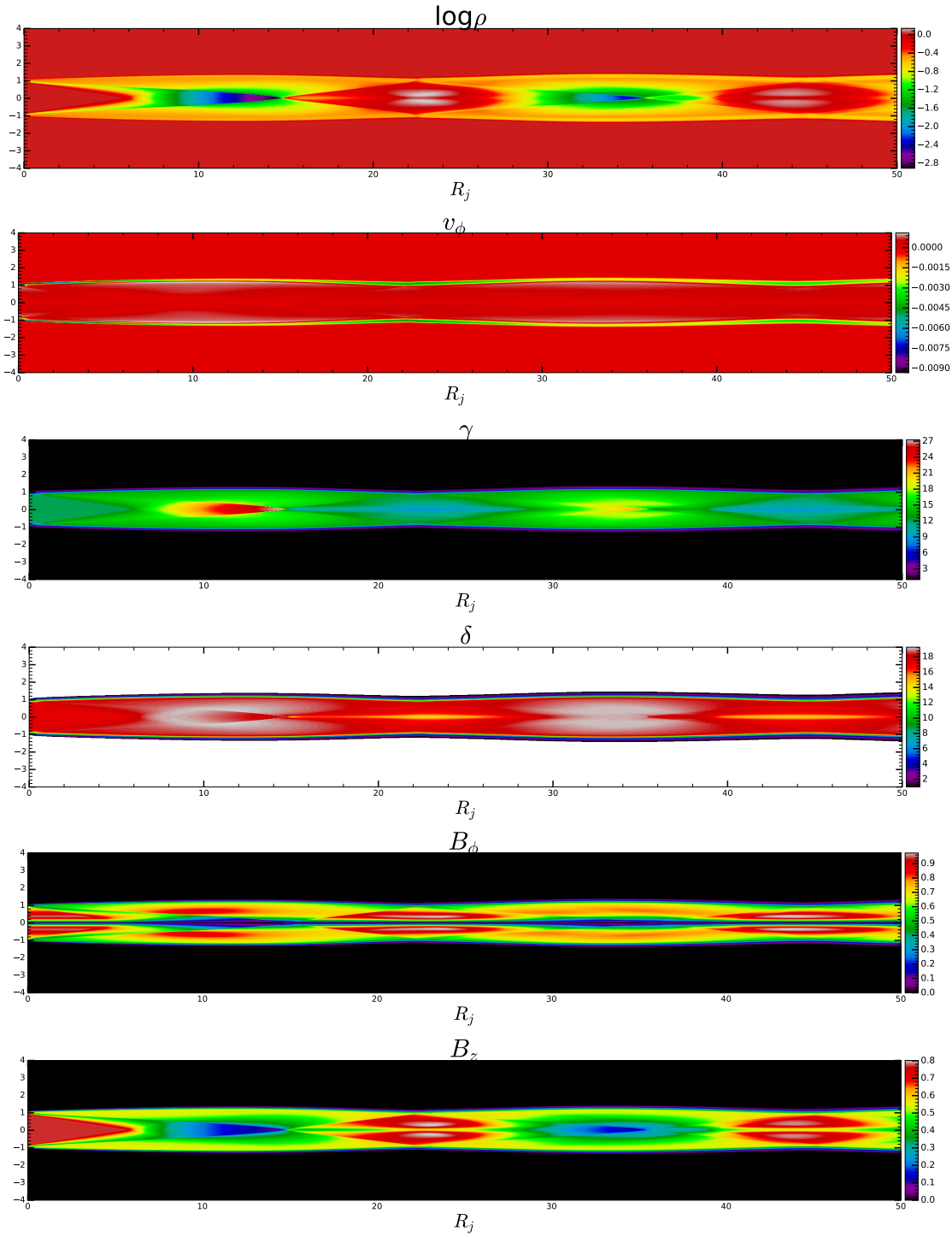

Figure 8.6: Steady structure of the jet model JL05 with $d_k = 2$ and rigid rotation with initial $v^\phi = 0.001$. From top to bottom, distributions of rest-mass density, toroidal flow velocity, flow Lorentz factor, flow Doppler factor, and toroidal and axial magnetic field components. Notice the different scales between the x and y axis. Models are expressed in units of the ambient medium density and pressure, ρ_a, p_a, and the jet radius at injection, R_j.

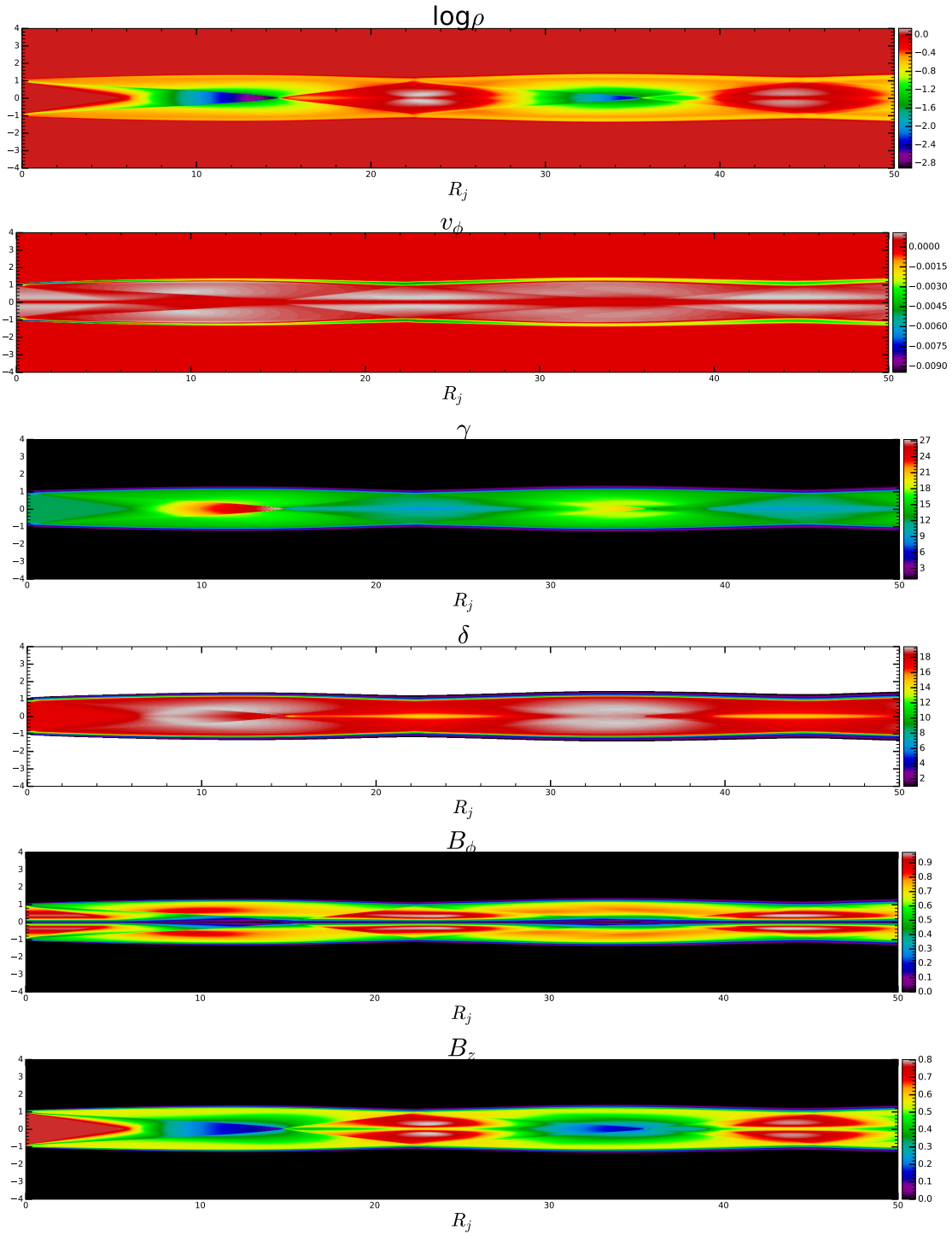

Figure 8.7: Steady structure of the jet model JL05 with $d_k = 2$ and differential rotation with initial $v^\phi = 0.001$. From top to bottom, distributions of rest-mass density, toroidal flow velocity, flow Lorentz factor, flow Doppler factor, and toroidal and axial magnetic field components. Notice the different scales between the x and y axis. Models are expressed in units of the ambient medium density and pressure, ρ_a, p_a, and the jet radius at injection, R_j.

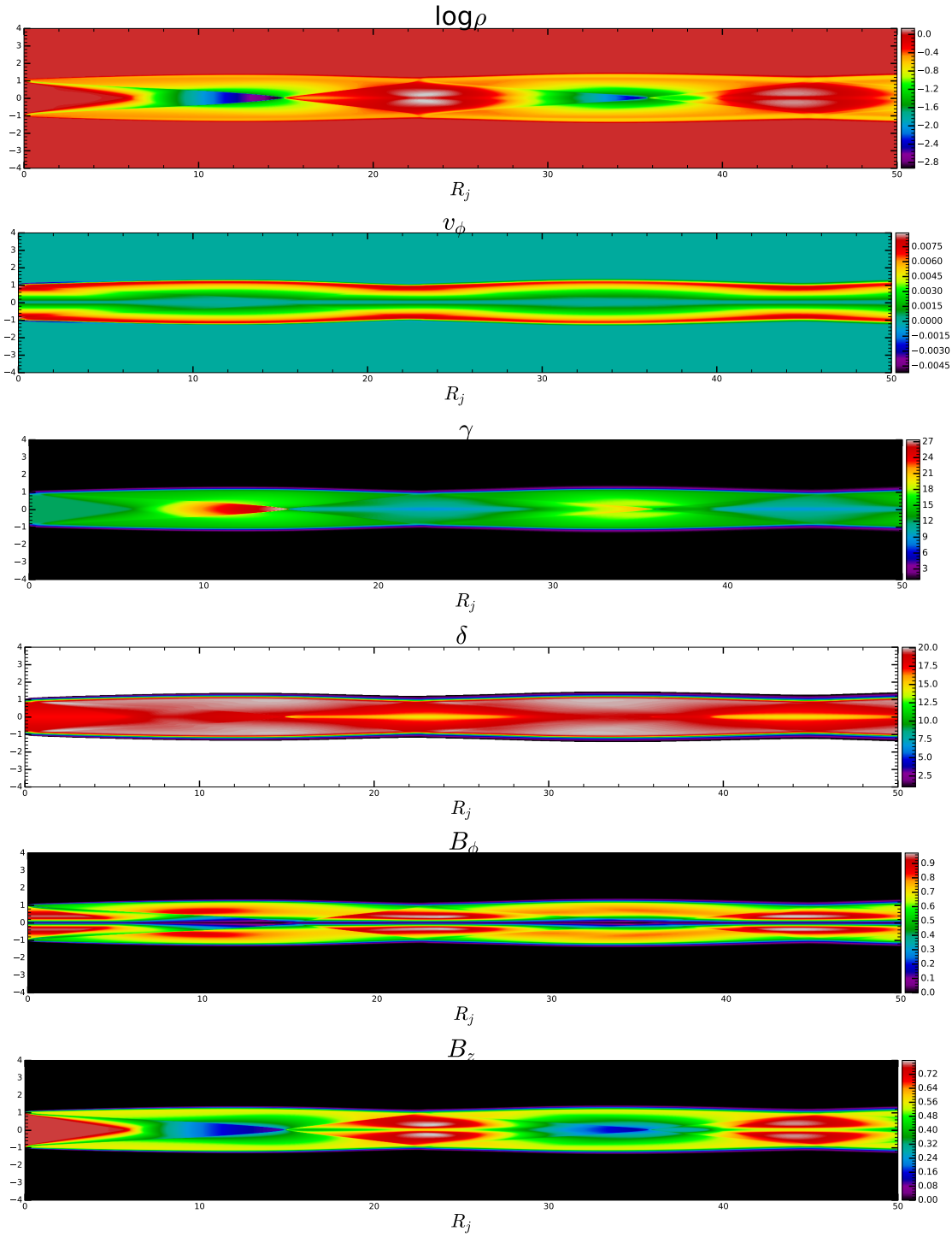

Figure 8.8: Steady structure of the jet model JL05 with $d_k = 2$ and rigid rotation with initial $v^\phi = 0.01$. From top to bottom, distributions of rest-mass density, toroidal flow velocity, flow Lorentz factor, flow Doppler factor, and toroidal and axial magnetic field components. Notice the different scales between the x and y axis. Models are expressed in units of the ambient medium density and pressure, ρ_a, p_a, and the jet radius at injection, R_j.

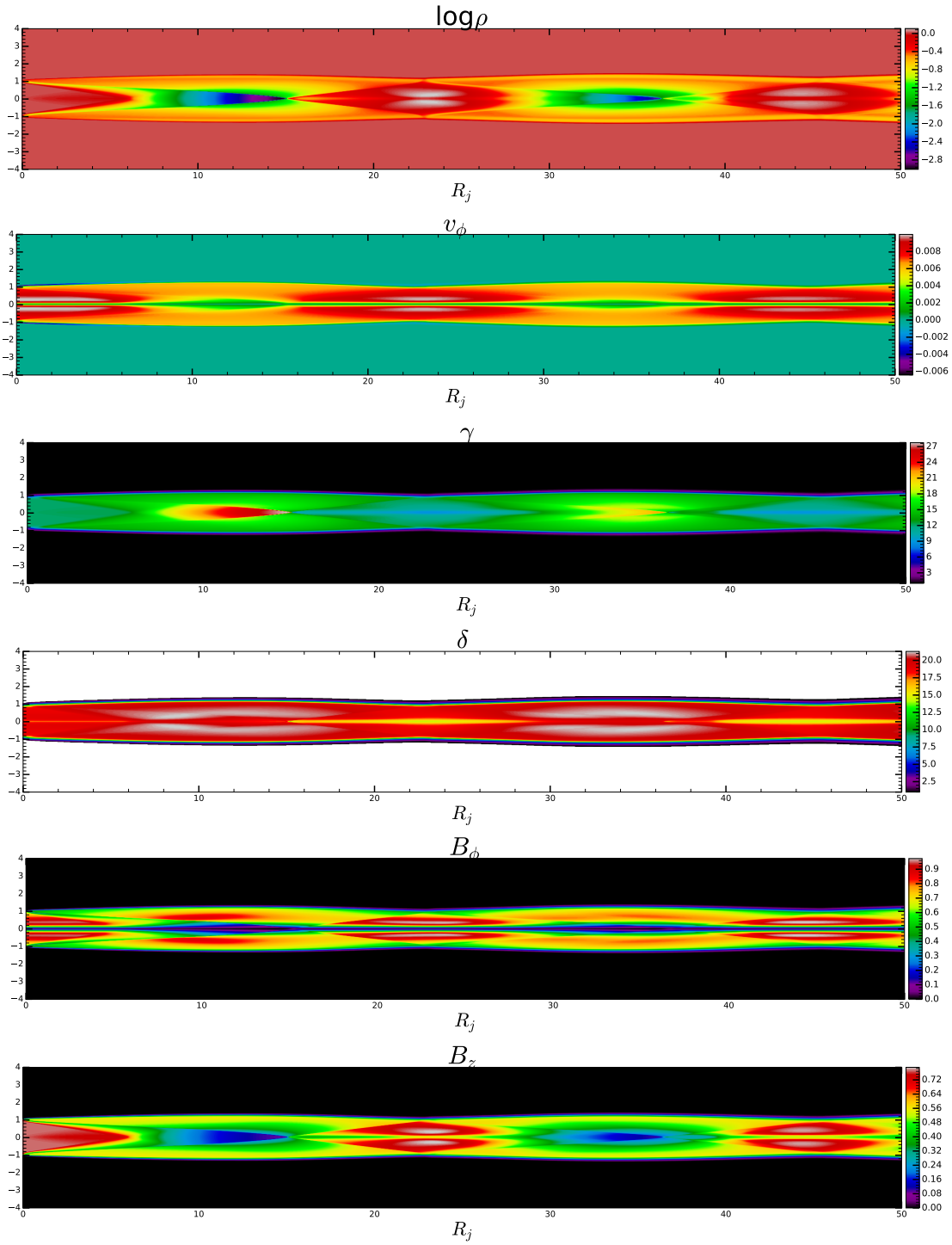

Figure 8.9: Steady structure of the jet model JL05 with $d_k = 2$ and differential rotation with initial $v^\phi = 0.01$. From top to bottom, distributions of rest-mass density, toroidal flow velocity, flow Lorentz factor, flow Doppler factor, and toroidal and axial magnetic field components. Notice the different scales between the x and y axis. Models are expressed in units of the ambient medium density and pressure, ρ_a, p_a, and the jet radius at injection, R_j.

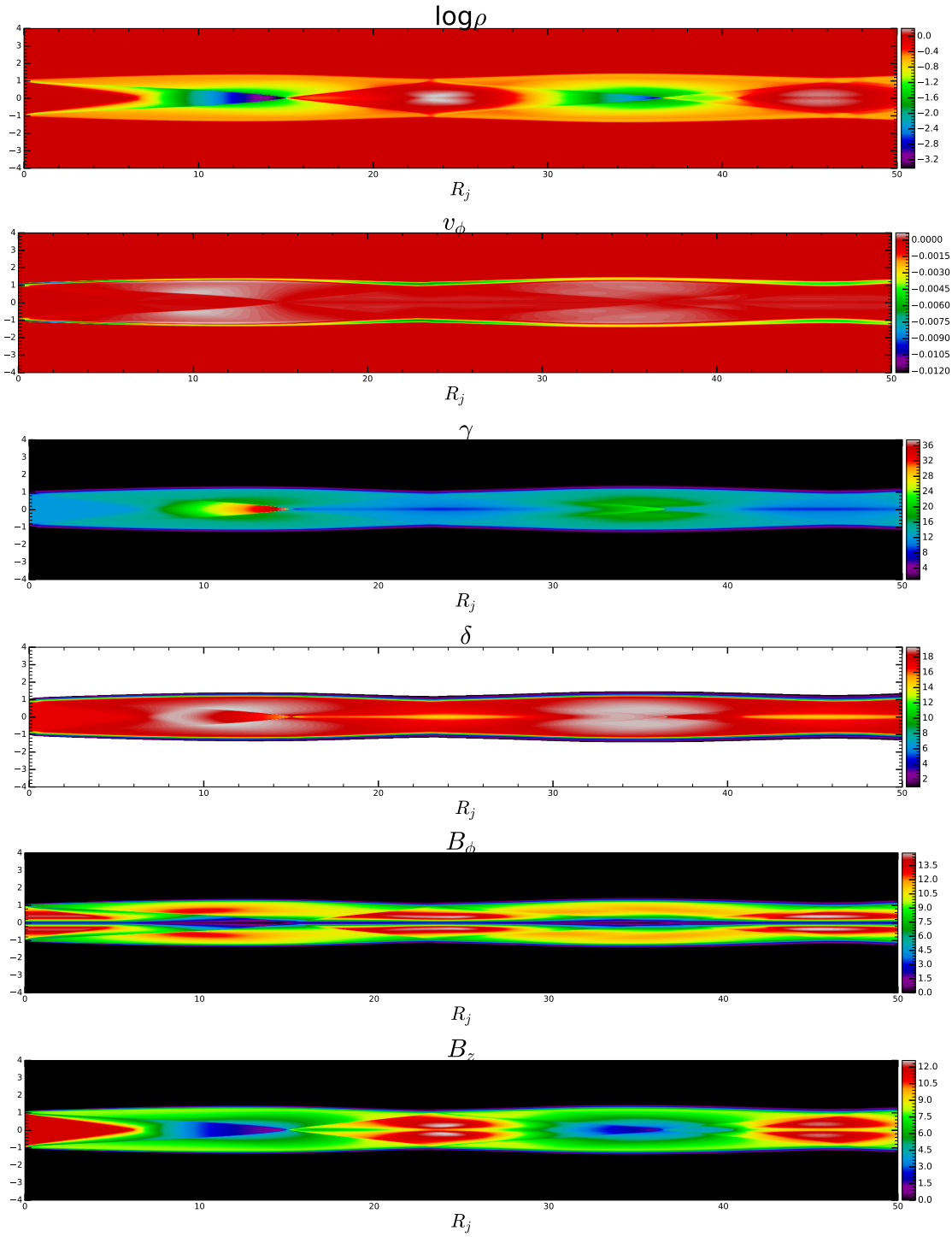

Figure 8.10: Steady structure of the jet model JL02 with $d_k = 2$ and no rotation. From top to bottom, distributions of rest-mass density, toroidal flow velocity, flow Lorentz factor, flow Doppler factor, and toroidal and axial magnetic field components. Notice the different scales between the x and y axis. Models are expressed in units of the ambient medium density and pressure, ρ_a, p_a, and the jet radius at injection, R_j.

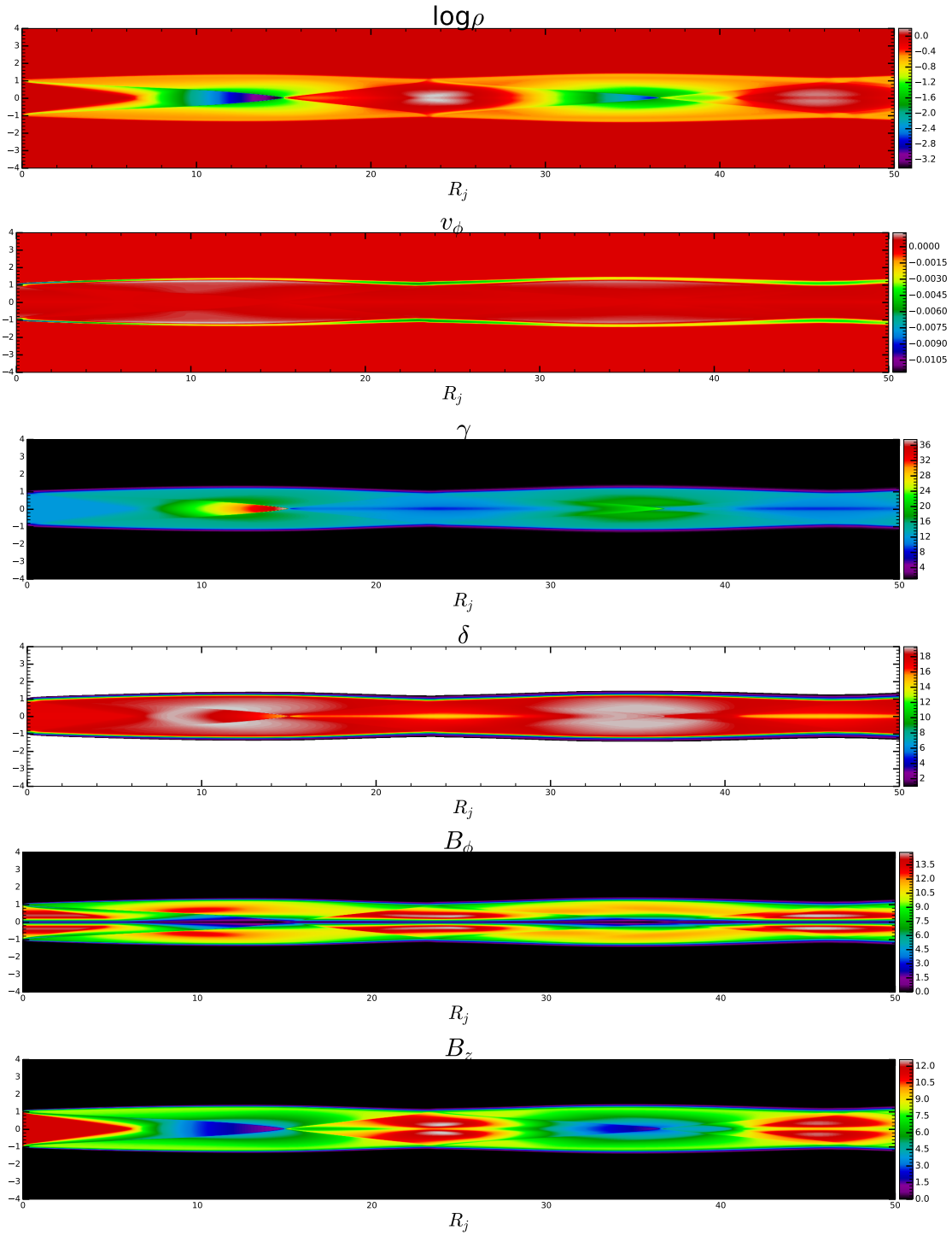

Figure 8.11: Steady structure of the jet model JL02 with $d_k = 2$ and rigid rotation with initial $v^\phi = 0.001$. From top to bottom, distributions of rest-mass density, toroidal flow velocity, flow Lorentz factor, flow Doppler factor, and toroidal and axial magnetic field components. Notice the different scales between the x and y axis. Models are expressed in units of the ambient medium density and pressure, ρ_a, p_a, and the jet radius at injection, R_j.

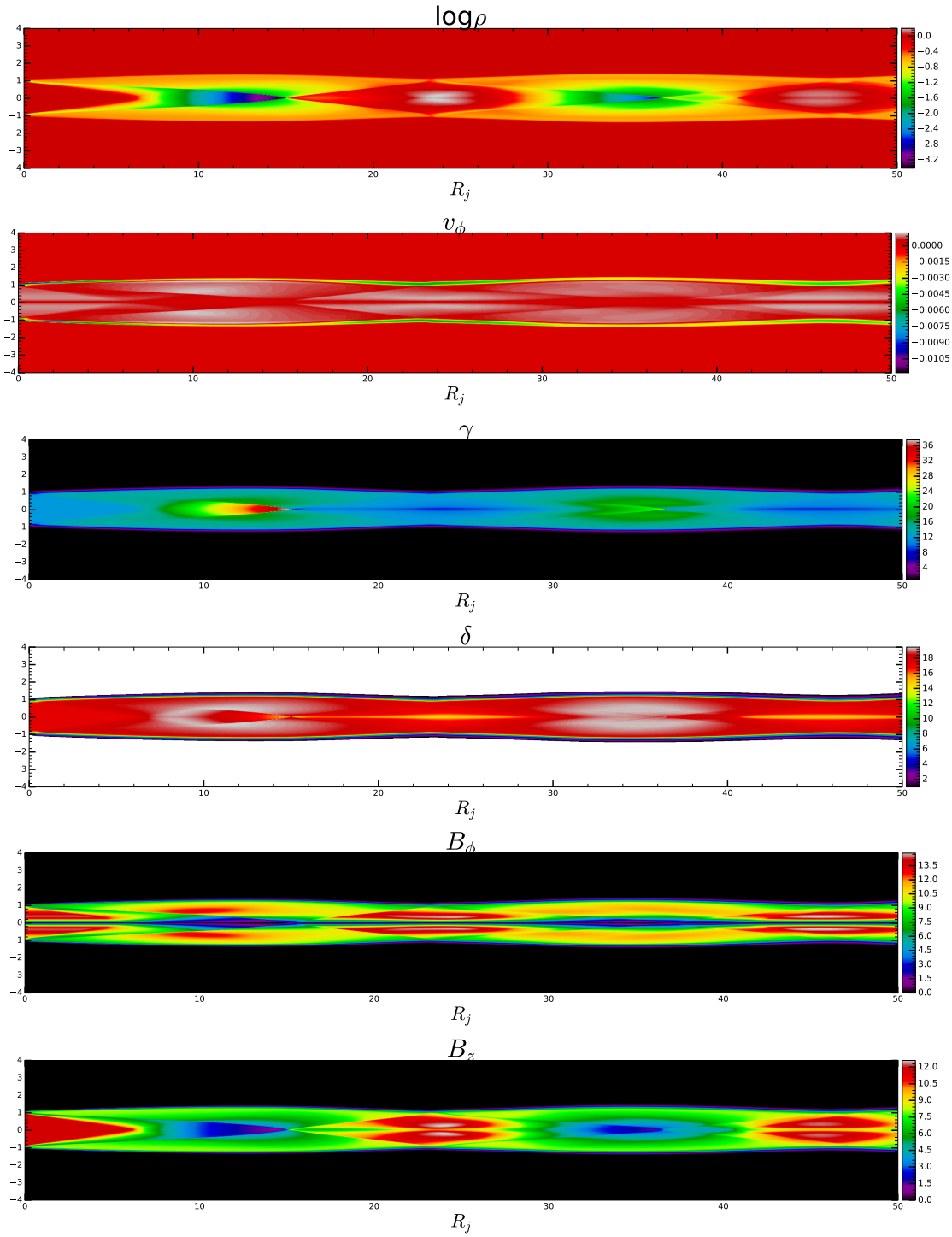

Figure 8.12: Steady structure of the jet model JL02 with $d_k = 2$ and differential rotation with initial $v^\phi = 0.001$. From top to bottom, distributions of rest-mass density, toroidal flow velocity, flow Lorentz factor, flow Doppler factor, and toroidal and axial magnetic field components. Notice the different scales between the x and y axis. Models are expressed in units of the ambient medium density and pressure, ρ_a, p_a, and the jet radius at injection, R_j.

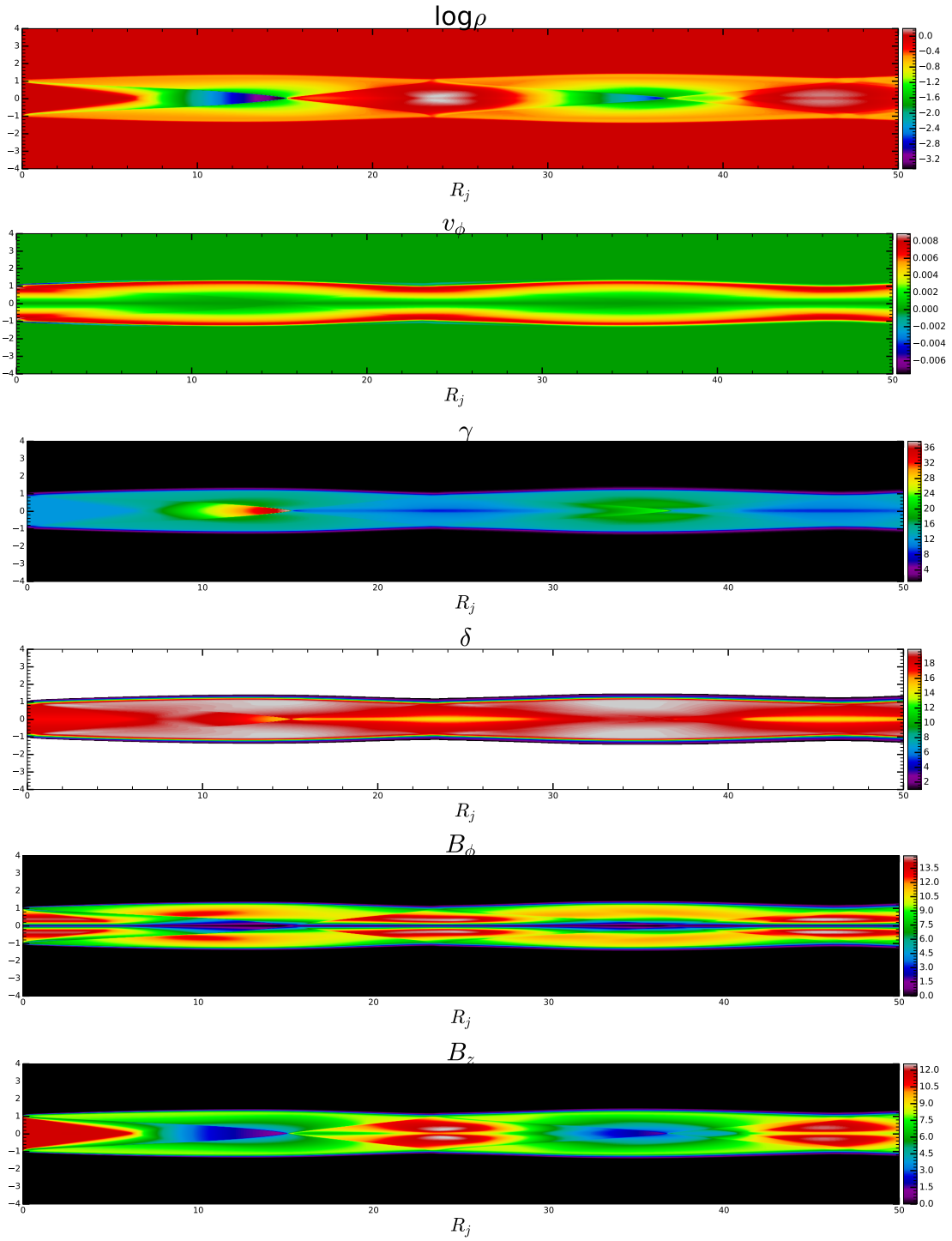

Figure 8.13: Steady structure of the jet model JL02 with $d_k = 2$ and rigid rotation with initial $v^\phi = 0.01$. From top to bottom, distributions of rest-mass density, toroidal flow velocity, flow Lorentz factor, flow Doppler factor, and toroidal and axial magnetic field components. Notice the different scales between the x and y axis. Models are expressed in units of the ambient medium density and pressure, ρ_a, p_a, and the jet radius at injection, R_j.

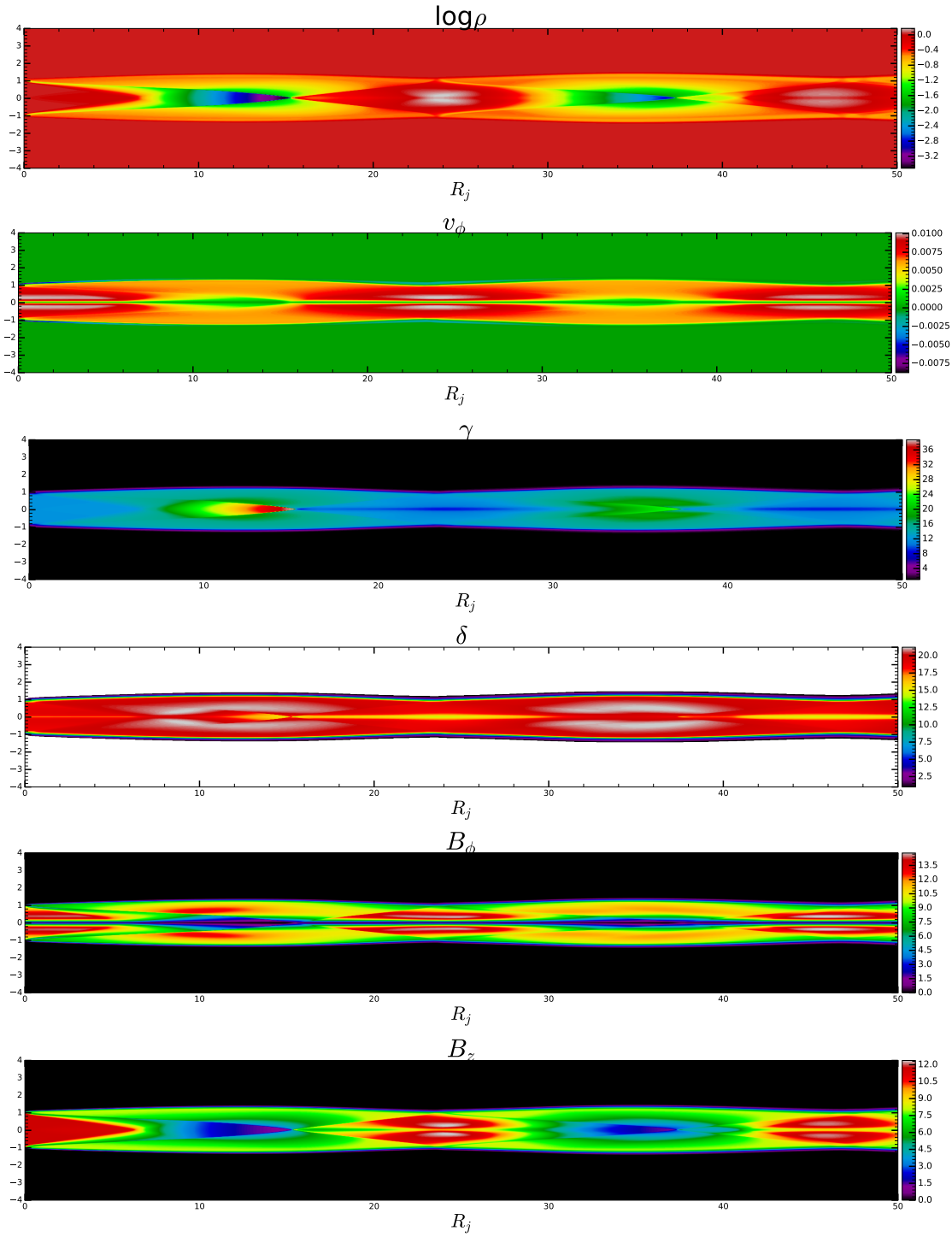

Figure 8.14: Steady structure of the jet model JL02 with $d_k = 2$ and differential rotation with initial $v^\phi = 0.01$. From top to bottom, distributions of rest-mass density, toroidal flow velocity, flow Lorentz factor, flow Doppler factor, and toroidal and axial magnetic field components. Notice the different scales between the x and y axis. Models are expressed in units of the ambient medium density and pressure, ρ_a, p_a, and the jet radius at injection, R_j.

Chapter 9

Summary and conclusions

In this thesis we studied the relativistic jet in four blazars, taking advantage of the high angular resolution achieved with the *RadioAstron* space antenna: 0836+710, 3C 273, 3C 345, and 1642+690. We summarize the main results on a source by source basis.

- **0836+710** We first obtained high resolution images of 0836+710 at 1.6 GHz, 5 GHz, and 22 GHz. The highest angular resolution image ever obtained for the source is the map at 22 GHz. This map shows an asymmetric structure that could be caused by the presence of rotation in the jet. Then, we performed a kinematic and a spectral analysis. We did a kinematic analysis between 2013 and mid 2017 using Boston University data at 43 GHz. The analysis revealed evidence of a recollimation shock close to the jet base, at a distance of $\sim$ 0.10 mas. Several other moving features with high apparent speeds of $\beta \sim 20$ were detected. We computed the variability Doppler factor for components where the flux density decreased exponentially for one or more time segments, for the Boston University data we analyzed and for kinematics results at 15 GHz from the MOJAVE team. We find a slight deceleration of the flow in the direction of propagation of the jet. Furthermore, we saw that the parsec-scale kinematics of 0836+710 can be related to its high-energy flaring activity. Flares are coincident with new component ejections, and the largest flares correspond to a component interacting with the recollimation shock. The brightest flare the source underwent was at the end of 2015, which lasted for several months. At the time of this flare, two moving components interacted with the recollimation shock. No further flares were observed following the end of interactions between components.

  We then performed a spectral analysis of 0836+710. The aligment between frequencies showed a plateau in the coreshift curve as a function of frequency, between 5 GHz and 15 GHz, at a location consistent with the position of the putative recollimation shock. A similar behaviour is observed when analyzing

archival data from 2003. Spectral index maps between frequency pairs were obtained. We should remark here the presence of a region with fairly constant spectral index between 10 mas and 40 mas. Using the cooling time, this allows us to obtain an upper limit for the magnetic field at those distance of $B < 0.01$ G. This leads to a magnetic power of the jet of $L_B \sim 0.28 \times 10^{46}$ erg/s. The spectral analysis also allowed us to estimate the magnetic field of the source using basic synchrotron theory, by studying the synchrotron spectrum in the core region, where it is possible to observe a spectral turnover. We compared these values to those obtained using the coreshift value and we found similar results corresponding to ∼0.03 G in the 5 GHz core.

Then, we studied the jet structure using a ridgeline analysis. We modelled the ridgeline as a sum of multiple oscillatory terms for the 1.6 GHz data. Different fits resulted in consistent results, and also similar to previously published values, using different arrays at different epochs. Assuming that these oscillations correspond to Kelvin-Helmoltz instability modes developing in the flow, we could derive the jet parameters both from approximations to the characteristic wavelengths of the instability (Hardee 2000) and using a new method based on the numerical solutions of the linear stability problem, for which we considered a wide range of values of the relevant jet parameters and compared the relative lengths at the maximum growth-rates for the identified modes with those derived from the ridge-line. Using the approximation of Hardee (2000), we obtained $M \sim 12$ for the jet classical Mach number and $\eta \sim 0.33$ for the density ratio between the jet and the ambient medium. The numerical analysis resulted in a jet Lorentz factor $\gamma \simeq 12$, consistent with (Otterbein et al. 1998), a density ratio of $\eta \sim 10^{-3}$, jet specific internal energy of $\varepsilon \sim 10^{-2}\, c^2$, and jet classical Mach number of $M \sim 12$. We also found that the observed radio jet is surrounded by a thin shear layer, with a width $\simeq 10$ % of the jet radius. The value derived for the specific internal energy and the Lorentz factor suggest a kinetically dominated jet. Furthermore, we see that moving knots or recollimation shocks in the jet can have some influence in the ridgeline, by modifying the observed offset and the flux profile. These effects are not especially relevant in 0836+710, and do not affect the performed modeling. Moreover, we also see a change in the internal structure of 0836+710 at distances larger than 60 mas, observing three peaked profiles. This could be explained by a change of the viewing angle at these scales, of a factor two due to the oscillations in the jet direction induced by the helical instability modes.

Finally, since the space VLBI image at 22 GHz showed asymmetric jet features, we performed simulations using the code of Martí (2015). We introduced models with rotational speeds and considered a small initial rotation speed $v^\phi = 0.001, 0.01$. We considered different overpressure factors, and hot

and kinematically dominated jets. We saw that rotation speeds of the order of $v^{\phi} = 0.001$ arise naturally from our models even if no rotation is considered initially. Furthermore, hot jets models showed a slightly higher maximum rotational speed. In order to see if these models can explain the asymmetry observed in the space VLBI image at 22 GHz, emission simulations are needed.

- **3C 273** The RadioAstron image of 3C 273 at 5 GHz shows the brightest regions of the jet that could indicate the brightest of the two ridgelines observed by Lobanov & Zensus (2001) or the middle point between them. The image at 22 GHz did provide significant additional information, due to the low number of antennas in the array. In order to investigate the evolution of the instability pattern suggested by Lobanov & Zensus (2001), the main analysis performed for this source was a direct comparison of the jet transversal structure between our observations and previous VSOP observations in 1997 at 5 GHz, revealing a change in the angle of injection of the jet ridge line. Comparing the offsets between the two ridgelines, we could estimate the propagation and rotation speed. This led to a propagation speed of 0.07c and a rotation speed with a maximum of 0.5c. We also obtained the same rotation speed with an independent analysis using a modelling of the two ridgelines. The rotation of the jet was verified using multiepoch MOJAVE archival data, resulting in the same rotation speed and a similar propagation speed of 0.05c. Furthermore, the multi-epoch analysis allowed us to see more clearly the effect of moving components in the underlying structure of the flow. The position of a large disturbance in the ridgeline was coinciding with a bright VLBI component presented in the MOJAVE data (Lister et al. 2013). This component modified the regular jet helical structure and how, after its passage, the jet recovered its original structure. This proves the presence of interactions between plasma instabilities and shocks.

- **1642+690** We obtained *RadioAstron* images of 1642+690 at 1.6 GHz and 5 GHz, while we did not detect any fringes at 22 GHz. Both images showed a feature that outshined the core at a distance of ∼0.7 mas. Performing a spectral analysis, we could see that this component likely corresponds to a recollimation shock, as suggested by a plateau in the coreshift curve between 1.6 GHz and 5 GHz. Furthermore, the spectral analysis allowed us to obtain a magnetic field in the region corresponding to this component of ~ 0.2 G. The magnetic field in the core seems to be quite high compared to the one we measured in 0836+710, with a value around 5 G at 22 GHz. Surprisingly, the brightness temperature of this source was also the highest, as was already estimated by the *RadioAstron* brightness temperature survey (Kovalev 2014).

- **3C 345** In the case of 3C 345, we were able detect fringes with *RadioAstron*

only for one scan at 5 GHz. The corresponding image suggests the presence of a counter jet. We also performed a spectral analysis of the source, which allowed us to obtain a magnetic field in the core at 5 GHz of $\sim$ 0.07 G, consistent with the values given in Schinzel (2011).

In conclusion, we found that the existence of recollimation shocks can modify the opacity in AGN jets. Such shocks manifest themselves as plateaus in the coreshift curve as a function of frequency, and as stationary components in multi-epoch VLBI images. Such plateaus in the coreshift curve have been observed before at high frequencies, between 43 GHz and 86 GHz but they were found to be related to the compact radio core. This is the first time that such an effect is seen to be associated with a recollimation shock, although its presence has been hinted at in simulations. We also showed that these recollimation shocks can be linked to high-energy flaring activity, when they interact with traveling shocks. Additionally, we found that shocks can affect the underlying jet structure and its Kelvin Helmholtz instability patterns observed at larger scales. Finally, we showed for the first time how studying jet stability can yield estimates of relevant jet parameters, and insight into the interplay between the jet and the ambient medium.

Appendix A

Derivation of hydrodynamics equations

In this appendix we include the derivation of the conservation equations of a in hydrodynamics. The starting point is the energy-momentum equation, Eq. 3.2: $T^{\mu\nu}_{\ ;\nu} = 0$ to derive the momentum equation. For that we consider the cases $\mu = 0$ and $\mu = i$, with $i = 1, 2, 3$.

For the case $\mu = 0$:

$$\frac{\partial}{\partial t}(\rho h u^0 u^0 + P g^{00}) + \nabla(\rho h u^0 u^i + P g^{i0}) = 0. \tag{A.1}$$

Replacing the four velocity terms and the metric tensor, Eq. A.1 is:

$$\frac{\partial}{\partial t}(\rho h \gamma^2) - \frac{\partial}{\partial t} P + \nabla(\rho h \gamma^2 \mathbf{v}) = 0. \tag{A.2}$$

Now, applying twice the divergence property, $\nabla(ab) = (a\nabla)b + (b\nabla)a + a \times (\nabla \times b) + b \times (\nabla \times a))$, where the rotors will vanish, Eq. A.2 takes the following form:

$$\gamma \frac{\partial}{\partial t}(\rho h \gamma) + \rho h \gamma \frac{\partial}{\partial t}(\gamma) - \frac{\partial}{\partial t} P + \rho h \gamma^2 \nabla \mathbf{v} + \rho h \gamma \mathbf{v} \nabla \gamma + \gamma \mathbf{v} \nabla(\rho h \gamma) = 0. \tag{A.3}$$

Putting some terms together:

$$\gamma \frac{\partial}{\partial t}(\rho h \gamma) + \gamma(\mathbf{v}\nabla)(\rho h \gamma) + \rho h \gamma \left[\frac{\partial}{\partial t}(\gamma) + (\mathbf{v}\nabla)\gamma + \gamma \nabla \mathbf{v} \right] - \frac{\partial}{\partial t} P = 0. \tag{A.4}$$

For the case $\mu = i$:

$$\begin{aligned}\frac{\partial}{\partial t}(\rho h u^0 u^i + P g^{0i}) + \nabla(\rho h u^i u^i + P g^{ii}) = 0 \\ \frac{\partial}{\partial t}(\rho h \gamma^2 \mathbf{v}) + \nabla(\rho h \gamma^2 \mathbf{v}^2) + \nabla P = 0.\end{aligned} \tag{A.5}$$

Applying the again the divergence property and putting the terms together. Eq. A.5 can be rewritten as:

$$\gamma \frac{\partial}{\partial t}(\rho h \gamma \mathbf{v}) + \gamma(\mathbf{v}\nabla)(\rho h \gamma \mathbf{v}) + \rho h \gamma \mathbf{v} \left[\frac{\partial}{\partial t}(\gamma) + (\mathbf{v}\nabla)\gamma + \gamma \nabla \mathbf{v}\right] + \nabla P = 0. \tag{A.6}$$

Now using both equations we can derive the conservation of momentum equation. Multiplying Eq. A.4 for $-v$ and adding it to Eq. A.6:

$$\rho h \gamma \left[\frac{\partial \gamma}{\partial t} + (\mathbf{v}\nabla)\mathbf{v}\right] = -\nabla P - \mathbf{v}\left(\frac{\partial P}{\partial t}\right), \tag{A.7}$$

which is the momentum equation, Eq. 3.9.

Following a similar procedure, the energy equation can be derived using $u_\mu T^{\mu\nu}_{;\nu} = 0$. The resulting equation is:

$$\gamma \left[\frac{\partial p}{\partial t} + (\mathbf{v}\nabla)\rho\right] = -\rho h \left[\frac{\partial \gamma}{\partial t} + (\mathbf{v}\nabla)\gamma + \gamma \nabla \mathbf{v}\right]. \tag{A.8}$$

which is the same equation as Eq. 3.10.

Lastly, the continuity equation can be also derived from $(n u^\mu)_{;\mu} = 0$:

$$\gamma \left[\frac{\partial}{\partial t}(n) + (\mathbf{v}\nabla)n\right] + n \left[\frac{\partial}{\partial t}(\gamma) + (\mathbf{v}\nabla)\gamma + \gamma \nabla \mathbf{v}\right] = 0. \tag{A.9}$$

Appendix B

Software developed during this thesis

During this thesis work I have developed two data analysis software based on a Graphical User Interface (GUI), which can be used to perform spectral analyses and kinematic analyses of jets, respectively.

Spectral analysis software

The spectral analysis software has several screens including the different steps of the analysis. First, when it is called, the software reads all the required files for each frequency and stores its location in memory. Then the user can use the toolbar to select the desired analysis. I will describe the different screens following a complete spectral analysis.

The first one is the convolution window (see Fig. B.1). It includes several check boxes with the different frequencies and a button underneath them that allows the user to select the beam of that frequency as common convolution beam. A radio button allows the user if he wants to select the corresponding circular beam or an elliptical beam. Clicking the button will write the selected beam in the corresponding boxes for the beam parameters. The user can also write the beam there manually or modify the selected one. The interface also has a button to select the pixel and map size, which, by default, are selected from the higher and lower frequency image, respectively. Then, it is possible to select the weighthing used to create the maps. When all the boxes turn green, this indicates that the inserted values are acceptable, and by pressing the convolve button all the frequencies will be convolved with the same map parameters. The resulting fits files are stores in a dedicated folder.

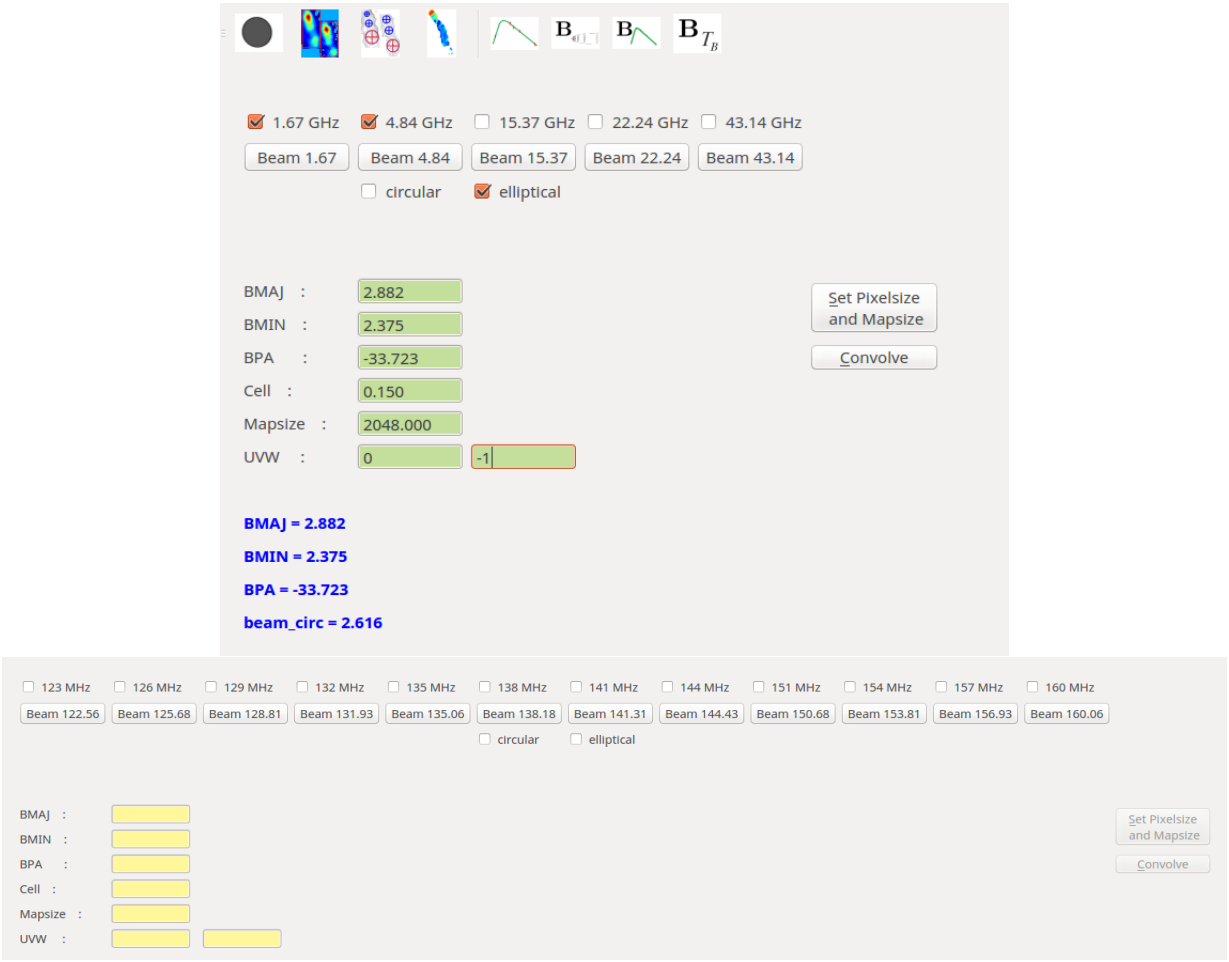

Figure B.1: Convolution screen for two different data sets with different amount of frequencies **Top panel:** global VLBI data set with five frequencies. **Bottom panel:** Lofar data set with 11 frequencies.

The next screens are related to the shifting using frequency pairs (see Fig. B.2). The first one uses the 2D cross correlation method and the second one uses the alignment based on modelfit components. To use the second, the user would need to create a modelfit folder with the modelfits for each frequency, to be used for the alignment. In both cases, the interface only allows the user to select two frequencies. Then, with the check button, it will verify that the selected files have the same map parameters. If it is the case, the name of the files and location will appear in green. However, if they do not have the same map parameters, the file names will appear in red and the interface will advise the user to go back to the convolution step. For the case of the 2D cross-correlation screen, by clicking on the shifting button, a window with the map of the source at the two frequencies will appear, where the user can select the map region of interest for the spectral analysis. Then a new window will open, allowing the user to select the optically

thin region to be used for the 2D cross=correlation alignment. The program shows the user the shifting values in pixels and milliarseconds in the main screen. Then, it calculates the shift between the frequencies again for the selected region for the newly created fits files to see if there is any residual shift, in which case a small pop up window appears asking the user if they want to shift by an additional amount. The software also gives the option to insert the shift values manually in milliarseconds. In the screen for shifting using the modelfit components, the user selects the number of components he wants to compare pressing the button "Select components". A pop up window will then show the maps of both frequencies, and the user can select the reference components by double-clicking on them on the map. Then the software will perform the shifting comparing the position of the two components, and show the result on the main screen. By pressing shifting, the shift is applied and the shifted maps are stored in a dedicated folder.

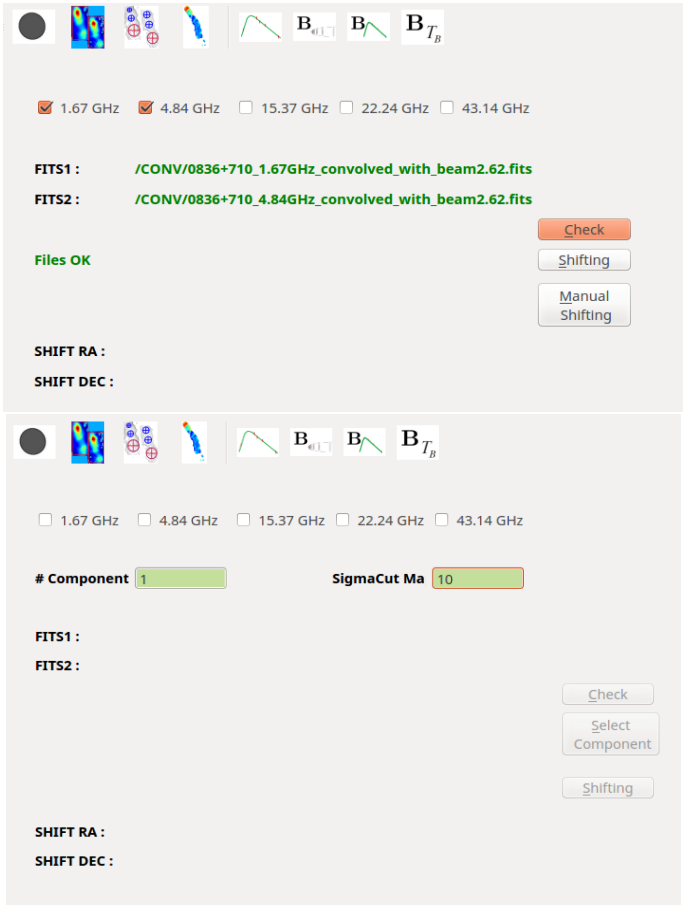

Figure B.2: Screens to perform a shifting between frequency pairs. **Top panel:** using the 2D cross correlation in an optically thin feature. **Bottom panel:** using optically thin modelfit components.

The next screen corresponds to the spectral index map (see Fig. B.3). It only

allows the user to select frequency pairs. It uses the stored shift files created in the previous step and calculates the value of the spectral index, as:

$$\alpha = \frac{\log(S_1/S_2)}{\log(\nu_1/\nu_2)}, \tag{B.1}$$

It is also possible to create a spectral index profile along the jet, by selecting the start and end point of the cut.

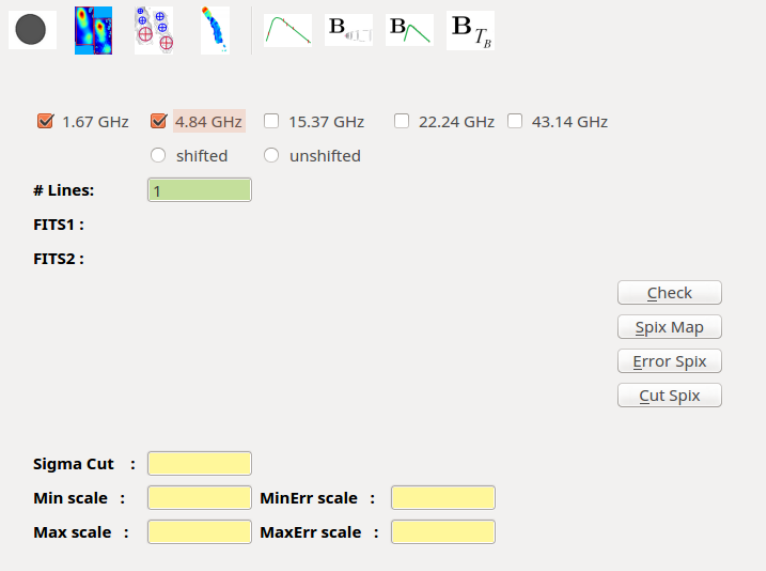

Figure B.3: Screen to calculate the spectral index map between frequency pairs.

Then, we have the turnover screen, for analysis of synchrotron spectra, which typically requires more than two frequencies. It is only possible to use it if each adjacent frequency pair has been properly aligned and shifted. All maps are then shifted with respect to the core of the chosen reference frequency. The user can then select the region in which they want to calculate the synchrotron spectrum. If there is no turnover, the user can choose to do a simple power law fitting. In the case of a turnover, it is possible to do a full spectral fit. The user can choose to fix the value of the optically thick part of the spectrum or leave it free. The software will then compute maps of turnover flux density and turnover frequency. The fitting is done using the `iminuit` package

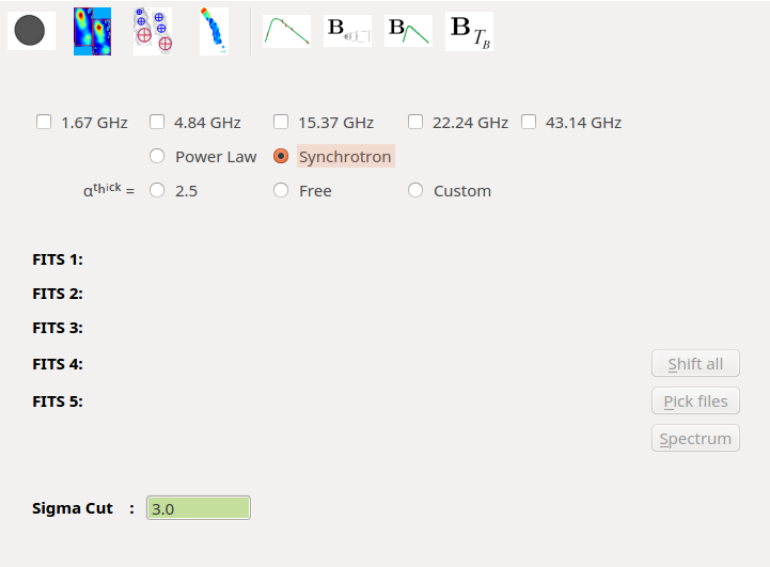

Figure B.4: Screen to obtain turnover frequency and turnover flux density maps by fitting the synchrotron spectrum.

We have two screens two calculate the magnetic field: one using the coreshift approach and another using the turnover spectrum approach (see Section 6.2.1 for more details). Since the luminosity distance and redshift are needed for the calculations, the program will get the values automatically from the NASA/IPAC Extragalactic Database (NED). If the source is not found, it will prompt for a more common source name, or ask to insert the values manually. In the screen for calculating the magnetic field using the coreshift approach, first a fit is performed to the coreshift as a function of frequency, in order to obtain k_r. Then the coreshift measurement (see Eq. 2.39) is calulated for each of the chosen frequency pairs. Finally, it is possible to select a frequency for which to calculate the magnetic field, filling all the data boxes given in the window: spectral index, α, Doppler factor, δ, viewing angle, θ, and opening angle, φ, and also the minimum and maximum particle Lorentz factor, $\gamma_{\rm min}$ and $\gamma_{\rm max}$ if the user wants to calculate the particle density (see the top panel of Fig. B.5). The user can chose if it wants to use the approximation formula, Eq. 2.48, to calculate the magnetic field at 1 pc, B_1, which assumes $k_r = 1$ and $\alpha = 0.5$ or not assume those values and use the fitted k_r and give a value for the spectral index, using Eq. 2.46.

In the screen for calculating the magnetic field using the turnover approach, the program reads the turnover frequency and turnover flux density values obtained in the turnover screen. Then, the user fills the data boxes given in the window: Lorent factor, γ, and Doppler factor, δ (see the bottom panel of Fig. B.5) and can obtain the magnetic field with the formula Eq. 2.35 and particle density with the formula Eq. 2.37 (giving also in this case the minimum and maximum particle Lorentz factor, $\gamma_{\rm min}$ and $\gamma_{\rm max}$), pressing the corresponding buttons.

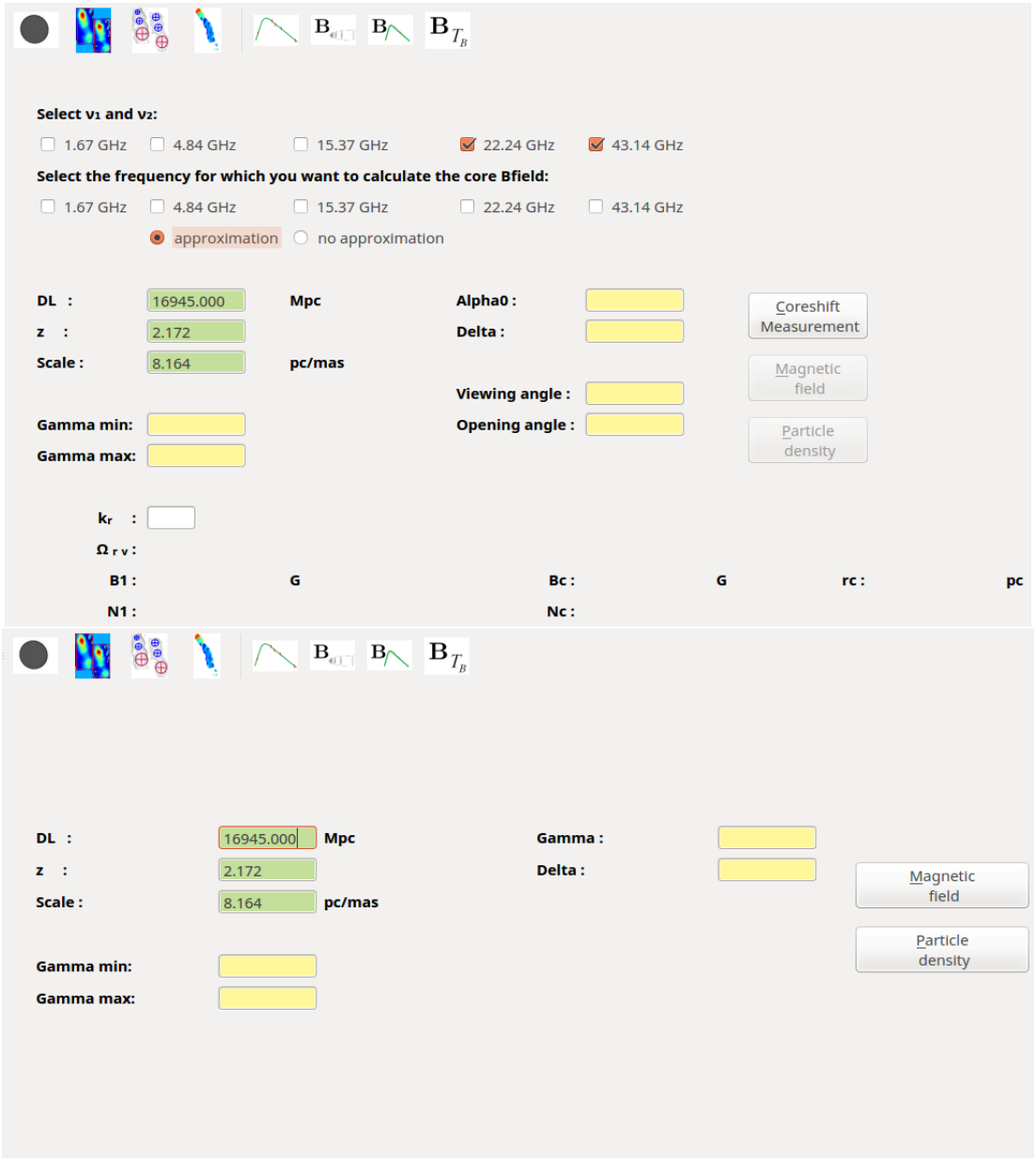

Figure B.5: Screens to obtain the magnetic field. **Top panel:** using the coreshift approach. **Bottom panel:** using the synchrotron spectrum.

At last, if modelfits are present, the software can also calculate the brightness temperature for each component and plot the different components in the contour map. It calculates also an estimation of the upper limit of the magnetic field from the brightness temperature (Eq. 6.14) giving the Lorent factor, γ (see Fig. B.6).

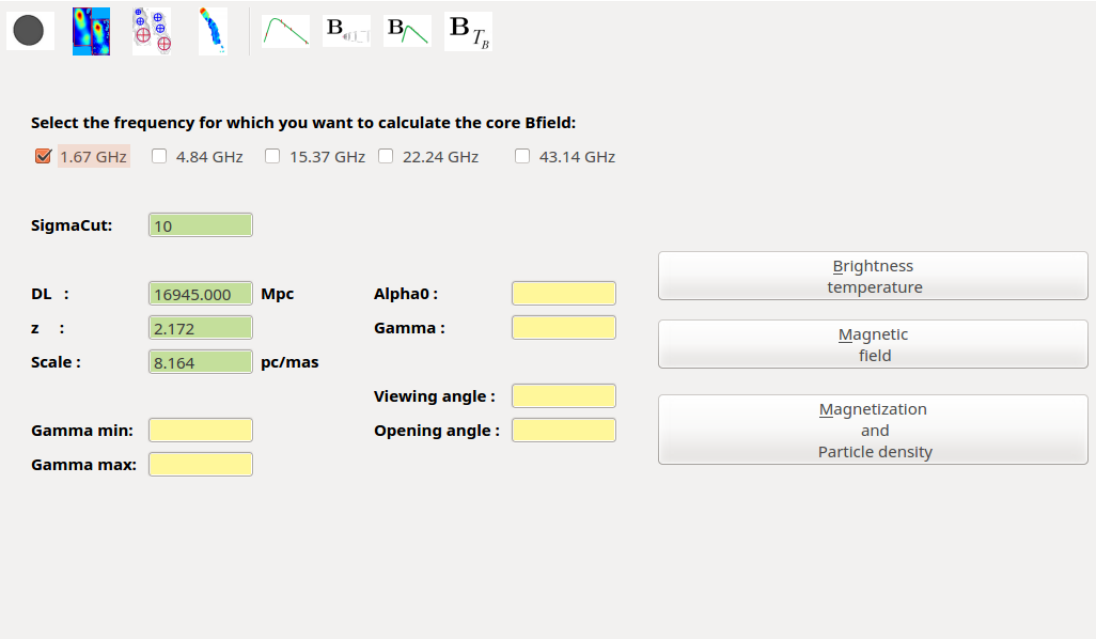

Figure B.6: Screens to calculate the brightness temperature for each modelfit component.

Kinematics analysis software

The kinematics analysis software, *kinepy*, has one main screen, including the steps one should follow in order to perform a kinematics analysis. The user should have two different folders, one with the clean maps, and the second with all the modelfits for each epoch. The program will load all the data corresponding to the same source. Then, the user can perform a kinematics analysis following the typical steps. First, the user can select the core component with the button "Select core". The user selects it in the first epoch and the program will identify the correspondent component in all epochs. If the user confirms that the automatic identification is correct, the program shifts all the images and components with respect so that the core is always at the origin of the map in all epochs. If the automatic identification was not correct, the user can change the identified component in the epochs were it was misidentified. Then, the user can select the different components. If a component is detected in all epochs, the user press the "Select component in all epochs" button and the program will look for the selected component in all the images, based on their distance. As in the case of the core component, if the user does not confirm all the epochs have the proper identification, it is possible to modify the selection in selected epochs. The button for selecting components with missing epochs works in the same manner, with the difference that the user selects first the epochs when the component is detected. When the selection of all components is made, the user can press the "Set all components" button,

and several plots such as the flux against time or component size agains time are produced, and an output file with the parameters for each component identification is created. The button "Fitting" will calculate the speed of each component and the ejection time using Eq. 6.1 in the case the component is detected in at least five epochs.

It is also possible to load a pre-existing identification with the "Load existing identification" button, and change the color and label of the components in the output plots.

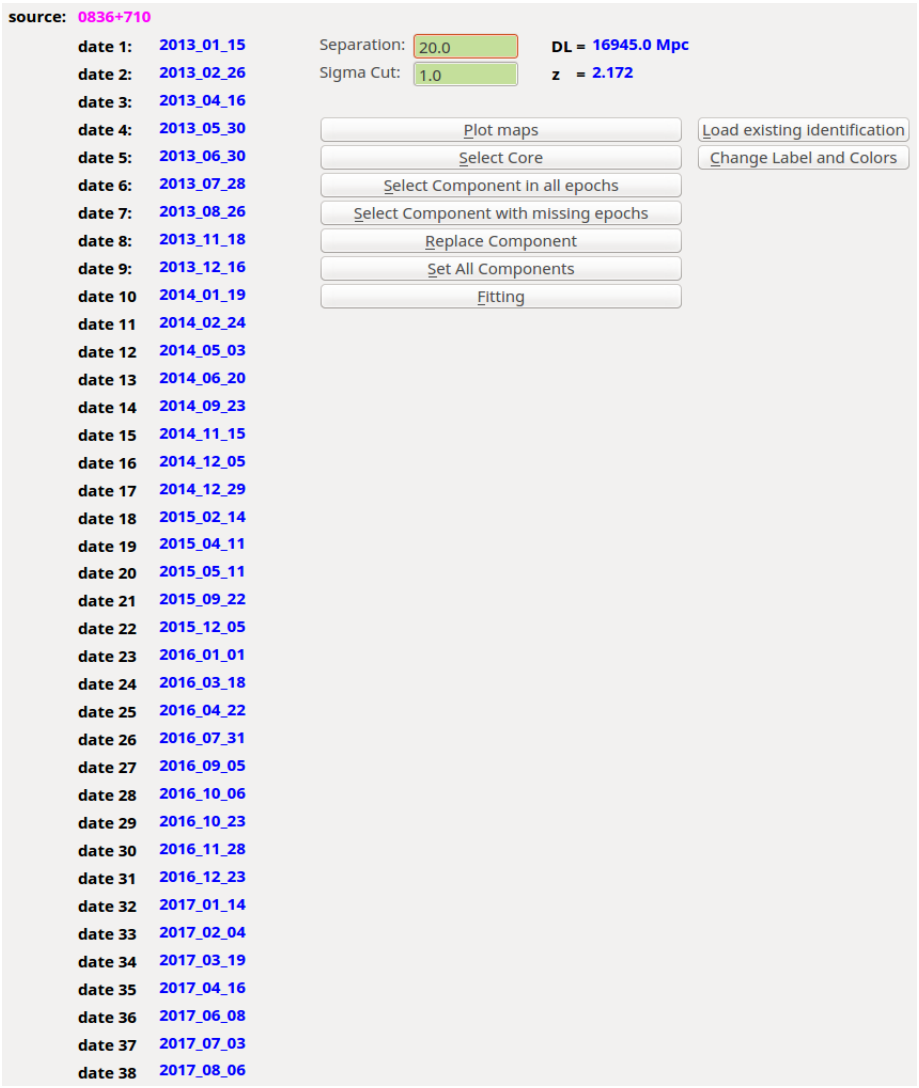

Figure B.7: Screen for the kinematics analysis sofware with the 0836+710 43 GHz data modelfitted loaded.

Appendix C

Modelfit parameters from the images

In this appendix we present the remaining modelfit parameters for all the sources and frequencies. The components in the VLBI maps and modelfits parameters of 0836+710 are presented in Fig. C.1 through C.6 and Table C.1 through Table C.6. The components in the VLBI maps and modelfits parameters of 3C 345 are presented in Fig. C.7 through C.10 and Table C.7 through Table C.10. The components in the VLBI maps and modelfits parameters of 1642+690 are presented in Fig. C.11 through C.14 and Table C.11 through Table C.14. The components in the VLBI maps and modelfits parameters of the space VLBI observations of 3C 273 at 5 GHz are presented in Fig. C.15 and Table C.15.

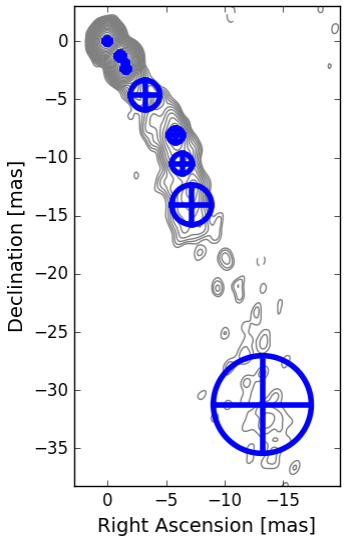

Figure C.1: Modelfit components for the ground array observations of 0836+710 at 5 GHz. The contour levels are drawn at $(-1, 1, \sqrt{2}, 2, \ldots)$ times 1.5 mJy/beam.

Table C.1: Modelfit parameters for the ground VLBI image of 0836+710 at 5 GHz

	S_y [Jy]	r [mas]	ψ [°]	x [mas]	y [mas]	size [mas]	$\theta_{\rm lim}$ [mas]
c	1.9257 ± 0.002	0.0 ± 0.2	91.78 ± 0.07	0.022 ± 0.007	−0.0 ± 0.2	0.3 ± 0.2	0.015
c7	0.0964 ± 0.00012	1.7 ± 0.2	−139.67 ± 0.13	−1.08 ± 0.17	−1.27 ± 0.15	0.3 ± 0.2	0.075
c8	0.24721 ± 0.00013	2.8 ± 0.2	−146.599 ± 0.018	−1.57 ± 0.19	−2.37 ± 0.12	0.3 ± 0.2	0.048
c9	0.049 ± 0.002	5.6 ± 0.6	−145 ± 15	−3.2 ± 1.0	−4.6 ± 1.3	1.3 ± 0.2	0.453
c10	0.1076 ± 0.0017	10.0 ± 0.3	−144.2 ± 1.4	−5.8 ± 0.3	−8.1 ± 0.3	0.6 ± 0.2	0.263
c11	0.0692 ± 0.0012	12.3 ± 0.4	−148.8 ± 1.6	−6.4 ± 0.4	−10.5 ± 0.4	0.9 ± 0.2	0.275
c12	0.142 ± 0.002	15.8 ± 0.9	−152.9 ± 1.6	−7.2 ± 0.8	−14.1 ± 0.5	1.7 ± 0.2	0.277
c15	0.095 ± 0.0016	34 ± 2	−157.0 ± 1.3	−13.3 ± 2.0	−31.2 ± 1.1	4.2 ± 0.2	0.269

Notes: Column designation: S_y: flux density; r: position of the component; ψ: position angle of the component; x: position of the component in RA; y: position of the component in DEC; θ_g: size of the gaussian component; $\theta_{\rm lim}$: limiting size of the gaussian component.

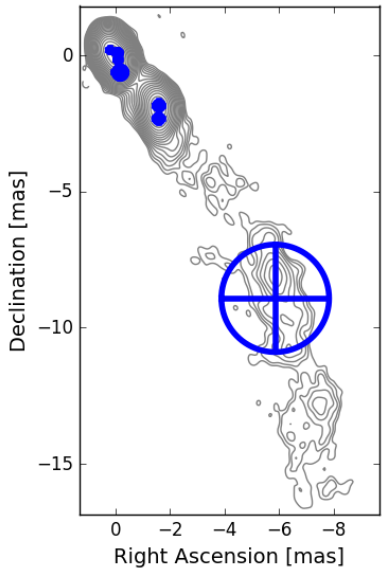

Figure C.2: Modelfit components for the ground array observations of 0836+710 at 15 GHz. The contour levels are drawn at (−1, 1, $\sqrt{2}$, 2, ...) times 0.75 mJy/beam.

Table C.2: Modelfit parameters for the ground VLBI image of 0836+710 at 15 GHz

	S_y [Jy]	r [mas]	ψ [°]	x [mas]	y [mas]	θ [mas]	$\theta_{\rm lim}$ [mas]
c	0.823 ± 0.003	0.28 ± 0.13	44.0 ± 1.3	0.19 ± 0.1	0.2 ± 0.09	0.08 ± 0.13	0.069
c2	0.993 ± 0.0012	0.19 ± 0.13	−147.6 ± 1.9	−0.1 ± 0.11	−0.16 ± 0.07	0.1 ± 0.13	0.044
d1	0.04 ± 0.007	0.65 ± 0.13	−160 ± 80	−0.2 ± 0.3	−0.6 ± 0.9	0.23 ± 0.13	0.506
c3	0.061 ± 0.007	0.14 ± 0.13	−40 ± 90	−0.09 ± 0.17	−0.11 ± 0.18	0.11 ± 0.13	0.418
c7	0.279 ± 0.002	2.43 ± 0.13	−139 ± 11	−1.6 ± 0.3	−1.8 ± 0.4	0.16 ± 0.13	0.108
c8	0.124 ± 0.0008	2.81 ± 0.13	−145.6 ± 0.5	−1.59 ± 0.11	−2.32 ± 0.08	0.15 ± 0.13	0.100
c10	0.079 ± 0.003	10.7 ± 1.0	−146.66 ± 0.14	−5.9 ± 0.8	−8.9 ± 0.5	1.98 ± 0.13	0.251

Notes: Column designation: S_y: flux density; r: position of the component; ψ: position angle of the component; x: position of the component in RA; y: position of the component in DEC; θ_g: size of the gaussian component; $\theta_{\rm lim}$: limiting size of the gaussian component.

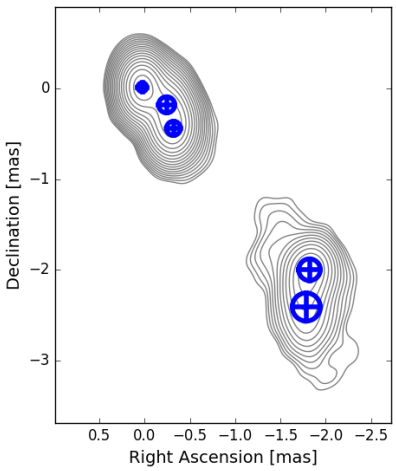

Figure C.3: Modelfit components for the ground array observations of 0836+710 at 22 GHz. The contour levels are drawn at (−1, 1, $\sqrt{2}$, 2, ...) times 1.0 mJy/beam.

Table C.3: Modelfit parameters for the ground VLBI image of 0836+710 at 22 GHz

	S_y [Jy]	r [mas]	ψ [°]	x [mas]	y [mas]	θ [mas]	$\theta_{\rm lim}$ [mas]
c	0.636 ± 0.002	0.04 ± 0.07	59 ± 8	0.03 ± 0.03	0.02 ± 0.06	0.05 ± 0.13	0.038
c2	0.4275 ± 0.0014	0.54 ± 0.07	−144.0 ± 0.4	−0.32 ± 0.05	−0.44 ± 0.04	0.08 ± 0.13	0.035
c3	0.3121 ± 0.0015	0.30 ± 0.07	−126.3 ± 1.4	−0.24 ± 0.04	−0.18 ± 0.05	0.09 ± 0.13	0.044
c7	0.1350 ± 0.0009	2.70 ± 0.07	−137.7 ± 0.3	−1.82 ± 0.05	−2.00 ± 0.05	0.12 ± 0.13	0.050
c8	0.1015 ± 0.0013	3.00 ± 0.07	−143.5 ± 0.7	−1.79 ± 0.06	−2.41 ± 0.05	0.15 ± 0.13	0.070

Notes: Column designation: S_y: flux density; r: position of the component; ψ: position angle of the component; x: position of the component in RA; y: position of the component in DEC; θ_g: size of the gaussian component; $\theta_{\rm lim}$: limiting size of the gaussian component.

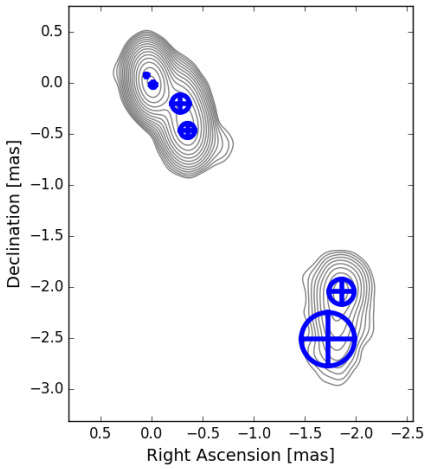

Figure C.4: Modelfit components for the ground array observations of 0836+710 at 43 GHz. The contour levels are drawn at (-1, 1, $\sqrt{2}$, 2, ...) times 2.5 mJy/beam.

Table C.4: Modelfit parameters for the ground VLBI image of 0836+710 at 43 GHz

	S_y [Jy]	r [mas]	ψ [°]	x [mas]	y [mas]	θ [mas]	$\theta_{\rm lim}$ [mas]
c	0.168 ± 0.004	0.09 ± 0.05	30 ± 30	0.05 ± 0.05	0.08 ± 0.05	0.01 ± 0.05	0.081
c1	0.429 ± 0.009	0.02 ± 0.05	−150 ± 70	−0.01 ± 0.05	−0.02 ± 0.04	0.03 ± 0.05	0.076
c2	0.187 ± 0.003	0.35 ± 0.05	−126 ± 12	−0.28 ± 0.07	−0.2 ± 0.06	0.09 ± 0.05	0.069
c3	0.239 ± 0.003	0.58 ± 0.05	−143 ± 3	−0.35 ± 0.05	−0.47 ± 0.04	0.07 ± 0.05	0.058
c7	0.084 ± 0.003	2.76 ± 0.06	−138 ± 7	−1.9 ± 0.2	−2.0 ± 0.2	0.12 ± 0.05	0.104
c8	0.05 ± 0.004	3.05 ± 0.13	−145 ± 19	−1.7 ± 0.6	−2.5 ± 0.8	0.26 ± 0.05	0.148

Notes: Column designation: S_y: flux density; r: position of the component; ψ: position angle of the component; x: position of the component in RA; y: position of the component in DEC; θ_g: size of the gaussian component; $\theta_{\rm lim}$: limiting size of the gaussian component.

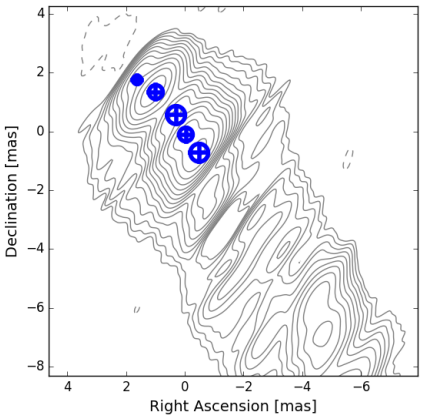

Figure C.5: Modelfit components for the space VLBI observations of 0836+710 at 1.6 GHz. The contour levels are drawn at (−1, 1, $\sqrt{2}$, 2, ...) times 0.10 mJy/beam.

Table C.5: Modelfit parameters for the space VLBI image of 0836+710 at 1.6 GHz

	S_y [Jy]	r [mas]	ψ [°]	x [mas]	y [mas]	θ [mas]	$\theta_{\rm lim}$ [mas]
0	0.0704 ± 0.0015	2.39 ± 0.17	43 ± 4	1.62 ± 0.17	1.75 ± 0.17	0.15 ± 0.17	0.231
1	0.168 ± 0.007	0.63 ± 0.17	30 ± 40	0.3 ± 0.2	0.6 ± 0.4	0.31 ± 0.17	0.325
2	0.385 ± 0.002	0.11 ± 0.17	−160 ± 12	−0.04 ± 0.16	−0.11 ± 0.06	0.23 ± 0.17	0.118
3	0.642 ± 0.004	0.88 ± 0.17	−146 ± 2	−0.49 ± 0.14	−0.73 ± 0.1	0.31 ± 0.17	0.131
4	0.257 ± 0.003	1.66 ± 0.17	36 ± 2	0.99 ± 0.14	1.34 ± 0.11	0.24 ± 0.17	0.170

Notes: Column designation: S_y: flux density; r: position of the component; ψ: position angle of the component; x: position of the component in RA; y: position of the component in DEC; θ_g: size of the gaussian component; $\theta_{\rm lim}$: limiting size of the gaussian component.

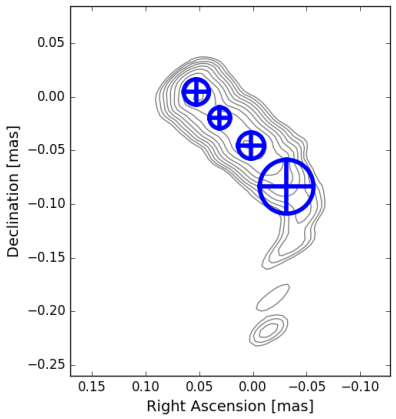

Figure C.6: Modelfit components for the space VLBI observations of 0836+710 at 22 GHz. The contour levels are drawn at (−1, 1, $\sqrt{2}$, 2, ...) times 5.0 mJy/beam.

Table C.6: Modelfit parameters for the space VLBI image of 0836+710 at 22 GHz

	S_y [Jy]	r [mas]	ψ [°]	x [mas]	y [mas]	θ [mas]	$\theta_{\rm lim}$ [mas]
0	0.139 ± 0.004	0.053 ± 0.006	85 ± 10	0.053 ± 0.009	0.004 ± 0.006	0.012 ± 0.005	0.007
1	0.108 ± 0.004	0.037 ± 0.005	123 ± 17	0.031 ± 0.01	−0.02 ± 0.007	0.01 ± 0.005	0.008
2	0.218 ± 0.004	0.046 ± 0.006	178 ± 7	0.002 ± 0.006	−0.045 ± 0.006	0.012 ± 0.005	0.006
3	0.12 ± 0.004	0.09 ± 0.013	−159 ± 8	−0.031 ± 0.013	−0.084 ± 0.013	0.025 ± 0.005	0.008

Notes: Column designation: S_y: flux density; r: position of the component; ψ: position angle of the component; x: position of the component in RA; y: position of the component in DEC; θ_g: size of the gaussian component; $\theta_{\rm lim}$: limiting size of the gaussian component.

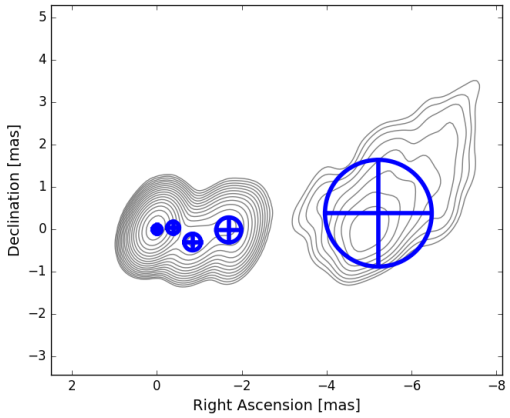

Figure C.7: Modelfit components for the ground array observations of 3C 345 at 15 GHz. The contour levels are drawn at (−1, 1, $\sqrt{2}$, 2, ...) times 3.5 mJy/beam.

Table C.7: Modelfit parameters for the ground VLBI image of 3C 345 at 15 GHz

	S_y [Jy]	r [mas]	ψ [°]	x [mas]	y [mas]	θ [mas]	$\theta_{\rm lim}$ [mas]
c	2.82 ± 0.02	0.0 ± 0.14	−120 ± 80	−0.0 ± 0.08	−0.0 ± 0.11	0.11 ± 0.14	0.115
c2	0.048 ± 0.01	0.39 ± 0.14	−80 ± 80	−0.4 ± 0.6	0.04 ± 0.15	0.14 ± 0.14	0.558
c3	0.632 ± 0.014	0.89 ± 0.14	−110 ± 11	−0.84 ± 0.16	−0.3 ± 0.14	0.2 ± 0.14	0.196
c4	0.678 ± 0.014	1.69 ± 0.15	−90 ± 6	−1.69 ± 0.19	−0.01 ± 0.15	0.29 ± 0.14	0.188
c5	0.797 ± 0.014	5.2 ± 0.6	−86 ± 4	−5.2 ± 0.4	0.4 ± 0.6	1.26 ± 0.14	0.172

Notes: Column designation: S_y: flux density; r: position of the component; ψ: position angle of the component; x: position of the component in RA; y: position of the component in DEC; θ_g: size of the gaussian component; $\theta_{\rm lim}$: limiting size of the gaussian component.

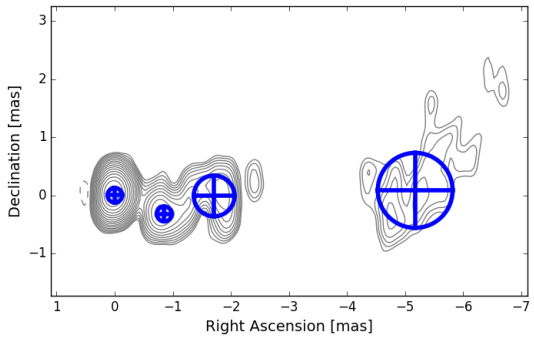

Figure C.8: Modelfit components for the ground array observations of 3C 345 at 22 GHz. The contour levels are drawn at (−1, 1, $\sqrt{2}$, 2, ...) times 5.4 mJy/beam.

Table C.8: Modelfit parameters for the ground VLBI image of 3C 345 at 22 GHz

	S_y [Jy]	r [mas]	ψ [°]	x [mas]	y [mas]	θ [mas]	$\theta_{\rm lim}$ [mas]
c	2.43 ± 0.03	0.01 ± 0.07	−40 ± 80	−0.0 ± 0.05	0.0 ± 0.04	0.13 ± 0.07	0.068
c3	0.355 ± 0.006	0.91 ± 0.07	−110 ± 3	−0.85 ± 0.06	−0.32 ± 0.06	0.13 ± 0.07	0.078
c4	0.434 ± 0.011	1.71 ± 0.18	−90 ± 7	−1.7 ± 0.2	−0.01 ± 0.18	0.35 ± 0.07	0.098
c5	0.344 ± 0.009	5.2 ± 0.3	−89 ± 4	−5.2 ± 0.4	0.1 ± 0.3	0.64 ± 0.07	0.099

Notes: Column designation: S_y: flux density; r: position of the component; ψ: position angle of the component; x: position of the component in RA; y: position of the component in DEC; θ_g: size of the gaussian component; $\theta_{\rm lim}$: limiting size of the gaussian component.

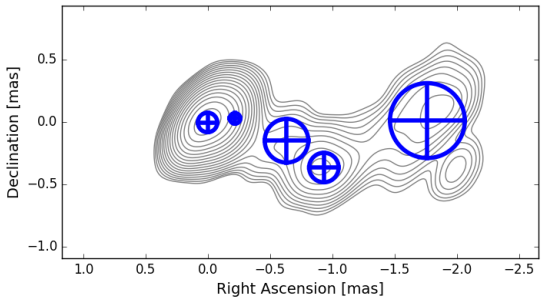

Figure C.9: Modelfit components for the ground array observations of 3C 345 at 43 GHz. The contour levels are drawn at (−1, 1, $\sqrt{2}$, 2, ...) times 5.5 mJy/beam.

Table C.9: Modelfit parameters for the ground VLBI image of 3C 345 at 43 GHz

	S_y [Jy]	r [mas]	ψ [°]	x [mas]	y [mas]	θ [mas]	$\theta_{\rm lim}$ [mas]
c	2.11 ± 0.04	0.0 ± 0.06	140 ± 90	0.0 ± 0.04	−0.0 ± 0.03	0.08 ± 0.06	0.072
c1	0.13 ± 0.08	0.22 ± 0.07	−80 ± 90	−0.2 ± 0.3	0.03 ± 0.08	0.04 ± 0.14	0.361
c2	0.22 ± 0.03	0.65 ± 0.09	−100 ± 60	−0.6 ± 0.7	−0.15 ± 0.18	0.18 ± 0.06	0.197
c3	0.14 ± 0.019	1.0 ± 0.06	−110 ± 40	−0.9 ± 0.7	−0.4 ± 0.3	0.12 ± 0.06	0.185
c4	0.273 ± 0.019	1.76 ± 0.15	−90 ± 19	−1.8 ± 0.6	0.01 ± 0.15	0.3 ± 0.06	0.136

Notes: Column designation: S_y: flux density; r: position of the component; ψ: position angle of the component; x: position of the component in RA; y: position of the component in DEC; θ_g: size of the gaussian component; $\theta_{\rm lim}$: limiting size of the gaussian component.

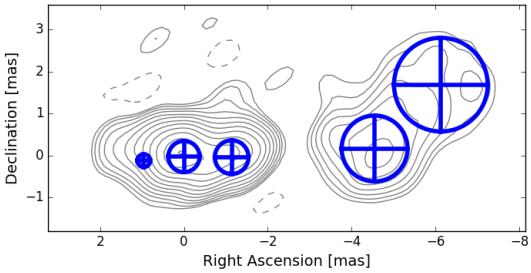

Figure C.10: Modelfit components for the space VLBI observations of 3C 345 at 5 GHz. The contour levels are drawn at (−1, 1, $\sqrt{2}$, 2, ...) times 35 mJy/beam.

Table C.10: Modelfit parameters for the space VLBI image of 3C 345 at 5 GHz

	S_y [Jy]	r [mas]	ψ [°]	x [mas]	y [mas]	θ [mas]	$\theta_{\rm lim}$ [mas]
0	0.99 ± 0.03	4.6 ± 0.4	−88 ± 12	−4.5 ± 0.9	0.2 ± 0.4	0.79 ± 0.15	0.233
1	0.615 ± 0.015	6.4 ± 0.6	−75 ± 10	−6.1 ± 1.1	1.7 ± 0.6	1.12 ± 0.15	0.217
2	1.26 ± 0.07	1.1 ± 0.2	−90 ± 40	−1.1 ± 0.9	−0.0 ± 0.2	0.4 ± 0.15	0.327
3	2.05 ± 0.07	0.02 ± 0.19	180 ± 90	0.0 ± 0.19	−0.02 ± 0.04	0.37 ± 0.15	0.255
4	0.206 ± 0.019	0.97 ± 0.15	100 ± 60	1.0 ± 0.9	−0.12 ± 0.19	0.15 ± 0.15	0.426

Notes: Column designation: S_y: flux density; r: position of the component; ψ: position angle of the component; x: position of the component in RA; y: position of the component in DEC; θ_g: size of the gaussian component; $\theta_{\rm lim}$: limiting size of the gaussian component.

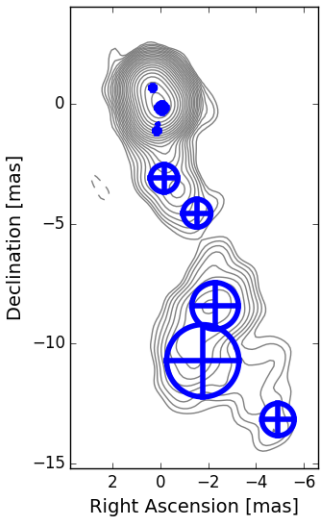

Figure C.11: Modelfit components for the ground array observations of 1642+690 at 5 GHz. The contour levels are drawn at $(-1,\ 1,\ \sqrt{2},\ 2,\ \ldots\ )$ times 80 mJy/beam.

Table C.11: Modelfit parameters for the ground VLBI image of 1642+690 at 5 GHz

	S_y [Jy]	r [mas]	ψ [°]	x [mas]	y [mas]	θ [mas]	$\theta_{\rm lim}$ [mas]
c	0.674 ± 0.002	0.7 ± 0.2	24.5 ± 1.0	0.3 ± 0.2	0.66 ± 0.09	0.1 ± 0.2	0.120
c1	1.233 ± 0.006	0.2 ± 0.2	−158 ± 7	−0.1 ± 0.2	−0.18 ± 0.09	0.2 ± 0.2	0.144
c2	0.04 ± 0.006	0.9 ± 0.2	170 ± 70	0.1 ± 0.2	−0.9 ± 1.1	0.0 ± 0.2	0.765
c3	0.021 ± 0.005	1.1 ± 0.2	170 ± 80	0.1 ± 0.3	−1.1 ± 1.6	0.1 ± 0.2	0.999
c4	0.03 ± 0.004	3.1 ± 0.3	−180 ± 70	−0.2 ± 0.3	−3 ± c6	0.6 ± 0.3	0.735
c5	0.0053 ± 0.0018	4.8 ± 0.3	−160 ± 70	−1.5 ± 1.8	−5 ± 5	0.6 ± 0.4	1.123
c6	0.0543 ± 0.0018	8.7 ± 0.5	−165 ± 10	−2.3 ± 0.6	−8.4 ± 1.5	1.0 ± 0.2	0.374
c7	0.0463 ± 0.001	10.9 ± 0.8	−171 ± 9	−1.8 ± 0.8	−10.7 ± 1.7	1.5 ± 0.2	0.302
c8	0.0059 ± 0.0005	14.1 ± 0.3	−160 ± 16	−4.9 ± 1.4	−13 ± 4	0.7 ± 0.2	0.574

Notes: Column designation: S_y: flux density; r: position of the component; ψ: position angle of the component; x: position of the component in RA; y: position of the component in DEC; θ_g: size of the gaussian component; $\theta_{\rm lim}$: limiting size of the gaussian component.

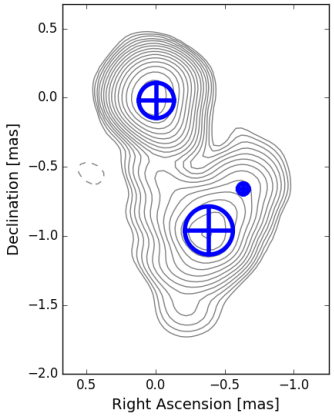

Figure C.12: Modelfit components for the ground array observations of 1642+690 at 22 GHz. The contour levels are drawn at $(-1,\ 1,\ \sqrt{2},\ 2,\ \ldots\ )$ times 9.0 mJy/beam.

Table C.12: Modelfit parameters for the ground VLBI image of 1642+690 at 22 GHz

	S_y [Jy]	r [mas]	ψ [°]	x [mas]	y [mas]	θ [mas]	$\theta_{\rm lim}$ [mas]
c	0.74 ± 0.08	0.02 ± 0.06	-160 ± 90	-0.01 ± 0.06	-0.02 ± 0.04	0.13 ± 0.05	0.155
c2	0.04 ± 0.019	0.92 ± 0.05	-140 ± 70	-0.6 ± 0.8	-0.7 ± 0.8	0.04 ± 0.1	0.303
c3	0.361 ± 0.017	1.03 ± 0.09	-160 ± 20	-0.39 ± 0.16	-1.0 ± 0.4	0.17 ± 0.05	0.106

Notes: Column designation: S_y: flux density; r: position of the component; ψ: position angle of the component; x: position of the component in RA; y: position of the component in DEC; θ_g: size of the gaussian component; $\theta_{\rm lim}$: limiting size of the gaussian component.

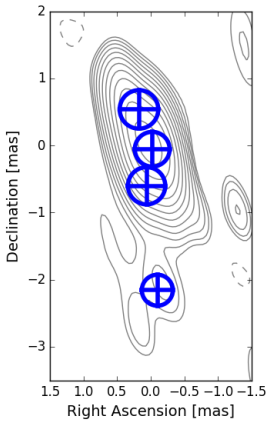

Figure C.13: Modelfit components for the space VLBI observations of 1642+690 at 1.6 GHz. The contour levels are drawn at $(-1,\ 1,\ \sqrt{2},\ 2,\ \ldots\ )$ times 20 mJy/beam.

Table C.13: Modelfit parameters for the space VLBI image of 1642+690 at 1.6 GHz

	S_y [Jy]	r [mas]	ψ [°]	x [mas]	y [mas]	θ [mas]	$\theta_{\rm lim}$ [mas]
0	0.336 ± 0.008	0.56 ± 0.12	18.0 ± 20.0	0.17 ± 0.13	0.54 ± 0.19	0.29 ± 0.12	0.178
1	0.801 ± 0.003	0.06 ± 0.12	−157.8 ± 11.0	−0.02 ± 0.11	−0.06 ± 0.05	0.26 ± 0.12	0.070
2	0.148 ± 0.002	0.6 ± 0.12	174.3 ± 11.0	0.06 ± 0.12	−0.6 ± 0.12	0.28 ± 0.12	0.146
3	0.059 ± 0.005	2.16 ± 0.12	−177.4 ± 29.0	−0.1 ± 0.13	−2.2 ± 1.1	0.23 ± 0.12	0.315

Notes: Column designation: S_y: flux density; r: position of the component; ψ: position angle of the component; x: position of the component in RA; y: position of the component in DEC; θ_g: size of the gaussian component; $\theta_{\rm lim}$: limiting size of the gaussian component.

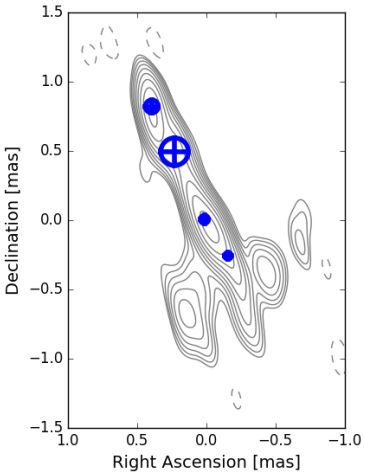

Figure C.14: Modelfit components for the space VLBI observations of 1642+690 at 5 GHz. The contour levels are drawn at $(-1,\ 1,\ \sqrt{2},\ 2,\ \ldots\ )$ times 23 mJy/beam.

Table C.14: Modelfit parameters for the space VLBI image of 1642+690 at 5 GHz

	S_y [Jy]	r [mas]	ψ [°]	x [mas]	y [mas]	θ [mas]	$\theta_{\rm lim}$ [mas]
0	0.337 ± 0.016	0.91 ± 0.07	26 ± 16	0.39 ± 0.13	0.8 ± 0.2	0.05 ± 0.07	0.150
1	0.33 ± 0.02	0.54 ± 0.07	20 ± 50	0.23 ± 0.19	0.5 ± 0.4	0.1 ± 0.07	0.171
2	0.522 ± 0.015	0.01 ± 0.07	80 ± 80	0.01 ± 0.02	0.0 ± 0.07	0.03 ± 0.07	0.114
3	0.323 ± 0.009	0.3 ± 0.07	−149 ± 18	−0.16 ± 0.08	−0.26 ± 0.09	0.02 ± 0.07	0.114

Notes: Column designation: S_y: flux density; r: position of the component; ψ: position angle of the component; x: position of the component in RA; y: position of the component in DEC; θ_g: size of the gaussian component; $\theta_{\rm lim}$: limiting size of the gaussian component.

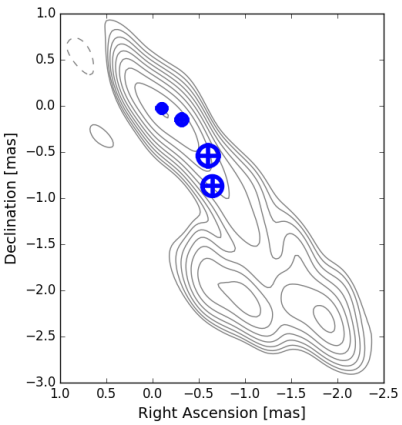

Figure C.15: Modelfit components for the space VLBI observations of 3C 273 at 5 GHz. The contour levels are drawn at (-1, 1, $\sqrt{2}$, 2, ...) times 42 mJy/beam.

Table C.15: Modelfit parameters for the space VLBI image of 3C 273 at 5 GHz

	S_y [Jy]	r [mas]	ψ [°]	x [mas]	y [mas]	θ [mas]	$\theta_{\rm lim}$ [mas]
0	0.55 ± 0.075	0.108 ± 0.083	−107.3 ± 84.0	−0.1 ± 0.15	−0.032 ± 0.092	0.047 ± 0.083	0.278
1	0.93 ± 0.17	0.354 ± 0.083	−115.9 ± 81.0	−0.32 ± 0.45	−0.15 ± 0.23	0.057 ± 0.083	0.319
2	0.378 ± 0.031	0.814 ± 0.083	−132.1 ± 39.0	−0.6 ± 0.42	−0.55 ± 0.38	0.113 ± 0.083	0.218
3	0.419 ± 0.053	1.089 ± 0.083	−143.4 ± 50.0	−0.65 ± 0.57	−0.87 ± 0.76	0.107 ± 0.083	0.267

Notes: Column designation: S_y: flux density; r: position of the component; ψ: position angle of the component; x: position of the component in RA; y: position of the component in DEC; θ_g: size of the gaussian component; $\theta_{\rm lim}$: limiting size of the gaussian component.

Appendix D

Modelfit component paramenters for the 43 GHz kinematic analysis

In this appendix we present the `Modelfit` parameters of the Gaussian components used for the kinematic analysis of 0836+710 described in Section 6.1.1. Tables D.1 through D.6. The position angle is given in the range $(\pi, -\pi)$, with the zero in the N-S direction (in image coordinates) and positive values in the counter-clockwise direction.

Table D.1: Difmap `Modelfit` parameters for the Gaussian components model from VLBA 43 GHz observations of 0836+710.

Epoch	ID	S [Jy]	d [mas]	ϕ [°]	Size [mas]
2013-01-16	core	0.548	0.00	50.43	0.05
	c1	0.022	0.15	-134.03	0.05
	c2	0.326	0.33	-147.98	0.07
	c7	0.134	2.75	-138.98	0.14
2013-02-26	core	0.401	0.00	-140.55	0.03
	c1	0.318	0.12	-131.38	0.05
	c2	0.347	0.40	-146.85	0.07
	c7	0.148	2.81	-139.33	0.14
2013-04-18	core	0.157	0.00	170.15	0.03
	c1	0.321	0.13	-128.33	0.07
	c2	0.281	0.44	-144.48	0.08
	c7	0.133	2.84	-139.21	0.16
2013-06-01	core	0.257	0.00	52.39	0.04
	c1	0.167	0.17	-134.18	0.09
	c2	0.183	0.44	-144.91	0.06
	c7	0.100	2.81	-139.46	0.13

Notes: Column designation: S: flux density; d: radial distance from the core; ϕ: position angle.

Table D.2: Difmap `Modelfit` parameters for the Gaussian components model from VLBA 43 GHz observations of 0836+710 (continued).

Epoch	ID	S [Jy]	d [mas]	ϕ [°]	Size [mas]
2013-07-02	core	0.338	0.00	65.84	0.02
	c1	0.240	0.15	-125.98	0.07
	c2	0.241	0.46	-143.21	0.09
	c7	0.127	2.81	-138.97	0.17
2013-07-30	core	0.399	0.00	98.71	0.02
	c3	0.055	0.22	-117.14	0.05
	c2	0.254	0.43	-142.41	0.08
	c7	0.102	2.80	-138.95	0.14
2013-08-27	core	0.329	0.00	-65.49	0.02
	c3	0.133	0.19	-128.32	0.08
	c2	0.214	0.49	-141.44	0.08
	c7	0.113	2.80	-138.45	0.18
2013-11-19	core	0.646	0.00	112.15	0.04
	c3	0.168	0.31	-125.20	0.09
	c2	0.222	0.57	-143.26	0.07
	c7	0.113	2.77	-138.53	0.16
2013-12-17	core	0.506	0.00	-149.22	0.04
	c3	0.140	0.36	-127.49	0.09
	c2	0.189	0.58	-143.11	0.07
	c7	0.114	2.82	-139.15	0.21
2014-01-19	core	0.128	0.00	169.95	0.01
	c1	0.359	0.11	-139.15	0.03
	c3	0.153	0.44	-128.49	0.09
	c2	0.195	0.67	-142.67	0.08
	c7	0.106	2.89	-138.70	0.20
2014-02-24	core	0.183	0.00	115.47	0.01
	c1	0.335	0.11	-137.29	0.02
	c3	0.140	0.46	-127.83	0.09
	c2	0.177	0.68	-141.95	0.07
	c7	0.107	2.93	-139.42	0.24
2014-05-05	core	0.397	0.00	-64.98	0.03
	c1	0.418	0.08	-133.93	0.02
	c3	0.191	0.46	-126.23	0.08
	c2	0.232	0.70	-142.67	0.07
	c7	0.118	2.91	-139.79	0.23
2014-06-22	core	0.434	0.00	-133.64	0.02
	c1	0.423	0.10	-139.12	0.02
	c3	0.170	0.49	-127.19	0.07
	c2	0.219	0.73	-143.15	0.07
	c7	0.105	2.88	-139.54	0.22

Notes: Column designation: S: flux density; d: radial distance from the core; ϕ: position angle.

Table D.3: Difmap `Modelfit` parameters for the Gaussian components model from VLBA 43 GHz observations of 0836+710 (continued).

Epoch	ID	S [Jy]	d [mas]	ϕ [°]	Size [mas]
2014-09-24	core	0.629	0.00	-147.16	0.03
	c1	0.889	0.10	-121.44	0.02
	c3	0.219	0.61	-128.41	0.07
	c2	0.211	0.80	-142.41	0.07
	c7	0.124	2.89	-139.31	0.21
2014-11-16	core	0.607	0.00	49.97	0.03
	c1	0.457	0.09	-115.86	0.03
	c3	0.140	0.61	-127.50	0.07
	c2	0.161	0.80	-141.75	0.08
	c7	0.095	2.85	-138.82	0.20
2014-12-06	core	0.770	0.00	36.94	0.03
	c1	0.396	0.09	-113.48	0.02
	c3	0.144	0.63	-127.06	0.06
	c2	0.171	0.81	-141.51	0.08
	c7	0.102	2.86	-139.15	0.20
2014-12-30	core	1.042	0.00	172.63	0.02
	c1	0.330	0.09	-108.88	0.01
	c3	0.141	0.63	-127.37	0.06
	c2	0.183	0.81	-141.17	0.09
	c7	0.113	2.88	-138.98	0.23
2015-02-14	core	1.417	0.00	171.26	0.02
	c1	0.255	0.09	-131.16	0.05
	c3	0.139	0.64	-127.12	0.07
	c2	0.170	0.84	-142.38	0.08
	c7	0.112	2.85	-139.48	0.21
2015-04-13	core	1.440	0.00	-136.82	0.02
	c1	0.624	0.07	-96.95	0.00
	c3	0.121	0.72	-128.47	0.06
	c2	0.165	0.86	-142.10	0.09
	c7	0.117	2.84	-139.02	0.21
2015-05-13	core	0.114	0.00	135.00	0.02
	c1	0.972	0.10	-145.41	0.01
	c4	0.656	0.16	-127.36	0.02
	c3	0.105	0.80	-129.79	0.08
	c2	0.128	0.97	-142.01	0.09
	c7	0.088	2.94	-139.22	0.21
	c1	1.433	0.08	-123.50	0.03
	c3	0.119	0.76	-128.75	0.11
	c2	0.158	0.94	-141.54	0.11

Notes: Column designation: S: flux density; d: radial distance from the core; ϕ: position angle.

Table D.4: Difmap `Modelfit` parameters for the Gaussian components model from VLBA 43 GHz observations of 0836+710 (continued).

Epoch	ID	S [Jy]	d [mas]	ϕ [°]	Size [mas]
2015-09-23	core	0.403	0.00	70.30	0.02
	c1	1.093	0.09	-134.57	0.02
	c4	0.508	0.19	-124.22	0.03
	c3	0.083	0.86	-130.06	0.08
	c2	0.120	1.03	-141.90	0.10
	c7	0.141	2.85	-138.31	0.25
2015-12-06	core	0.199	0.00	-153.57	0.03
	c7	0.086	2.89	-139.02	0.19
2016-01-01	core	0.181	0.00	-53.34	0.02
	c1	0.796	0.10	-133.38	0.02
	c4	0.297	0.21	-125.27	0.04
	c3	0.051	0.91	-129.73	0.08
	c2	0.089	1.08	-142.52	0.11
	c7	0.069	2.91	-138.87	0.20
2016-03-20	core	0.230	0.00	-141.14	0.02
	c1	0.638	0.11	-147.12	0.02
	c4	0.265	0.23	-132.94	0.04
	c5	0.047	0.36	-130.66	0.06
	c3	0.041	0.96	-130.92	0.08
	c2	0.095	1.13	-143.06	0.13
	c7	0.070	2.96	-139.41	0.22
2016-04-23	core	0.210	0.00	67.14	0.02
	c1	0.738	0.11	-143.68	0.02
	c4	0.214	0.23	-132.93	0.04
	c5	0.078	0.35	-128.74	0.07
	c3	0.036	0.98	-130.75	0.08
	c2	0.091	1.15	-143.10	0.13
	c7	0.060	2.93	-138.86	0.20
2016-08-02	core	0.263	0.00	-43.46	0.02
	c1	0.697	0.13	-142.63	0.03
	c4	0.234	0.29	-131.16	0.06
	c5	0.049	0.45	-132.54	0.03
	c3	0.022	1.02	-130.33	0.06
	c2	0.118	1.20	-142.84	0.15
	c7	0.042	2.92	-138.67	0.14
2016-09-06	core	0.301	0.00	-52.99	0.03
	c1	0.601	0.13	-140.56	0.02
	c4	0.224	0.29	-130.71	0.06
	c5	0.046	0.46	-130.82	0.03
	c3	0.022	1.02	-131.95	0.07
	c2	0.099	1.22	-143.19	0.14
	c7	0.032	2.92	-139.28	0.12

Notes: Column designation: S: flux density; d: radial distance from the core; ϕ: position angle.

Table D.5: Difmap `Modelfit` parameters for the Gaussian components model from VLBA 43 GHz observations of 0836+710 (continued).

Epoch	ID	S [Jy]	d [mas]	ϕ [°]	Size [mas]
2016-10-07	core	0.224	0.00	61.36	0.01
	c1	0.586	0.14	-139.45	0.01
	c4	0.237	0.35	-133.10	0.05
	c5	0.034	0.52	-128.46	0.03
	c3	0.016	1.03	-131.54	0.07
	c2	0.119	1.24	-142.13	0.16
	c7	0.041	2.96	-138.72	0.15
2016-10-24	core	0.232	0.00	-82.69	0.02
	c1	0.325	0.14	-139.14	0.03
	c4	0.177	0.33	-130.98	0.07
	c5	0.027	0.53	-132.93	0.03
	c3	0.011	1.01	-130.37	0.08
	c2	0.087	1.25	-142.17	0.16
	c7	0.034	2.96	-138.99	0.19
2016-11-29	core	0.198	0.00	-135.80	0.02
	c1	0.215	0.14	-141.61	0.02
	c4	0.130	0.29	-132.00	0.07
	c5	0.062	0.45	-130.61	0.06
	c3	0.009	1.02	-133.97	0.06
	c2	0.072	1.26	-142.67	0.17
	c7	0.024	2.94	-139.27	0.15
2016-12-24	core	0.348	0.00	62.79	0.02
	c1	0.341	0.14	-141.97	0.04
	c4	0.228	0.34	-130.30	0.09
	c5	0.036	0.55	-137.19	0.06
	c2	0.120	1.25	-141.64	0.17
	c7	0.020	2.89	-138.28	0.10
2017-01-14	core	0.387	0.00	-15.19	0.02
	c1	0.244	0.13	-140.21	0.02
	c4	0.171	0.33	-130.43	0.08
	c5	0.044	0.51	-132.38	0.04
	c2	0.105	1.26	-141.76	0.18
	c7	0.021	2.92	-138.54	0.12
2017-02-04	core	0.440	0.00	85.58	0.02
	c1	0.219	0.13	-143.67	0.03
	c4	0.146	0.35	-130.19	0.08
	c5	0.040	0.53	-132.07	0.05
	c2	0.090	1.26	-142.11	0.18
	c7	0.028	3.02	-139.67	0.18

Notes: Column designation: S: flux density; d: radial distance from the core; ϕ: position angle.

Table D.6: Difmap `Modelfit` parameters for the Gaussian components model from VLBA 43 GHz observations of 0836+710 (continued).

Epoch	ID	S [Jy]	d [mas]	ϕ [°]	Size [mas]
2017-03-21	core	0.439	0.00	116.72	0.02
	c1	0.166	0.11	-142.38	0.02
	c4	0.107	0.34	-129.29	0.09
	c5	0.036	0.54	-132.86	0.05
	c2	0.067	1.30	-141.57	0.17
	c7	0.019	2.93	-138.78	0.19
2017-04-18	core	0.441	0.00	140.07	0.03
	c1	0.190	0.08	-140.47	0.03
	c4	0.124	0.36	-128.48	0.10
	c5	0.026	0.58	-134.47	0.04
	c2	0.065	1.30	-142.00	0.17
	c7	0.018	2.91	-138.82	0.14
2017-06-10	core	0.300	0.00	140.53	0.02
	c1	0.862	0.08	-133.25	0.01
	c6	0.083	0.19	-140.10	0.05
	c4	0.137	0.42	-127.28	0.06
	c5	0.060	0.62	-133.32	0.06
	c2	0.100	1.36	-141.65	0.18
	c7	0.027	3.00	-139.06	0.17
2017-07-05	core	0.181	0.00	-130.80	0.01
	c1	0.937	0.10	-133.56	0.02
	c6	0.056	0.22	-139.68	0.04
	c4	0.142	0.45	-127.88	0.07
	c5	0.056	0.66	-133.61	0.07
	c2	0.089	1.41	-141.34	0.18
	c7	0.016	2.97	-139.35	0.12
2017-08-07	core	0.198	0.00	-142.09	0.01
	c1	0.666	0.11	-132.39	0.02
	c6	0.026	0.26	-141.57	0.02
	c4	0.099	0.45	-127.09	0.05
	c5	0.048	0.66	-133.26	0.07
	c2	0.065	1.41	-141.11	0.18
	c7	0.011	2.95	-138.51	0.12

Notes: Column designation: S: flux density; d: radial distance from the core; ϕ: position angle.

Appendix E

Spectral index map with cut line

Here we present the cuts along the jet of our sources, that were used to produce the spectral index profiles shown in Chapter 6.

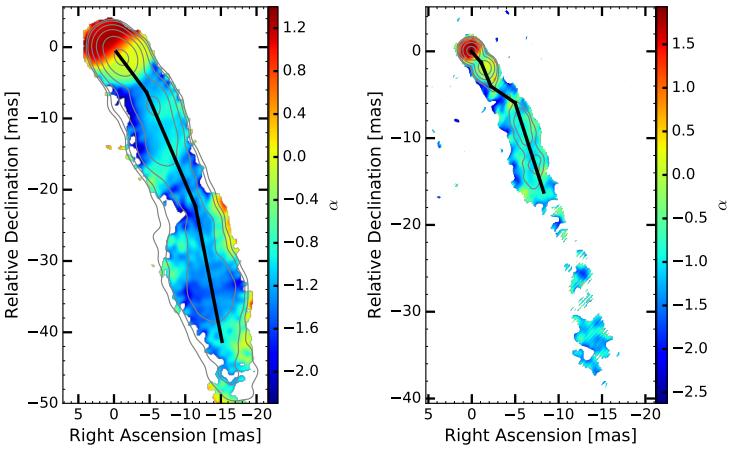

Figure E.1: Line in which the spectral index map between 1.6 GHz ground observations (left)/ or space VLBI observations (right) and 5 GHz ground image for 0836+710 was made. The corresponding spectral index profile are presented in Fig. 6.7 and 6.11, respectively.

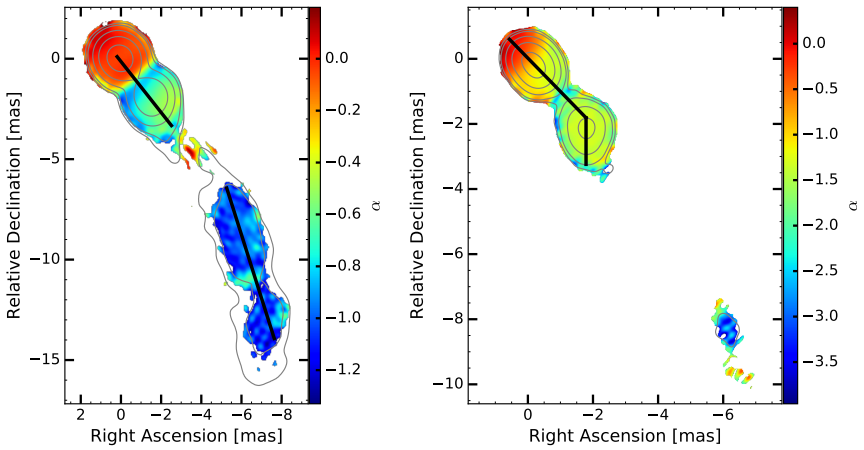

Figure E.2: Line in which the spectral index map between 5 GHz and 15 GHz (left) and between 15 GHz and 22 GHz (right) ground VLBI observations for 0836+710 was made. The corresponding spectral index profile are presented in Fig. 6.8 and 6.9, respectively.

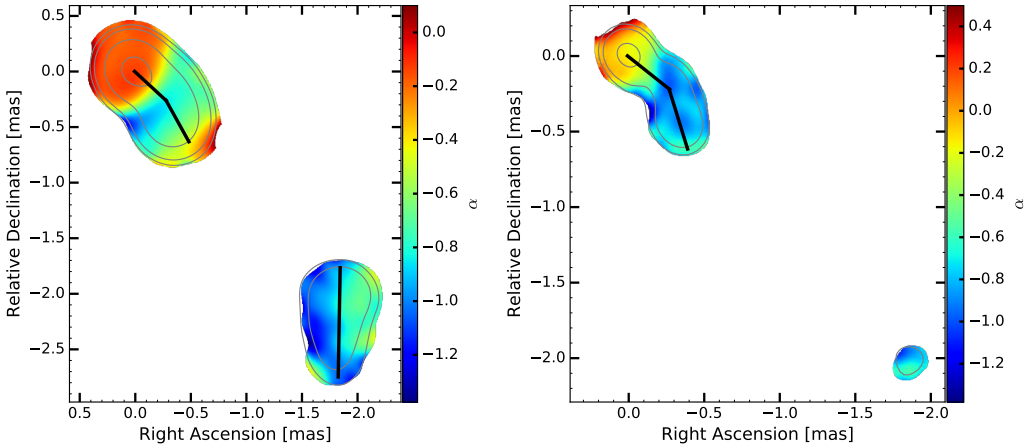

Figure E.3: Line in which the spectral index map between 22 GHz ground observations (left)/ or space VLBI observations (right) and 43 GHz ground image for 0836+710 was made. The corresponding spectral index profile are presented in Fig. 6.10 and 6.14, respectively.

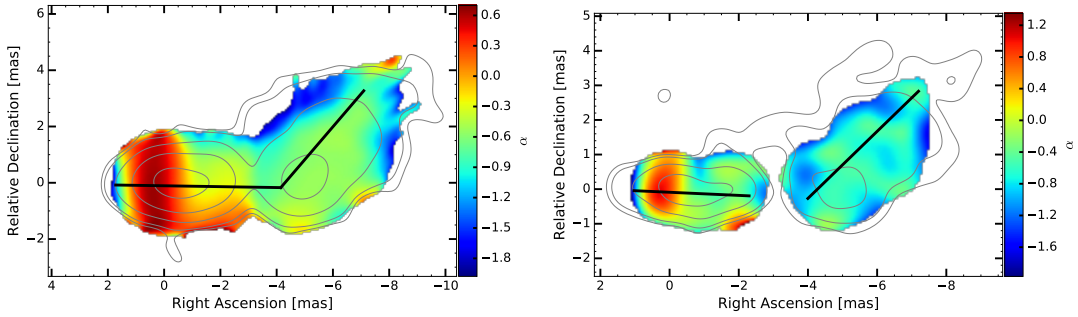

Figure E.4: Line in which the spectral index map between 5 GHz ground observations (left)/ or space VLBI observations (right) and 15 GHz ground image for 3C 345 was made. The corresponding spectral index profile are presented in Fig. 6.25 and 6.28, respectively.

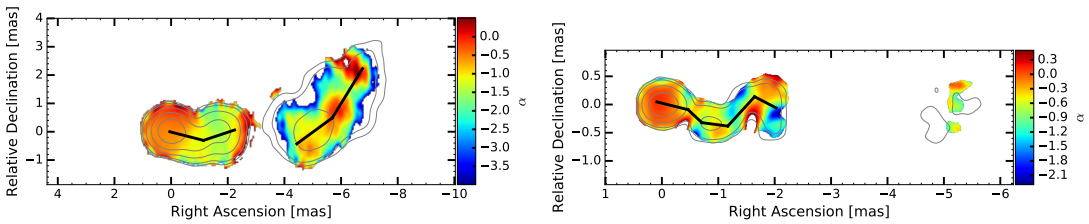

Figure E.5: Line in which the spectral index map between 15 GHz and 22 GHz (left) and between 22 GHz and 43 GHz (right) ground VLBI observations for 3C 345 was made. The corresponding spectral index profile are presented in Fig. 6.26 and 6.27, respectively.

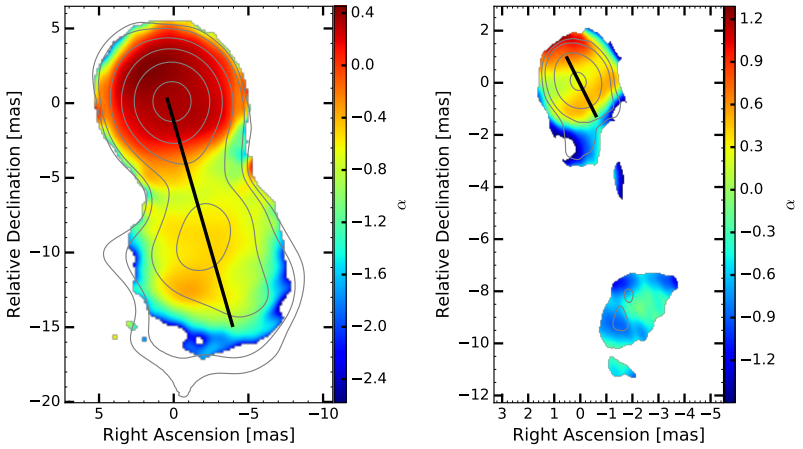

Figure E.6: Line in which the spectral index map between 1.6 GHz ground observations (left)/ or space VLBI observations (right) and 5 GHz ground image for 1642+690 was made. The corresponding spectral index profile are presented in Fig. 6.34 and 6.36, respectively.

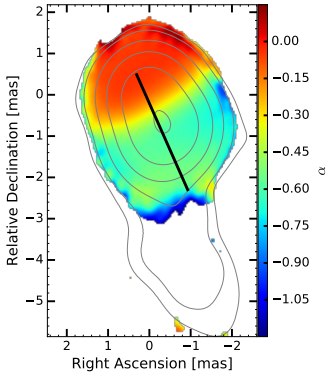

Figure E.7: Line in which the spectral index map between 5 GHz and 15 GHz ground observations for 1642+690 was made. The corresponding spectral index profile are presented in Fig. 6.35.

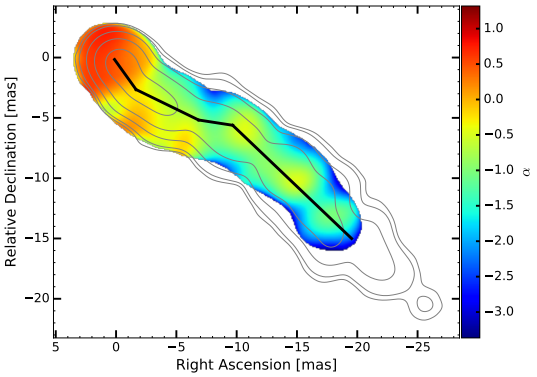

Figure E.8: Line in which the spectral index map between our ground observations at 5 GHz and 15 GHz MOJAVE observations for 3C 273was made. The corresponding spectral index profile are presented in Fig. 6.40.

Appendix F

Results from the numerical calculations of the stability analysis

Here we present the tables with all the values of the simulated observed wavelengths and the estimated Mach number values for all the calculations presented in Chapter 7, section 7.2.4.b. We also present the remaining plots of λ_{obs} as a function of the density ratio obtained from this analysis.

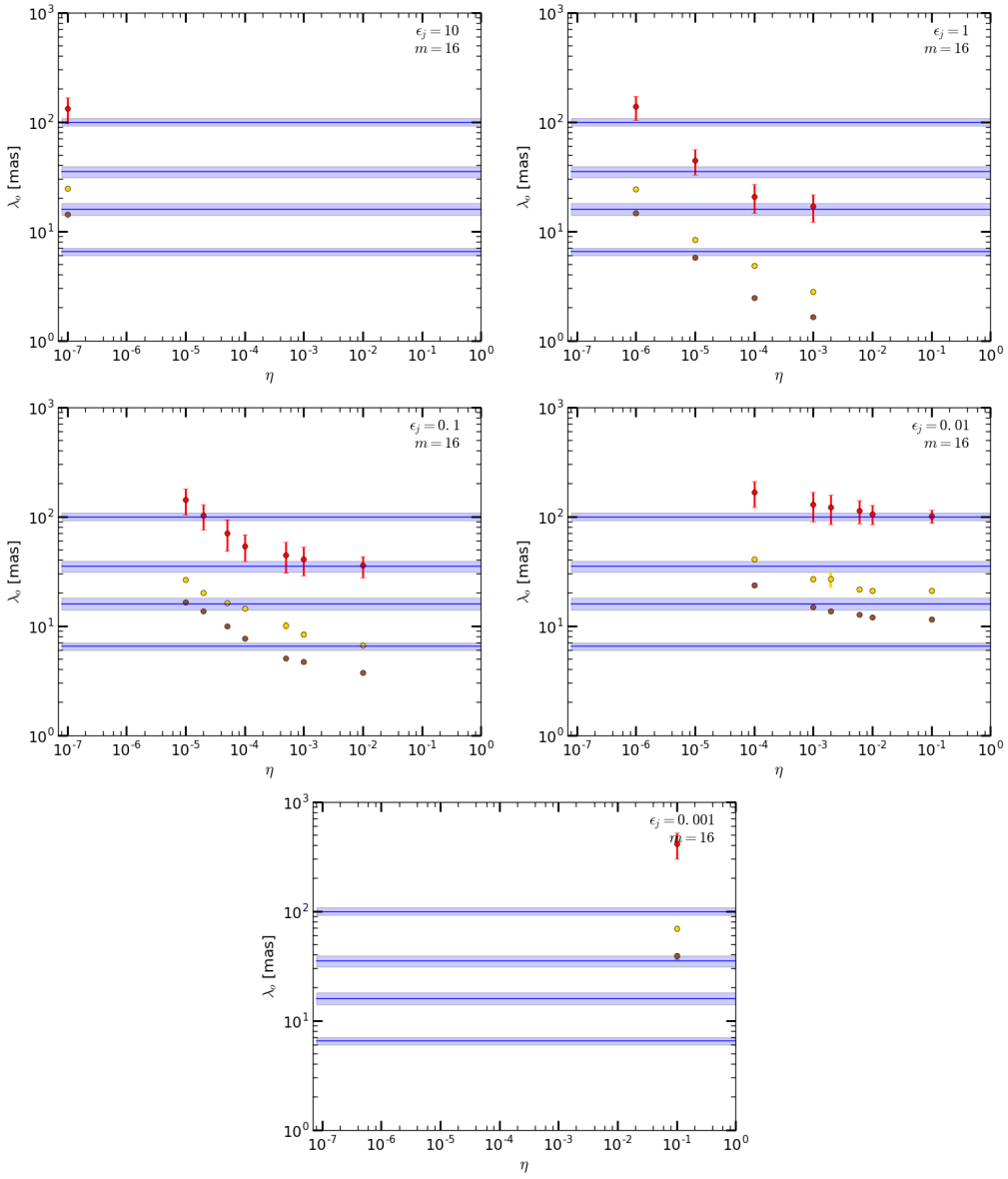

Figure F.1: Corresponding observed wavelengths from the calculations for $m = 16$. The color scale and the meaning of the horizontal lines are the same as used in Fig 7.15. The corresponding jet internal energy for each plot is written in the figure.

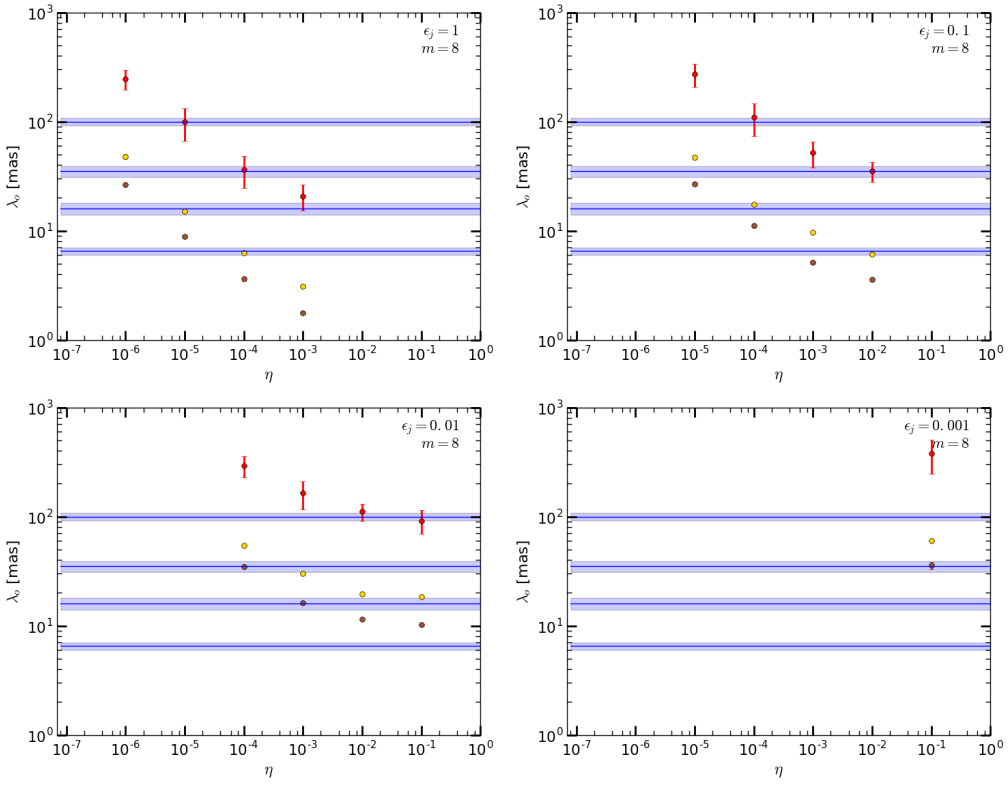

Figure F.2: Corresponding observed wavelengths from the calculations for $m = 8$. The color scale and the meaning of the horizontal lines are the same as used in Fig 7.15. The corresponding jet internal energy for each plot is written in the figure.

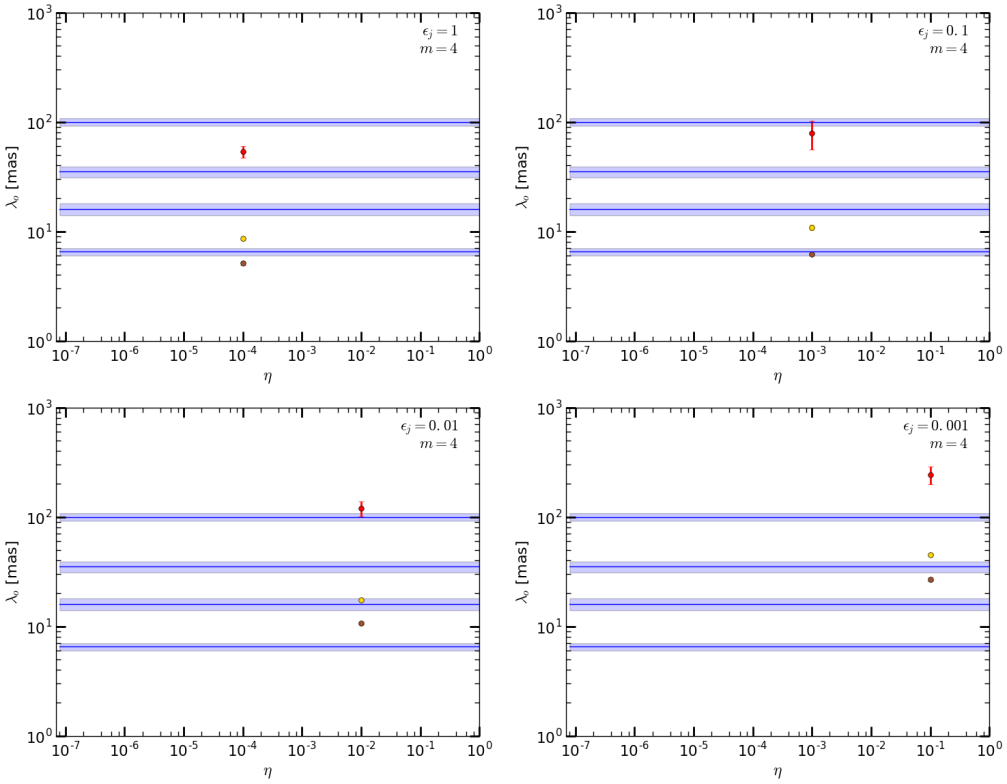

Figure F.3: Corresponding observed wavelengths from the calculations for $m = 4$. The color scale and the meaning of the horizontal lines are the same as used in Fig 7.15. The corresponding jet internal energy for each plot is written in the figure.

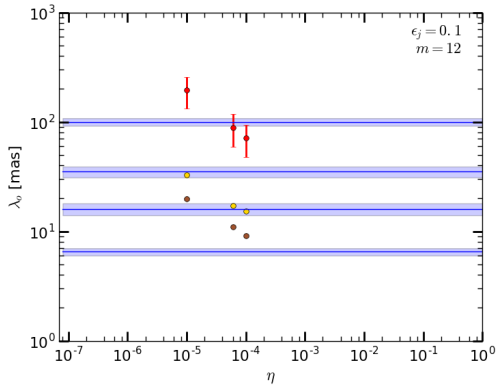

Figure F.4: Corresponding observed wavelengths from the calculations for $m = 12$. The color scale and the meaning of the horizontal lines are the same as used in Fig 7.15. The corresponding jet internal energy for each plot is written in the figure.

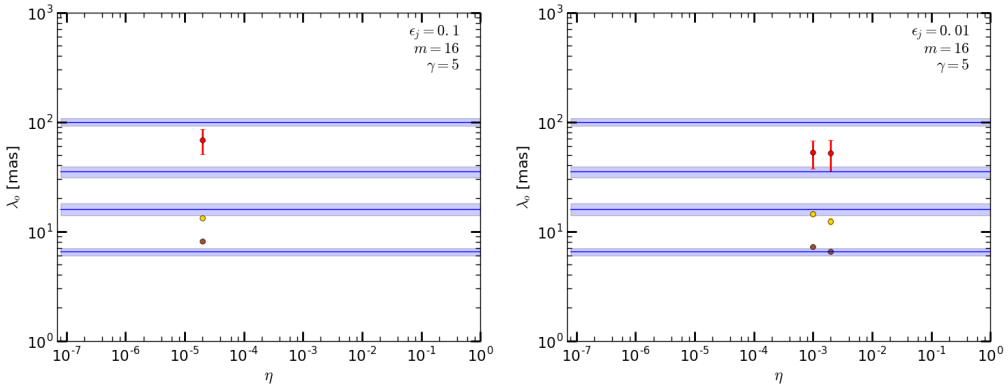

Figure F.5: Corresponding observed wavelengths from the calculations for $m = 16$ and $\gamma = 5$. The color scale and the meaning of the horizontal lines are the same as used in Fig 7.15. The corresponding jet internal energy for each plot is written in the figure.

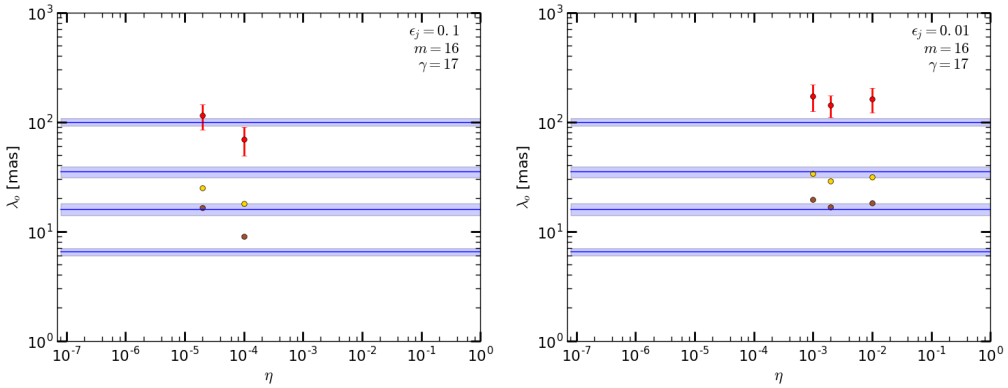

Figure F.6: Corresponding observed wavelengths from the calculations for $m = 16$ and $\gamma = 17$. The color scale and the meaning of the horizontal lines are the same as used in Fig 7.15. The corresponding jet internal energy for each plot is written in the figure.

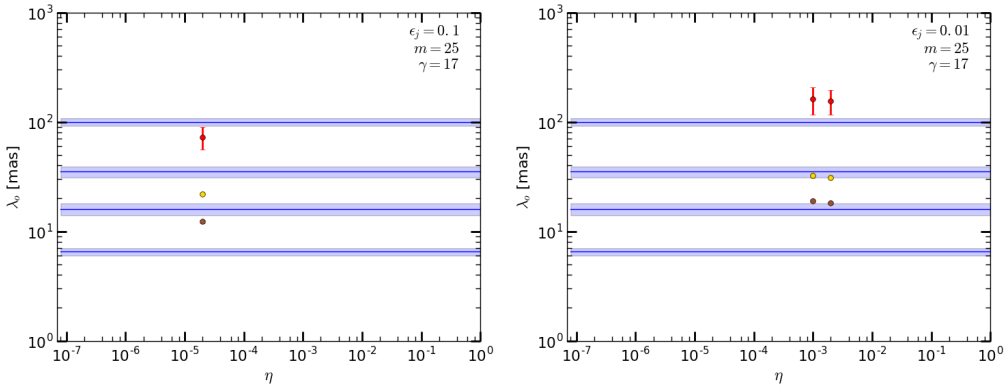

Figure F.7: Corresponding observed wavelengths from the calculations for $m = 25$ and $\gamma = 17$. The color scale and the meaning of the horizontal lines are the same as used in Fig 7.15. The corresponding jet internal energy for each plot is written in the figure.

Table F.1: Solutions of the dispersion relation for $m = 16$ and $\gamma = 12$

Mode	m	$\varepsilon_{\rm j}$	η	$M_{\rm j}$	ω $[c/R_{\rm j}]$	$\Re(k)$ $[1/R_{\rm j}]$	λ [mas]	Dispersion
H_s	16	10	10^{-7}	1.55	0.0019−0.0052	0.0054−0.0117	96.69−167.61	
H_{b_1}	16	10	10^{-7}	1.55	0.0053−0.014	0.0310−0.0380	23.82−25.59	0.135
H_{b_2}	16	10	10^{-7}	1.55	0.0070−0.0120	0.0520−0.0590	14.00−14.62	
H_s	16	1	10^{-6}	1.94	0.0018−0.0050	0.0052−0.0110	103.97−171.92	
H_{b_1}	16	1	10^{-6}	1.94	0.0050−0.010	0.0310−0.0380	23.48−25.29	0.171
H_{b_2}	16	1	10^{-6}	1.94	0.0060−0.0125	0.0500−0.0590	14.15−14.96	
H_s	16	1	10^{-5}	1.94	0.0055−0.0150	0.0160−0.0340	32.91−55.65	
H_{b_1}	16	1	10^{-5}	1.94	0.0150−0.0280	0.0900−0.1100	8.02−8.77	0.774
H_{b_2}	16	1	10^{-5}	1.94	0.0205−0.0400	0.1300−0.1600	5.48−6.01	
H_s	16	1	10^{-4}	1.94	0.012−0.034	0.033−0.076	14.7−26.7	
H_{b_1}	16	1	10^{-4}	1.94	0.050−0.090	0.180−0.230	4.69−5.05	1.207
H_{b_2}	16	1	10^{-4}	1.94	0.050−0.090	0.310−0.365	2.39−2.53	
H_s	16	1	0.001	1.94	0.023−0.056	0.046−0.105	12.23−21.57	
H_{b_1}	16	1	0.001	1.94	0.086−0.151	0.310−0.400	2.63−2.93	1.358
H_{b_2}	16	1	0.001	1.94	0.127−0.221	0.520−0.630	1.61−1.67	
H_s	16	0.1	10^{-5}	4.21	0.0018−0.0050	0.0050−0.0110	103.97−180.10	
H_{b_1}	16	0.1	10^{-5}	4.21	0.0050−0.010	0.0290−0.0360	25.28−27.40	0.187
H_{b_2}	16	0.1	10^{-5}	4.21	0.0060−0.0110	0.0450−0.0520	16.05−16.87	
H_s	16	0.1	2×10^{-5}	4.21	0.0025−0.0067	0.0070−0.0150	75.20−128.62	
H_{b_1}	16	0.1	2×10^{-5}	4.21	0.0064−0.0120	0.0380−0.0460	19.34−20.81	0.183
H_{b_2}	16	0.1	2×10^{-5}	4.21	0.010−0.0220	0.0570−0.0710	13.42−14.00	
H_s	16	0.1	5×10^{-5}	4.21	0.0040−0.010	0.010−0.0230	48.22−93.20	
H_{b_1}	16	0.1	5×10^{-5}	4.21	0.010−0.0190	0.0500−0.0600	16.04−16.45	0.332
H_{b_2}	16	0.1	5×10^{-5}	4.21	0.0130−0.0260	0.0770−0.0940	9.67−10.28	
H_s	16	0.1	10^{-4}	4.21	0.0045−0.0126	0.0129−0.0286	38.88−68.18	
H_{b_1}	16	0.1	10^{-4}	4.21	0.0160−0.0330	0.0600−0.0800	13.98−14.94	0.487
H_{b_2}	16	0.1	10^{-4}	4.21	0.0170−0.0325	0.1−0.1200	7.51−7.92	
H_s	16	0.1	5×10^{-4}	4.21	0.0060−0.0160	0.0150−0.0360	30.45−58.02	
H_{b_1}	16	0.1	5×10^{-4}	4.21	0.0300−0.0500	0.0900−0.1200	9.35−10.90	0.755
H_{b_2}	16	0.1	5×10^{-4}	4.21	0.0300−0.0600	0.1600−0.1900	5.06−5.06	
H_s	16	0.1	0.001	4.21	0.007−0.017	0.017−0.038	28.71−53.06	
H_{b_1}	16	0.1	0.001	4.21	0.033−0.057	0.107−0.140	7.88−8.84	0.972
H_{b_2}	16	0.1	0.001	4.21	0.050−0.090	0.186−0.236	4.50−4.84	
H_s	16	0.1	0.01	4.21	0.019−0.035	0.030−0.056	27.79−43.23	
H_{b_1}	16	0.1	0.01	4.21	0.063−0.110	0.160−0.210	6.56−6.77	0.972
H_{b_2}	16	0.1	0.01	4.21	0.080−0.140	0.250−0.320	3.65−3.87	
H_s	16	0.01	10^{-4}	12.53	0.0015−0.0041	0.0042−0.0092	121.71−211.18	
H_{b_1}	16	0.01	10^{-4}	12.53	0.0050−0.010	0.0200−0.0260	39.00−41.94	0.499
H_{b_2}	16	0.01	10^{-4}	12.53	0.0054−0.010	0.0320−0.0390	22.68−24.73	
H_s	16	0.01	10^{-3}	12.53	0.0024−0.0055	0.0054−0.0122	89.69−166.25	
H_{b_1}	16	0.01	10^{-3}	12.53	0.0110−0.0190	0.0340−0.0450	25.14−28.41	0.096
H_{b_2}	16	0.01	10^{-3}	12.53	0.0160−0.0310	0.0600−0.0760	14.61−14.95	
H_s	16	0.01	2×10^{-3}	12.53	0.0030−0.0060	0.0060−0.0130	85.19−157.74	
H_{b_1}	16	0.01	2×10^{-3}	12.53	0.0120−0.0200	0.0330−0.0490	22.55−31.01	0.075
H_{b_2}	16	0.01	2×10^{-3}	12.53	0.0190−0.0330	0.0660−0.0830	13.14−13.99	
H_s	16	0.01	6×10^{-3}	12.53	0.0045−0.0084	0.0078−0.0152	85.60−140.39	
H_{b_1}	16	0.01	6×10^{-3}	12.53	0.0150−0.0250	0.0440−0.0570	20.47−22.59	0.155
H_{b_2}	16	0.01	6×10^{-3}	12.53	0.0210−0.0360	0.0720−0.0890	12.40−12.89	
H_s	16	0.01	0.01	12.53	0.006−0.011	0.01−0.018	84.37−126.43	
H_{b_1}	16	0.01	0.01	12.53	0.019−0.033	0.049−0.066	19.86−21.85	0.174
H_{b_2}	16	0.01	0.01	12.53	0.025−0.045	0.079−0.100	11.95−12.18	
H_s	16	0.01	0.1	12.53	0.015−0.022	0.020−0.029	87.23−114.63	
H_{b_1}	16	0.01	0.1	12.53	0.047−0.078	0.077−0.111	19.85−21.84	0.183
H_{b_2}	16	0.01	0.1	12.53	0.070−0.120	0.125−0.180	10.94−11.94	
H_s	16	0.001	0.1	39.36	0.005−0.007	0.006−0.009	302.69−520.51	
H_{b_1}	16	0.001	0.1	39.36	0.016−0.021	0.025−0.031	65.50−72.76	9.963
H_{b_2}	16	0.001	0.1	39.36	0.027−0.035	0.045−0.051	41.00−36.48	

Table F.2: Solutions of the dispersion relation for $m = 8$ and $\gamma = 12$

Mode	m	$\varepsilon_{\rm j}$	η	$M_{\rm j}$	ω $[c/R_{\rm j}]$	$\Re(k)$ $[1/R_{\rm j}]$	λ [mas]	Dispersion
H_s	8	1	10^{-6}	1.94	0.0010−0.0020	0.0030−0.0052	195.02−296.18	
H_{b_1}	8	1	10^{-6}	1.94	0.0030−0.0044	0.0160−0.0190	45.03−50.57	2.166
H_{b_2}	8	1	10^{-6}	1.94	0.0035−0.0047	0.0280−0.0300	26.01−26.86	
H_s	8	1	10^{-5}	1.94	0.0024−0.0071	0.0065−0.0164	66.41−131.81	
H_{b_1}	8	1	10^{-5}	1.94	0.0080−0.0160	0.0500−0.0620	14.29−15.66	0.384
H_{b_2}	8	1	10^{-5}	1.94	0.010−0.0200	0.0820−0.0970	8.54−9.14	
H_s	8	1	10^{-4}	1.94	0.007−0.019	0.018−0.044	24.59−48.24	
H_{b_1}	8	1	10^{-4}	1.94	0.024−0.047	0.126−0.156	6.03−6.45	0.989
H_{b_2}	8	1	10^{-4}	1.94	0.030−0.060	0.205−0.249	3.48−3.76	
H_s	8	1	0.001	1.94	0.019−0.038	0.038−0.077	15.33−26.25	
H_{b_1}	8	1	0.001	1.94	0.061−0.114	0.265−0.336	2.96−3.22	1.307
H_{b_2}	8	1	0.001	1.94	0.083−0.161	0.445−0.540	1.74−1.82	
H_s	8	0.1	10^{-5}	4.21	0.0010−0.0022	0.0027−0.0052	206.16−335.70	
H_{b_1}	8	0.1	10^{-5}	4.21	0.0026−0.0053	0.0160−0.0200	44.57−49.07	2.956
H_{b_2}	8	0.1	10^{-5}	4.21	0.0032−0.0064	0.0270−0.0320	25.70−27.65	
H_s	8	0.1	10^{-4}	4.21	0.0024−0.0066	0.0060−0.0150	73.34−146.59	
H_{b_1}	8	0.1	10^{-4}	4.21	0.0075−0.0140	0.0440−0.0530	16.86−18.02	0.269
H_{b_2}	8	0.1	10^{-4}	4.21	0.010−0.0210	0.0680−0.0820	10.78−11.35	
H_s	8	0.1	0.001	4.21	0.006−0.013	0.014−0.029	37.84−65.61	
H_{b_1}	8	0.1	0.001	4.21	0.022−0.042	0.090−0.110	9.65−9.66	0.738
H_{b_2}	8	0.1	0.001	4.21	0.025−0.047	0.150−0.180	4.95−5.26	
H_s	8	0.1	0.01	4.21	0.016−0.027	0.028−0.048	28.09−42.24	
H_{b_1}	8	0.1	0.01	4.21	0.044−0.080	0.150−0.190	5.97−6.20	1.003
H_{b_2}	8	0.1	0.01	4.21	0.051−0.091	0.230−0.280	3.48−3.67	
H_s	8	0.01	10^{-4}	12.53	0.0010−0.0021	0.0026−0.0048	227.82−355.68	
H_{b_1}	8	0.01	10^{-4}	12.53	0.0024−0.0045	0.0140−0.0170	52.60−56.70	3.931
H_{b_2}	8	0.01	10^{-4}	12.53	0.0032−0.0068	0.0220−0.0260	34.26−35.00	
H_s	8	0.01	10^{-3}	12.53	0.0020−0.0043	0.0044−0.0095	116.13−210.87	
H_{b_1}	8	0.01	10^{-3}	12.53	0.0070−0.0140	0.0280−0.0364	29.31−31.28	0.404
H_{b_2}	8	0.01	10^{-3}	12.53	0.0080−0.0150	0.0480−0.0565	15.85−16.45	
H_s	8	0.01	0.01	12.53	0.005−0.009	0.009−0.015	90.54−130.82	
H_{b_1}	8	0.01	0.01	12.53	0.014−0.025	0.046−0.060	18.76−20.52	0.208
H_{b_2}	8	0.01	0.01	12.53	0.017−0.030	0.073−0.088	11.33−11.74	
H_s	8	0.01	0.1	12.53	0.012−0.017	0.017−0.026	69.32−114.11	
H_{b_1}	8	0.01	0.1	12.53	0.035−0.056	0.070−0.092	17.98−18.76	0.260
H_{b_2}	8	0.01	0.1	12.53	0.043−0.078	0.106−0.143	10.11−10.44	
H_s	8	0.001	0.1	39.36	0.004−0.005	0.005−0.008	246.47−507.97	
H_{b_1}	8	0.001	0.1	39.36	0.012−0.016	0.023−0.027	59.67−59.69	7.850
H_{b_2}	8	0.001	0.1	39.36	0.023−0.030	0.040−0.050	32.83−38.62	

Table F.3: Solutions of the dispersion relation for $m = 4$ and $\gamma = 12$

Mode	m	ε_j	η	M_j	ω $[c/R_\mathrm{j}]$	$\Re(k)$ $[1/R_\mathrm{j}]$	λ [mas]	Dispersion
H_s	4	1	0.0001	1.94	0.005−0.01	0.015−0.023	47.11−59.81	
H_{b_1}	4	1	0.0001	1.94	0.013−0.028	0.086−0.108	8.22−9.01	0.765
H_{b_2}	4	1	0.0001	1.94	0.016−0.035	0.140−0.170	4.87−5.31	
H_s	4	0.1	0.001	4.21	0.005−0.009	0.01−0.020	55.56−101.93	
H_{b_1}	4	0.1	0.001	4.21	0.013−0.026	0.070−0.090	10.27−11.54	0.606
H_{b_2}	4	0.1	0.001	4.21	0.015−0.033	0.120−0.140	6.15−6.27	
H_s	4	0.01	0.01	12.53	0.004−0.007	0.008−0.013	100.35−138.85	
H_{b_1}	4	0.01	0.01	12.53	0.01−0.019	0.047−0.058	16.86−17.78	0.280
H_{b_2}	4	0.01	0.01	12.53	0.013−0.026	0.073−0.089	10.44−10.97	
H_s	4	0.001	0.1	39.36	0.003−0.004	0.005−0.007	197.60−287.79	
H_{b_1}	4	0.001	0.1	39.36	0.014−0.018	0.027−0.032	43.65−46.53	2.09
H_{b_2}	4	0.001	0.1	39.36	0.014−0.018	0.039−0.041	27.79−25.73	

Table F.4: Solutions of the dispersion relation for $m = 12$ and $\gamma = 12$

Mode	m	ε_j	η	M_j	ω $[c/R_\mathrm{j}]$	$\Re(k)$ $[1/R_\mathrm{j}]$	λ [mas]	Dispersion
H_s	12	0.01	10^{-5}	4.21	0.0012−0.0036	0.0034−0.0083	133.23−257.61	
H_{b_1}	12	0.01	10^{-5}	4.21	0.0039−0.0079	0.0230−0.0290	31.15−34.43	0.912
H_{b_2}	12	0.01	10^{-5}	4.21	0.0045−0.0088	0.0370−0.0430	19.24−20.25	
H_s	12	0.01	6×10^{-5}	4.21	0.0030−0.0080	0.0077−0.0185	59.55−117.70	
H_{b_1}	12	0.01	6×10^{-5}	4.21	0.0080−0.0150	0.0455−0.0547	16.56−17.54	0.280
H_{b_2}	12	0.01	6×10^{-5}	4.21	0.0120−0.0240	0.0700−0.0850	10.78−11.34	
H_s	12	0.1	10^{-4}	4.21	0.0030−0.010	0.0090−0.0230	47.94−93.90	
H_{b_1}	12	0.1	10^{-4}	4.21	0.0110−0.0210	0.0530−0.0650	14.94−15.66	0.376
H_{b_2}	12	0.1	10^{-4}	4.21	0.0140−0.0280	0.0840−0.1020	8.89−9.40	

Table F.5: Solutions of the dispersion relation for $m = 16$ and $\gamma = 5$

Mode	m	ε_j	η	M_j	ω $[c/R_\mathrm{j}]$	$\Re(k)$ $[1/R_\mathrm{j}]$	λ [mas]	Dispersion
H_s	16	0.01	0.001	12.53	0.004−0.010	0.012−0.027	37.26−67.77	
H_{b_1}	16	0.01	0.001	12.53	0.019−0.036	0.062−0.084	13.68−15.38	0.508
H_{b_2}	16	0.01	0.001	12.53	0.014−0.026	0.103−0.118	7.10−7.36	
H_s	16	0.01	0.002	12.53	0.004−0.011	0.012−0.028	35.49−68.72	
H_{b_1}	16	0.01	0.002	12.53	0.021−0.037	0.071−0.094	11.55−13.20	0.590
H_{b_2}	16	0.01	0.002	12.53	0.025−0.054	0.123−0.156	6.45−6.71	
H_s	16	0.1	2×10^{-5}	4.21	0.003−0.008	0.010−0.021	50.50−85.77	
H_{b_1}	16	0.1	2×10^{-5}	4.21	0.008−0.016	0.056−0.068	12.64−13.86	0.467
H_{b_2}	16	0.1	2×10^{-5}	4.21	0.009−0.017	0.088−0.100	7.93−8.32	

Table F.6: Solutions of the dispersion relation for $\gamma = 17$

Mode	m	ε_j	η	M_j	ω $[c/R_\mathrm{j}]$	$\Re(k)$ $[1/R_\mathrm{j}]$	λ [mas]	Dispersion
H_s	25	0.01	0.001	12.55	0.002−0.005	0.005−0.010	116.90−206.14	
H_{b_1}	25	0.01	0.001	12.55	0.009−0.015	0.028−0.036	30.57−34.39	0.380
H_{b_2}	25	0.01	0.001	12.55	0.017−0.026	0.050−0.062	18.50−19.57	
H_s	25	0.01	0.002	12.55	0.003−0.006	0.005−0.011	115.94−195.36	
H_{b_1}	25	0.01	0.002	12.55	0.011−0.018	0.031−0.040	29.61−32.61	0.310
H_{b_2}	25	0.01	0.002	12.55	0.017−0.027	0.052−0.064	17.66−18.55	
H_s	25	0.1	2×10^{-5}	4.21	0.004−0.009	0.010−0.020	56.13−89.37	
H_{b_1}	25	0.1	2×10^{-5}	4.21	0.011−0.021	0.040−0.052	21.56−22.45	0.165
H_{b_2}	25	0.1	2×10^{-5}	4.21	0.012−0.022	0.063−0.077	11.87−12.76	
H_s	16	0.01	0.001	12.53	0.002−0.004	0.004−0.009	125.88−219.63	
H_{b_1}	16	0.01	0.001	12.53	0.008−0.014	0.027−0.035	32.00−35.60	0.531
H_{b_2}	16	0.01	0.001	12.53	0.014−0.024	0.047−0.058	19.03−19.93	
H_s	16	0.01	0.002	12.53	0.003−0.005	0.005−0.010	122.05−203.81	
H_{b_1}	16	0.01	0.002	12.53	0.010−0.016	0.030−0.038	29.80−32.57	0.400
H_{b_2}	16	0.01	0.002	12.53	0.014−0.024	0.050−0.061	17.67−18.51	
H_s	16	0.01	0.01	12.55	0.003−0.005	0.005−0.010	122.05−203.81	
H_{b_1}	16	0.01	0.01	12.55	0.010−0.016	0.030−0.038	29.80−32.57	0.397
H_{b_2}	16	0.01	0.01	12.55	0.014−0.024	0.050−0.061	17.67−18.51	
H_s	16	0.1	10^{-4}	4.21	0.004−0.010	0.010−0.023	49.14−90.37	
H_{b_1}	16	0.1	10^{-4}	4.21	0.015−0.029	0.051−0.067	17.27−18.58	0.319
H_{b_2}	16	0.1	10^{-4}	4.21	0.015−0.027	0.086−0.103	8.74−9.25	
H_s	16	0.1	2×10^{-5}	4.21	0.002−0.006	0.006−0.013	84.23−144.92	
H_{b_1}	16	0.1	2×10^{-5}	4.21	0.006−0.010	0.032−0.038	24.15−25.40	0.088
H_{b_2}	16	0.1	2×10^{-5}	4.21	0.009−0.018	0.048−0.059	16.03−16.99	

Bibliography

Abdo, A. A., Ackermann, M., Ajello, M., et al. 2010, ApJ, 714, L73

Abraham, Z., Carrara, E. A., Zensus, J. A., & Unwin, S. C. 1996, A&AS, 115, 543

Akyuz, A., Thompson, D. J., Donato, D., et al. 2013, A&A, 556, A71

Alef, W. & Porcas, R. W. 1986, A&A, 168, 365

Aloy, M.-A., Gómez, J.-L., Ibáñez, J.-M., Martí, J.-M., & Müller, E. 2000, ApJ, 528, L85

Andreyanov, V. V., Kardashev, N. S., & Khartov, V. V. 2014, Cosmic Research, 52, 319

Antonucci, R. 1993, ARA&A, 31, 473

Antonucci, R. R. J. & Miller, J. S. 1985, ApJ, 297, 621

Asada, K., Inoue, M., Uchida, Y., et al. 2002, PASJ, 54, L39

Asada, K., Nakamura, M., Inoue, M., Kameno, S., & Nagai, H. 2010, ApJ, 720, 41

Baade, W. & Minkowski, R. 1954, ApJ, 119, 215

Baczko, A.-K., Schulz, R., Kadler, M., et al. 2016, A&A, 593, A47

Begelman, M. C. 1979, MNRAS, 187, 237

Bennett, A. S. 1962, MmRAS, 68, 163

Beuchert, T., Kadler, M., Perucho, M., et al. 2018, A&A, 610, A32

Bevington, P. R. & Robinson, D. K. 1992, Data reduction and error analysis for the physical sciences

Birkinshaw, M. 1984, MNRAS, 208, 887

Birkinshaw, M. 1991, MNRAS, 252, 505

Blandford, R. D. & Königl, A. 1979, ApJ, 232, 34

Blandford, R. D. & Rees, M. J. 1974, MNRAS, 169, 395

Blumenthal, G. R. & Gould, R. J. 1970, Reviews of Modern Physics, 42, 237

Boccardi, B. 2015, PhD thesis, Universität zu Köln

Bruni, G., Anderson, J. M., Alef, W., Lobanov, A. P., & Zensus, J. A. 2015, in Proceedings of Science, Vol. EVN 2014, Proceedings of the 12th European VLBI Network Symposium, 119

Clausen-Brown, E., Lyutikov, M., & Kharb, P. 2011, MNRAS, 415, 2081

Cotton, W. D. 1995, in Astronomical Society of the Pacific Conference Series, Vol. 82, Very Long Baseline Interferometry and the VLBA, ed. J. A. Zensus, P. J. Diamond, & P. J. Napier, 189

Dodson, R., Rioja, M. J., Molina, S. N., & Gómez, J. L. 2017, ApJ, 834, 177

Edge, D. O., Shakeshaft, J. R., McAdam, W. B., Baldwin, J. E., & Archer, S. 1959, MmRAS, 68, 37

Elitzur, M. 2006, New A Rev., 50, 728

Ester, M., Kriegel, H.-P., Sander, J., & Xu, X. 1996, in (AAAI Press), 226–231

Fanaroff, B. L. & Riley, J. M. 1974, MNRAS, 167, 31P

Ferrari, A., Trussoni, E., & Zaninetti, L. 1978, A&A, 64, 43

Fomalont, E. B. 1999, in Astronomical Society of the Pacific Conference Series, Vol. 180, Synthesis Imaging in Radio Astronomy II, ed. G. B. Taylor, C. L. Carilli, & R. A. Perley, 301

Ford, H. A., Anderson, R., Belousov, K., et al. 2014, in Proceedings of the SPIE, Vol. 9145, id. 91450

Fromm, C. 2015, Spectral Evolution in Blazars: The Case of CTA 102

Fromm, C. M., Perucho, M., Mimica, P., & Ros, E. 2016, A&A, 588, A101

Fromm, C. M., Perucho, M., Porth, O., et al. 2018, A&A, 609, A80

Fromm, C. M., Ros, E., Perucho, M., et al. 2013a, A&A, 551, A32

Fromm, C. M., Ros, E., Perucho, M., et al. 2013b, A&A, 557, A105

Fromm, C. M., Ros, E., Perucho, M., et al. 2013c, A&A, 557, A105

Gabuzda, D. C. 2015, in Astrophysics and Space Science Library, Vol. 414, The Formation and Disruption of Black Hole Jets, ed. I. Contopoulos, D. Gabuzda, & N. Kylafis, 117

Gabuzda, D. C., Gómez, J. L., & Agudo, I. 2001, MNRAS, 328, 719

Georganopoulos, M. & Kazanas, D. 2004, ApJ, 604, L81

Ghisellini, G., ed. 2013, Lecture Notes in Physics, Berlin Springer Verlag, Vol. 873, Radiative Processes in High Energy Astrophysics

Gould, R. J. 1979, A&A, 76, 306

Greisen, E. W. 1990, in Acquisition, Processing and Archiving of Astronomical Images, ed. G. Longo & G. Sedmak, 125–142

Gu, M., Cao, X., & Jiang, D. R. 2001, MNRAS, 327, 1111

Gupta, A. C., Krichbaum, T. P., Wiita, P. J., et al. 2012, MNRAS, 425, 1357

Haardt, F. & Maraschi, L. 1991, ApJ, 380, L51

Hardee, P. E. 1982, ApJ, 257, 509

Hardee, P. E. 1984, ApJ, 287, 523

Hardee, P. E. 1986, ApJ, 303, 111

Hardee, P. E. 1987, ApJ, 313, 607

Hardee, P. E. 2000, ApJ, 533, 176

Hardee, P. E. 2006, in American Institute of Physics Conference Series, Vol. 856, Relativistic Jets: The Common Physics of AGN, Microquasars, and Gamma-Ray Bursts, ed. P. A. Hughes & J. N. Bregman, 57–77

Hirotani, K. 2005, ApJ, 619, 73

Hodgson, J. A. 2015, PhD thesis, Universität zu Köln

Högbom, J. A. 1974, A&AS, 15, 417

Hovatta, T., Aller, M. F., Aller, H. D., et al. 2014, AJ, 147, 143

Hughes, P. A. 1991, Beams and jets in astrophysics

Ichikawa, K. & Inayoshi, K. 2017, ApJ, 840, L9

Jackson, J. D. 1962, Classical Electrodynamics

Jorstad, S., Marscher, A., Larionov, V., et al. 2013, in European Physical Journal Web of Conferences, Vol. 61, European Physical Journal Web of Conferences, 04003

Jorstad, S. G., Marscher, A. P., Lister, M. L., et al. 2005, AJ, 130, 1418

Kellermann, K. I., Sramek, R., Schmidt, M., Shaffer, D. B., & Green, R. 1989, AJ, 98, 1195

Kollgaard, R. I., Wardle, J. F. C., & Roberts, D. H. 1989, AJ, 97, 1550

Komissarov, S. 2012, Central Engines: Acceleration, Collimation and Confinement of Jets, ed. M. Boettcher, D. E. Harris, & H. Krawczynski, 81–114

Komissarov, S. S., Porth, O., & Lyutikov, M. 2015, Computational Astrophysics and Cosmology, 2, 9

Komissarov, S. S., Vlahakis, N., Königl, A., & Barkov, M. V. 2009, MNRAS, 394, 1182

Konigl, A. 1981, ApJ, 243, 700

Kovalev, Y. 2014, in COSPAR Meeting, Vol. 40, 40th COSPAR Scientific Assembly

Krichbaum, T., Witzel, A., & Zensus, J. A. 2000, in EVN Symposium 2000, Proceedings of the 5th european VLBI Network Symposium, ed. J. E. Conway, A. G. Polatidis, R. S. Booth, & Y. M. Pihlström, 25

Krichbaum, T. P., Hummel, C. A., Quirrenbach, A., et al. 1990, A&A, 230, 271

Lewis, J. P. 1995, in Vision Interface '95, 120

Lister, M. L., Aller, M. F., Aller, H. D., et al. 2013, AJ, 146, 120

Lister, M. L., Aller, M. F., Aller, H. D., et al. 2016, AJ, 152, 12

Liu, W.-P. & Shen, Z.-Q. 2009, Research in Astronomy and Astrophysics, 9, 520

Lobanov, A. 2015, A&A, 574, A84

Lobanov, A. P. 1996, PhD thesis, New Mexico Institute of Mining and Technology

Lobanov, A. P. 1998a, A&AS, 132, 261

Lobanov, A. P. 1998b, A&A, 330, 79

Lobanov, A. P. 2005, ArXiv Astrophysics e-prints [astro-ph/0503225]

Lobanov, A. P., Krichbaum, T. P., Witzel, A., et al. 1998, A&A, 340, L60

Lobanov, A. P., Krichbaum, T. P., Witzel, A., & Zensus, J. A. 2006, PASJ, 58, 253

Lobanov, A. P. & Zensus, J. A. 1999, ApJ, 521, 509

Lobanov, A. P. & Zensus, J. A. 2001, Science, 294, 128

Longair, M. S. 2011, High Energy Astrophysics

Lynden-Bell, D. 1969, Nature, 223, 690

Lynds, C. R., Stockton, A. N., & Livingston, W. C. 1965, ApJ, 142, 1667

Lyutikov, M., Pariev, V. I., & Gabuzda, D. C. 2005, MNRAS, 360, 869

Marscher, A. P. 1983, ApJ, 264, 296

Marscher, A. P. & Gear, W. K. 1985, ApJ, 298, 114

Martí, J.-M. 2015, MNRAS, 452, 3106

Martí, J. M., Perucho, M., & Gómez, J. L. 2016, ApJ, 831, 163

McKinney, J. C. & Blandford, R. D. 2009, MNRAS, 394, L126

Mezcua, M. 2017, International Journal of Modern Physics D, 26, 1730021

Mignone, A. & Bodo, G. 2006, MNRAS, 368, 1040

Mimica, P. & Aloy, M. A. 2012, MNRAS, 421, 2635

Mimica, P., Aloy, M.-A., Agudo, I., et al. 2009, ApJ, 696, 1142

Mimica, P., Giannios, D., & Aloy, M. A. 2010, MNRAS, 407, 2501

Minkowski, R. & Greenstein, J. L. 1954, ApJ, 119, 238

Moran, J. M. & Dhawan, V. 1995, in Astronomical Society of the Pacific Conference Series, Vol. 82, Very Long Baseline Interferometry and the VLBA, ed. J. A. Zensus, P. J. Diamond, & P. J. Napier, 161

Netzer, H. 2006, in Lecture Notes in Physics, Berlin Springer Verlag, Vol. 693, Physics of Active Galactic Nuclei at all Scales, ed. D. Alloin, 1

Osher, S. & Sethian, J. A. 1988, Journal of Computational Physics, 79, 12

O'Sullivan, S. P. & Gabuzda, D. C. 2009, MNRAS, 400, 26

Otterbein, K. 1996, PhD thesis, PhD thesis, University Göttingen., (1996)

Otterbein, K., Krichbaum, T. P., Kraus, A., et al. 1998, in Astronomical Society of the Pacific Conference Series, Vol. 144, IAU Colloq. 164: Radio Emission from Galactic and Extragalactic Compact Sources, ed. J. A. Zensus, G. B. Taylor, & J. M. Wrobel, 73

Payne, D. G. & Cohn, H. 1985, ApJ, 291, 655

Pearson, T. J., Barthel, P. D., Lawrence, C. R., & Readhead, A. C. S. 1986, ApJ, 300, L25

Pearson, T. J., Unwin, S. C., Cohen, M. H., et al. 1981, Nature, 290, 365

Perucho, M. 2012, in International Journal of Modern Physics Conference Series, Vol. 8, International Journal of Modern Physics Conference Series, 241–252

Perucho, M., Hanasz, M., Martí, J.-M., & Miralles, J.-A. 2007, Phys. Rev. E, 75, 056312

Perucho, M., Kovalev, Y. Y., Lobanov, A. P., Hardee, P. E., & Agudo, I. 2012a, ApJ, 749, 55

Perucho, M. & Lobanov, A. P. 2007, A&A, 469, L23

Perucho, M. & Lobanov, A. P. 2011, A&A, 533, C2

Perucho, M., Lobanov, A. P., & Martí, J. M. 2005, Mem. Soc. Astron. Italiana, 76, 110

Perucho, M., Lobanov, A. P., Martí, J.-M., & Hardee, P. E. 2006, A&A, 456, 493

Perucho, M., Martí, J. M., Cela, J. M., et al. 2010, A&A, 519, A41

Perucho, M., Martí, J. M., & Hanasz, M. 2004, A&A, 427, 431

Perucho, M., Martí-Vidal, I., Lobanov, A. P., & Hardee, P. E. 2012b, A&A, 545, A65

Pier, E. A. & Krolik, J. H. 1993, ApJ, 418, 673

Press, W. H., Teukolsky, S. A., Vetterling, W. T., & Flannery, B. P. 1992, Numerical recipes in FORTRAN. The art of scientific computing

Readhead, A. C. S. 1994, ApJ, 426, 51

Rees, M. J. 1966, Nature, 211, 468

Rees, M. J. 1978, MNRAS, 184, 61P

Ros, E., Zensus, J. A., & Lobanov, A. P. 2000, A&A, 354, 55

Rowan-Robinson, M. 1977, ApJ, 213, 635

Rybicki, G. B. & Lightman, A. P. 1979, Radiative processes in astrophysics

Salpeter, E. E. 1964, ApJ, 140, 796

Sambruna, R. M., Gambill, J. K., Maraschi, L., et al. 2004, ApJ, 608, 698

Schinzel, F. 2011, PhD thesis, Universität zu Köln

Schinzel, F. K., Lobanov, A. P., Taylor, G. B., et al. 2012, A&A, 537, A70

Schmidt, M. 1963, Nature, 197, 1040

Seyfert, C. K. 1943, ApJ, 97, 28

Shakura, N. I. & Sunyaev, R. A. 1973, A&A, 24, 337

Shepherd, M. C., Pearson, T. J., & Taylor, G. B. 1995, in BAAS, Vol. 27, Bulletin of the American Astronomical Society, ed. B. J. Butler & D. O. Muhleman, 903

Shu, C.-W. & Osher, S. 1988, Journal of Computational Physics, 77, 439

Shu, C.-W. & Osher, S. 1989, Journal of Computational Physics, 83, 32

Singal, A. K. 2009, ApJ, 703, L109

Soltan, A. 1982, MNRAS, 200, 115

Stickel, M. & Kuehr, H. 1993, A&AS, 100, 395

Swanenburg, B. N., Bennett, K., Bignami, G. F., et al. 1978, Nature, 275, 298

Tagliaferri, G., Ghisellini, G., Perri, M., et al. 2015, ApJ, 807, 167

Taylor, G. B., Carilli, C. L., & Perley, R. A., eds. 1999, Astronomical Society of the Pacific Conference Series, Vol. 180, Synthesis Imaging in Radio Astronomy II

Thirring, H. 1918, Physikalische Zeitschrift, 19

Türler, M., Courvoisier, T. J.-L., & Paltani, S. 1999, A&A, 349, 45

Türler, M., Courvoisier, T. J.-L., & Paltani, S. 2000, A&A, 361, 850

Unwin, S. C., Cohen, M. H., Pearson, T. J., et al. 1983, ApJ, 271, 536

Urry, C. M. & Padovani, P. 1995, PASP, 107, 803

van Cittert, P. 1934, Physica, 1, 201

Venturi, T., Pearson, T. J., Barthel, P. D., & Unwin, S. C. 1997, A&A, 325, 484

Vlahakis, N. & Königl, A. 2004, ApJ, 605, 656

Walker, R. C., Hardee, P. E., Davies, F. B., Ly, C., & Junor, W. 2018, ApJ, 855, 128

Wehrle, A. E., Cohen, M. H., Unwin, S. C., et al. 1992, ApJ, 391, 589

Weinberg, S. 1972, Gravitation and Cosmology: Principles and Applications of the General Theory of Relativity, 688

Whitney, A. R., Shapiro, I. I., Rogers, A. E. E., et al. 1971, Science, 173, 225

Zel'dovich, Y. B. & Novikov, I. D. 1964, Soviet Physics Doklady, 9, 246

Zensus, J. A., Cohen, M. H., & Unwin, S. C. 1995, ApJ, 443, 35

Zernike, F. 1938, Physica, 5, 785

Acknowledgements

This work would not have been completed without the contribution of several people who I would like to acknowledge here. A special thanks goes to Prof. Dr. Anton Zensus, for the opportunity of carrying my research at the MPIfR, his trust, resources, and the support I have received during this period. I would also like to thank Prof. Dr. Andreas Eckart for reviewing this work.

I would also like to express my gratitude to my advisor Dr. Andrei Lobanov and my co-advisor Prof. Dr. Manel Perucho from the University of Valencia for all the support, discussions, and advice given during this time. I would also like to thank Prof. Dr. Manel Perucho for letting me work at the University of Valencia when it was necessary for the progress of my research, and Prof. Dr. Jose Maria Martí for letting me use his numerical code in order to perform the numerical simulations.

I also want to express my gratitude to the other fellow doctoral researches in the group: Celine, Thalia, Felix and especially to Roberto, Jae-Young, and Anne. I am also grateful to the fellow young researchers in the group: Nick, Bia, Carolina, Victor, and Dhanya. I would also like to give a special thanks to Prof. Dr. Eduardo Ros for his comments and help during the thesis.

In these three years I have also met many nice people who made my life in Bonn easier. Therefore I would like to thank Rebecca, Hans, Maitraiyee, Joseph, and Frederic.

I am also thankful to the IMPRS of which I was part of during my reasearch. A special thanks goes to Rainer and Simone, who have made a big effort in their work for the benefit of all the doctoral researchers in the institute.

I would like also to thank to my friends in Valencia, Jesús, Adrián, David, Samuel, Miguel, and Susana for making my trips to Valencia more enjoyable. Especially, I would like to express my gratitude to Sergio Peréz and Arantxa Triana for their advice, for listening to me and supporting me.

También quiero expresar mi gratitud a mi familia, a mis tios Alberto y Toni, a mi abuela, a mi hermano, y sobretodo a mis padres, por siempre haber estado ahí y por todo el apoyo y cariño dado durante esta tesis. Solo daros las gracias no es suficiente.

Erklärung

Ich versichere, dass ich die von mir vorgelegte Dissertation selbständig angefertigt, die benutzten Quellen und Hilfsmittel vollständig angegeben und die Stellen der Arbeit, einschließlich Tabellen, Karten und Abbildungen, die anderen Werken im Wortlaut oder dem Sinn nach entnommen sind, in jedem Einzelfall als Entlehnung kenntlich gemacht habe; dass diese Dissertation noch keiner anderen Fakultät oder Universität zur Prüfung vorgelegen hat; dass sie, abgesehen von unten angegebenen Teilpublikationen – noch nicht veröffentlicht worden ist sowie, dass ich eine solche Veröffentlichung vor Abschluss des Promotionsverfahrens nicht vornehmen werde. Die Bestimmungen der Promotionsordnung sind mir bekannt. Die von mir vorgelegte Dissertation ist von Prof. Dr. Andreas Eckart und Prof. Dr. J. Anton Zensus betreut worden.

Köln, den 25.02.2019

Publication/Teilpublikationen

- "Probing the innermost regions of AGN jets and their magnetic fields with RadioAstron. II. Observations of 3C 273 at minimum activity", Bruni, G.; Gómez, J. L.; Casadio, C.; Lobanov, A.P.; Kovalev, Y. Y.; Sokolovsky, K. V.; Lisakov, M. M.; Bach, U.; Marscher, A.; Jorstad, S.; Anderson, J. M.; Krichbaum, T. P.; Savolainen, T.; **Vega-García, L.**; Fuentes, A.; Zensus, J. A.; Alberdi, A.; Lee, S.-S.; Lu, R.-S.; Pérez-Torres, M.; Ros, E., 2017, *Astronomy & Astrophysics* 604, 111

- "Derivation of the physical parameters of the jet in S5 0836+710from stability analysis", **Vega-García, L.**; Perucho, M; Lobanov, A.P., submitted to *Astronomy & Astrophysics*

- "Multiband *RadioAstron* space VLBI imaging of the jet in the quasar S5 0836+710", **Vega-García, L.**; Lobanov, A.P.; Perucho, M; Bruni, G.; Ros, E.; Anderson, J.M.; Agudo, I.; Davis, R.; Gómez, J.L.; Kovalev, Y.Y.; Krichbaum, T.P.; Savolainen, T.; Schinzel, F.; Zensus, J.A., submitted to *Astronomy & Astrophysics*